Quantitative analysis of defects in composite material by means of optical lockin thermography

Dissertation

Zur Erlangung des akademischen Grades
einer Doktorin der Ingenieurwissenschaften (Dr.-Ing.)

der Naturwissenschaftlischen Technischen Fakultät III
Chemie, Pharmazie, Bio- und Werkstoffwissenschaften
der Universität des Saarlandes
und
der Ecole Doctorale MIM
der Université Paul-Verlaine/Metz

vorgelegt von

Christine Marguerite Zöcke
aus Saarbrücken

Saarbrücken und Metz, Dezember 2009

Résumé

Les matériaux composites carbone-époxy connaissent un intérêt grandissant dans le domaine de l'aéronautique. Des tests de contrôle non-destructif permettent de détecter des défauts. Ce travail s'attache particulièrement au contrôle non-destructif de matériaux composite carbone-époxy par la thermographie optique lockin. Il élargit le domaine de l'analyse quantitative des mesures thermographiques. Les paramètres géométriques tels la profondeur, la taille et la forme des défauts sont déterminés dans des pièces en matériau composite anisotrope et globalement homogène.

Dans un but d'évaluation quantitative des défauts, des techniques de traitement d'image sont appliquées à des images de longues pièces aéronautiques pour former des vues panoramiques. Des images thermiques prises avant et après chargement mécanique sont superposées afin de pouvoir déterminer un endommagement. Différentes images thermale (lockin et excitation ultrasonore) sont fusionnées afin d'obtenir plus d'information sur des défauts du type impacts.

La formation d'images est modélisée par une fonction de point qui dépend de la profondeur du défaut et de la fréquence de modulation. Un modèle est calculé en utilisant des fonctions de Green et adapté à des matériaux anisotropes. Les grandeurs : profondeur, taille et forme du défaut sont déterminées par des problèmes inverses. Les mesures sont comparées aux simulations numériques et un algorithme de reconstruction des défauts planaires est validé.

Zusammenfassung

In der Luft- und Raumfahrt werden verstärkt kohlefaserverstärkte Kunstoffe (CFK) einge-setzt, die mit Methoden der zerstörungsfreien Prüftechnik auf Defekte hin überprüft wer-den müssen. Diese Dissertation befasst sich mit optischer Lockin Thermographie als zer-störungsfreie Prüftechnik für CFK Werkstoffe. Im Rahmen der Arbeit wurde die quan-titative Analyse von Defekten in global homogenem und anisotropem CFK Material er-weitert.

Im Rahmen der quantitativen Bestimmung von Defekten werden Bildverarbeitungsal-gorithmen auf thermischen Bilder angewandt, um Panorama-Bilder von großen, langen Bauteilen zu erzeugen. Messungen vor- und nach einer Belastung werden verglichen, um ein potentielles Defektwachstum zu bestimmen. Thermische Bilder der Lockin und der Ultraschall angeregten Thermographie werden im Sinne von "Data-Fusion" überlagert, um bessere quantitativen Informationen über Defekte wie Impaktschäden zu erzielen.

Die thermischen Bilder werden durch eine Punktbildfunktion, die von der Tiefe des De-fektes und der Modulationsfrequenz abhängt, modelliert. Die Funktion wird mit Hilfe Green'scher Funktionen aufgestellt und an anisotropem Material adaptiert. Die Param-eter Tiefenlage, Größe und Form eines Defektes werden über die Lösung eines inversen Problem mit numerischen Filter bestimmt. Die Messungen werden mit numerischen Sim-ulationen verglichen. Ein Algorithmus zur Rekonstruktion flacher Defekte wird validiert.

Abstract

In the aerospace industry, carbon-fiber reinforced plastic (CFRP) materials are becoming increasingly popular. Due to mechanical fracture and hence safety related issues, CFRP components must be inspected for defects with non-destructive methods. This thesis focuses on non-destructive testing of CFRP materials with optical lockin thermography. The field of quantitative analysis of thermographic measurements is enhanced. The data of geometrical parameters e.g. depth, size and shape of defects in structures of globally homogeneous and anisotropic CFRP materials is required for fracture mechanics.

To evaluate defects in a quantitative way, image processing algorithms are applied to thermographic phase images in order to get panoramic views of extended aircraft parts and to compare measurements before and after a fatigue load in order to determine potential defect growth. Images of lockin and ultrasound excited thermography are combined with data-fusion techniques to get improved information on defects such as impacts.

The image formation process can be modeled through a point-spread function, which depends on the depth of the defect and the modulation frequency. A function is computed by using Green's functions and is adapted to anisotropic materials. The quantities depth, size and shape of a defect are determined through inverse numerical filters. Measurements are compared to numerical simulations and a reconstruction algorithm of planar subsurface defects is validated.

Nomenclature

Symbol	Unit	Designation
a	Wm^{-3}	Volume heating
A		Volume heating in Fourier space
Am		Amplitude
AOI		Area of interest
$\alpha = \frac{k}{\rho c_P}$	$m^2 s^{-1}$	Thermal diffusivity
C_P	$J^1 kg^{-1} K^{-1}$	Thermal capacity
CFRP		Carbon-fiber reinforced plastic
CMT		Cadmium mercur-tellurid
d	m	Depth of a defect
dB		Decibel
DoG		Difference-of-Gaussian
f	Hz=s^{-1}	Frequency
f_b	Hz=s^{-1}	Blind frequency
f_o	Hz=s^{-1}	Optimal frequency
F	Wm^{-2}	Heat flux
FFT		Fast Fourier transform
FMLT		Frequency modulated lockin thermography
FWHM		Full-width half-maximum

$f_i(t)$		Specified boundary function of kind i
g		Green's function in the time domain
G		Green's function in the Fourier domain
h		Complex point-spread function
h_a		Complex point-spread function in anisotropic material
$h_{\Delta\Phi}$		Point-spread function of phase contrast images in an isotropic material
$h_{\Delta\Phi a}$		Point-spread function of phase contrast images in an anisotropic material
h_i		Kind of boundary conditions called constant-with-time heat-transfer coefficient or contact conductance
Im		Imaginary part of a complex function
InSb		Indium antimonide
k_i		Kind of boundary conditions
k	$W^1 m^{-1} K^{-1}$	Thermal conductivity
Λ		Two-dimensional conductivity tensor
L		Differential operator
$\mu = \sqrt{\frac{2\alpha}{\omega}}$	m	Thermal penetration depth
μ_g		Mean value
NDT/NDE		Non-destructive testing, Non-destructive evaluation
NETD		Noise equivalent temperature difference
OLT		Optical lockin thermography
ω	s^{-1}	Angular frequency

PSF		Point-spread function
PT		Pulsed thermography
PPT		Pulse-phased thermography
Φ	rad	Phase angle
q	s^{-1}	Rate of heat flux
r	m	Position in the cartesian system
R		Reflection coefficient
Re		Real part of a complex function
RTM		Resin transfer molding
RFI		Resin film infusion
$\mathbb{R}^n$		n-dimensional real-space
ρ	$kg^1 m^{-3}$	Density of the material
S	m^2	Surface
SIFT		Scale invariant feature transformation
SNR		Signal-to-noise ratio
SURF		Speeded-up robust features
$\sigma = (1+i)\sqrt{\frac{\omega}{2\alpha}} = \frac{(1+i)}{\mu}$	m^{-1}	
σ_g		Standard deviation
t	s	Time
T	K	Temperature
$\dot{T}$		Time derivative of the variable T
T_i		i^{th} coordinate of the variable T
$T_{,i} = \frac{\partial T}{\partial x_i}$		Spatial derivative of the variable T in respect to the ith

coordinate uing Einstein's notation

$T_{,ij} = \frac{\partial^2 T}{\partial x_i \partial x_j}$ Second spatial derivative of the variable T in respect to

the ith coordinate

$T_i = \sum\limits_{i=1}^{n} T_i$ Sum of the coordinates of the variable T (in an

equation in $\mathbb{R}^n$)

θ Fourier transform of temperature

UIT   Ultrasound induced thermography

VAP   Vacuum-assisted process

$x_i,\ x_j,\ x_k$ m Cartesian coordinates

ZOI   Zone of interest

Contents

Introduction and objective

Context

In recent years, there has been an increasing interest in composite materials and specifically in carbon-fiber reinforced plastics (CFRP) in the aerospace industry and many other fields due to their lower weight and preferable mechanical properties in comparison to metals. CFRP components have to be tested for quality assurance after manufacturing or during in-service inspections performed on the aircraft itself where defects are to be detected. Therefore, a series of non-destructive testing and evaluation methods (NDT&E) are used.

Three strategies exist in the aerospace industry to test and qualify the structure of components that must support loads during flight: the safe-life, the fail-safe and the damage tolerance principles.

Safe-life design products are designed to survive a specific design life with a chosen reserve. The safe-life design technique is employed in critical systems which are either very difficult to repair or may cause severe damage to life and property. These systems are designed to work for years without the requirement of any repairs. The drawback is that products designed with a safe-life approach are over-dimensioned, which may be uneconomical.

The fail-safe method is based on the fact that components fail after a given number of load cycles. In order to avoid failure, the structure construction is several times statically overdetermined so that when a component fails, another can take over its task. The minimum load has to be supported by the neighboring component.

The damage tolerance principle has been developed in the early 1970's. Following the military Handbook [Lab], "the United States Air Force (USAF) developed a damage tolerance philosophy to help eliminate the type of structural failures and cracking problems that had been encountered on various military aircraft. The Air Force review of structural failures had revealed that the safe-life philosophy did not protect against designs that were intolerant to defects that could be introduced during manufacturing or during in-service use. From the standpoint of flight safety, it was found prudent to assume that new airframe structures could contain initial damage (e.g. scratches, flaws, burrs, cracks, etc) and that not all cracks would be found during inspections of older airframes. Accordingly, a damage tolerance philosophy was formulated based on the demonstration of structural safety under the assumption that pre-existing damage would be present at critical locations of all structurally significant details. The intention was to ensure that the maximum possible initial damage would not grow to a size that would endanger flight safety during the service life of the aircraft".

The Federal Aviation Regulations (§29.305) describes how avionic structures have to be tested with respect to strength and deformation:

(a) The structure must be able to support limit loads without detrimental or permanent deformation. At any load up to limit loads, the deformation may not interfere with safe operation.

(b) The structure must be able to support ultimate loads without failure. This must be shown by-

(1) Applying ultimate loads to the structure in a static test for at least three seconds; or

(2) Dynamic tests simulating actual load application.

For each structure, the evaluation of the following parameters is required:

- Design category

- Degree of in-service inspectability

- Inspection intervals

- Initial damage, in-service damage and continuing damage assumptions

- Minimum required residual strength

- Damage size growth limits

- Period of unrepaired service usage

- Remaining structure damage sizes
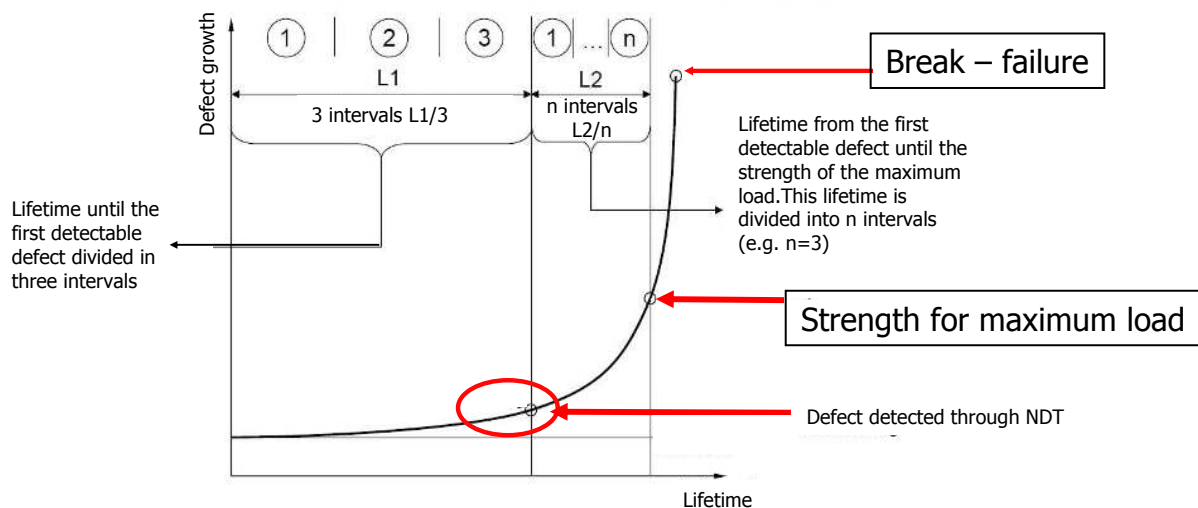
Figure 1: Scheme of a typical damage behavior before a component fails and determination of inspection intervals in the damage tolerance principle.

The basic premise in arriving at the initial damage sizes is the assumption that the fabricated structure contains flaws of a size just smaller than the smallest detectable flaw size found with the NDT procedures used on the production line. Fig. 1 shows a typical diagram of the damage size with respect to time. In the damage tolerance principle, the time interval until a defect becomes detectable with NDT techniques for the first time is divided into three inspection intervals. The time interval between the visual recognition of a defect and the component failure is divided into n inspection intervals.

The inspection intervals are determined through these calculations. Generally, the shortest interval is taken to simplify the inspection procedure. Damage tolerance is only used for components where defects grow slowly. For components where a defect grows more rapidly from the moment it becomes visible, the lifetime is determined through a combination of the damage tolerance and the safe-life principles. The time at which a defect is detectable through NDT is reported on a plot of the load force with respect to the number of cycles. Through the knowledge of the statistical distribution of load forces during a flight, the lifetime is predicted by using Miner's rule.

The fatigue and load simulations always are in accordance with NDT and test procedures to qualify defects. Simulations must be able to show that components with defects having the minimal size detectable with NDT techniques will support the maximal applicable load and will not fail. Fatigue and load tests are simulated in avionic components containing defects. The knowledge of the exact position, size and depth of defects allows one to perform trustful simulations.

Problem statement

Thermography is an NDT method having the advantage that thermographic systems are mobile and are produced nowadays in the size of small suitcases. The mobility of these systems enables direct inspection on the airplane or helicopter. This is one reason why thermography is becoming more and more appealing for the aerospace industry.

Active thermography comprises several methods where thermal or mechanical energy is artificially introduced in the material. With thermal energy either introduced in the form of a pulse (pulsed thermography) or in a modulated form (lockin thermography), internal defect boundaries like delaminations or cracks produce a reflection of the induced wave. Consequently, the changes of the temperature distribution produced at the surface of the component can be imaged with an infrared camera. In a closely related method, ultrasonic thermography, mechanical energy in the form of ultrasound waves is introduced into the component. Friction occurs at closed cracks which produce heat through a hysteresis effect. Again, the changes of the temperature distribution are measured at the surface of the component with an infrared camera.

This work particularly focuses on lockin thermography. The advantage of the method is the insensitivity to inhomogeneous illumination and the high signal-to-noise ratio (SNR) of the resulting phase and amplitude images. Compared to pulsed thermography, the registration time is long but modern system technology allows entering several lockin frequencies and thus performing multiple measurements simultaneously. A further advantage is that the method is contact-free. Ultrasound thermography, in contrast, requires a coupling of the ultrasound generating sonotrode with the inspected component so that the ultrasound waves can penetrate material.

Objective

The objective of this work is to enhance quantitative thermography with mathematical and image processing methods. A quantitative analysis is necessary and the depth, size, and shape of defects have to be determined. Until now, thermographic systems allowed defects to be registered and visualized, but limited quantitative defect information was

available from standard systems. Fig. 2 describes the actual status of general thermographic systems: the test-pieces are excited with external energy and the surface temperature distribution is registered with an infrared camera. The inner structure and defects can be visualized on a monitor. The next step is to provide quantitative information on the defects. The aim of this work is to improve the signal analysis of thermal data applied to anisotropic CFRP material.
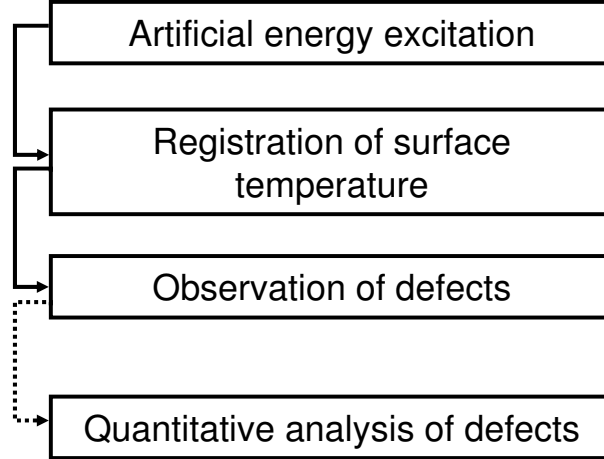

Figure 2: Scheme of thermographic inspection.

To enhance the analysis of measurements with thermographic methods, image and signal processing methods have to be used and combined. Thermal images appear blurred. The blurring effects have to be eliminated by an inverse algorithm. For comparison of sizes and measurements, CFRP test-pieces with artificial defects simulating delaminations are manufactured. The defect sizes and shapes are chosen so that the resolution limits of the thermographic method can be determined. The thesis is organized in the following way:

- Actual thermographic systems provides only a limited quantitative analysis of defects. The aim is to develop a model allowing the retrieval of the depth and size of defects. At lower lockin frequencies and at greater depths, the defects appear more and more blurred i.e. the defects appear larger than they actually are. The goal is to model the image formation process and to retrieve by an inverse algorithm, the geometric defect parameters. The model takes into account the anisotropy of CFRP material.

- CFRP parts with determined defects of known sizes and depths are manufactured. Thermographic measurements with parameters such as lockin frequencies to be determined are performed.

- Numerical simulations are performed and compared to measurements.

- Another goal is to investigate the limits of optical excited thermography (OLT) through the phase and amplitude images in the detection and characterization of the shape of defects in composite materials.

- It is not always possible in the case of long-term load experiments to perform thermographic imaging under the same reproducible aspects. Phase images are stitched

first to get an image of extended aircraft part and second images of the same region taken at different times under slightly different aspect angles are overlaid. To compare images, techniques that allow arranging fragment images of long curved aircraft parts are applied. The goal is to create panoramic images that facilitate the evaluation of a potential defect growth. Methods are developed to compare two images. The same methods are applied to combine images of several NDT techniques (data-fusion).

- The methods are tested on CFRP parts used in the aerospace industry.

Outline

The thesis is organized in several chapters, as follows:

- Chapter 1 introduces relevant aspects of composite materials. The development and impact of the material in the aerospace industry is discussed. The manufacturing process of the CFRP boards with the artificial defects is described.

- In chapter 2, the state of the art of thermography is presented. An overview of the different excitation methods and time sequence evaluation is given. In this chapter the optical lockin thermography technique is discussed.

- In chapter 3, a model is derived to describe heat conduction in a CFRP material. In order to solve the heat equation for the case of periodic waves of lockin thermography, the method of Green functions is used. The general case of Green's functions is described and the differential equation is solved for the case of the semi-infinite plate. Thereby, a simple analytical form of the PSF is computed for homogeneous and anisotropic material.

- An overview of image processing algorithms for non-destructive testing is given in chapter 4.

- In chapter 5 experimental results are shown. A method is presented to determine, in semi-automated ways, quantitative information on defects in material. Two different methods to determine the defect depth are presented and applied to different CFRP test-pieces with circular and rectangular artificial defects.

- In chapter 6, in order to be able to image a potential defect growth during a fatigue test, it is described how individual thermographic images are stitched; first, to get an image of extended aircraft parts, and second, to overlay images of the same region taken at different times before and after a fatigue load under slightly different aspect angles. Artificial markers that are visible in the infrared and phase images, are fixed on the components. Results of the panorama techniques conducted on low contrast thermal images are shown.

- In chapter 7, the limits for both ultrasound and lockin thermography are presented and compared. Since these methods reveal different physical properties, a data fusion technique is applied to use the defect information of both techniques.

Chapter 1

CFRP material

In the aerospace industry, composite materials have become more and more popular in the construction of aircraft, helicopters, missiles or satellites launchers. Fig. 1.1 [1] illustrates the weight percentage of composite materials used in different products of the EADS company and shows that this percentage has been increasing since 1975. The primary objective of using composites is to keep the weight of aircraft components as low as possible. By replacing metals in aircrafts with composite material, a mass reduction of up to 40% can be obtained.
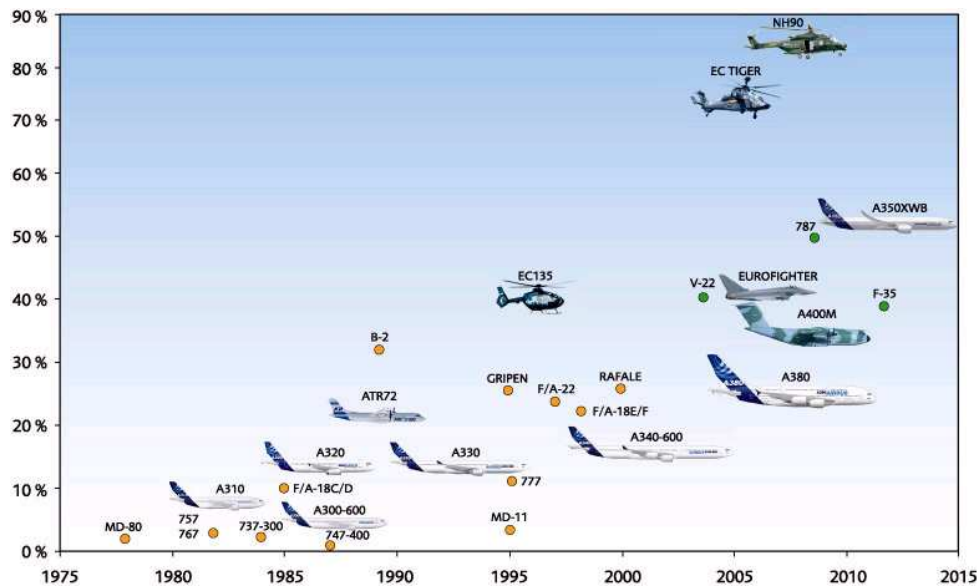
Figure 1.1: Percentage by weight of composites in different products of the EADS company.

Composites are materials made up mostly of two kinds of materials: a matrix and a reinforcement material. The incorporated materials can be particles, whiskers, fibers, lamellae, or a mesh.
The most common materials are carbon-fiber reinforced plastics (CFRPs), whose masses are composed of 60% fiber and 40% resin. The epoxy resin matrix is reinforced with carbon fibers. Another group of materials are sandwich structures, composed of honeycomb

---

[1] www.eads.com

or synthetic material surrounded by two CFRP layers. In addition, there are glass fiber-reinforced plastics (GFRPs) and ceramic fiber-reinforced plastics for components exposed to high temperatures such as rocket motors.

CFRP materials have the advantage of a better resistance against fatigue and corrosion. Their formability facilitates the manufacturing of a precise geometry. Compared to metals, complex shapes (for example spherical) can be manufactured easily. Since they are composed of only a few sub-systems, the number of assembly components is reduced, which diminishes the problems of structure resistance. Composites sometimes vary in thickness or rigidity and their mechanical resistance depends on temperature and humidity. In some cases, they are more sensitive to mechanical impacts such as hail or collision with birds compared to metals. Another drawback of composites is their high manufacturing cost. This is the reason why research is performed on new technologies that could automatize the manufacturing processes: (1) the automated placement of fibers and the addition of resin with an injection called resin transfer molding (RTM) or (2) the addition of resin through infiltration known as resin film infusion (RFI) are two main tasks that should be automated. Hence, the goal is to avoid autoclave manufacturing.

In this thesis, different kinds of CFRPs and their composition are introduced in order to understand the structure of the material. The manufacturing methods with prepreg material and of vacuum-assisted process (VAP) with dry fibers are described.

1.1 Carbon-fiber reinforced plastic

Carbon fibers are produced through controlled oxidation, carbonization, and graphitization of carbon material. The mechanical properties of composite material are provided by the fibers: the strength and stiffness are very good, as well as the thermal, chemical, and electric properties. In addition, the weight is lower than that of metals. Some typical material properties are listed in Tab. 1.1. Fig 1.2 shows a microscopic image taken at a zoom factor of 25.

The role of the epoxy matrix is to bind and protect the fiber's surface from damage, to distribute forces and to compensate for fractured fibers. The resin matrix influences the properties of the composite as the electrical and fire resistance are improved. There are different types of resins, all with advantages and drawbacks. Epoxy resin is the most commonly used and the material used in this work is also composed of this kind of resin. The manufacturing of CFRP components involves different technologies and the raw material is presented in two main categories: preimpregnated fibers (Prepreg) and dry fibers.

1.1.1 Prepreg

Prepreg material is the designation used for a material where fibers are preimpregnated with a resin. It consists of unidirectional tapes with parallel fibers or fabric tapes with several fiber orientations where fibers are bonded by a film of semi-cured resin (Fig. 1.3). It is attractive because it is easy to handle and the impregnation process is avoided during curing. The layers of Prepreg can easily be cut to the pattern needed and overlaid into the desired form. They have to be pressed together in order to eliminate the main part of air bubbles. Therefore, a spool is used to press the layers against each other.

<div align="center">(a)   (b)</div>

<div align="center">(c)   (d)</div>
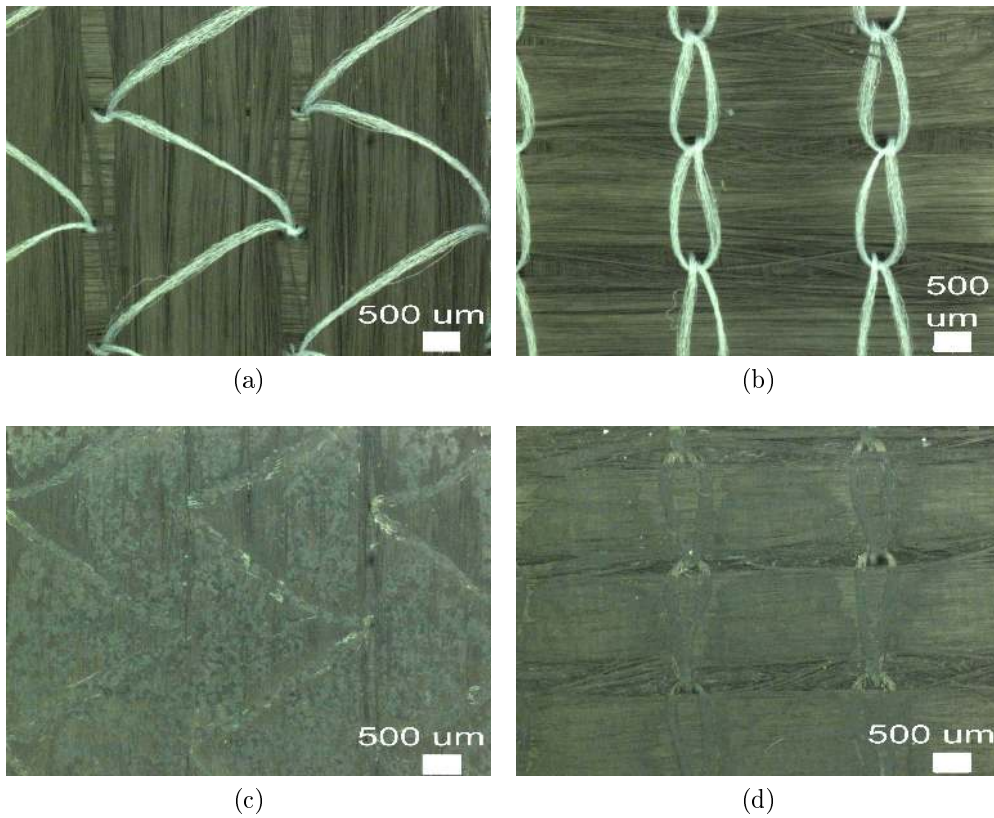
Figure 1.2: Microstructure (a-b) of carbon fibers on the front and back sides in a bidirectional fabric and (c-d) in a sample cured with epoxy resin obtained with an optical microscope.
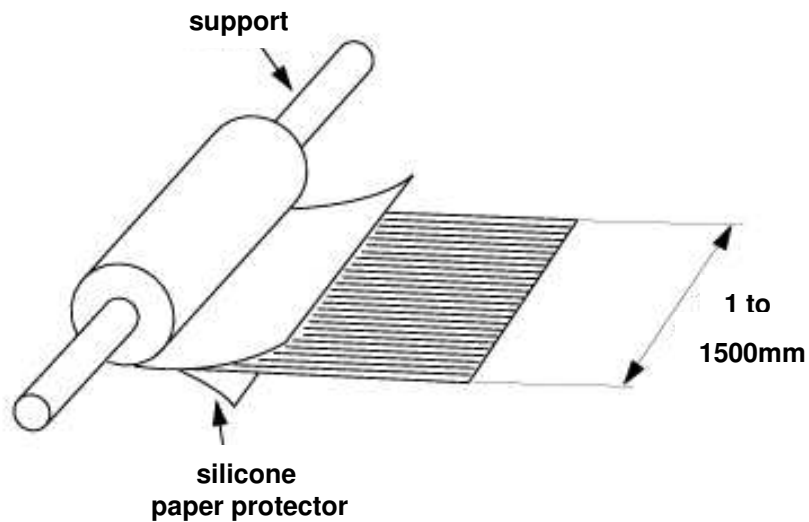

Figure 1.3: Commercial Prepreg material [Hex05].

An inconvenience is that the material has to be stored at low temperatures (-18°C) because the shelf-life at ambient conditions is very low (less than 24 hours). Its shelf-life at low temperatures is typically one year.

CFRP properties at room temperature of HexPly®M18/1 with G939 fibers		
Thermal conductivity $k \parallel$	4	$[Wm^{-1}K^{-1}]$
Thermal conductivity $k \perp$	0.83	$[Wm^{-1}K^{-1}]$
Thermal diffusivity $\alpha \parallel$	2	$[10^{-6}m^2s^{-1}]$
Thermal diffusivity $\alpha \perp$	0.4	$[10^{-6}m^2s^{-1}]$
Thermal effusivity $\parallel$	440	$[Ws^{-0,5}K^{-1}m^{-2}]$
Thermal effusivity $\perp$	1000	$[Ws^{-0,5}K^{-1}m^{-2}]$
Tensile strength $\parallel$	800	$[MPa]$
Tensile strength $\perp$	800	$[MPa]$
Tensile modulus $\parallel$	65	$[GPa]$
Tensile modulus $\perp$	67	$[GPa]$
Compressive strength $\parallel$	800	$[MPa]$
Compressive strength $\perp$	800	$[MPa]$
Compressive modulus $\parallel$	62	$[GPa]$
Compressive modulus $\perp$	64	$[GPa]$
Shear strength	100	$[MPa]$
Epoxy resin properties		
Thermal conductivity k	0.2	$[Wm^{-1}K^{-1}]$
Thermal diffusivity α	0.09	$[10^{-6}m^2s^{-1}]$
Tensile strength	66	$[MPa]$
Tensile modulus	4.2	$[GPa]$

Table 1.1: Some typical material properties. The symbols $\parallel$ and $\perp$ signify the property values respectively along and across the fiber orientation [Hex05].

1.1.2 Preform technology

Another technique consists of using dry fibers that are not impregnated with resin. The (preform) material is a textile composed of stitched carbon fibers. The fibers are stitched together either in a crimped or in a non-crimped (the fibers are straight) manner. For this technique, the fibers need to be impregnated with resin during curing. Therefore, the VAP vacuum assisted process [LKGH04] is used for the curing. This technique has been improved and patented at EADS Innovation Works in 2001 [FLSU01]. With this technique, any component's geometry can be realized.

1.2 Vacuum bag molding lay-up

There are two main types of manufacturing techniques for CFRP material, which depend on whether Prepreg or dry-fibers are used for the manufacturing process.

1.2.1 Stack composition

The fiber layers or Prepreg are assembled in different ways. The fibers can be mono-directional or follow several fiber orientations (Fig. 1.4). In the quasi-isotropic lay-up, the
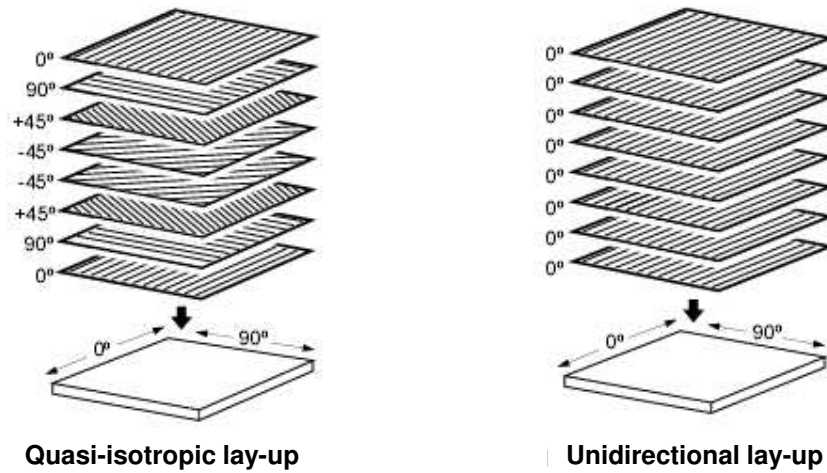
Figure 1.4: Orientation of the layers of fibers in the stack [Hex05].

fibers are oriented following 0°-45°-90°-0° orientation. In the middle, an inversion occurs (for example, 0°-45°-45°-0°) in order to ensure the quasi-isotropy in the plane. There are stacks with bidirectional fiber orientations of 0°-90°. For the unidirectional lay-up, the fibers are all oriented in the same direction. This lay-up presents a high anisotropy, whereas the quasi-isotropic lay-up can be assumed to be isotropic in x- and y-directions.

1.2.2   Vacuum-assisted process
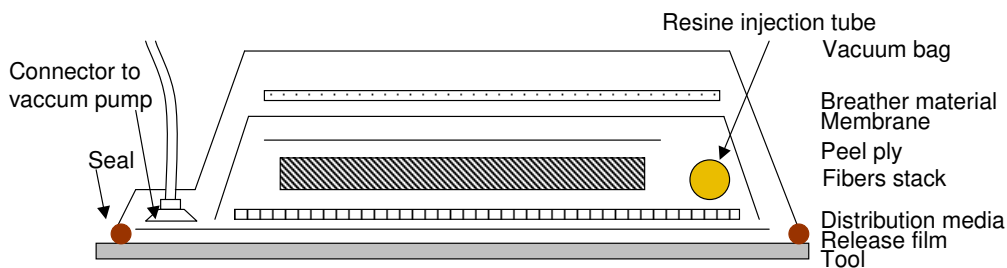
Figure 1.5: Layers of the set-up of a vacuum bag molding with dry fibers material.

The lay-up for the curing is shown in Fig. 1.5. Once the fibers have been overlaid, they are covered with a breather material that absorbs the superfluous resin. For dry fibers, a tube is also introduced to infiltrate the resin. Then, a vacuum bag is fixed around the component in order to ensure a vacuum in the lay-up. The role of the different components is the following:
Tool: The tool is a metal component on which the assembly is laid.

Release film: This film is placed on the metal plate to avoid resin drying on it and to allow a better drop-off of the lay-up.

Distribution media: The grid is placed under the fiber stack and allows good circulation of the resin from the injection tube to the fibers.

Peel ply: Peel plies are placed on and under the fiber stack in order to ensure an even surface. The peel ply breaks away after the curing.

Membrane: The membrane is a micro-porous material that is impermeable to the resin at high pressures and lets gas escape. It allows the resin to stay inside the lay-up and provides continuing degassing of the resin.

Breather material: This is a compacted fleece placed on the membrane that allows the absorption of the superfluous resin. It retains its thickness even under compaction pressure so that gas can still escape through it.

Vacuum bag: The vacuum bag is placed all around the lay-up and fixed on the tool with a seal.

1.2.3   Process for Prepreg

For Prepreg material, the lay-up is quite similar. Here, the injection tube is not necessary. The fiber layers are assembled by pressing them together with a spool. The plate has to be put in a press every 8 to 10 layers so that the air between the layers can escape. The composition of the different layers of the lay-up is summarized in Fig. 1.6.
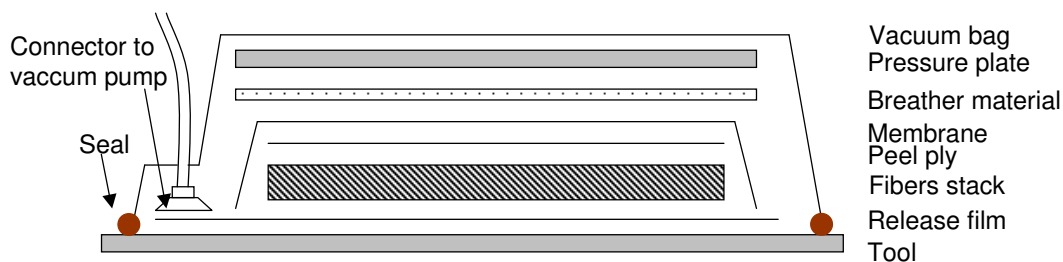
Figure 1.6: Layers of the set-up of vacuum bag molding of Prepreg material.

1.2.4   Curing

Finally, the lay-up is cured in the oven following a curing cycle. Fig. 1.7 shows a typical curing cycle of the material in the oven. The maximum temperature is 180°C. Three phases can be observed: a heating phase, a baking phase and an annealing phase.

1.3   Manufacturing of test-parts

A well-known task in quantitative non-destructive testing is to properly create test-pieces with artificial defects with known sizes and depths. Most studies employ parts with blind holes or insert pieces of teflon foils or aluminium sheet. For the investigations, two composite plates with artificial defects with known depths and sizes were manufactured. In Fig. 1.8, one can see the typical lay-up for the manufacturing of a part with dry fibers using the vacuum assisted VAP procedure. Blind holes are inserted into different depths and

Figure 1.7: Cure cycle of the material in the oven [Hex05].
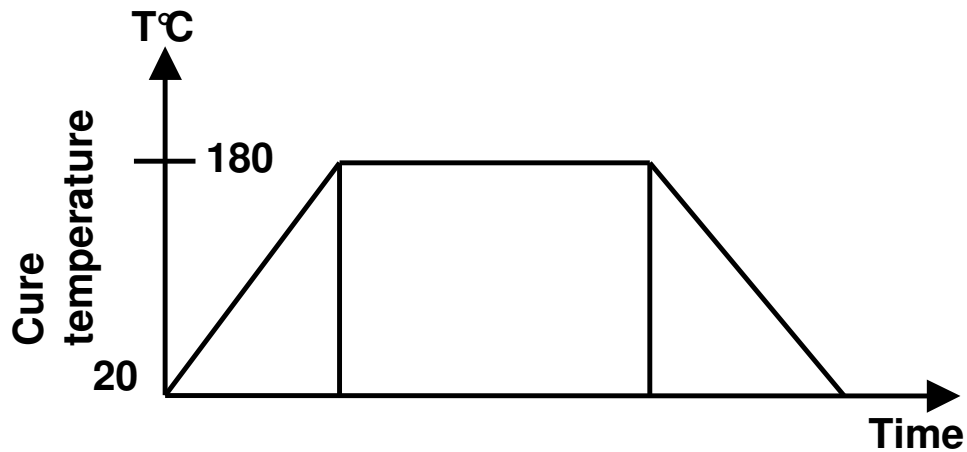
shapes that allow modeling delaminations. During measurements, the plate is observed on the back side of the blind holes.

The parts used in Chap. 5 are manufactured with the Prepreg material Hexply M18/1 from the company Hexcel, which contains an epoxy resin matrix. To obtain a part of approximately 10 mm thickness with each layer being 0.125 mm thick after curing, 80 layers were overlaid following the quasi-isotropic lay-up (Fig. 1.4). The resulting parts are visualized in Fig. 1.9. In Fig. 1.10 and 1.11 schemes of the test parts of composite material are shown. Plate I is prepared with circular blind holes of varying depths and sizes. The sizes vary from 6 to 20 mm and the depths from 1 to 5 mm. Plate II has square blind holes and a staircase-shaped wedge. The square blind holes have sizes of 5 mm to 20 mm and depths varying from 2 to 7 mm. The depths of the crosses are 2 and 4 mm, respectively.

(a)   (b)

Figure 1.8: Scheme of the lay-up of self-manufactured parts; (a) The injection tube and fiber stack with peel ply can be observed; (b) The vacuum bag, the connector to vacuum tube, and the fiber stack with the breather material can be observed.

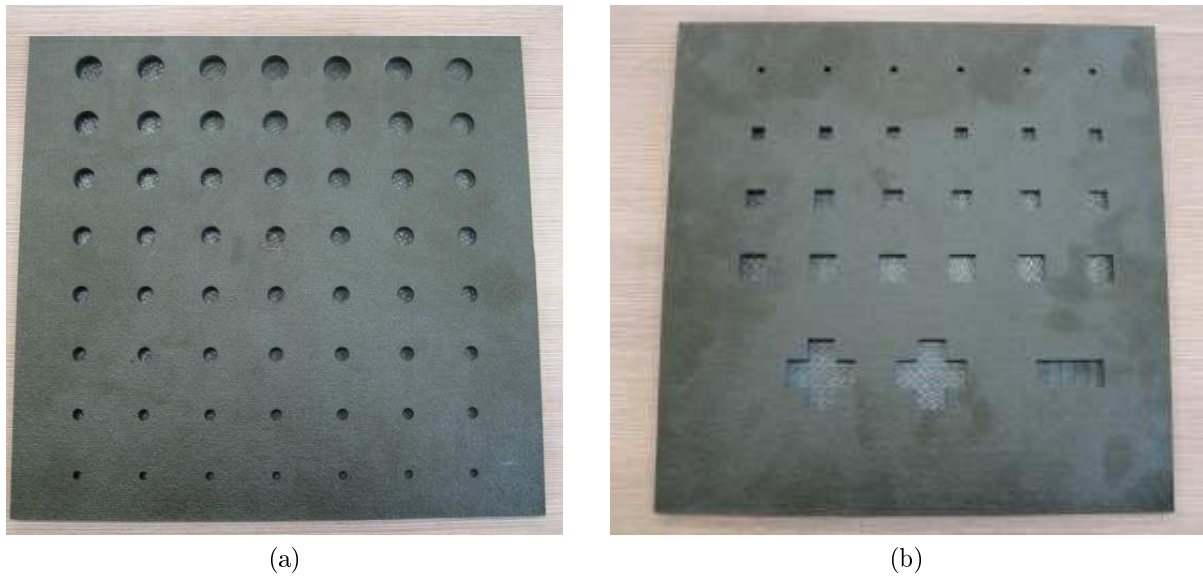(a)   (b)

Figure 1.9: Images of manufactured parts; (a) Plate I with circular blind holes; (b) Plate II with rectangular blind holes and a wedge.
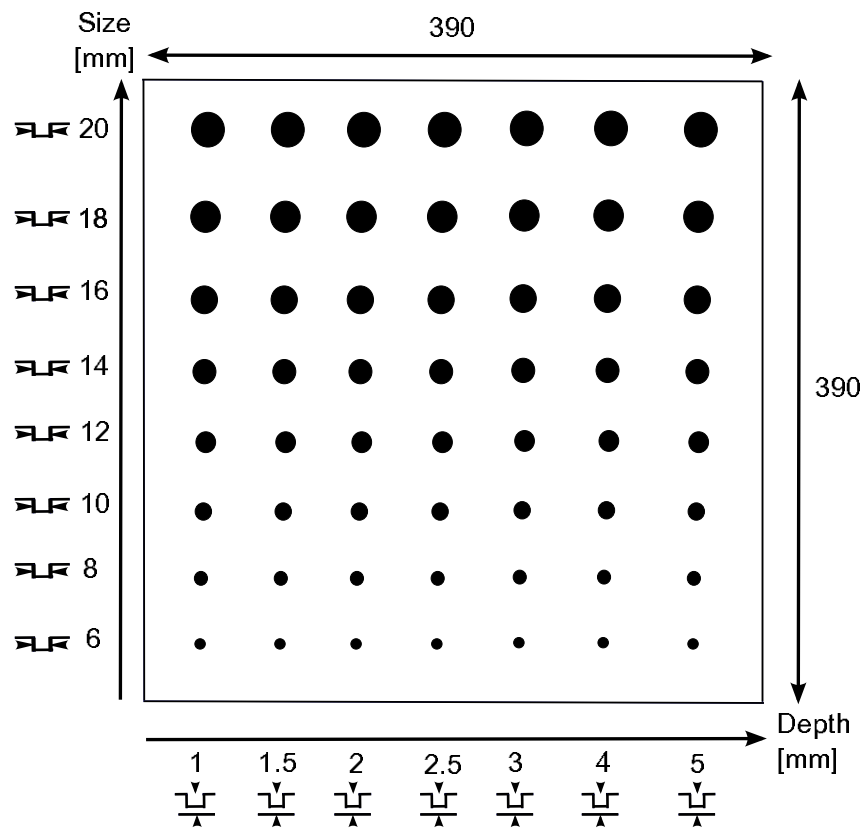

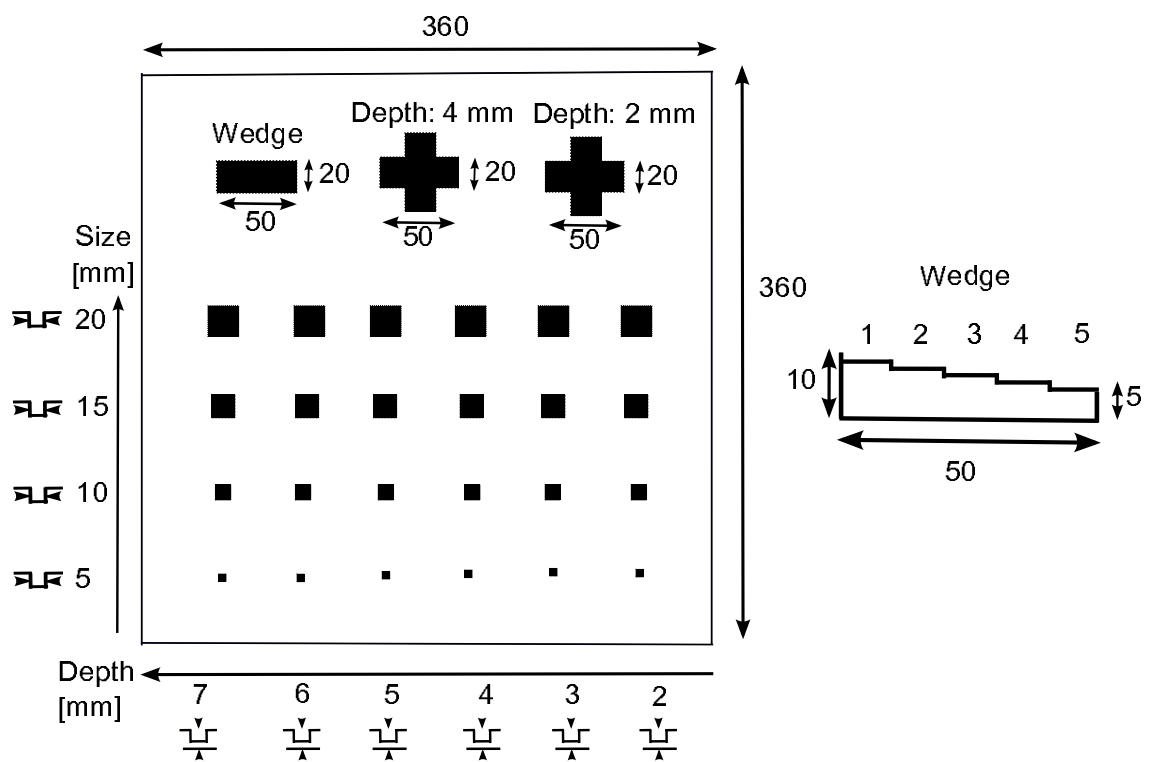Figure 1.10: Scheme of plate I with circular defects. The size are given in mm.

Figure 1.11: Scheme of plate II with square defects. The size are given in mm.

Chapter 2

Thermography

2.1 Non-destructive testing in the aerospace industry

In the aerospace industry, NDT is employed in production as well as during in-service maintenance or for the inspection of flaw-repairs. According to the currently applied norm DIN EN 4179, the defects to be detected in composite material are:

- delaminations / gap between plies

- porosity or lack of resin / dry fibers

- impact damages

- debondings / gap between the inner facesheet and the core in sandwich panels

- fiber waviness

- foreign body inclusion

- water in honeycomb structures.

Before applying an NDT technique, operators use visual inspection. Impact or surface damages can often be recognized immediately. A pilot has to perform a visual check before flying an airplane to assure himself that it is all right. The detected damages may be critical to flight safety. Once a defect is detected visually, other NDT techniques are used to analyse the extend of the defect.

Testing by tapping is the second method used for initial detection of field damage. A simple coin, a tap hammer or an instrumented tap hammer (so-called Fokker bond test) can be used to localize defects. A tap on the surface of a good area will produce a sound of high frequency whereas a similar tap on the surface of a delaminated or disbonded area will yield a sound of low frequency. The method is suited for defects situated near the surface. The accuracy of the method decreases with the depth of the defect.

The five standard methods following the norm DIN EN 4179 are ultrasonic testing, eddy-current testing, x-ray testing, penetration testing and magnetic particle testing. The last method requires a ferro-magnetic material like steel whereas eddy-current testing is preferred for aluminium to detect surface cracks. The first three methods are well-known in the testing of composite materials [SH06].

Ultrasonic testing is the most widespread method. There are manual and automated ultrasonic testing system with single element transducers and linear phased array devices that can work either in pulse echo or in transmission mode. Ultrasonic testing is used to detect defects such as inclusions, porosity, debondings and delaminations. Used in the pulsed echo mode, there is a linear relationship between the percentage of volume porosity and the backwall echo reduction [SH06]. It allows a quantitative evaluation and can be automated. If the distance between the transducer and the part is known, the defect sizes can be computed in production lines where a fast inspection is needed. Automated scanning systems are used to test components while spraying water to allow coupling between transducer and component. They also allow investigating complex shaped components. Phased arrays of transducers were first used only a few years ago [SH06] and are particularly useful to investigate large parts.

Water is usually used as a coupling medium to inject ultrasound waves in the component with minimal losses. At the material surface, waves are reflected. The reflection coefficient at the interface air-material is much higher than that of water-material. However, some components should have no contact with water, for example honeycomb or sandwich panels. Water may infiltrate at delaminations into the structure, making them heavier and creating additional damages. Air-coupled ultrasonic testing [Sto04] is better suited for these components. In recent years a lot of work was devoted to improving the design of transducers and optimizing the coupling between the air and test-piece. High sound frequencies (between 50 kHz and 100 kHz) must be used to compensate losses due to the high reflection coefficient.

Other testing methods such as computed tomography, thermography, shearography or laser ultrasonics called 'special' methods are employed. Computed tomography is an expensive method but has a very high resolution even down to a few μm. The resolution is given by the size of the x-ray tube focus. This limits the penetration and therefore indirectly the size of the component. It is used in production or for in-service inspections. In shearography, two images are taken in a loaded and in an unloaded state and are sheared using a Michelson mirror. Research is still performed on this technique for example to optimize the shear displacement. The resulting images show two images of the defect that are sheared one against the other letting the defect appear like a butterfly. The advantages are that the method is contact free and that one measurement delivers an image. Stringer debondings or impact damages can be detected well but some defects like porosity are difficult to detect. Shearography should therefore be used for in-service inspections where porosity is not of concern. But until now, the method is not commonly used in production or in-service.

Laser ultrasonic testing has the advantage that it is contactless. It allows the testing of porosity and delaminations [FKvKJ06]. The main advantage of laser ultrasonics is that the sound waves propagate always perpendicularly to the component's surface and are independent of the incident angle of the laser. Parts with complex geometries can be easily inspected whereas those with phased array devices are not. Laser ultrasonic devices are currently very expensive, and the scanning is very slow since only one point can be measured at any one time. Some developments are still necessary. Thus, many parameters influence the choice of the most suitable inspection method and they all undergo a lot of development.

2.2   Thermography

The method dominantly employed in this thesis is thermography where research is still required for a quantitative analysis of defects. Infrared thermography is a technology that measures the invisible radiation in the infrared spectrum of an object with a camera. The intensity of this radiation depends on the temperature of the body's surface and on the thermal emissivity of the body. The advantages are that it is an imaged-based and contact-free method. The measurement of large surface areas can be done rapidly. Thermal images can be easily registered. For the aerospace industry, an advantage is that thermographic systems are mobile so that measurements on airplane components can be undertaken directly in the inspection hall.

2.2.1   Thermal radiation

Infrared radiation was discovered by William Herschel in 1800. In an experiment, he spread the sunlight into a rainbow of colors and then measured the temperature of each color. He found out that the thermometer indicated a high temperature when placed just below the red strip. He had discovered thermal radiation also called infrared.
The infrared electromagnetic spectrum spans wavelengths from 780 nm to 1 mm. The radiation is divided in three categories: near infrared (780 nm - 1400 nm), middle infrared (1400 nm - 3000 nm), and far infrared (3000 nm - 1 mm).
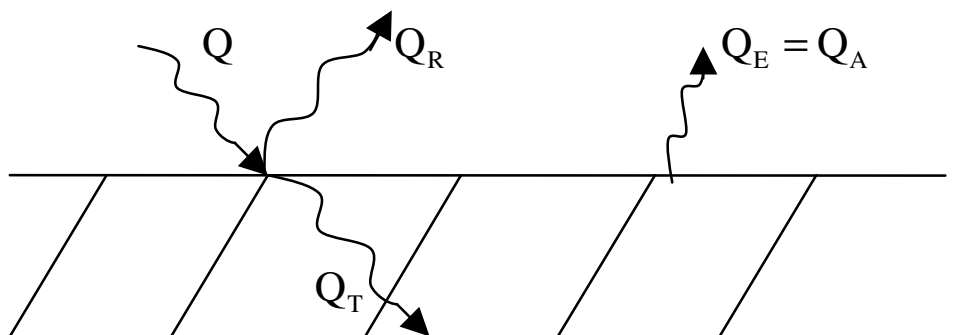
Figure 2.1: Thermal energy transfer.

Each body is submitted to a radiation Q where Q is the quantity of energy in Joules. Quantities of energy are absorbed (Q_A), transmitted (Q_T), reflected (Q_R), and emitted (Q_E). These quantities are described by the coefficients

- $\alpha = \frac{Q_A}{Q}$: absorption;

- $\rho = \frac{Q_R}{Q}$: reflection;

- $\tau = \frac{Q_T}{Q}$: transmission;

- $\epsilon = \frac{Q_E}{Q}$: emissivity.

Following the energy conservation law, the condition

$$Q = Q_E + Q_R + Q_T \Rightarrow \alpha + \rho + \tau = 1 \tag{2.1}$$

has to be fulfilled.

2.2.2 Thermographic methods
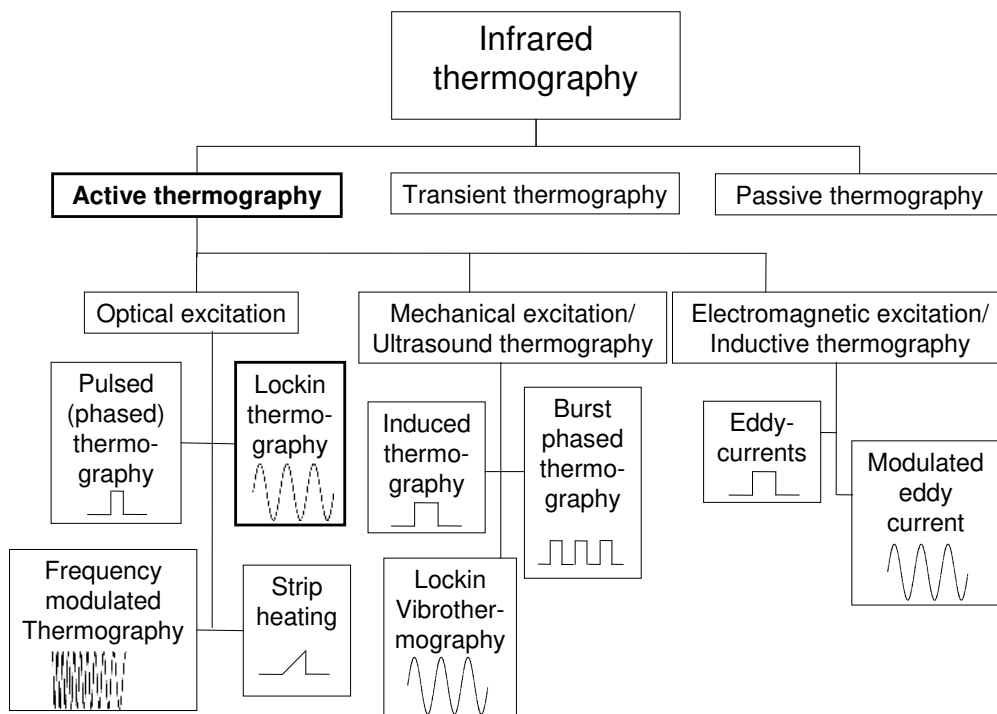
Figure 2.2: Overview of thermographic techniques.

With thermography, the distribution of heat and its change with time on the surface of test parts is detected through an infrared camera. Fig. 2.2 shows an overview of the different thermographic techniques. The way the measurements are performed can be grouped into three categories:

- Passive thermography
  With passive thermography, the temperature distribution of a part is observed with a thermographic camera. This method finds its current application in the testing of buildings in order to detect heat losses.

- Transient thermography
  The surrounding temperature is abruptly elevated or diminished, and the temperature change at the surface is recorded with an infrared camera. Applications are in civil engineering of buildings [MWBR04].

- Active thermography
  With active thermography, energy is injected into the component to be tested. The

resulting temperature at the surface is recorded with an infrared camera. The observed temperature distribution is changed by the waves reflected or emitted from internal defects. Active thermography is used in the industry as a non-destructive testing tool.

In this work, only active thermography is considered. Fig. 2.3 shows the general principle of active thermography. Several excitation sources can be used. Depending on the kind of energy and the way the thermographic sequence is analyzed, the techniques have different names. The most widespread excitation methods are light, ultrasound, and eddy-currents. The form of the excitation source can be a pulsed or burst excitation, sinusoidally or frequency modulated.
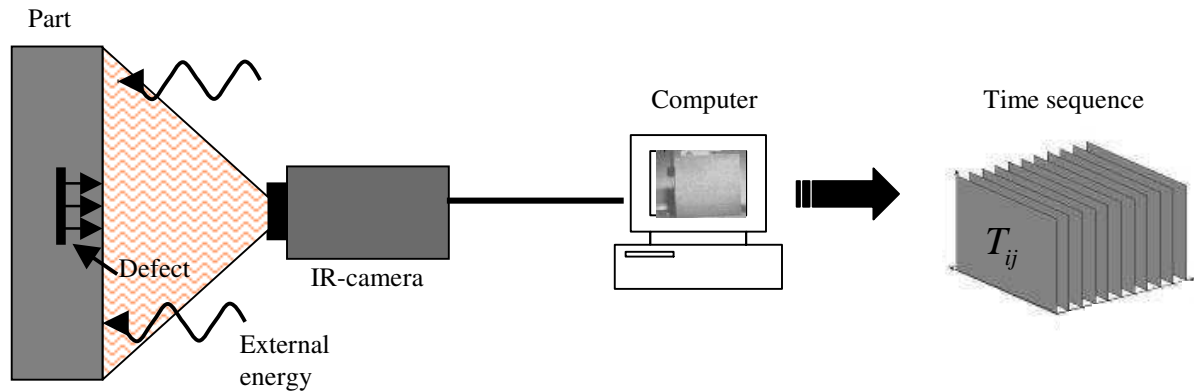

Figure 2.3: Principle of active thermography.

2.2.3 Overview of thermographic techniques

The advantages and disadvantages of the different thermographic techniques are listed in Tab. 2.1. Beside the advantage that thermographic inspection allows inspecting large areas at once, thermographic systems are portable allowing in-situ inspections. Important facts that should be noted when selecting a method are

- using an ultrasonic excitation (see Appendix B), the sonotrode injecting the ultrasounds has to be in contact with the part and may damage the surface of the component especially when using high powers;

- when performing a phase analysis, an inhomogeneous light distribution is suppressed in the images. This analysis requires more computational time;

- a sinusoidal excitation lasts longer (for CFRP material, it can take some minutes) than a pulse excitation (some ms).

In the experimental part, most results are obtained with optical lockin thermography. This technique is described in the following sections. Other techniques are described in Appendix B. In Chap. 7, the application of ultrasound induced thermography (UIT) is discussed because disbonded CFRP skins or gaps between plies called delaminations are better detected with UIT. Data fusion of thermal images is performed. A description of ultrasound induced thermography is given in Appendix B. A comparison of lockin and

	Advantages	Drawbacks
PT/UIT	- fast	- images have lower SNR
PPT/ BPT	- fast	- inhomogeneous distribution of energy in phase sequence
Optical lockin	- depth resolved method	- images with high SNR - very slow
FMLT	- depth resolved method	- homogeneous distribution of energy in phase sequence - slow - images have lower SNR

Table 2.1: Advantages and disadvantages of some methods of active thermography.

pulsed phased thermography is also given in this appendix since both methods have similar properties. The results of a test performed with frequency modulated thermography are shown in this appendix.
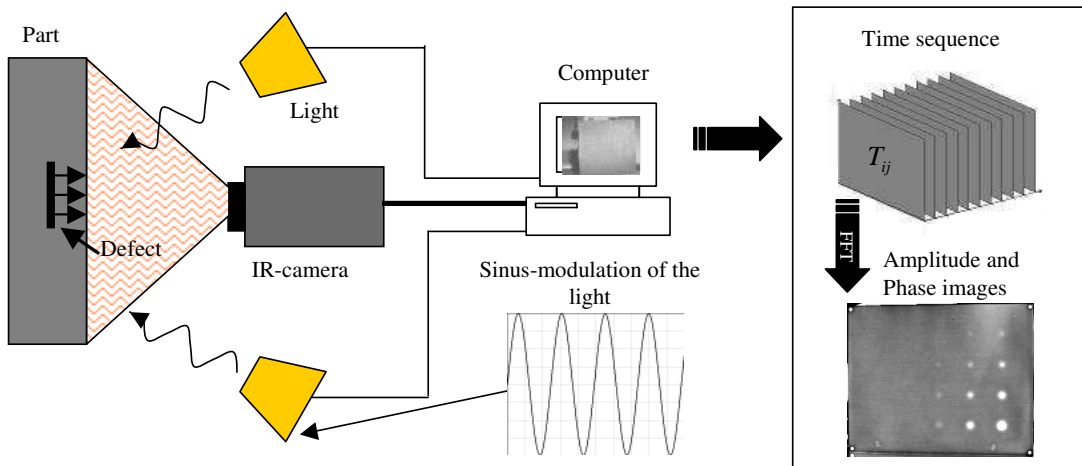
2.3 Lockin / modulated thermography

Figure 2.4: Principle of optical lockin thermography.

Photothermal imaging can be considered as the ancestor of lockin thermography. A modulated laser source is used to illuminate point-wise the object's surface. The amplitude and phase images are computed by means of a lock-in amplifier (see Appendix A for detailed information). Amplitude and phase images from lockin thermography can be analyzed in the same way as those of photothermal imaging with the advantage that the points constituting the images can be registered at once.

Optical lockin thermography (also known as modulated thermography) [Bus79, BWK92] is a technique which has been applied for the investigation of electronic devices [BL03a, BL03b]. It allows extracting signal information from a noisy background. Fig. 2.4 shows

a schematic representation of the lockin thermography set-up. Through light excitation, a thermal wave is induced at the surface of the material. Energy is absorbed and a thermal wave penetrates into the material. This wave is described by a position and time temperature modulation. The wave penetrates into the material and is reflected at internal interfaces. The reflected wave interferes with the incident wave and generates a measurable temperature modulation at the surface of the component. This temperature distribution is measured with an infrared camera. For lockin thermography, the part is illuminated with a sinusoidally modulated light. In Fig. 2.5, some recorded images of a timegram (time sequence) are shown. The surface is heated with a periodic light source. Defects cannot be directly detected. For that purpose, phase and amplitude images have to be computed. These quantities are the amplitude and phase shift between the incident and the reflected waves (Fig. 2.6). In practice, different methods are used to compute phase and amplitude images and will be described in the next sections.
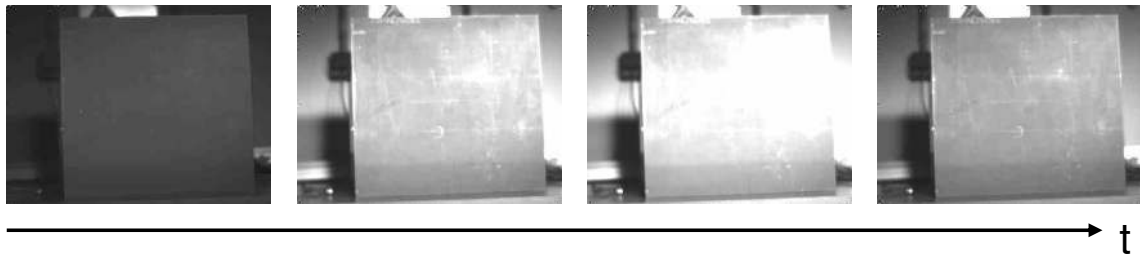
Figure 2.5: Surface temperature vs. time with a sinusoidal excitation.

Figure 2.6: Computation of phase and amplitude images.

2.3.1 Four-point algorithm to compute amplitude and phase images

In the special case of sinusoidal excitation, the amplitude and phase images can be retrieved by knowing the coordinates of four equidistant points in the reference and in the recorded signals following the equations [BWK92, Wu96]:

$$A = \sqrt{(S_1 - S_3)^2 + (S_2 - S_4)^2} \tag{2.2}$$

21

$$\Phi = \arctan\left(\frac{S_1 - S_3}{S_2 - S_4}\right) \qquad (2.3)$$

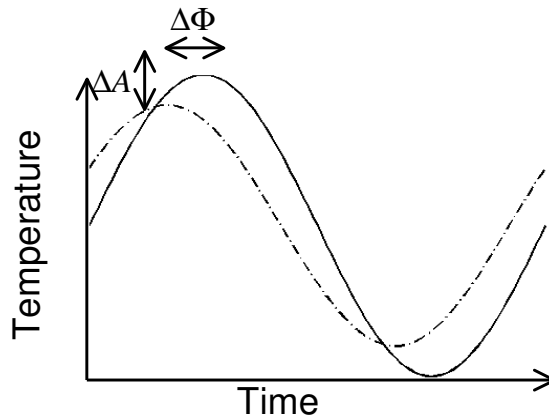where S_i is the photothermal signal of a point taken at time t_i. A schematic representation of this retrieval method called four-point algorithm is given in Fig. 2.7. However, the result is corrupted by noise when using four single points. In practice, multiple periods are registered to reduce noise by averaging.
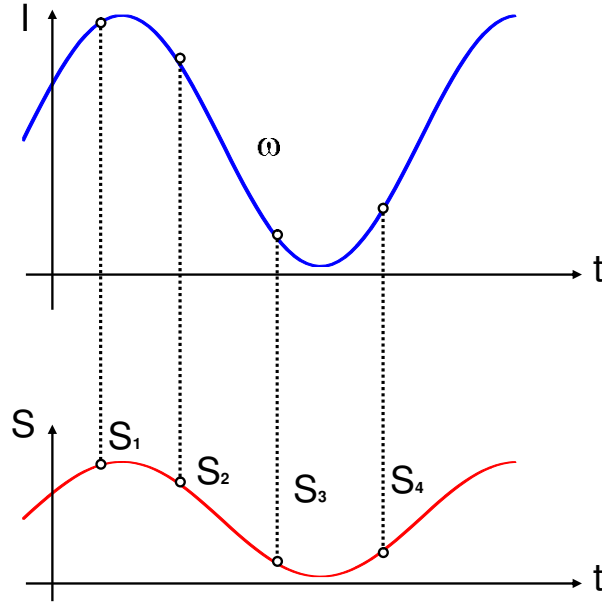

Figure 2.7: Four-point algorithm principle for the computation of amplitude and phase images in the presence of a sinusoidal excitation [IC05].

2.3.2   Fourier transform to compute amplitude and phase images

Another way to compute amplitude and phase images is based on the Fourier transform. Image sequences are analyzed pixel by pixel. The values of each pixel in consecutive image frames from a time series are analyzed. The timegram is transformed pixel-wise using the discrete Fourier transform. Thereby, the signal is decomposed into a real and imaginary part:

$$F_n = \Delta t \sum_{k=0}^{N-1} S(k\Delta t)e^{-j2\pi nk/N} = \mathrm{Re}_n + i\,\mathrm{Im}_n, \qquad (2.4)$$

where $\Delta t = \frac{T}{N}$ is the sample interval, T is the period and $n \in \{0, 1, ..., N\}$ is the number of the sample points. Re_n and Im_n are, respectively, the real and imaginary parts of the Fourier transform F_n. The amplitude A_n and phase ϕ_n signals are computed from the real and imaginary parts by:

$$A_n = \sqrt{\mathrm{Re}_n^2 + \mathrm{Im}_n^2} \quad and \quad \phi_n = \tan^{-1}\left(\tfrac{\mathrm{Im}_n}{\mathrm{Re}_n}\right). \qquad (2.5)$$

In practice, the Fast Fourier Transform (FFT)[CT65] is used. The amplitude and phase sequences are composed of several amplitude and phase images. They are currently called amplitudegram and phasegram [IC05].

For sinusoidal excitation, only one phase and one amplitude images for each corresponding excitation (lockin) frequency are calculated. The energy of the signal concentrates in a single frequency as it is shown shematically in Fig. 2.8 by the spectrum of a sinusoidal signal. The Fourier transform of a sinusoidal signal is given by

$$\Im\left(\sin(2\pi f_0 t)\right) = -\delta(f - f_0) + \delta(f + f_0) \tag{2.6}$$

where δ is the Dirac function. Therefore, the signal-to-noise ratio (SNR) of the phase and amplitude images is very high. This procedure is repeated for several lockin frequencies. The result is a set of phase and amplitude images (amplitude- and phasegram). An advantage of the phase images is that they are insensitive to inhomogeneous illumination and reflections due to the geometry of the object compared to the infrared and amplitude images.
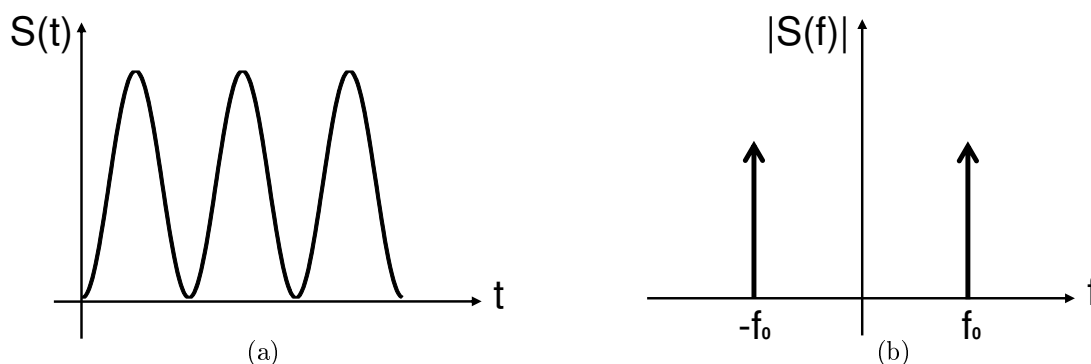
Figure 2.8: (a) Sinusoidal excitation and (b) its Fourier transform.

2.4 Detection of defects with optical lockin thermography

Optical lockin thermography (OLT) allows the detection of many kinds of defects in composite materials. A good overview is given by Dillenz and Zenzinger in [DZ08]. The following kinds of defects can be detected:

- porosity or lack of resin / dry fibers;

- impact damages;

- fiber waviness;

- foreign body inclusion;

- water in honeycomb structures.

Fig. 2.9 shows an example of detection of impact damage in sandwich CFRP test-part. In a given frequency range (here, for example, for 0.1 Hz), delaminations present the characteristic shape of a butterfly, which means that two sides are darker than the background (negative phase contrast), and two sides are brighter than the background (positive phase contrast). Porosity can also be easily detected (Fig. 2.10). Fig. 2.11 shows phase images taken at different frequencies of an aircraft part with impact damage. Low frequencies are necessary to detect deep defects. In fact, the damage resulting from impact damage is more extended in deeper composite plies.

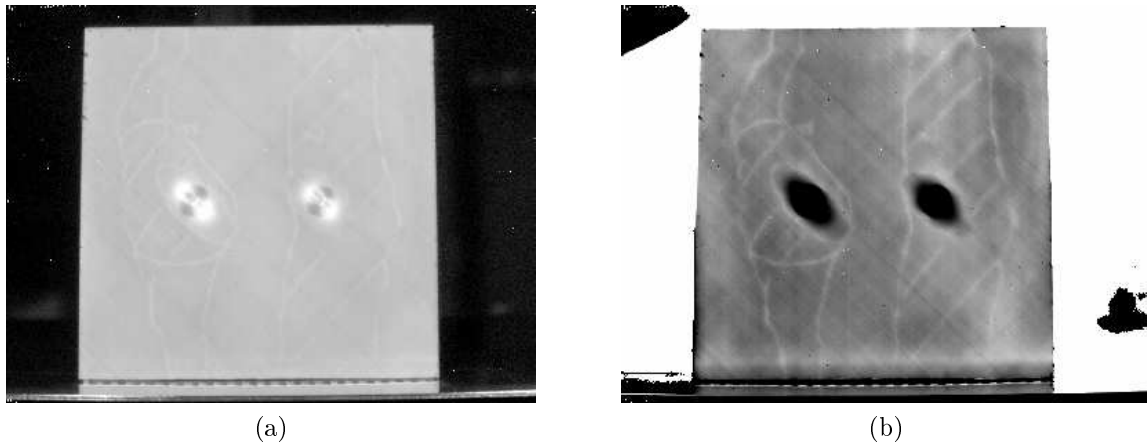(a)   (b)

Figure 2.9: Phase images of a part of composite with impact damages at (a) 0.1 Hz and (b) 0.03 Hz excitation frequencies.

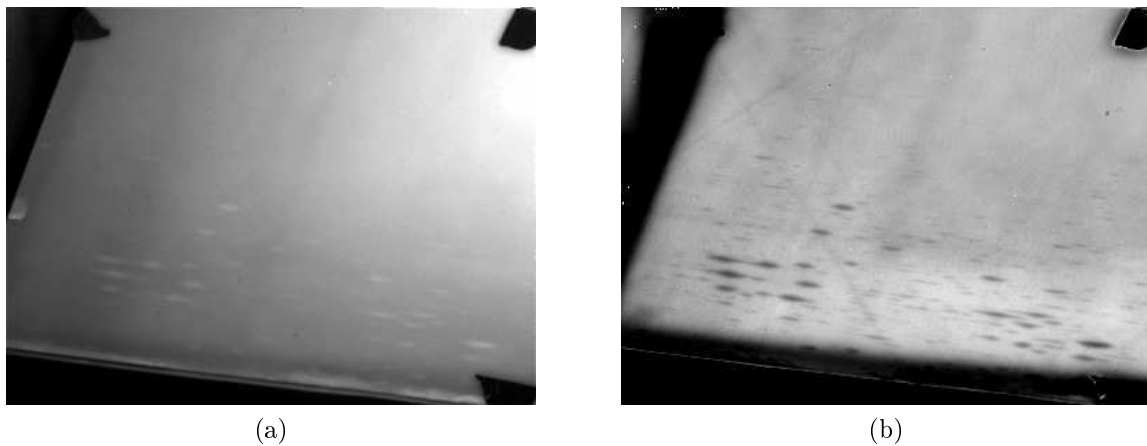(a)   (b)

Figure 2.10: (a) Amplitude and (b) phase images of a composite part with porosity (0.05 Hz).
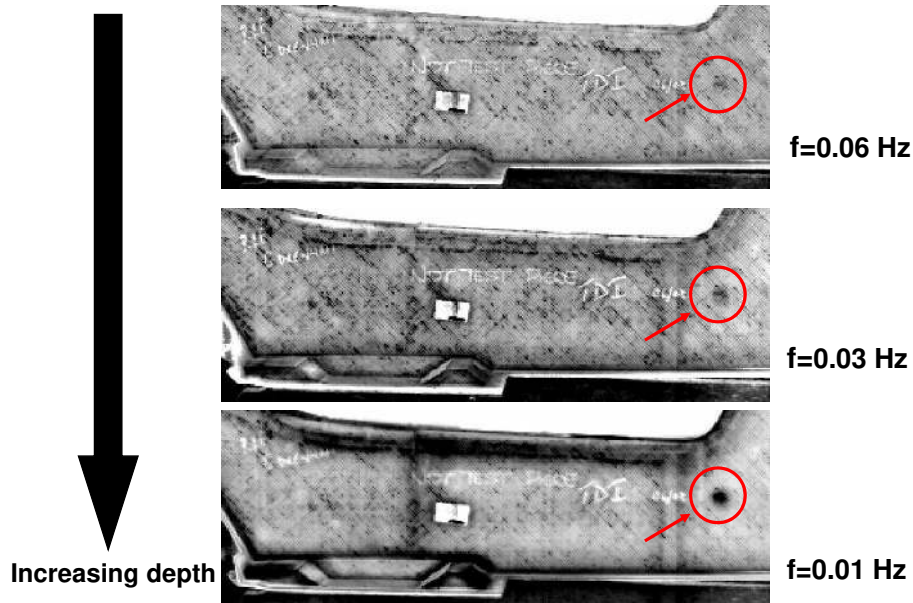
Figure 2.11: Example of lockin phase images of an impact damage in a CFRP component obtained at different frequencies.

2.5 Properties of lockin thermography

2.5.1 Blind frequency

In Fig. 2.12, phase images of plate I are shown at several frequencies. When the excitation frequency is decreased, deeper defect become visible in the phase image. A defect indication first appears brighter than the background, then, at a lower frequency, it disappears and at lower frequency it appears darker than the background. This can be clearly observed at a frequency of 0.005 Hz for the defects situated at depths of 1 mm and 1.5 mm, respectively. For deeper defects, lower frequencies should be taken to observe the phase inversion. The frequency at which the defect indication disappears is commonly called 'blind frequency'[BW01, WWJ07].

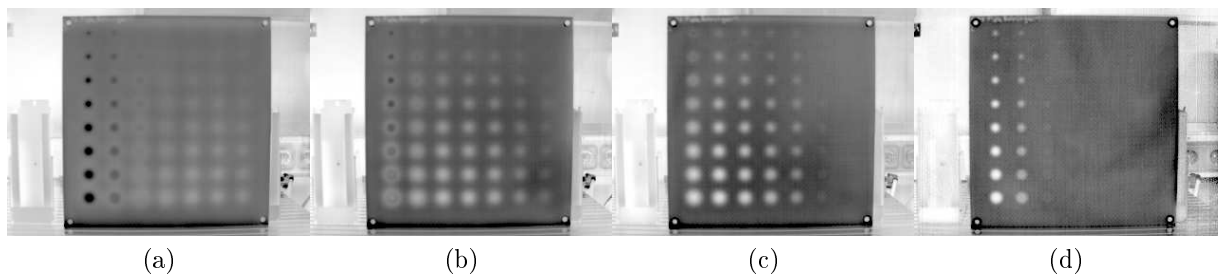Figure 2.12: Example of lockin phase images obtained for different frequencies (a) 0.005 Hz, (b) 0.01 Hz, (c) 0.02 Hz, and (d) 0.08 Hz.

In reality, there is another less-visible blind frequency just before the defect gets brigther than the background. The defect appears darker than the background at higher frequencies. This phenomenon is difficult to notice in Fig. 2.12 due to the gray-scale of the images,

but it will be studied in detail in Chap. 3. A theoretical model will be derived and simulated. In the comparisons between the model and the measurements, both phase inversions are visible. This first blind frequency that appears at higher frequencies will be called f_b in the following chapters.

2.5.2 Relationship between defect depth and blind frequency

For sinusoidal modulation, the temperature distribution in the material in one dimension is given by [Man01]

$$T(z,t) = T_0 e^{-z/\mu} e^{i(\omega t - z/\mu)}, \tag{2.7}$$

where μ is the thermal penetration depth and $\omega = 2\pi f$ is the angular frequency. Thermal waves are damped. After a distance corresponding to the penetration depth μ, the amplitude decreases to 0.2% of the initial value. Fig. 2.13 illustrates the temperature distribution inside the material at different times.
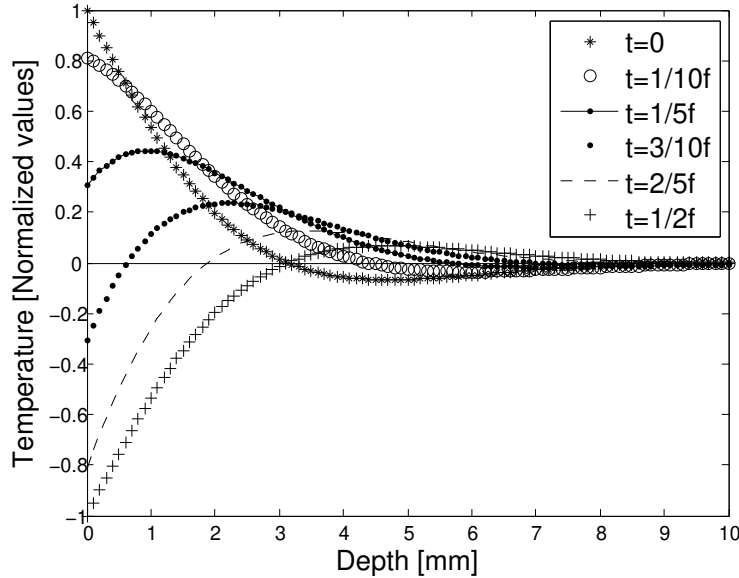

Figure 2.13: Theoretical one-dimensional propagation of heat in material at different times.

To measure deeper defects, one has to decrease the lockin frequency. The registration time is thereby long, especially when working with low frequencies to achieve greater depths. For CFRP material, the thermal conductivity is low ($0.2 \, \mathrm{mm^2 s^{-1}}$) so that the measurement time takes some minutes when working at typical frequencies of 0.005 to 0.01 Hz. In Fig. 2.12, it can be seen that at lower frequencies, deeper defects become visible through optical lockin thermography. Thus, the frequency chosen has to be small enough to observe deeper defects. The depth of a defect to be detected should be at least equal to one time the thermal penetration depth [She97]. For one measurement, only one phase image at one frequency (the lockin excitation frequency) is obtained. In order to become a depth-resolved method, several frequencies have to be applied. It was first shown by Busse [Bus79], and then confirmed in [TPW+79, LJT+81, BP82, Bus84, IC05] that the depth range for amplitude images corresponds to the penetration depth μ, while the maximum depth d_{max} that can be inspected using phase images, is roughly twice the

thermal penetration depth: $d_{max} \approx 2\mu$:

$$\mu = \sqrt{\frac{k}{\pi \cdot f \cdot \rho \cdot C_p}} = \sqrt{\frac{\alpha}{\pi \cdot f}}, \tag{2.8}$$

where ρ is the mass density, C_p is the thermal capacity, k is the heat conductivity, and α is the thermal diffusivity. By considering the blind frequency f_b in the phasegram, the depth d of a defect can be retrieved through the relationship

$$d = C\sqrt{\frac{\alpha}{\pi \cdot f_b}}. \tag{2.9}$$

So, by knowing the blind frequency, the depth of a defect can be retrieved. In Chap. 5, it will be shown that the parameter C also depends on the size of the defect. Small defect indications disappear at higher frequencies in the phasegram than larger defects.

2.6   Previous and related work

In thermal images, the disturbance of heat diffusion is at the origin of the contrast for defect detection. This thermal diffusion process influences the apparent shape of defects, making them appear blurred. To obtain the original size, an inverse problem has to be solved. It has been shown [FHSW92, SH$^+$95] that in photothermal imaging, which is a comparable method to optical lockin thermography with a laser excitation, the blurring effect can be modeled by a convolution of the defect shape function and a point-spread function (PSF). By knowing the PSF, defects can be deconvolved to retrieve the defect shape.

Several models have been developed to simulate photothermal imaging and to express the image formation through a convolution between a point-spread function (PSF) and the defect shape. One can find examples of successful modeling in [BA06, BGM$^+$07, CFKT93, FHSW92, VIN84, OHS05, Rei97, SWB94, TFCK92]. For example, [CFKT93] computed the point-spread function for pulsed thermography:

$$h(x, y, t, d) =$$
$$\frac{1}{2\pi(\pi\alpha t)^{1/2}} \frac{\partial}{\partial d}\left(\exp\left\{-\frac{\left(\sqrt{x^2 + y^2 + d^2} + d\right)}{4\alpha t}\right\} \frac{1}{\sqrt{x^2 + y^2 + d^2}}\right). \tag{2.10}$$

The author of [CFKT93] successfully demonstrated the improvement of deblurring thermal images. A cross-like defect is deblurred and the shape appears much sharper after deconvolution.

For photothermal imaging or lockin thermography, Bennet and Patty [BP82] developed a one-dimensional point-spread function

$$h(f) = \frac{1 + R_b e^{-2\sigma d}}{1 - R_b R_g e^{-2\sigma d}} \tag{2.11}$$

but this model did not predict the phenomenon of the blind frequency (R_b and R_g are reflection coefficients). In the field of lockin thermography, Breitstein and Altmann

[BL03b, BA06] used the two-dimensional point-spread function that they applied to phase images of electronic boards supposed to be infinitely thin:

$$h(x, y, \omega, l) = \frac{A}{r} \cdot e^{-r\sqrt{\frac{i\omega c_p \rho}{\lambda}}} e^{i\omega t}, \tag{2.12}$$

with $\rho = \sqrt{x^2 + y^2}$ derived from [CJ46]. This two-dimensional model requires the component to be very thin. Friedrich et al [FHSW92], derived a point-spread function in three dimensions for an isotropic material

$$h(x, y, \omega, d) = \frac{\pi}{2}\sigma^2 \frac{1}{\sqrt{x^2 + y^2 + d^2}} \exp\left\{-\sigma \cdot \left(\sqrt{x^2 + y^2 + d^2} + d\right)\right\}$$
$$\left(\frac{A}{\sqrt{x^2 + y^2 + d^2}} \left(1 + \frac{1}{\sigma\sqrt{x^2 + y^2 + d^2}}\right) + B\right), \tag{2.13}$$

where A and B are the defect constants in m^3. The model of the PSF for a solid of infinite thickness for photothermal imaging was later generalized by Seidel et al [SH$^+$95, SLW$^+$97]. The point-spread function is composed of two parts, h_A and h_B, following

$$h(x, y, \omega, d) = A \cdot h_A(x, y, \omega, d) + B \cdot h_B(x, y, \omega, d) \tag{2.14}$$

with

$$h_B(x, y, \omega, d) = \frac{\pi}{2}\sigma^2 \frac{1}{\sqrt{x^2 + y^2 + d^2}} \exp\left\{-\sigma \cdot \left(\sqrt{x^2 + y^2 + d^2} + d\right)\right\}$$
$$h_A(x, y, \omega, d) = h_B(x, y, \omega, d) \left(\frac{d}{\sqrt{x^2 + y^2 + d^2}} \left(1 + \frac{1}{\sigma\sqrt{x^2 + y^2 + d^2}}\right)\right). \tag{2.15}$$

$A = \Delta k / k_0$ and $B = \Delta(\rho c)/(\rho c)_0$ represent the variations of the thermal parameters. Finally, in [PA08] a finite element method to simulate lockin thermography in three dimensions and the phase contrast response, was used.

Only few works are related to anisotropic materials: In [VIN84], a theoretical model based on an anisotropic point-spread function was presented. Only simulations of the model are provided. Bai et al [BW01] developed a one-dimensional model for determining the thermal response of defects in a composite material. The material is supposed to be composed of several layers of different materials. The composite material is modeled by a stack of n layers. The study shows good correspondence between simulations and measurements. There is a frequency called optimal frequency that creates maximal phase contrast between the intact area and the defective area. This frequency should be used for inspection. The blind frequency should be avoided since no signal information of the defect is present.

In [CKP$^+$08] a method was proposed for evaluating the size of subsurface defects with lockin thermography. The phase contrast image is sheared by δs and subtracted from the phase contrast image

$$\Delta\varphi_{SP} = \Delta\varphi(x + \delta s, y) - \Delta\varphi(x, y). \tag{2.16}$$

This method is equivalent to performing a spatial derivative and the shear image provides zero phase values that correspond to inflexion points. It is equivalent to computing the size

of the defect by taking the width of the defect at the full-width half-maximum (FWHM). In the field of defect size determination, the criterion of FWHM is a commonly used method and is applied in this work as well.

For all studies, a calibration to determine the material properties is necessary. A test-piece with artificial defects in definite depths is used, notably to determine the accuracy, resolution and probability of detection of the method. In Chap. 3, a similar model to Eq. 2.13 [FHSW92] will be derived using Green's functions in particular and will be adapted to anisotropic material.

Chapter 3

Heat diffusion

The solution of the heat equation allows obtaining a link between thermal measurements and heterogeneities in the material. This is an important task in thermographic NDT. The defect signatures visible in the infrared images are due to the diffusion of thermal waves in the material. Waves are reflected at thermal boundaries and the reflected waves interfere with the excitation waves. In order to perform quantitative analysis of defects, a theoretical model is required. Because anisotropy of the composite materials has to be taken into account, the three-dimensional conduction process has to be formulated generally for inhomogeneous and anisotropic materials.

3.1 Heat conduction

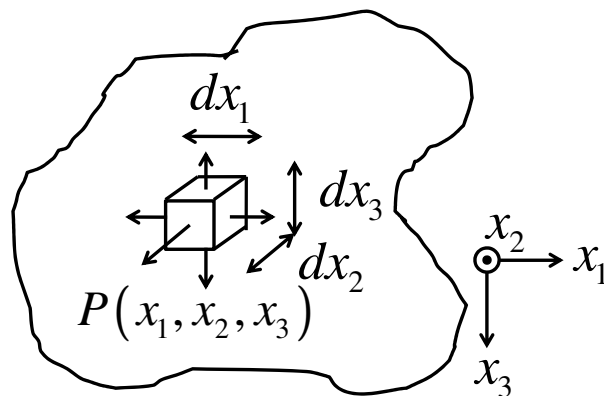### 3.1.1 Heat conduction in an anisotropic medium

Figure 3.1: Flow of heat in a volume element.

The heat conduction is the transfer of thermal energy between neighboring molecules in a material due to a temperature gradient. Temperature gradients lead to heat flow. They can be produced by an external heat source on a part of the solid. For example, the periodic temperature profile at Earth's surface during the period of one day is due to the sun's radiation and leads to the conduction of heat inside the earth. An equilibrium is reached after a temporal transient regime leading to stationary temperature distribution. Fig. 3.1 shows an element of volume dV around a point P in a body. The rate of flow q_i

in an anisotropic medium is proportional to the gradient of the temperature T: $T_{,j} = \frac{\partial T}{\partial x_j}$, following

$$q_1 = -k_{11}T_{,1} - k_{12}T_{,2} - k_{13}T_{,3}$$
$$q_2 = -k_{21}T_{,1} - k_{22}T_{,2} - k_{23}T_{,3} \quad (3.1)$$
$$q_3 = -k_{31}T_{,1} - k_{32}T_{,2} - k_{33}T_{,3}$$

or more generally by using Einstein's notation

$$q_i = -\sum_{j=1}^{3} k_{ij}\frac{\partial T}{\partial x_j} = -k_{ij}\frac{\partial T}{\partial x_j} \quad (3.2)$$
$$q_i = -k_{ij}T_{,j}$$

This law is also known as 'Fourier's law'. If the solid is isotropic, the equation reduces to

$$k_{ij} = k\delta_{ij} \quad (3.3)$$

where δ is the Kronecker's symbol and the thermal conductivity k is a scalar. In this case, the Fourier's law reduces to

$$q_i = -k\delta_{ij}T_{,j} = -kT_{,i}. \quad (3.4)$$
$$(3.5)$$

- If the material is homogeneous: the thermal conductivity k is independent of the position x_i

- If the material is heterogeneous, the thermal conductivity k depends on the position: $k(x_i)$.

For anisotropic bodies, the heat flux can be written as [BCHSL92, CJ46]:

$$q = -\Lambda \cdot \nabla T, \quad (3.6)$$

where ∇ is the differential operator $\nabla = \left(\frac{\partial}{\partial x_1}, \frac{\partial}{\partial x_2}, \frac{\partial}{\partial x_3} \right)$ in $\mathbb{R}^3$ and Λ is the two-dimensional symmetric conductivity tensor

$$\Lambda = \begin{bmatrix} k_{11} & k_{12} & k_{13} \\ k_{21} & k_{22} & k_{23} \\ k_{31} & k_{32} & k_{33} \end{bmatrix} \quad (3.7)$$

where $k_{ij} = k_{ji}$ due to the symmetry of the tensor.

3.1.2 Law of conservation of energy

The increase of the temperature in a closed system is due to

- heat conduction

- the contribution of volume sources a.

The specific enthalpy h gets increased:

$$\rho \frac{\partial h}{\partial t} = -q_{i,i} + a.$$

(3.8)

With $q_i = -k_{ij}T_{,j}$, one obtains

$$\rho \frac{\partial h}{\partial t} = (k_{ij}T_{,j})_{,i} + a$$

(3.9)

and since $h = C_P T$,

$$\boxed{\rho C_P \dot{T} = (k_{ij}T_{,j})_{,i} + a}$$

(3.10)

where C_P is the thermal capacity $[J \cdot kg^{-1} \cdot K^{-1}]$ and ρ is the density of the material $[kg \cdot m^{-3}]$. This equation is the general formulation of the heat equation in heterogeneous, anisotropic material. If the material is homogeneous, the equation reduces to

$$\boxed{\rho C_P \dot{T} = k_{ij}T_{,ij} + a}$$

(3.11)

and for an isotropic and homogeneous material,

$$\rho C_P \dot{T} = kT_{,ii} + a$$
$$\rho C_P \dot{T} = k\Delta T + a.$$

(3.12)

For a stationary system without a volume source, the equation simplifies into

$$\Delta T = 0.$$

(3.13)

3.1.3   Link between isotropic and anisotropic material

A transformation to a new system of rectangular coordinates, called principal axes of conductivity, can be found in [CJ46]. In this case, the equation reduces to

$$\rho C_P \dot{T} - k_i T_{,ii} = a,$$

(3.14)

with k_1, k_2, k_3 being the principal conductivities. Further, the diagonalized conductivity matrix is given by

$$\Lambda = \begin{bmatrix} k_1 & 0 & 0 \\ 0 & k_2 & 0 \\ 0 & 0 & k_3 \end{bmatrix}.$$

(3.15)

By performing a change of variable,

$$x_i \rightarrow x_i \sqrt{\frac{k_i}{k}},$$

(3.16)

Eq. 3.14 becomes

$$\rho C_P \dot{T} - k T_{,ii} = a.$$

This equation corresponds to the heat equation of isotropic and homogeneous solids (Eq. 3.12). In order to preserve the volumes through the change of variable, the following condition has to be respected:

$$\begin{vmatrix} \frac{k}{k_1} & 0 & 0 \\ 0 & \frac{k}{k_2} & 0 \\ 0 & 0 & \frac{k}{k_3} \end{vmatrix} = \frac{k^3}{k_1 k_2 k_3} = 1. \tag{3.17}$$

This leads to

$$k = (k_1 k_2 k_3)^{1/3}. \tag{3.18}$$

The heat equation with given boundary conditions will be solved for the simple case of an isotropic material. The changes of variables of Eq. 3.16 and Eq. 3.18 allows obtaining the solution of an anisotropic and homogeneous material.

In the following sections, some one-dimensional simple cases are presented in order to achieve some general properties from Eq. 3.10.

3.1.4 Example of analysis of the transient response

The goal is to determine the temperature distribution at the surface of a semi-infinite solid in one dimension. The component should be subject to a harmonic excitation beginning at $t = 0$. It should have no volume sources and have an isotropic and homogeneous material. The heat equation for this problem is

$$\dot{T} = \alpha T_{,11} \tag{3.19}$$

with $\alpha = \frac{k}{\rho C_P}$. The temperature distribution can be interpreted as the superposition of a transient and a dynamic term [Wu96]:

$$T = T_{trans}(x, t) + T_{dyn}(x) \cdot e^{i2\pi ft}, \tag{3.20}$$

with the first term arising from a transient heat flux and the second from a modulated heat flux at the surface of the component. Two problems have to be solved separately. The transient temperature distribution T_{trans} is solved by considering a constant heat flux

$$F(x = 0, t) = -kT_{,i}\big|_{x=0} = \frac{1}{2}F_0$$

at the surface of the component. The temperature distribution is found to be [CJ46]

$$T_{trans}(x, t) = \frac{2F_0}{k} \left[\sqrt{\frac{\alpha t}{\pi}} e^{\frac{-x^2}{4\alpha t}} - \frac{x}{2} erfc \frac{x}{2\sqrt{\alpha t}} \right] \tag{3.21}$$

and at the surface $x = 0$, the temperature is

$$T_{trans}(x = 0, t) = \frac{2F_0}{k} \sqrt{\frac{\alpha t}{\pi}}. \tag{3.22}$$

33

The dynamic temperature distribution T_{dyn} is obtained by considering periodic boundary conditions and by taking a surface flux at $x = 0$ of

$$F(x = 0, t) = \frac{1}{2}F_0 e^{i2\pi ft}$$

into account. The solution is [CJ46]

$$T_{dyn}(x, t > 0) = \frac{F_0}{\sqrt{2}k}\sqrt{\frac{\pi f}{\alpha}}e^{i(2\pi ft - \sqrt{\frac{\pi f}{\alpha}}x - \frac{\pi}{4})} \qquad (3.23)$$

Some properties of harmonic wave-fields are important. First, the amplitude of the harmonic response decreases with distance as

$$e^{-\sqrt{\frac{\pi f}{\alpha}}x} = e^{-2\pi\frac{x}{\lambda}}, \qquad (3.24)$$

and thus decreases more rapidly for a large excitation frequency f. Then, there is a constant $(-\frac{\pi}{4})$ phase lag due to the temperature oscillation and a progressive lag,

$$\sqrt{\frac{\pi f}{\alpha}}x, \qquad (3.25)$$

that depends on the frequency f. Furthermore, the temperature modulation is highly damped. After a distance corresponding to a wavelength $\lambda = 2\pi\mu$, the amplitude decreases to a value of $exp[-2\pi] = 0.19\%$ of the initial value. This means that the model of a semi-infinite solid can be taken for test parts with a thickness of one or two wavelengths. CFRP material has a thermal diffusivity of typically $0.2 \cdot 10^{-6}$ $m^2 s^{-1}$ (see Chap. 5.4.1). The thickness L of the test piece has to be greater than 2λ. That gives a minimal frequency of

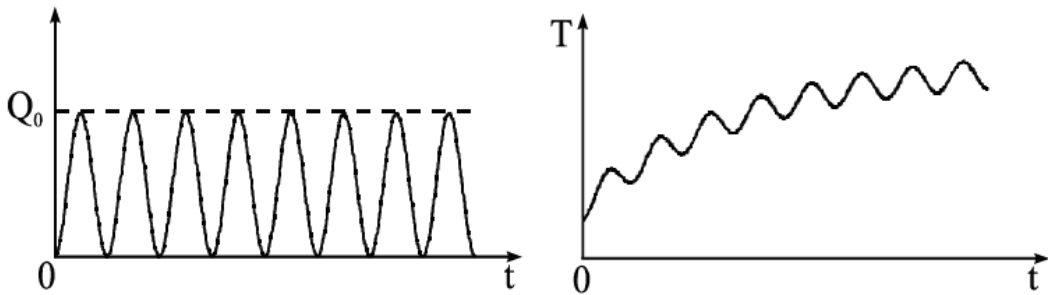$$f_{\min} = \frac{4\pi}{L^2}\alpha. \qquad (3.26)$$

Figure 3.2: (a) Periodic heat modulation and (b) surface temperature vs. time in the non-stationary case [Wu96].

For a CFRP part 2 mm thick, the minimal frequency to be used is 0.62 Hz, while for a part 3 mm thick, it is 0.28 Hz. Finally, it should be noted that the thermal wave propagates into the solid with a phase velocity of

$$\sqrt{4\alpha\pi f} = \sqrt{2\alpha\omega}. \qquad (3.27)$$

Here, $\omega = 2\pi f$ is the angular frequency. The diffusivity α can be determined either by measuring the phase and amplitude at a certain position x or by measuring the velocity of the wave. This fact is used in Chap. 7.3. The temperature response of harmonic excitation in one dimension is plotted in Fig. 3.2. The transient response can be well-observed and a steady state is reached after some periods.

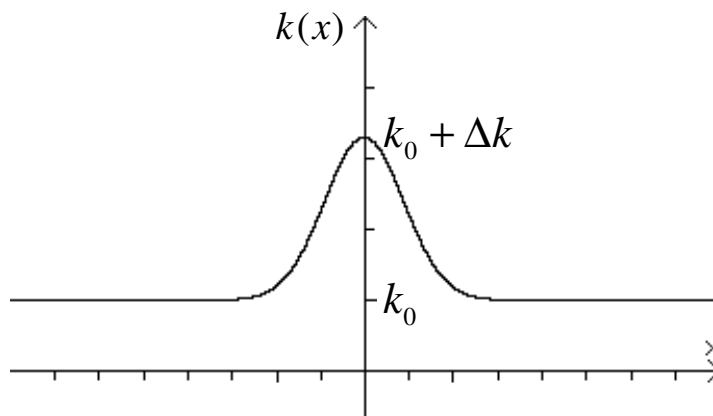### 3.1.5 Example of a one-dimensional heterogeneous problem

Figure 3.3: Representation of the heterogeneity function.

The problem is solved in one dimension for simplification purposes. The body is supposed to contain a heterogeneity. The problem is stationary: $\dot{T} = 0$. The volume sources a are supposed to be constant. The heterogeneity is expressed as

$$k(x) = k_0 + \Delta k e^{-\left(\frac{x}{l}\right)^2} \tag{3.28}$$

and is represented in Fig. 3.3. The goal is to find the temperature distribution in the body. The general formulation of the heat equation is given by

$$\rho C_P \dot{T} = (k_{ij} T_{,j})_{,i} + a. \tag{3.29}$$

It is a one-dimensional and stationary problem and the body is isotropic. The equation reduces to:

$$(kT_{,1})_{,1} + a = \left(\left(k_0 + \Delta k e^{-\left(\frac{x}{l}\right)^2}\right) T_{,1}\right)_{,1} + a = 0 \tag{3.30}$$

and this leads to:

$$k_0 T_{,11} + \Delta k \left(e^{-\left(\frac{x}{l}\right)^2}\right)_{,1} T_{,1} + \Delta k e^{-\left(\frac{x}{l}\right)^2} T_{,11} + a = 0. \tag{3.31}$$

If k is uniform, $\Delta k = 0$ and one obtains again the equation $k_0 T_{,11} + a = 0$.
I think that it was interesting to show how to derive an equation of a simple problem with a heterogeneous material. It could be shown that this equation is the sum of the basic problem ($k_0 T_{,11} + a = 0$) and a term that depends on the heterogeneity:

$\Delta k \left(e^{-\left(\frac{x}{l}\right)^2} \right)_{,1} T_{,1} + \Delta k e^{-\left(\frac{x}{l}\right)^2} T_{,11}$. The heterogeneity influences the response through its geometric properties (l) that correspond to the size and position of a defect and its thermal properties (Δk) corresponding to the thermal properties of a defect.

Eq. 3.31 can be interpreted as the heat equation for isotropic and homogeneous material

$$k_0 T_{,11} + a' = 0 \tag{3.32}$$

with the volume sources a' being a term depending on the heterogeneity's properties and the thermal response itself:

$$a' = a + \Delta k \left(e^{-\left(\frac{x}{l}\right)^2} \right)_{,1} T_{,1} + \Delta k e^{-\left(\frac{x}{l}\right)^2} T_{,11}. \tag{3.33}$$

3.2 Green's functions

3.2.1 General formulation

Green's functions are used to solve inhomogeneous linear differential equations. They are named in honor of the English mathematician and physicist George Green (1793-1841). The Green's function method is based on the principle that the solution of any given problem with any boundary and initial conditions can be computed by using the solution of the problem with elementary conditions. The source has the form of a Dirac Delta function in a spatial and time domain, and the initial and boundary conditions are homogeneous everywhere. The primordial solution is called the 'Green's function'[CJ46]. An inhomogeneous linear differential equation has the form:

$$Lu(x) = f(x), \tag{3.34}$$

where L is a differential operator, x is the position vector and f is a function. The Green's function G is defined by

$$LG(x, x') = \delta(x - x'). \tag{3.35}$$

L operates on the variable x'. The solution for u is given by

$$u(x) = \int f(x')G(x, x')dx'. \tag{3.36}$$

To get the general solution (called homogeneous solution) - i.e. to satisfy boundary conditions - a solution of the homogeneous problem can be added to the particular solution. A particular solution is given by:

$$y(t) = \sqrt{2\pi} \left(G \otimes f \right)(t) = \sqrt{2\pi} \int_{-\infty}^{+\infty} G(t - t')f(t')dt'. \tag{3.37}$$

3.2.2 Green's functions for the heat equation

The thermal diffusion equation in isotropic material is (see Eq. 3.10)

$$T_{,ii} - \frac{1}{\alpha} \dot{T} = -\frac{1}{k} a. \tag{3.38}$$

By using Green's functions, the problem reduces to finding a function g that satisfies the heat diffusion equation:

$$g_{,ii}(r,t;r_0,t_0) - \frac{1}{\alpha}\dot{g}(r,t;r_0,t_0) = -\frac{1}{k}\delta(r-r_0,t-t_0). \tag{3.39}$$

Depending on the initial and boundary conditions, simple solutions can be found. It is easy to find Green's functions in the literature for given geometries. A set of Green's functions for rectangular coordinates is provided in [BCHSL92]. Green's functions are also given in [Man01] for the particular case of periodic heating. The solutions are given for different simple geometries. One distinguishes:

- the infinite region: the body has no boundary;

- the semi-infinite body: the body has one boundary (generally situated at position $x = 0$);

- the slab: the body is bounded by two planes (at $x = 0$ and $x = d$ where d is the thickness of the part).

3.2.3 Initial and boundary conditions

In order to solve the heat equation, some knowledge of the initial and boundary conditions is necessary. The initial conditions express a condition for the temperature at time t=0. They have the form

$$T(x_i, t=0) = F(x_i). \tag{3.40}$$

Boundary conditions are also necessary to get well-posed problems and to be able to solve the heat equation. They express the heat or flux that is applied on the boundaries of the body. They may be one of three types at each boundary:

$$k_i T_{,i}(r,t) - h_i T(r,t) = f_i(t) \tag{3.41}$$

at the i-th boundaries ($i \in \{0..5\}$). $f_i(t)$ is a specified boundary function. The values h_i and k_i represent the kind of boundary conditions at the limiting values of the coordinate r. The parameter h_i is called a 'constant-with-time heat transfer coefficient' (or contact conductance). There are six different cases (see Tab. 3.1):

- boundary condition of zeroth kind: there is no physical boundary;

- boundary of first kind or Dirichlet condition: a specified temperature is imposed on the boundary

$$T(r,t) = f_i(t); \tag{3.42}$$

- boundary of second kind or Neumann condition: a specified heat flux is imposed on the boundary

$$k_i T_{,i}(r,t) = f_i(t); \tag{3.43}$$

- boundary of third kind or Robin condition: a combination of specified temperature and heat flux (convective condition)

$$k_i T_{,i}(r,t) - h_i T(r,t) = f_i(t);$$ (3.44)

- boundary of fourth kind or Carslaw condition concerns a thin film without convection

$$k_i T_{,i}(r,t) = f_i(t) - (\rho C_P d)_i \left. \dot{T} \right|_{r_i};$$ (3.45)

The product $(\rho C_P d)_i$ is taken for the film at its l-th surface and d represents its thickness.

- boundary of fifth kind or Jaeger condition concerns a thin film with convection

$$k_i T_{,i}(r,t) - h_i T(r,t) = f_i(t) - (\rho C_P d)_i \left. \dot{T} \right|_{r_i}.$$ (3.46)

The solution of any problem with specified boundary conditions can be computed in the following way:

$$
\begin{aligned}
T(x,t) &= \int_{x'=-\infty}^{\infty} g(x,t/x',0) F(x') dx' \\
&+ \frac{\alpha}{k} \int_{t'=0}^{t} \int_{x'=-\infty}^{\infty} g(x,t/x',t') a(x',t') dx' dt'.
\end{aligned}
$$ (3.47)

The equation is composed of two terms, one containing the initial condition F (called a 'particular solution') and the other containing the volumetric heat sources a.

Table 3.1: Summary of the different boundary conditions [BCHSL92].

Kind	Kind of boundary condition	Description of boundary condition
0	zeroth kind	No physical boundary
1	first kind or Dirichlet condition	Imposed temperature, Eq. 3.42
2	second kind or Neumann condition	Imposed heat flux, Eq. 3.43
3	third kind or Robin condition	Convective condition, Eq. 3.44
4	fourth kind or Carslaw condition	Thin film, no convection, Eq. 3.45
5	fifth kind or Jaeger condition	Thin film, convection, Eq. 3.2.3

3.2.4 Methods for the derivation of Green's functions

There are different methods of computing Green's functions [BCHSL92], namely:

- Laplace transform

- Method of images

- Method of separation of variables

- Product solution.

3.3 Green's functions for periodic thermal wave-fields

In lockin thermography, periodic heating of the surface of the component is performed. The theory of periodic thermal wave-fields, as derived by Mandelis [Man01], is used to solve the heat equation with periodic heating.

3.3.1 Use of the Fourier transform

The solution is sought in Fourier space and interpreted as the steady-periodic response at a single frequency. If the Fourier transform of the temperature field $T(r,t)$ exists:

$$\theta(r,f) = \int_{-\infty}^{\infty} T(r,t)e^{-i2\pi ft}dt, \tag{3.48}$$

and by taking the Fourier transform of the heat equation (Eq. 3.10), one obtains

$$\frac{1}{\alpha}\int_{-\infty}^{\infty} \dot{T}(r,t)e^{-i2\pi ft}dt - \left(\int_{-\infty}^{\infty} T(r,t)e^{-i2\pi ft}dt\right)_{,ii} = \frac{1}{k}\int_{-\infty}^{\infty} a(r,t)e^{-i2\pi ft}dt. \tag{3.49}$$

By performing an integration by parts in the first term and by using the boundary condition, $T(r,t) \xrightarrow{\pm\infty} 0$, one obtains the heat equation in the Fourier space with volume sources

$$\theta_{,ii}(r,f) - \sigma^2 \cdot \theta(r,f) = -\frac{1}{k}A(r,f), \tag{3.50}$$

where

$$\sigma = (1+i)\sqrt{\frac{\pi f}{\alpha}} = \frac{(1+i)}{\mu} \tag{3.51}$$

and μ is the thermal penetration depth in $[m]$. The quantity σ has the physical meaning of a dispersive complex wave number.

In the special case where the thermal source is harmonically modulated at a frequency f_0, the temperature function can be written as

$$T(r,t) = \tau(r)e^{i2\pi f_0 t}. \tag{3.52}$$

One has

$$\int_{-\infty}^{\infty} e^{-i2\pi(f-f_0)t}dt = 2\pi\delta(f-f_0). \tag{3.53}$$

By computing the Fourier transform of the temperature distribution as in Eq. 3.48 and by using some properties of the Dirac function, one obtains

$$\theta(r,f) = \int_{-\infty}^{\infty} \tau(r,f_0)e^{-i2\pi(f-f_0)t}dt = 2\pi\tau(r,f_0)\delta(f-f_0). \tag{3.54}$$

This equation shows that the energy of the harmonic field is concentrated at the single frequency f_0 and is represented by a Delta-function in the spectrum. Here, it is more useful

to use $\tau(r, f)$, instead of $\tau(r, f_0)$, to describe thermal wave-fields. Since the volumetric sources should be harmonic, its Fourier transform is proportional to $\delta(f - f_0)$. So, by using Eq. 3.54, the Dirac-peak can be suppressed in Eq. 3.50, leading to the equation of thermal wave-fields

$$\tau_{,ii}(r, f) - \sigma^2 \tau(r, f) = -\frac{1}{k} A(r, f), \tag{3.55}$$

that is noted

$$\theta_{,ii}(r, f) - \sigma^2(f)\theta(r, f) = -\frac{1}{k} A(r, f) \tag{3.56}$$

for convenience. In this equation, the modulation factor was eliminated to compute the temperature field directly. The temperature in the time domain is directly given using Eq. 3.52 by multiplying the computed thermal wave-field with the harmonic term $e^{i2\pi ft}$

$$T(r, t) = T(r, f)e^{i2\pi ft}. \tag{3.57}$$

3.3.2   General solution of heat equation

Let's consider the Green's function that satisfies Eq. 3.56 as

$$G_{,ii}(r; r_0, f, t_0) - \sigma^2(f)G(r; r_0, f, t_0) = -\frac{1}{k}\delta(r - r_0)e^{-i2\pi ft}. \tag{3.58}$$

G is the Fourier transform of the function g

$$G(r, t; f, t_0) = \int_{-\infty}^{\infty} g(r, t; r_0, t_0)e^{-ift}dt \tag{3.59}$$

that would satisfy the heat conduction equation Eq. 3.58 in the time domain. The general solution of Eq. 3.56 is

$$\begin{aligned} \theta(r, f) &= \left(\frac{\alpha}{k}\right) \iiint_V A(r, r_0, f)G(r, r_0, f)dV \\ &+ \alpha \oint_S [G(r, r_0, f)\theta_{,i}(r, r_0, f) - \theta(r, r_0, f)G_{,i}(r, r_0, f)] \cdot dS. \end{aligned} \tag{3.60}$$

The solution is the superposition of two terms: the first term contains the volumetric sources and the second term the Green's function.

3.3.3   Typical problems

Green's functions can easily be found for some simple geometries. The Green's functions differentiate according to the kind of boundary conditions (first, second or third order). For example, the Green's functions for a semi-infinite body with boundary conditions of the second kind (the flux is imposed on the surface) is given by:

$$G(r, r', f_0) = \frac{1}{4\pi\alpha}\left(\frac{e^{-\sigma r}}{r} + \frac{e^{-\sigma r'}}{r'}\right), \tag{3.61}$$

where

$$\begin{aligned} r &= \sqrt{(x_1 - x_{10})^2 + (x_2 - x_{20})^2 + (x_3 - x_{30})^2} \tag{3.62} \\ r' &= \sqrt{(x_1 - x_{10})^2 + (x_2 - x_{20})^2 + (x_3 + x_{30})^2}. \tag{3.63} \end{aligned}$$

40

3.4 Modeling of the image formation process of subsurface defects

The apparent size of the detected defects in the infrared image depends on the lockin frequency and the depth of the defects. Deeper defects appear larger and more blurred. One of the main objectives of the thesis is to model the image formation process of lockin thermography. The images of defects are characterized by heat diffusion in the material. In order to compute the point-spread function for thermal fields, Green's functions are used. The point-spread function that describes the image formation at the surface of one defective point can be computed for simple problem formulations of homogeneous material with simple boundary conditions, as is the case for the semi-infinite part. For the special case of lockin thermography, Mandelis' theory [Man01] of periodic thermal wave-fields, is used. In the following, a static case that means that the defect shape does not change during the measurement process is described.
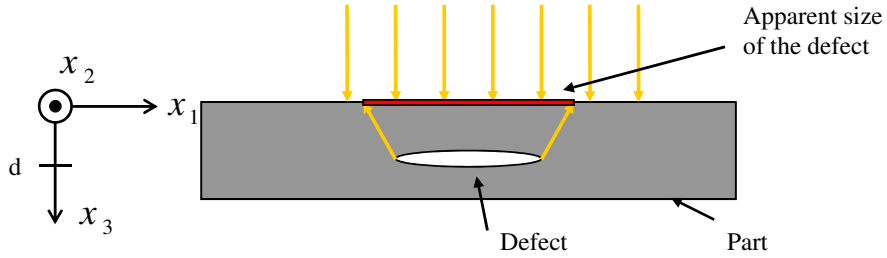

Figure 3.4: Modeling of the image formation process at the surface of the material.

3.4.1 Theoretical modeling of image formation for the homogeneous semi-infinite part

To solve the heat equation (Eq. 3.56), some assumptions are necessary. The following assumptions are made:

- the size of the test part is sufficiently large (semi-infinite part);

- there is no volume source;

- the illumination is homogeneous on the entire surface;

- a time harmonic flux is imposed on the surface $x_3 = 0$ (Fourier domain)

$$F(r^s, t) = \frac{1}{2}F_0\delta(f - f_0);$$ (3.64)

- Neumann conditions exist at the surface

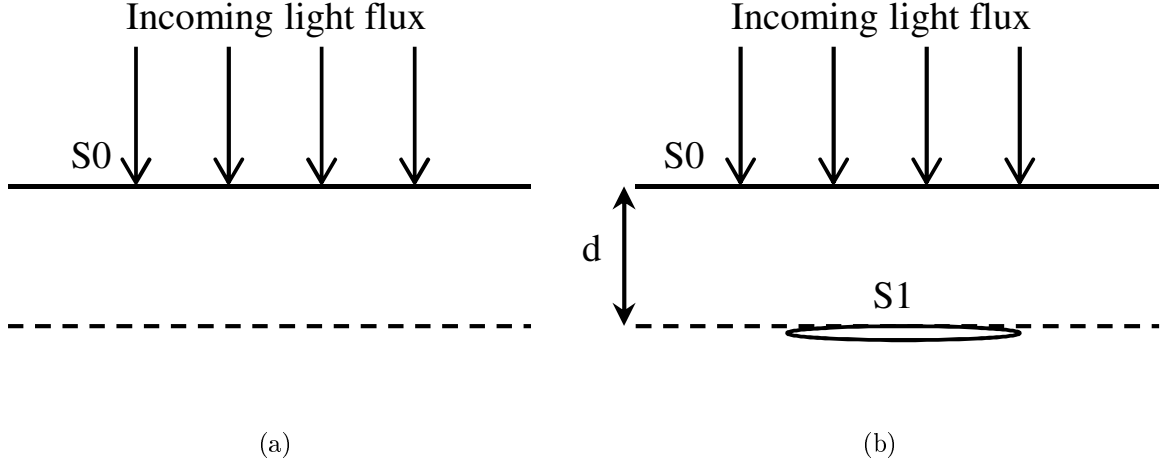$$(G(r, r', f)dS)_{,i}\big|_{x_3=0} = 0.$$ (3.65)

Figure 3.5: Scheme of the light flux on the semi-infinite part; (a) without a defect and (b) with a defect. The defect is represented by S_1 and is at a depth d.

Semi-infinite part without a defect

First the problem of the semi-infinite part without a defect (Fig. 3.5a) is considered. The Green's function that satisfies the homogeneous Neumann boundary conditions (second kind) on the planar surface of the semi-infinite region is given by Eq. 3.61:

$$G(r, r', f_0) = \frac{1}{4\pi\alpha} \left(\frac{e^{-\sigma r}}{r} + \frac{e^{-\sigma r'}}{r'} \right), \tag{3.66}$$

where

$$r = \sqrt{(x_1 - x_{10})^2 + (x_2 - x_{20})^2 + (x_3 - x_{30})^2} \tag{3.67}$$

$$r' = \sqrt{(x_1 - x_{10})^2 + (x_2 - x_{20})^2 + (x_3 + x_{30})^2}. \tag{3.68}$$

Due to the Neumann condition at the surface and the lack of volume sources, Eq. 3.60 reduces to:

$$\theta(r, f_0) = \alpha \oint_{S_0} [G_{,i}(r, r', f_0)\theta(r, r', f_0)] \cdot dS. \tag{3.69}$$

The surface flux can be expressed as

$$F(r^S, f_0) = k \frac{\delta}{\delta x_3} \theta(x_{10}, x_{20}, x_{30}, f_0) \Big|_{x_3=0}, \tag{3.70}$$

where k is the thermal conductivity. This leads to

$$\Rightarrow \theta_{,i}(r, r', f_0)|_{x_3=0} = \frac{F_0}{2k} \delta(f - f_0). \tag{3.71}$$

By inserting this result in Eq. 3.69, one obtains

$$\theta(r, f_0) = \alpha \int_{-\infty}^{+\infty} \frac{1}{4\pi\alpha} \left(\frac{e^{-\sigma \cdot r}}{r} + \frac{e^{-\sigma \cdot r'}}{r'} \right) \cdot \frac{F_o}{2k} \delta(f - f_0) \cdot dx_{10} dx_{20}. \tag{3.72}$$

At the surface of the component, the parameter $x_{30} = 0$, so that

$$\theta(r, f_0) = \frac{F_o}{4\pi k} \delta(f - f_0) \int_{-\infty}^{+\infty} \left(\frac{e^{-\sigma \cdot r_o}}{r_o} \right) \cdot dx_{10} dx_{20} \tag{3.73}$$

with $r_0 = \sqrt{(x_1 - x_{10})^2 + (x_2 - x_{20})^2 + x_3^2}$. By performing a change of variable

$$\begin{cases} x_1 - x_{10} = \rho \cos\theta \\ x_2 - x_{20} = \rho \sin\theta \\ \rho^2 = (x_1 - x_{10})^2 + (x_2 - x_{20})^2, \end{cases} \tag{3.74}$$

the following equation is obtained:

$$\theta(r, \omega_0) = \frac{F_0}{4\pi k} \delta(\omega - \omega_0) \int_0^{+\infty} \frac{\rho d\rho}{\sqrt{\rho^2 + x_3^2}} e^{-\sigma \cdot \sqrt{\rho^2 + x_3^2}} \int_0^{2\pi} d\theta \tag{3.75}$$

and the solution of the temperature distribution in the semi-infinite part is yielded:

$$\theta_0(r, f_0) = \frac{F_0}{2k} \delta(f - f_0) \sigma e^{-\sigma \cdot x_3}, \quad \sigma = (1 + i) \sqrt{\frac{\pi f_0}{\alpha}} \ . \tag{3.76}$$

Semi-infinite part with a defect

The problem of the infinite part with a planar defect S_1 situated at a depth d and of unknown shape (Fig. 3.5b) is now considered. The thermal wave-field can be interpreted as the sum of the thermal wave-field without a defect and with the field scattered by the defect. From Eq. 3.60, one obtains

$$\begin{aligned} \theta(r, f) &= \theta_0(r, f_0) + \theta_{scattered}(r, f_0) \\ &= \theta_0(r, f_0) - \alpha \int_{S_1} [G(r, r', f_0)\theta_{,i}(r, r', f_0) - \theta(r, r', f_0)G_{,i}(r, r', f_0)] \cdot dS_1 \\ &= \theta_0(r, f_0) - \alpha \int_{S_1} \left[\frac{\delta}{\delta x_3} (G(r, r', f_0) \theta(r, r', f_0)) \right] \cdot dS_1. \end{aligned} \tag{3.77}$$

The solution depends on the solution itself. To be able to solve the equation, the Born approximation is used: the thermal field at a depth d is approximated by the surface thermal field subjected to attenuation. The Green's function can also be approximated by the Green's function of the surface since the same boundary conditions should be on the defect.

$$\begin{aligned} \theta(r, f_0) &= R \cdot (\theta_0(r, f_0) + \Delta\theta(r, f_0)) \\ G(r, f_0) &= R \cdot (G_0(r, f_0) + \Delta G(r, f_0)). \end{aligned} \tag{3.78}$$

Here, R is the reflection coefficient on the defect boundary. Following the first Born approximation, the second term in the integral is neglected, which leads to:

$$\theta(r, f) - \theta_0(r, f_0) = -\alpha \cdot R^2 \int_{S_1} \left[\frac{\delta}{\delta x_3} (G_0(r, r', f_0) \theta_0(r, r', f_0)) \right] \cdot dS_1. \tag{3.79}$$

43

The temperature distribution can be expressed as the convolution of the point-spread function (PSF), h, with the defect shape

$$\theta(r, f) - \theta_0(r, f_0)$$

$$= -\alpha \cdot R^2 \int\limits_{-\infty}^{+\infty} \left[\frac{\delta}{\delta x_3} \left(G_0(r, r', f_0) \, \theta_0 \left(r, r', f_0 \right) \right] \cdot sh(x_1 - x_{10}, x_2 - x_{20}) \cdot dS \qquad (3.80)$$

$$= h(x_1, x_2; f, x_3) \otimes sh(x_1 - x_{10}, x_2 - x_{20}).$$

The function

$$sh(x_1, x_2) = \begin{cases} 0 & (x_1, x_2) \in S \\ 1 & (x_1, x_2) \notin S \end{cases} \qquad (3.81)$$

describes the shape of the defect and equals one on the defect shape and zero outside the defect. The partial derivative of Eq. 3.79 will be computed to obtain the point-spread function

$$h = -\alpha R^2 \frac{\partial}{\partial x_3} G_0 \theta_0 = -\alpha R^2 \frac{\partial}{\partial x_3} \left(\frac{1}{4\pi\alpha} \frac{e^{-\sigma r}}{r} \times \frac{F_0}{2k} \sigma e^{-\sigma x_3} \right). \qquad (3.82)$$

- The partial derivative of the right hand side contains:

$$\frac{\partial}{\partial x_3} \left(\frac{e^{-\sigma r}}{r} \times e^{-\sigma x_3} \right) =$$

$$\left(\frac{\partial}{\partial x_3} \frac{1}{r} \right) e^{-\sigma r} e^{-\sigma x_3} + \left(\frac{\partial}{\partial x_3} e^{-\sigma r} \right) \frac{1}{r} e^{-\sigma x_3} + \left(\frac{\partial}{\partial x_3} e^{-\sigma x_3} \right) \frac{e^{-\sigma r}}{r}.$$

- The first expression in the sum reduces to

$$\frac{\partial}{\partial x_3} \frac{1}{r} = -\frac{x_3}{r^3}.$$

- The second expression is given by

$$\frac{\partial}{\partial x_3} e^{-\sigma r} = -\sigma e^{-\sigma r} \frac{x_3}{r}.$$

- and finally

$$\frac{\partial}{\partial x_3} e^{-\sigma x_3} = -\sigma e^{-\sigma x_3}.$$

- Thus one obtains

$$\frac{\partial}{\partial x_3} \left(\frac{e^{-\sigma r}}{r} \times e^{-\sigma x_3} \right) = -e^{-\sigma r} e^{-\sigma x_3} \frac{\sigma}{r} \left(\frac{x_3}{\sigma r^2} + \frac{x_3}{r} + 1 \right) =$$

$$-e^{-\sigma r} e^{-\sigma x_3} \frac{\sigma}{r} \left(\frac{x_3}{r} \left(\frac{1}{\sigma r} + 1 \right) + 1 \right). \qquad (3.83)$$

44

By inserting Eq. 3.83 into Eq. 3.82, the following expression of the PSF is determined:

$$h(x_1, x_2, x_3; f_0) = \frac{F_0}{4\pi k} \cdot R^2 \cdot \frac{\sigma^2 \cdot e^{-\sigma \cdot (r + x_3)}}{r} \left(\frac{x_3}{r} \left(1 + \frac{1}{\sigma r} \right) + 1 \right). \tag{3.84}$$

By denoting the depth by d, the point-spread function h can be written as

$$h(x_1, x_2; f_0, d) = \frac{F_0}{4\pi k} \cdot R^2 \cdot \frac{\sigma^2 \cdot e^{-\sigma \cdot (r + d)}}{r} \left(\frac{d}{r} \left(1 + \frac{1}{\sigma r} \right) + 1 \right), \tag{3.85}$$

where $r = \sqrt{x_1^2 + x_2^2 + d^2}$.

3.4.2 Green's functions and PSF for anisotropic solids

A change in variables as described in Chap. 3.1.3 is performed. Therefore, the variable x_i is transformed using

$$x_i \rightarrow x_i \sqrt{\frac{k}{k_i}}. \tag{3.86}$$

The goal is to eliminate the unknown parameters k_i as well as ρ and C_P to get an equation that contains only the variable μ. The following results are obtained:

- First, one has

$$
\begin{aligned}
\sigma r &\rightarrow (1 + i) \sqrt{\frac{\pi f_0 \rho C_P}{k}} \sqrt{x_i^2 \frac{k}{k_i}} = (1 + i) \sqrt{x_i^2 \frac{\pi f_0 \rho C_P}{k_i}} \\
&= (1 + i) \sqrt{\frac{x_i^2}{\mu_i^2}} = (1 + i) r
\end{aligned}
\tag{3.87}
$$

  with $r = \sqrt{\frac{x_i^2}{\mu_i^2}}$.

- In a similar manner, one obtains

$$\sigma d \rightarrow (1 + i) \sqrt{\frac{\pi f_0 \rho C_P}{k}} d \sqrt{\frac{k}{k_3}} = (1 + i) d \sqrt{\frac{\pi f_0 \rho C_P}{k_3}} = (1 + i) \frac{d}{\mu_3}. \tag{3.88}$$

- Then

$$\frac{d}{r} \rightarrow \frac{d \sqrt{\frac{k}{k_3}}}{\sqrt{x_i^2 \frac{k}{k_i}}} = \frac{\frac{d}{\sqrt{k_3}}}{\sqrt{\frac{x_i^2}{k_i}}} = \frac{d \sqrt{\frac{\pi f_0 \rho C_P}{k_3}}}{\sqrt{x_i^2 \frac{\pi f_0 \rho C_P}{k_i}}} = \frac{d}{\mu_3 \sqrt{\frac{x_i^2}{\mu_i^2}}} = \frac{d}{\mu_3 r} \tag{3.89}$$

- and finally

$$\frac{\sigma^2}{r} \rightarrow \frac{(1 + i)^2 \frac{\pi f_0 \rho c}{k}}{\sqrt{x_i^2 \frac{k}{k_i}}} = \frac{(1 + i)^2 (\pi f_0 \rho c)^{3/2}}{k^{3/2} \sqrt{x_i^2 \frac{\pi f_0 \rho c}{k_i}}} = \frac{(1 + i)^2 (\pi f_0 \rho c)^{3/2}}{k^{3/2} \sqrt{\frac{x_i^2}{\mu_i^2}}}.$$

45

By taking into account Eq. 3.18, one obtains

$$k^{3/2} = (k_1 k_2 k_3)^{1/2}$$

and

$$k_i^{1/2} \rightarrow \left(\frac{k_i}{\pi f_0 \rho c}\right)^{1/2} (\pi f_0 \rho c)^{1/2} = \mu_i (\pi f_0 \rho c)^{1/2}$$

and

$$k^{3/2} = \mu_1 \mu_2 \mu_3 (\pi f_0 \rho c)^{5/2}.$$

Finally

$$\frac{\sigma^2}{r} \rightarrow \frac{(1+i)^2}{r \mu_1 \mu_2 \mu_3}. \tag{3.90}$$

The results of Eq. 3.87- 3.90 are combined. By inserting the results in Eq. 3.85, the point-spread function in the Fourier space for anisotropic solids is found:

$$h_a(x_1, x_2; f_0, d) =$$
$$\frac{F_o}{4\pi k} \cdot R^2 \cdot \frac{(1+i)^2}{\mu_1 \mu_2 \mu_3} \cdot \frac{e^{-(1+i)\left(r+\frac{d}{\mu_3}\right)}}{r} \cdot \left(\frac{d}{\mu_3 \cdot r}\left(1 + \frac{1}{(1+i)r}\right) + 1\right) \tag{3.91}$$

where $r = \sqrt{\frac{x_i^2}{\mu_i^2}}$ and $\mu_i = \sqrt{\frac{k_i}{\pi f_0 \rho C_P}} = \sqrt{\frac{\alpha_i}{\pi f_0}}$, $i \in \{1..3\}$, which is the thermal penetration depth. The presence of the parameter k does not matter the implementation of the function as it is a constant of the material.

3.4.3 Phase contrast

Instead of working with absolute phase values, the phase contrast function is used. The phase contrast function

$$\Delta\Phi = \Phi_{S_1} - \Phi_{S_0} = \arg(S_1) - \arg(S_0) \tag{3.92}$$

expresses the difference between a defect-free area, S_0, and the signal of the defect area, S_1. Here, Φ_{S_1} is the phase for a defective area and Φ_{S_0} is the phase value for a defect-free area. It has been demonstrated [FHSW92] that the phase contrast can be approximated by the imaginary part of the convolution of the shape function with the complex point-spread function:

$$\Delta\Phi \approx \text{Im}\,(sh * h). \tag{3.93}$$

For amplitude images, the amplitude contrast function can be approximated by the real part of the complex point-spread function:

$$\Delta Am \approx \text{Re}\,(sh * h). \tag{3.94}$$

Since the shape function is a real function, the phase contrast point-spread function can be approximated by the imaginary part of the complex point-spread function. The point-spread function of phase images for isotropic material is

$$h_{\Delta\Phi}(x_1, x_2; f_0, d) =$$
$$\text{Im}\left[\frac{F_0}{4\pi k} \cdot R^2 \cdot \frac{\sigma^2 \cdot e^{-\sigma \cdot (r+d)}}{r}\left(\frac{d}{r}\left(1 + \frac{1}{\sigma r}\right) + 1\right)\right] \tag{3.95}$$

with $r = \sqrt{x_1^2 + x_2^2 + d^2}$ and for anisotropic material it is

$$h_{\Delta\Phi a}(x_1, x_2; f_0, d) = \mathrm{Im}\left[\frac{F_o}{4\pi k} \cdot R^2 \cdot \frac{(1+i)^2}{\mu_1\mu_2\mu_3} \cdot \frac{e^{-(1+i)\left(r+\frac{d}{\mu_3}\right)}}{r} \cdot \right.$$
$$\left. \left(\frac{d}{\mu_3 \cdot r} \left(1 + \frac{1}{(1+i)r} \right) + 1 \right) \right] \tag{3.96}$$

where $r = \sqrt{\frac{x_i^2}{\mu_i^2}}$ and $\mu_i = \sqrt{\frac{k_i}{\pi f_0 \rho C_P}} = \sqrt{\frac{\alpha_i}{\pi f_0}}$, $i \in \{1..3\}$. This is an important result for the implementation of the PSF. The function has real values and can easily be used for simulation or to deconvolve blurred defects. Detailed information on the deconvolution of blurred images will be given in Chap. 4.4.

3.5 Simulations

To validate the model of simulation of phase contrast images of Eq. 3.96, defects are simulated and compared to measurements. For simulating the fiber texture of CFRP material, a fiber texture pattern is taken and the profile of the simulated defect is overlaid on the pattern. A value of $\alpha = [0.5\ 0.5\ 0.28]$ mm^{2}s^{-1} is taken for the thermal diffusivity in Eq. 3.96. In Fig. 3.6 the effect of the depth is studied, whereas in Fig. 3.7, the effect of the frequency is compared. Fig. 3.6 represents the simulation results and measurements for different depths. The simulations correspond to the measurements.

Fig. 3.7 shows simulation (on the left) and measurements (on the right) of a defect of plate I. The phase contrast image is represented for different frequencies and for different depths of a defect. The images reveal the dependency of the phase image with the lockin frequency. In summary, if the theoretical PSF is known, it is then possible to retrieve the correct shape of the defect.
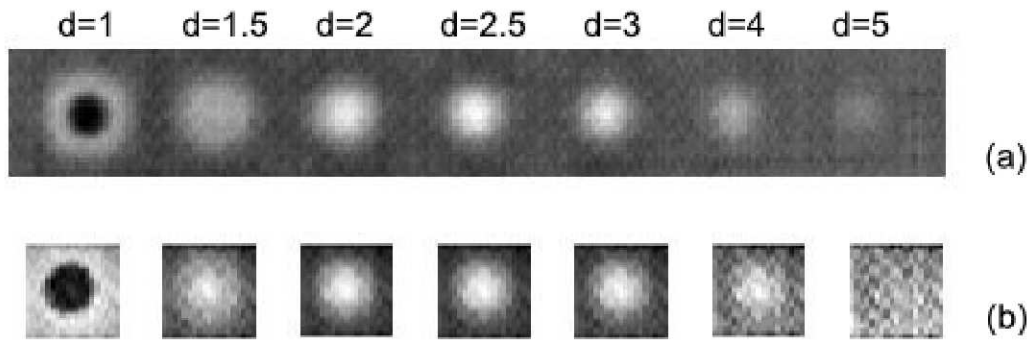

Figure 3.6: (a) Defect measurements for defects situated at different depths; (b) Simulations of the defects by taking $\alpha = [0.5\ 0.5\ 0.28]$ mm$^2 \cdot s^{-1}$ at a lockin frequency of 0.01 Hz.

(a) Phase image 2 mm

(b) Simulation 2 mm

(c) Phase image 3 mm

(d) Simulation 3 mm

(e) Phase image 4 mm

(f) Simulation 4 mm
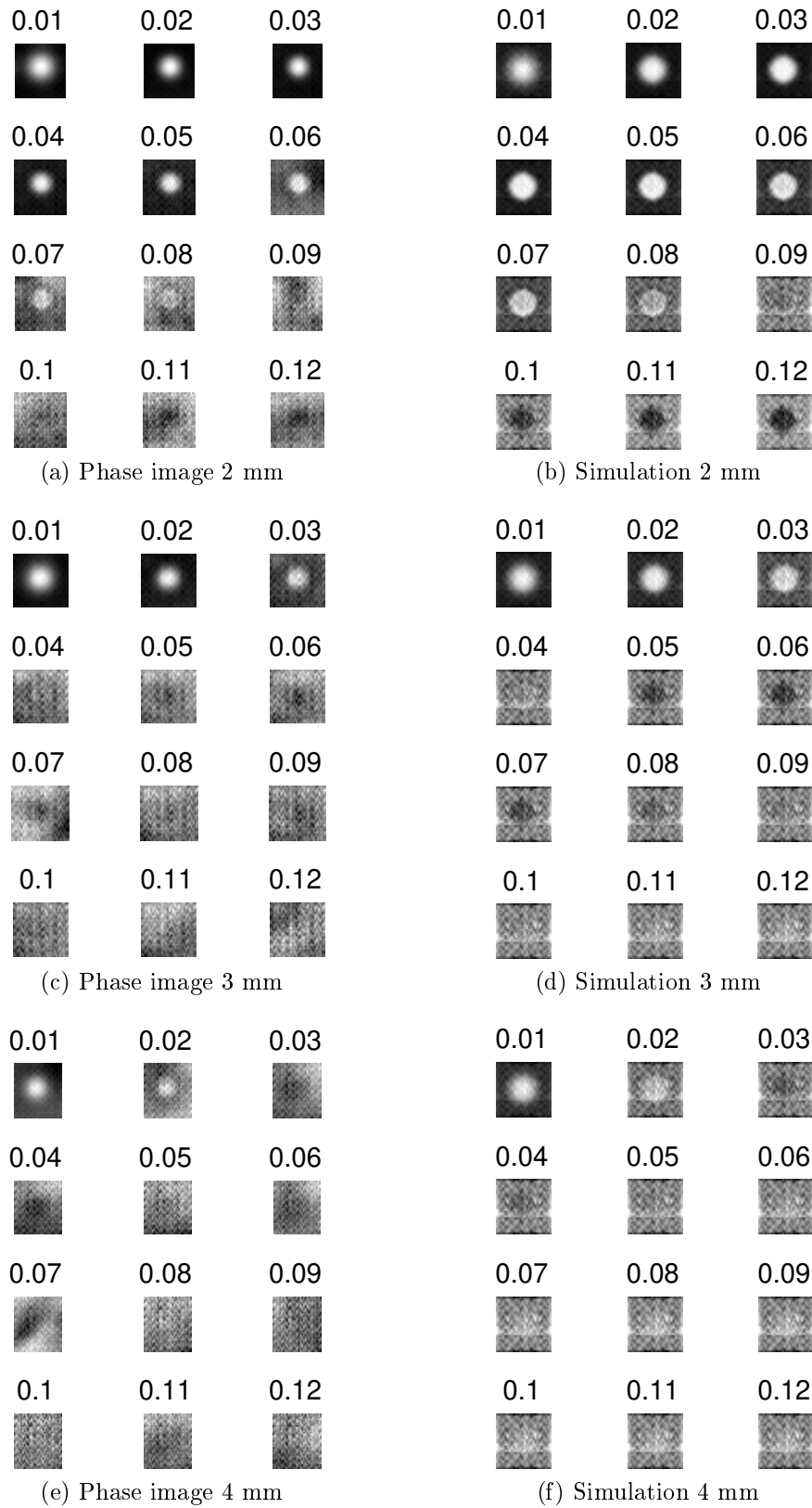
Figure 3.7: Defect measurements (a-c-e) and simulations with $\alpha = [0.5\ 0.5\ 0.27]$ mm$^2 \cdot s^{-1}$ (b-d-f) for different depth and lockin frequencies.

Chapter 4

Image processing algorithms for NDT

This chapter presents the image processing algorithms used for the analysis of the NDT images of the examined components. The algorithms are adapted and applied to thermal images in order to automate the quantitative evaluation of defects. The algorithms allow (1) processing the thermal image sequences, (2) filtering the images and (3) extracting qualitative and quantitative defect information. The chapter describes four different classes of algorithms used for different tasks. The following algorithms are discussed:

- Stitching and overlaying of images: in order to automate the deskew or overlay of images, reference points (called features) that have to be selected automatically are used to compute the transformation between two images. The employed algorithms and the methods to match feature points in two images are discussed.

- Segmentation of defective pixels: a task in NDT is to find a criterion that accurately separates background from defect.

- Clustering: a further task after the pixels have been segmented is the step called clustering where the defective points are grouped (clustered).

- Point-spread function and deconvolution: blurred images can be expressed through a convolution between a sharp image and a point-spread function. The goal is to retrieve the sharp image. It is an inverse problem called deconvolution.

4.1   Stitching and overlaying images

In Chap. 5, photogrammetric methods are used to rectify single phase images. To calculate the transformation between image pairs of the same object and to combine images of different NDT methods, the projective transformation is also used to perform data fusion in Chap. 7. Photogrammetric methods are used to combine thermographic images to extended panoramas (Chap. 6). The procedure of matching, overlaying, and stitching images, for example, for creating panoramas is summarized in Fig. 4.1. First, features have to be detected either manually or automatically in both images. Then, the automated detected features have to be matched. From these matched features, it is possible to compute the parameters of the transfomation that links both images.
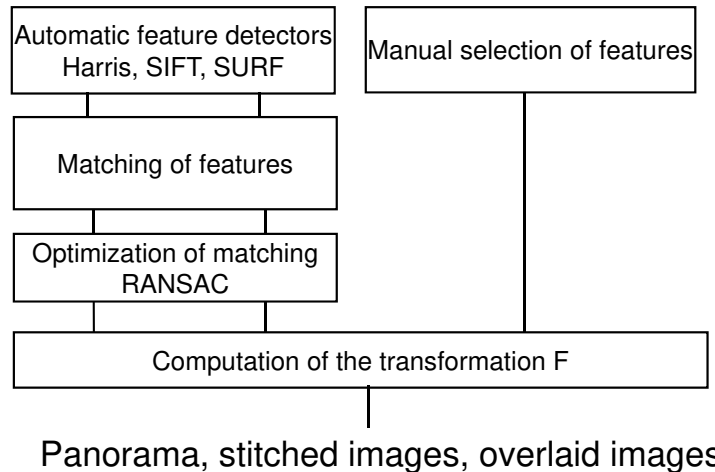In the following sections, the different steps of the procedure are described in detail.

```
┌─────────────────────────────┐   ┌─────────────────────────────┐
│ Automatic feature detectors │   │ Manual selection of features │
│       Harris, SIFT, SURF    │   │                             │
└─────────────────────────────┘   └─────────────────────────────┘
          │                                      │
┌─────────────────────────────┐                  │
│     Matching of features     │                 │
└─────────────────────────────┘                  │
          │                                      │
┌─────────────────────────────┐                  │
│   Optimization of matching   │                 │
│           RANSAC             │                 │
└─────────────────────────────┘                  │
          │                                      │
┌──────────────────────────────────────────────────┐
│       Computation of the transformation F        │
└──────────────────────────────────────────────────┘
                      │
```

Panorama, stitched images, overlaid images

Figure 4.1: Scheme of the required steps to compute the transformation F. After features have been selected either manually or automatically, they have to be matched and the outliers have to be eliminated with the algorithm RANSAC.

4.1.1   Feature detection

Features are needed to compute the transformation F between two images. These interest points with associated local descriptors are generally edges, corners or textures that are easy to determine automatically. The applications of automated feature detectors comprise camera calibration, 3D reconstruction, object tracking, object recognition, and panorama computation from multiple single views.

In thermographic images, thermal contrast is often low and no structure is detectable in the images. Retro-reflective labels are stitched onto the components and are visible in the infrared spectrum. The reference labels can be detected either manually or with an automated image processing method. The well-known feature detection methods are the Harris Corner Detector [ST94], SIFT features [Low99], and Surf features [BTVG06]. The following section describes the markers used in the tests and the algorithms used to detect features automatically.

Markers

Different kinds of markers are used in the experiments and tests. First, for introducing a scale in the images, round markers from the Aicon company (Fig. 4.3a) manufactured on a special retro-reflective material are used. They have a high reflection coefficient in infrared. The advantage of these labels is that they have a reference point situated at their center. This allows the precise measurement of the distances between the markers with a ruler. The labels should delimit the zone of interest (ZOI) particularly on extended components, as it is shown in Fig. 4.2.

For creating panoramas (Chap. 6), other markers cut from aluminum tabs are used (Fig. 4.3b) and are used as reference points in low-contrasted phase images. The advantage is that corners are well-detected through automated feature detectors.

These labels are detectable in infrared images, in optical images as well as in images of other non-destructive testing methods - for example in B- and C-scans of ultrasonic testing. So, another purpose of using labels is to facilitate the combination of images of
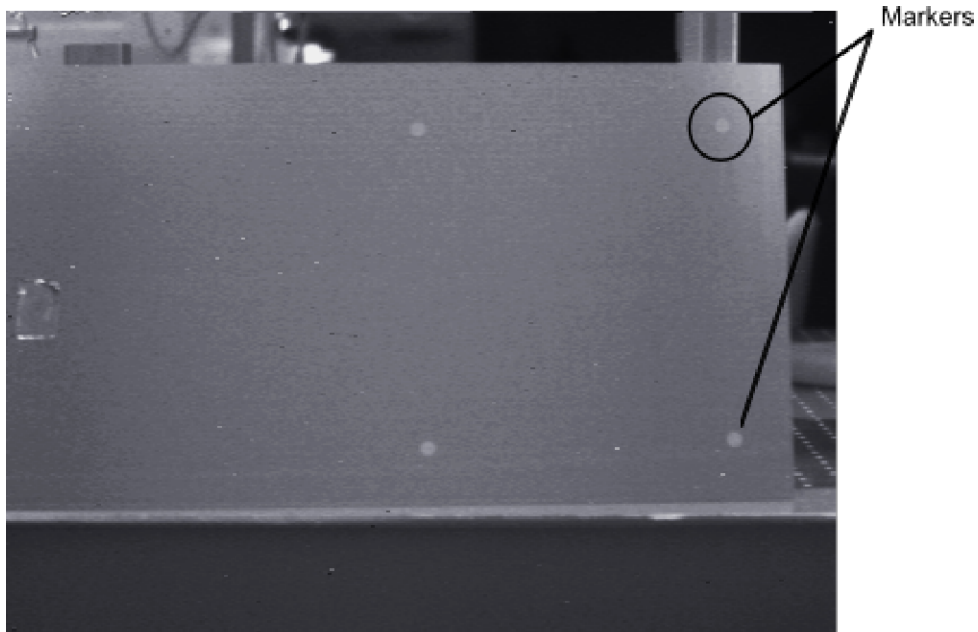
Figure 4.2: UIT measurement performed on a large part. Round markers are stitched to delimit the ZOI.
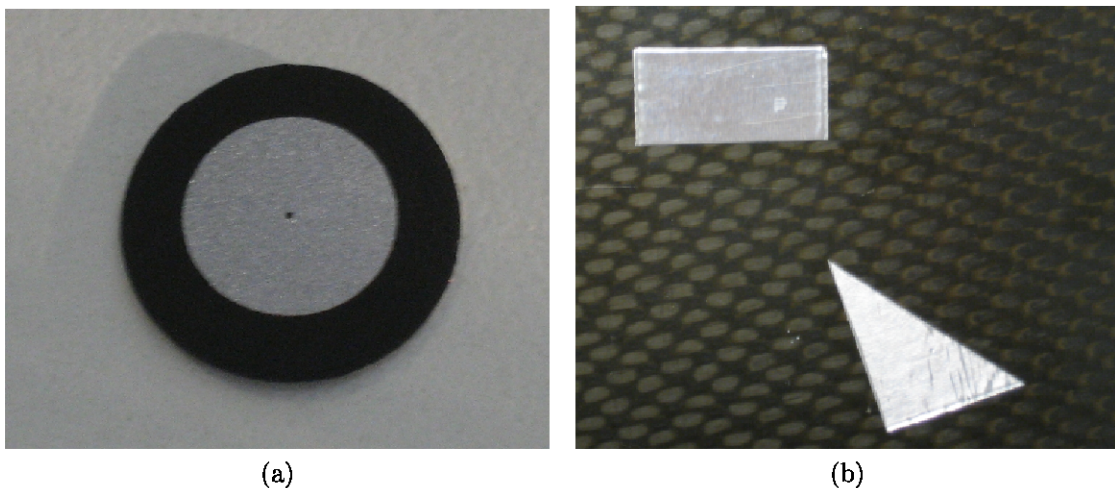

(a)   (b)

Figure 4.3: Different types of used markers: (a) round markers with a point situated at the center composed of a special retro-reflective material of the Aicon company; (b) diverse rectangular and triangular markers cut from aluminum tabs.

various measurements for data fusion (Chap. 7).

Fit of ellipses for the detection of round markers

For the detection of the markers, a thresholding method, the Canny detector [Can86], is used to detect the borders. Then, an ellipse detection algorithm is used for determining the center of these markers. In [FPF99], a robust and fast method for fitting ellipses is presented. The ellipse-equation is retrieved from the set of points of the ellipse border or of an arc of the ellipse border.

Generally, the method consists of retrieving the parameter $a = \begin{bmatrix} a & b & c & d & e & f \end{bmatrix}^T$ from the equation of a conic

$$F(a, x) = ax^2 + bxy + cy^2 + dx + ey + f \qquad (4.1)$$

from a set of points (x,y). The fitting consists of minimizing the sum $D_A(a) = \sum_{i=1}^{N} F(x_i)^2$. To avoid arriving at the trivial solution $a=0$ (and since a multiple of a solution is also solution), a constraint on the parameter a has to be found. The authors of [FPF99] propose setting the constraint at

$$4ac - b^2 = 1 \Leftrightarrow a^T C a = 1, \text{ where } C = \begin{bmatrix} 0 & 0 & 2 & 0 & 0 & 0 \\ 0 & -1 & 0 & 0 & 0 & 0 \\ 2 & 0 & 0 & 0 & 0 & 0 \\ 0 & 0 & 0 & 0 & 0 & 0 \\ 0 & 0 & 0 & 0 & 0 & 0 \\ 0 & 0 & 0 & 0 & 0 & 0 \end{bmatrix}.$$

Using the Lagrange multipliers, the equation can be expressed as

$$\begin{aligned} D^T D a - \lambda C a &= 0 \\ a^T C a &= 1, \end{aligned} \qquad (4.2)$$

where $D = \begin{bmatrix} x_1 & x_2 & ... & x_N \end{bmatrix}^T$. This reduces to

$$\begin{aligned} Sa &= \lambda C a \\ a^T C a &= 1 \end{aligned} \qquad (4.3)$$

where $S = D^T D$. By solving the generalized eigenvector system, six pairs of eigenvalues and eigenvectors (λ_i, u_i) are obtained. This demonstrates that the system of equations admits only one solution, $a_i = \mu_i u_i$ with $\mu_i = \sqrt{\frac{1}{u_i^T S u_i}} = \sqrt{\frac{1}{u_i^T C u_i}}$, corresponding to the unique eigenvalue $\lambda_i > 0$.

An example of ellipse detection and fitting is shown in Fig. 4.4. The image was thresholded to get the contours of each ellipse. The fit of the ellipse allows the determination of the center of the ellipse.

Harris corner detector

The following described detectors are applied in Chap. 6 to detect features automatically. The Harris corner detector was first introduced in 1988 [HS88] and is probably the most widely used corner detector. It uses the Hessian matrix defined by

$$H(x, y, \sigma) = \begin{bmatrix} L_x^2(x, y, \sigma) & L_x L_y(x, y, \sigma) \\ L_x L_y(x, y, \sigma) & L_y^2(x, y, \sigma) \end{bmatrix}, \qquad (4.4)$$

where $L_x^2(x, y, \sigma)$ is the convolution of the Gaussian second order derivative $\frac{\partial^2}{\partial x^2} g(x, y, \sigma)$ with the image I at point (x, y) and with a scale σ, and similarly for L_y^2 and $L_x L_y$. The
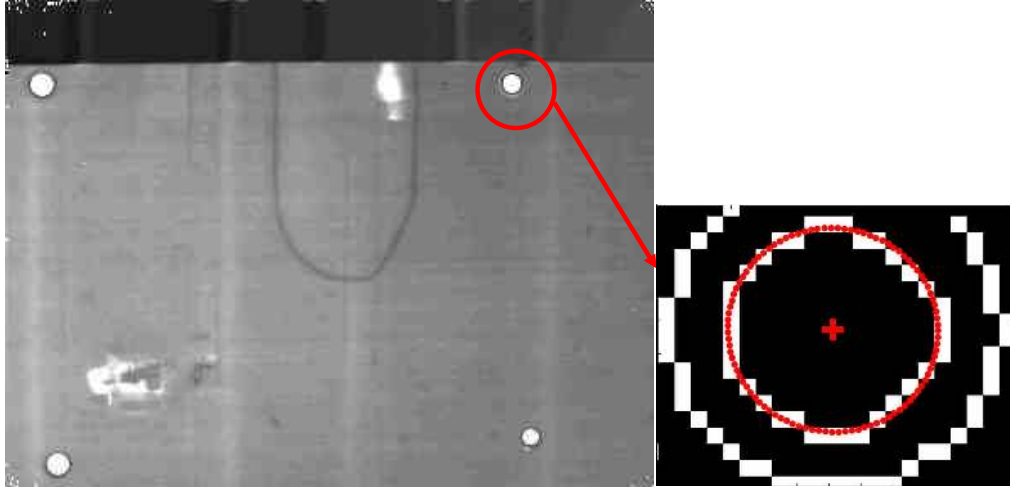
Figure 4.4: Edge detection and ellipse fitting on a marker in an OLT image.

derivatives in the Hessian matrix are the mean values over a window centered at (x,y). The typical window size is a few pixel. The Gaussian function equation is

$$g(x, y, \sigma) = \frac{1}{\sqrt{2\pi}\sigma} e^{-(x^2+y^2)/2\sigma^2}. \tag{4.5}$$

The response of a point is given by

$$R = \det(H) - k \cdot trace^2(H), \tag{4.6}$$

where k is a real value. Corners can easily be determined since R is positive in the corner region and negative in the edge regions. Generally, a value of $k = 0.04$ [HS88] is taken.

The Harris-corner method was refined by Shi and Tomasi [ST94] and is often referred to as the 'Shi-Tomasi detector'. It is quite similar to the Harris corner detector. Here, the Hessian matrix H is also considered, but another detection criterion is used. When both eigenvalues $\lambda 1$ and $\lambda 2$ of matrix H are higher than a given threshold λ

$$min(\lambda 1, \lambda 2) > \lambda, \tag{4.7}$$

the window is selected and considered to be a feature. Fig. 4.5 shows an example of detected features in OLT phase images. The rectangular pieces are aluminum markers. The corners of these markers are well-detected. The Harris detector implemented by Kovesi[1] is taken to detect the corners of markers.

SIFT features

The shortcoming of Harris features is that the detection is not scale-invariant, which is a problem in the field of object recognition. Lindeberg [Lin98] first introduced a scale invariant method and employed the determinant of the Hessian matrix, as well as the Laplacian, the trace of the Hessian matrix. The method was refined in [MS01]. A combination of the Harris corner detector at different scales and the Laplacian was used. The determinant of the Hessian matrix was used to localize the features and the Laplacian was used to select a scale.

---

[1]http://www.csse.uwa.edu.au/
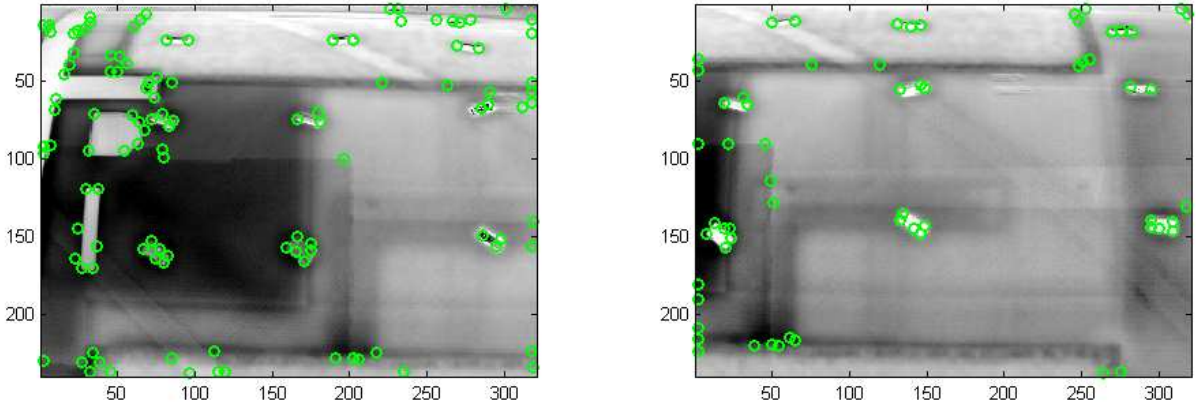
Figure 4.5: Features detected in two OLT phase images (0.01 Hz).
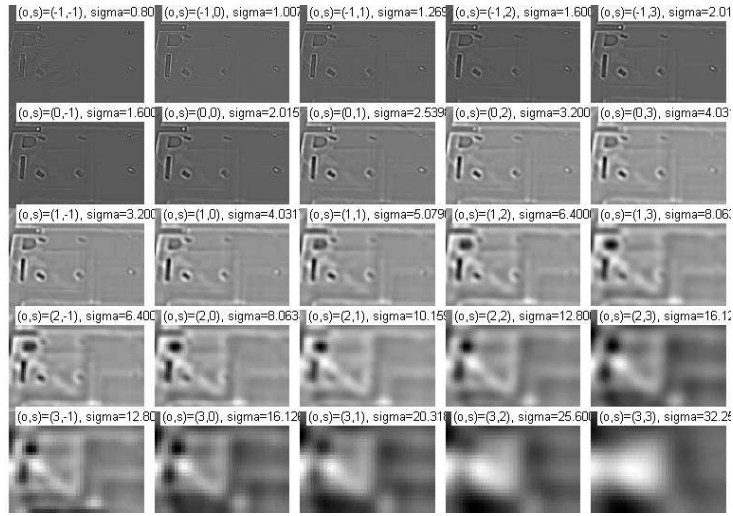
Figure 4.6: Downsampling of the spatial resolution of the phase image for determination of SIFT features.

Finally, Lowe and Brown [Low99, BL07] introduced an additional approximation of the Gaussian's Laplacian by the difference-of-Gaussian (DoG) leading to faster computation of the features. The operator DoG is expressed as

$$D(x, y, \sigma) = L(x, y, k_i\sigma) - L(x, y, k_j\sigma), \tag{4.8}$$

where $L(x, y, k\sigma)$ is the convolution of the image I taken at point (x, y) with the Gaussian function $G(x, y, k\sigma)$. The features are the maxima and minima of the difference-of-Gaussian function.

The scale invariant features (SIFT features) are robust. The algorithm builds a pyramid of the initial image at different scales and looks for features presented at these different scales. The image size is iteratively downsampled (Fig. 4.6), making new features appear in a downsampled image. A scale and orientation are attributed to each feature. Each point is used for generating feature vectors (SIFT keys) that describe the image region with respect to its scale level. At each feature location, a gradient magnitude and an orientation are detected. A feature descriptor composed of 128 bins is achieved.

Fig. 4.7 shows an example of the detection of SIFT features in two OLT phase images at

54

a frequency of 0.01 Hz. Vevaldi's algorithm implementation [2] is taken. The disadvantage of SIFT is the high dimension of the descriptor vector, containing 128 bins, which makes the selection of features and the matching time-consuming.
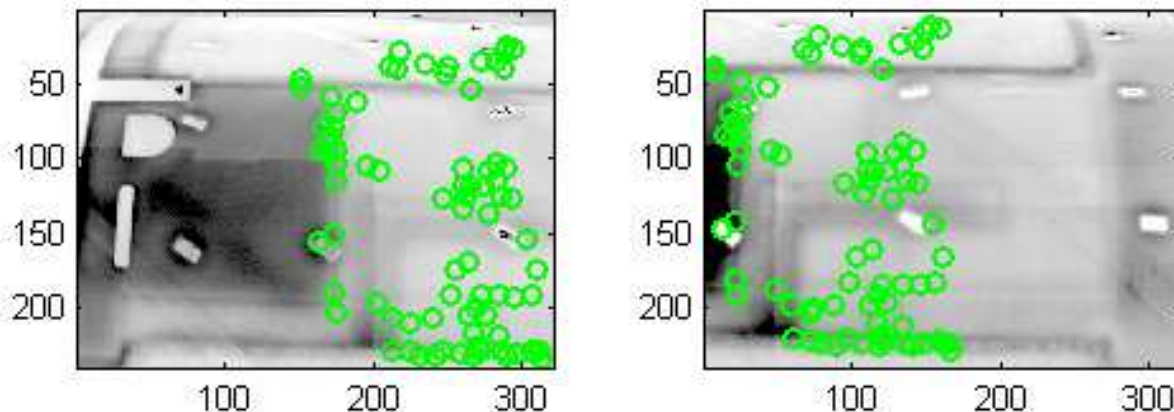
Figure 4.7: The detected and matched SIFT features in two neighboring OLT phase images are plotted on the phase images (0.01 Hz).

SURF features
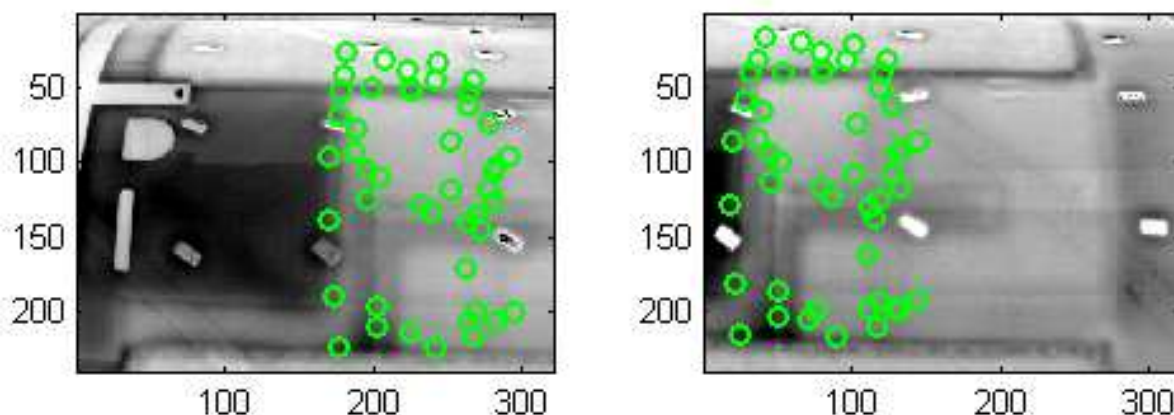
Figure 4.8: The detected and matched SURF features in two neighboring OLT phase images are plotted on the phase images (0.01 Hz).

Another method, the speeded-up robust features detector (SURF), has been proposed by Bay et al [BTVG06]. The technique is also based on the Hessian matrix but uses another approximation of the Gaussian second derivatives that are called box filters. The descriptor contains only 64 bins and yields nearly the same efficiency, yet it is much faster. Fig. 4.8 shows an example of the detection of SURF features in two OLT phase images at a frequency of 0.01 Hz. The algorithm proposed by Bay et al is taken [3].

---

[2]http://vision.ucla.edu/ vedaldi/code/sift/sift.html
[3]http://www.vision.ee.ethz.ch/ surf/papers.html'

4.1.2 Matching feature points

Once feature points have been selected automatically, a next step consists of matching the points together and finding the corresponding interest points in the second image. In most instances, automated matching algorithms produce a high number of outliers. Only with correct matches can the required transformation be computed with accuracy. For manual feature selection, the transformation F can be computed directly. The automated feature detectors require a matching step. The implementations of SIFT and SURF (see Chap. 6.2.2) have intrinsic matching algorithms that is based on correlation of the detected features in both images. For Harris features, the algorithm k-d tree is used to perform a match. Some matches may not be correct. Therefore, an additional algorithm - here RANSAC [FB81] - is used to remove so-called outliers.

K-d tree

K-d tree [Ben75] is a recursive method that partitions space in a binary fashion. It can be used to efficiently compute the nearest neighbor to a given point. For matching, the nearest neighbor of a reference feature in the corresponding image has to be found. An initial transformation of one image to the other is needed as input. Here an initial approximating translation is taken.

The algorithm RANSAC

After the matching steps, falsely matched points called 'outliers' are often left in the set of matched feature points and affect the resulting transformation. A way to compute the precise transformation is given using the random sample consensus algorithm (RANSAC) [FB81]. The method utilizes a minimal set of randomly used points (a consensus denoted as r) and computes the resulting transformation (projective or, here, polynomial for panorama of curved surfaces in Chap. 6). The procedure is repeated many times and the transformation that has the maximal number of inliers is selected. If p_i is the relative fraction of outliers, the probability that an outlier is chosen each time for n iteration is

$$p(Hiscorrect) = (1 - (1 - p_i)^r)^n. \tag{4.9}$$

For example, for $p_i = 0.5$ and $r = 8$, the probability that an outlier is selected after 1000 trials is only 2 % and after 10000 trials 10^{-15} %.

Fig. 4.9 shows an example of the result of the RANSAC algorithm. Both images are overlaid. The features detected automatically - here, the reference points which are determined using the SIFT method - are plotted on the overlaid images and the blue straight lines link the corresponding points. One notices that after using RANSAC, double-matches and outliers are all suppressed.

4.1.3 Different transfomations

Photogrammetric methods are used to derive position information of objects from image data. The main applications are in the fields of geodesy, architecture [HW97] and analysis of aerial photos.

Photogrammetric methods enable the correction of a single image, even if the parameters of the camera such as distortions or the distance between the lens and the imaging plane
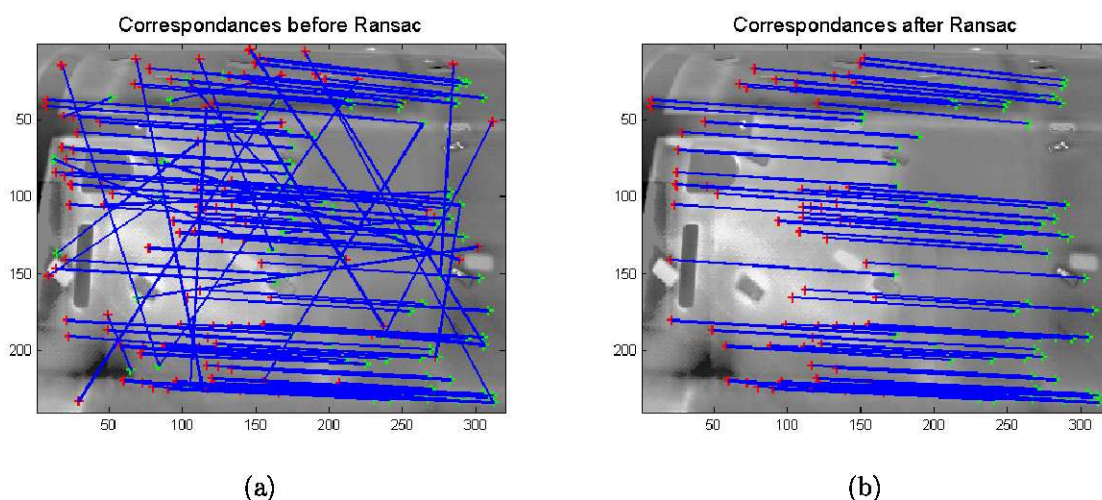
Figure 4.9: Both thermographic images to be matched are overlaid. The features detected with the automated feature detector SIFT in both images are plotted. The blue lines links the corresponding points (a) before and (b) after applying the algorithm RANSAC that eliminates outliers.

are unknown. The goal is to compute the transformation parameters which allow switching from one image coordinate system to another. Generally, to overlay two images, the parameters of the transformation F,

$$(X, Y) = F(x, y),\qquad(4.10)$$

that describe the passage between two images must be determined.
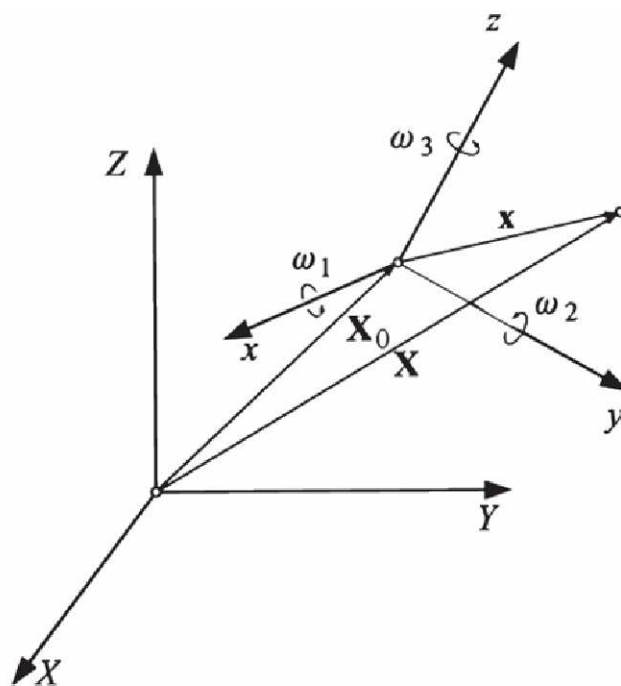
Figure 4.10: Transformation parameters.

57
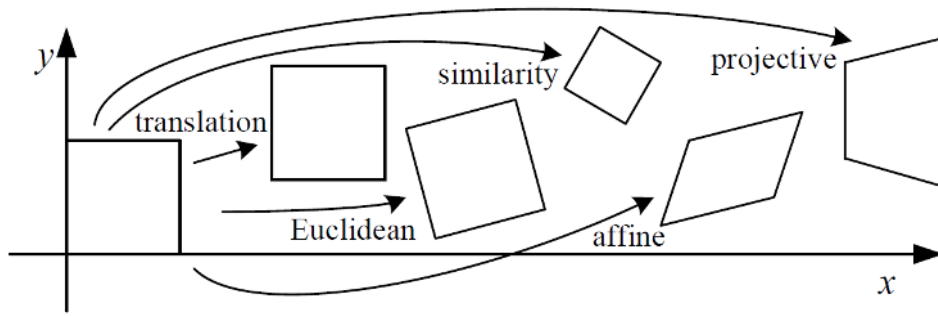
Figure 4.11: Overview of possible transformations [Sze04].

Depending on the geometry of the inspected components, different types of transforma-tions are used. A scheme of the transformation parameters of a 3D-rotation is represented in Fig. 4.10. In Fig. 4.11, an overview of the possible transformations that can be applied to an image is given. For a projective transformation, the parameters of translation, rota-tion and scale have to be evaluated. These parameters can be determined from reference points (see Chap. 4.1.1). Both images can then be overlaid.

Rectification of flat components

In quantitative problems, the first task is to introduce a scale into the images. An easy way is to attach a one-dimensional scale on the part. However, being one-dimensional, if the part is inclined toward the camera, the image will be distorted. Another way to get quantitative information is when the distance between the sensor and the inspected part is known. For example, some cameras own an integrated laser for measuring the distance to an object. In ultrasound testing, the distance between the ultrasound sensor and the part is also known.

For recording thermographic images, the inspected parts must often be inclined with respect to the camera to avoid reflection effects that disturb the measurements. The inclination leads to a distortion of the image. To properly quantify defects, the image has to be deskewed.

A projective transformation, the Helmert-transformation [Luh03], is utilized. To calculate the transformation parameters, four reference points have to be known. The Helmert-transformation model does not take into account the distortions produced by the lenses. Seven parameters are needed: three translations (X_0, Y_0, Z_0), three rotation angles $(\omega_1,$ $\omega_2, \omega_3)$, and one scale-factor m. The transformation can be written as:

$$\overrightarrow{X} = \overrightarrow{X}_0 + m \cdot R \cdot \overrightarrow{x}, \tag{4.11}$$

where $\overrightarrow{X} = \begin{pmatrix} X_0 \\ Y_0 \\ Z_0 \end{pmatrix}$ is the translation vector, $\overrightarrow{x} = \begin{pmatrix} x \\ y \\ z \end{pmatrix}$ is the coordinate vector, and

$$\mathrm{R} = \mathrm{R}_{\omega 1} \cdot R_{\omega 2} \cdot R_{\omega 3}$$

$$= \begin{bmatrix} 1 & 0 & 0 \\ 0 & \cos\omega_1 & -\sin\omega_1 \\ 0 & \sin\omega_1 & \cos\omega_1 \end{bmatrix} \begin{bmatrix} \cos\omega_2 & 0 & \sin\omega_2 \\ 0 & 1 & 0 \\ \sin\omega_2 & 0 & \cos\omega_2 \end{bmatrix} \begin{bmatrix} \cos\omega_3 & -\sin\omega_3 & 0 \\ \sin\omega_3 & \cos\omega_3 & 0 \\ 0 & 0 & 1 \end{bmatrix}$$

$$= \begin{bmatrix} \cos\omega_2 \cos\omega_3 & -\cos\omega_2 \sin\omega_3 \\ \cos\omega_1 \sin\omega_3 + \sin\omega_1 \sin\omega_2 \cos\omega_3 & \cos\omega_1 \cos\omega_3 - \sin\omega_1 \sin\omega_2 \sin\omega_3 \\ \sin\omega_1 \sin\omega_3 - \cos\omega_1 \sin\omega_2 \cos\omega_3 & \sin\omega_1 \cos\omega_3 + \cos\omega_1 \sin\omega_2 \sin\omega_3 \end{bmatrix} \quad (4.12)$$

$$\begin{bmatrix} \sin\omega_2 \\ -\sin\omega_1 \cos\omega_2 \\ \cos\omega_1 \cos\omega_2 \end{bmatrix}$$

$$= \begin{bmatrix} r_{11} & r_{21} & r_{31} \\ r_{21} & r_{22} & r_{23} \\ r_{31} & r_{32} & r_{33} \end{bmatrix}$$

is the rotation matrix [Luh03]. By inverting the system and eliminating the scale factor, the following equations, called the basic equations of the photogrammetry, are yielded:

$$\mathrm{X} - \mathrm{X}_0 = (\mathrm{Z\text{-}Z}_0) \cdot \frac{r_{11} \cdot \mathrm{x} + r_{21} \cdot \mathrm{y} + r_{31} \cdot \mathrm{z}}{r_{13} \cdot \mathrm{x} + r_{23} \cdot \mathrm{y} + r_{33} \cdot \mathrm{z}} + \Delta\mathrm{x}$$

$$(4.13)$$

$$\mathrm{Y\text{-}Y}_0 = (\mathrm{Z\text{-}Z}_0) \cdot \frac{r_{12} \cdot \mathrm{x} + r_{22} \cdot \mathrm{y} + r_{32} \cdot \mathrm{z}}{r_{13} \cdot \mathrm{x} + r_{23} \cdot \mathrm{y} + r_{33} \cdot \mathrm{z}} + \Delta\mathrm{y},$$

where $\Delta\mathrm{x}, \Delta\mathrm{y}$ is an added distortion vector. By neglecting the radial distortion $(\Delta\mathrm{x}, \Delta\mathrm{y})$, the system of equations

$$\mathrm{X}' = \frac{a_1\mathrm{x} + b_1\mathrm{y} + c_1}{a_3\mathrm{x} + b_3\mathrm{y} + 1}, \mathrm{Y}' = \frac{a_2\mathrm{x} + b_2\mathrm{y} + c_2}{a_3\mathrm{x} + b_3\mathrm{y} + 1} \quad (4.14)$$

is obtained. Here, X', Y' are the coordinates of the reference points in the corrected image S (in m), x, y are the coordinates of the four reference points in the original image S_P (in number of pixels) and $a_i, b_i, c_i, i \in \{1...3\}$ are the parameters of the transformation. The parameters are obtained by solving the linear system of equations via the knowledge of the position of four reference points.

To illustrate the effect of rectification, it is applied to a flat component. Fig. 4.12 shows the results of image equalization and the introduction of a scale. The image is rectified as if it would have been taken in a parallel plane. This step is important to compute quantitative sizes of defects.

Projective transformation is commonly used to create panoramas of landscapes because the detected points are far from the camera and can be considered to lie in a plane. However, for near-field measurements of curved components, it appears that this transformation is not sufficient. Therefore, for curved surfaces, polynomial transformation is preferable. The general form of the transformation is

$$\mathrm{X} = a_0 + \mathrm{a}_1\mathrm{x} + \mathrm{a}_2\mathrm{y} + \mathrm{a}_3\mathrm{x}^2 + \mathrm{a}_4\mathrm{y}^2 + ..., \ \mathrm{Y} = b_0 + b_1\mathrm{x} + \mathrm{b}_2\mathrm{y} + \mathrm{b}_3\mathrm{x}^2 + \mathrm{b}_4\mathrm{y}^2 + ... \quad (4.15)$$

A polynomial of order 2 is used to calculate the transformation. If one uses a polynomial of order 3, unwanted distortions occur. The method is applied to measurements in Chap. 6 to compute panoramas of long and curved components.
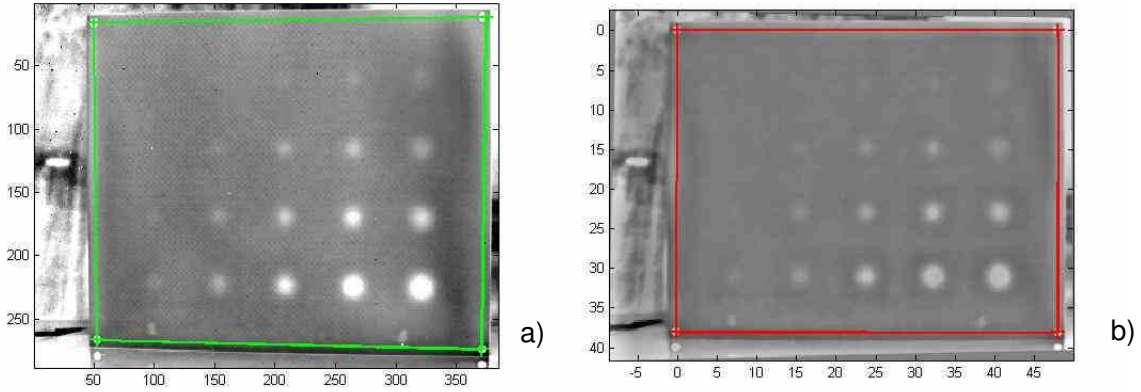
Figure 4.12: Equalization of images using photogrammetry; (a) Original image (OLT, phase image, 0.01 Hz); (b) rectified image with scale.

4.2 Segmentation of defective pixels

The first task is to find a criterion to determine whether a point belongs to a defective area or not, a step called segmentation. Many methods exists, like region growing or threshold methods. Maldague et al [MKP90] proposed an interesting method for extracting defects in thermal images.

In ultrasound NDT, defects are only consideres as defects if they are at least 6 dB above noise. The SNR is computed using

$$SNR = 10 \cdot log_{10} \cdot \frac{P_{signal}}{P_{noise}} = 20 \cdot log_{10} \cdot \frac{A_{signal}}{A_{noise}}, \qquad (4.16)$$

where P is the average power and A is the average root mean square amplitude. In practice, a manual method is used to compute the SNR. The maximum A_{max} of the signal, the maximum N_{max}, and the minimum N_{min} of the noise are evaluated from a profile line across the defect. The SNR is then evaluated through

$$SNR = 20 \cdot log_{10} \cdot \frac{A_{max} - N_{min}}{N_{max} - N_{min}}. \qquad (4.17)$$

In the following, a method to compute the SNR automatically to perform an automated image segmentation is developed.

4.2.1 Background correction

For the calculation of the SNR, inhomogeneous background illumination effects have to be corrected. It is very difficult to obtain a homogeneous illumination field during measurements. The inhomogeneous illumination distribution can be modeled in the following way:

$$I_{inh} = I * S_M + S_A \qquad (4.18)$$

where I_{inh} is the inhomogeneous image, I is the corrected image with a homogeneous field, S_M is the multiplicative component and S_A is the additive component. The goal

60
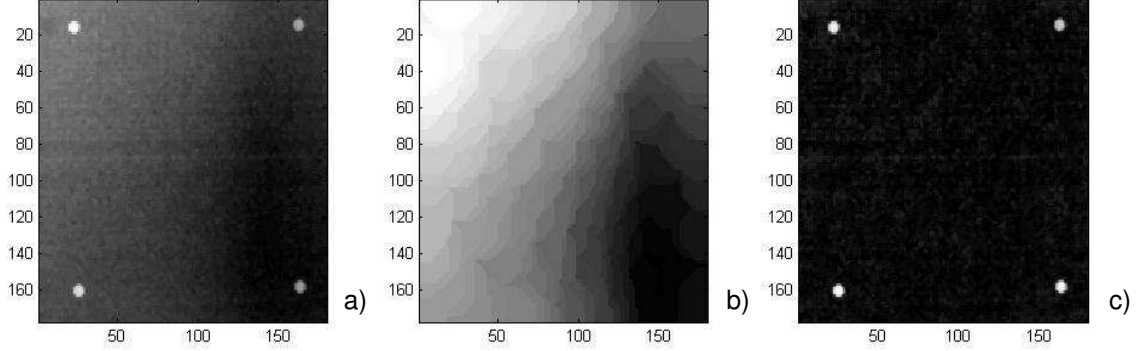
Figure 4.13: The figure shows the rectification of an inhomogeneous illumination distribution in a raw thermal live image. (a) Original thermal image, (b) background model and (c) corrected image.

of the retro-reflective illumination correction is to retrieve the multiplicative and/or the additive component from the information contained in the image automatically.

In our work, the correction in Omar et al [OHSA05] is used, which consists of the retrieval of the additive component S_A. The multiplicative component S_M is assumed to be constant. For this task, the average of a surround $T_{surr}(i,j,t)$ is subtracted from each pixel value $T_{pix}(i,j,t)$ following:

$$T(i,j,t) = T_{pix}(i,j,t) - T_{surr}(i,j,t) \qquad (4.19)$$

An example of correction is given in Fig. 4.13. This step is also known as inhomogeneous background correction or retrospective shading correction. For more complex component geometries, the methods of 2D-polynomial fitting [IC05], based on entropy minimization [LVV03] or of [SHZW06] can be used.

4.2.2 Automated SNR for the detection of defective areas

To determine the SNR, an automated method is used:

$$SNR = 10 \times log10 \Big(\frac{\sum_i \sum_j [Therm(i,j)^2]/(ncol \times nrow)}{1/2[\sigma_g(N(i))]^2} \Big), \qquad (4.20)$$

where the denominator is the mean value of the signal, (i,j) are the coordinates of the pixel, and *ncol*, *nrow* are the number of rows and columns. The numerator represents the mean signal-to-noise ratio, and σ_g the standard deviation of the noise $N(i,j)$. The noise is estimated by subtracting a line from the precedent one.

4.2.3 Automated method to threshold the images

In order to calculate the SNR threshold, the histograms of each image were analyzed. From Fig. 4.14, it can be seen that the histograms are in good Gaussian approximation. A corresponding curve with the equation

$$f(x) = \frac{1}{\sigma_g \sqrt{2\pi}} \exp\left(-\frac{1}{2}\left(\frac{x - \mu_g}{\sigma_g}\right)^2\right), \qquad (4.21)$$

61

where μ_g is the mean and σ_g the standard deviation of the Gaussian curve, and is fitted to the histogram of each phase image by means of a least-square regression. They contain the information required. The defective area is determined by the region on the Gaussian curve situated above and below a given limit that is determined by a relationship between the mean and the width of the Gaussian curve

$$\mu \pm n \cdot \sigma. \tag{4.22}$$

depending on whether the defect appears brighter or darker than the background. The number n is a value that lies between 0.5 and 3. With a low n value, the defect area is greater than on an area with a high n value. By considering in turn the 6 dB defect-detection criteria, one has

$$SNR = 20log_{10}\left(\frac{A_{sig}}{\sigma_g}\right) = 6dB \Rightarrow A_{sig} = \underbrace{10^{6/20}}_{\approx 2}\sigma_g, \tag{4.23}$$

where A_{sig} is the amplitude of the signal. The limit is determined under the condition that the threshold is

$$\mu_g \pm 2 \cdot \sigma_g. \tag{4.24}$$
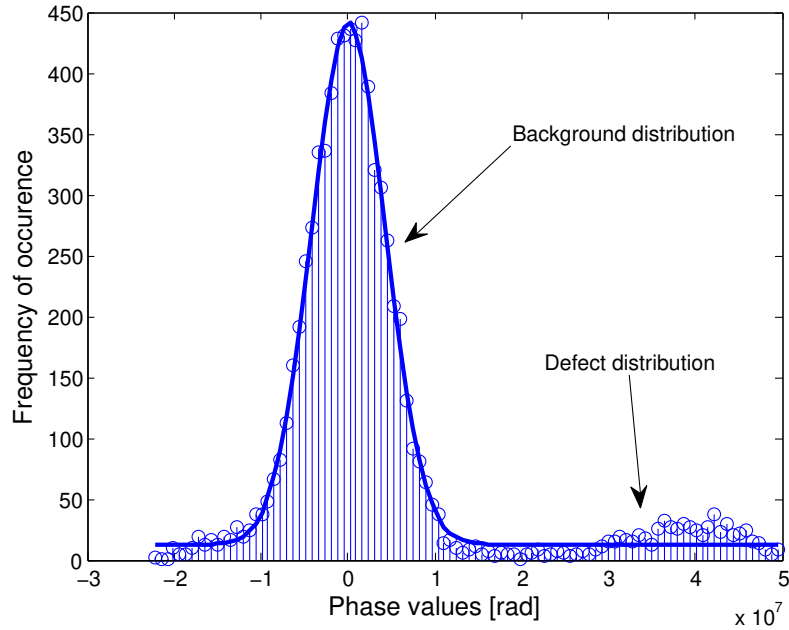
Figure 4.14: Fit of a Gaussian curve to the histogram of the image.

4.3 Clustering

After the calculation of the 6 dB level and the detection of potentially faulty pixels in the image, it is advantageous to sort the pixels into groups and defective regions. The number of defects, the size and the position of a defect can be easily calculated.

4.3.1 K-means

The most popular unsupervised clustering method, i.e. one that does not require a priori information, is the k-means algorithm of Mac Queen [Mac67]. It is a simple and a fast method that allows the determination of clusters and of their centers. It deals with the minimization of the objective function

$$J = \sum_{j=1}^{k} \sum_{i=1}^{n} \left\| x_i^{(j)} - c_j \right\|^2, \tag{4.25}$$

where $\left\| x_i^{(j)} - c_j \right\|^2$ is a distance measurement between points $x_i^{(j)}$ of the cluster and its center c_j. The aim of the algorithm is to minimize this cost function. The points are iteratively assigned to the closest center and then the centers of each cluster are recalculated, until they no longer change.

The drawback of this method is that the number of clusters has to be fixed as entrance input so that no automation is possible. Then, the result of the clustering strongly depends on the initial position of the centers. An improvement to the method, where a number M of clusters has to be given as an input parameter, is the global k-means algorithm proposed by Likas et al [LVV03]. The algorithm is based on the k-means algorithm and works in an incremental way. It first starts with one cluster where the solution is trivial, and continues until a fixed number M of clusters are achieved. At each step, the initial position of the cluster centers are optimal since they are determined at step M-1. For the remaining M-th center, several initial positions are taken. So, the drawback of initial positions of the centers is suppressed, but nevertheless, the number of clusters must be fixed at the beginning. A solution consists of determining a stop criterion by taking the density of points situated in the convex hull of each cluster, as proposed in the next section.

4.3.2 N-Cuts

The N-Cuts algorithm of Shi and Malik [SM00] is a clustering method. It is an iterative bi-segmentation algorithm, which computes the optimal partition between a cloud of points belonging to two separate clusters. It performs a graph partitioning to the minimizing of the 'cut' coefficient defined by

$$\text{cut}(A, B) = \sum_{u \in A, v \in B} w(u, v), \tag{4.26}$$

where W is the weight matrix. This leads to the minimizing of the Rayleigh coefficient

$$y = \arg\min \left(y^t (D - W) y / y^t D y \right), \tag{4.27}$$

where D is a diagonal matrix with $\text{d}(i) = \sum_j w(i, j)$ on its diagonal. To get the solution, the generalized eigenvalue system

$$(D - W)y = \lambda D y \tag{4.28}$$

has to be solved. The eigenvector with the second smallest eigenvalue is taken for the bipartition. A solution is obtained in the form of an index vector y, containing values 0 or 1, which indicates to which cluster a point belongs.

The process is iterated until the density of the points within the convex hull of the clusters reaches a given threshold. In Fig. 4.15, the result of clustering and the clustering-tree describing the different stages is visualized. Fig. 4.16 gives an example of the result and the output of the segmentation algorithm. The algorithm provides correct computation of clusters but is discarded because the computational time is very long.

Segmentation of
defects with the
6 dB criterion

Bi-Segmentation approach
based on the normalized cut
algorithm.
Output: Numbered list of fault-
regions comprising area,
convex hull and fault density
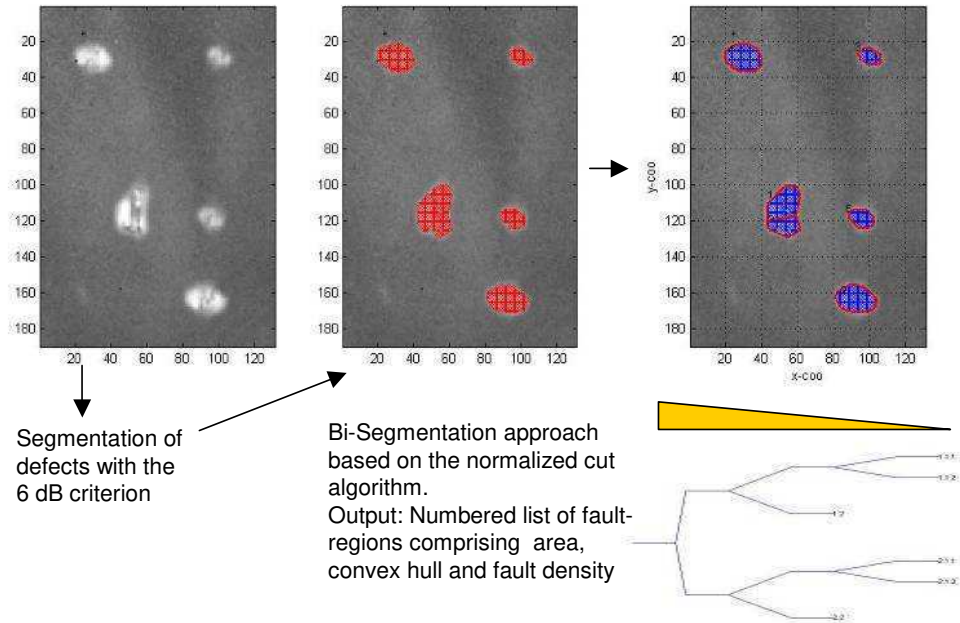
Figure 4.15: Example of clustering with N-Cuts.


```
faultregion.Number:      n
faultregion.Position:    [2x1 double]
faultregion.Density:     d
faultregion.ConvexHull:  [m x 2 double]
faultregion.Pixel:       [n x 2 double]
```
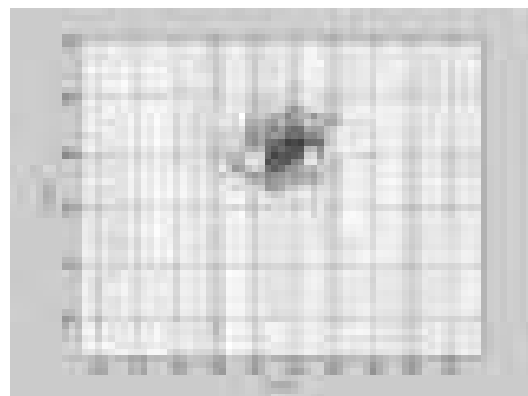
Figure 4.16: Example of result of segmentation algorithm.

4.4 Point-spread function and deconvolution

In many fields of applications like astronomy or in optics, image degradation occurs. This degradation can be due to distortions caused by lenses, out-of focus imaging, movements with respect to the object, or atmospheric turbulences, and is modeled by a point-spread function (PSF). In our case, the blurring effect is due to the diffusion of heat in material (see Chap. 3).

Generally, the degradation process can be modeled by the equation

$$g(x,y) = f(x,y) \otimes h(x,y) + \eta(x,y). \tag{4.29}$$

where f is the original undistorted image, g is the registered blurred image and $\otimes$ denotes the convolution product between two signals (here in the spatial domain (x,y)), i.e.

$$g(x,y) = f(x,y) \otimes h(x,y) = \iint_{-\infty}^{+\infty} f(x_0, y_0) \cdot h(x - x_0, y - y_0) dx_0 \cdot dy_0. \tag{4.30}$$

The degradation process is schematically shown in Fig. 4.17. The goal is to find a technique to restore the image by knowing the degradation function, and to invert the blurring effect.
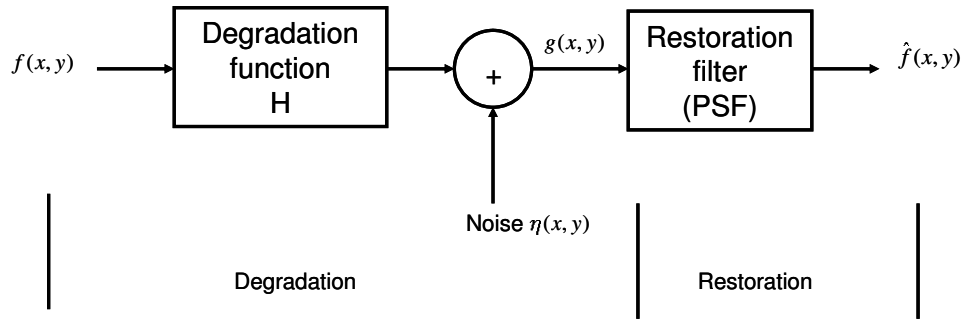
Figure 4.17: Degradation and restoration model.

In order to compute the restored signal $\hat{f}(x,y)$, the Fourier transform property that the Fourier transform of a convolution product is the product of the Fourier transforms of both functions is exploited:

$$\Im \left(f(x,y) \overset{x,y}{\otimes} h(x,y) \right) = F(u,v) \cdot H(u,v), \tag{4.31}$$

where $H(u,v)$ is the Fourier transform of $h(x,y)$, $H^*(u,v)$ is its complex conjugate and (u,v) are spatial frequencies. By multiplying the degraded function by the inverse filter,

$$I(u,v) = \frac{H^*(u,v)}{abs(H(u,v))^2}, \tag{4.32}$$

the original image would be retrieved. However, the points where the filter equals zero diverge. To avoid this drawback, different filtering techniques are used in practice. With the Wiener-filter, a number is added to the denominator of the inverse filter in order to avoid divergence. The filter is implemented as

$$W(u,v) = \frac{H^*(u,v)}{abs(H(u,v))^2 + \frac{P_n(u,v)}{P_g(u,v)}}, \tag{4.33}$$

where $P_n(u,v)$ is the noise power spectrum, and $P_g(u,v)$ is the power spectrum of the original undegraded image. A general filter implementation $G(u,v)$ may be written as

$$G(u,v) = I(u,v)^\alpha \cdot W(u,v)^{1-\alpha},\tag{4.34}$$

where α is a parameter. For $\alpha = 0$ the standard Wiener filter and for $\alpha = 1$, the standard inverse filter is obtained. By varying alpha between 0 and 1 one may emphasize the relative effect of each filter. The so-called geometric mean filter is obtained by setting $\alpha = 0.5$. This geometric mean filter was introduced in [TFCK92] as an attempt to de-emphasize the low-frequency dominance of the Wiener filter while avoiding the early singularity of the inverse filter.

In the experiments, the Richardson-Lucy deconvolution technique [Luc74, Ric72] is used. It is a frequently used filter in the processing of astronomical images to remove the degradation and blurring effects of star observations. It is an iterative method that attempts to maximize the likelihood of the restored image by comparing it to the observed distribution. The reconstructed image is computed following

$$\hat{f}_{n+1} = \hat{f}_n \left(h \cdot \frac{g}{h \otimes \hat{f}_n} \right) = \psi\left(\hat{f}_n\right),\tag{4.35}$$

where f_n is the n-th iteration of the function f.

In [BA97] a method is proposed for accelerating the implementation of the iterative image restoration techniques by the method

$$\hat{f}_n = x_n + \alpha_n h_n,\tag{4.36}$$

where

$$\begin{aligned}
h_n &= x_n - x_{n-1} \\
x_{n+1} &= \hat{f}_n + g_n \\
g_n &= \psi(\hat{f}_n) - \hat{f}_n.
\end{aligned}\tag{4.37}$$

The iterative step is accelerated by a correction technique where the parameter α_n is computed in each iteration following

$$\alpha_n = \frac{\sum g_{n-1} \cdot g_{n-2}}{\sum g_{n-2} \cdot g_{n-2}}, 0 < \alpha_n < 1,\tag{4.38}$$

where the dot sign designates the element-wise multiplication of the matrix and $\sum$ means the sum of the matrix elements.

The method of the software Matlab[4] is used to deconvolve the images. The filter h corresponds to the PSF, g and $\hat{f}_0$ to the initial registered blurred image.

---

[4]www.mathworks.com

Chapter 5

Quantitative analysis of planar subsurface defects in CFRP material

In this chapter the thermographic testing equipment in the EADS-IW laboratories used for the experiments and tests carried out in the course of this thesis is presented. The measurement hardware is assembled to perform lockin thermography. The hardware allows one to register thermal time sequences and to compute the corresponding amplitude and phase images.
Further analysis of the amplitude and phase images is performed on a PC based Matlab programming environment. Algorithms are formulated as Matlab scripts. The Matlab image processing toolbox is extensively used.
The retrieval of depth and size of defects based on thermal image data, is demonstrated with a newly developed set of algorithms together with the methods introduced in Chap. 4.

5.1   Test equipment

For the tests, two thermographic systems are used. Fig. 5.1 shows the thermographic device of the Thermosensorik company. It is employed to register thermographic image sequences and to compute phase and amplitude images as well as to take ultrasound induced thermal images. An advantage of this device is that thermal raw sequences can be registered simultaneously so that amplitude and phase images using the frequency modulated lockin thermography (FMLT) technique (see Appendix B) can be computed outside the provided software. The set-up uses a Thermosensorik CMT 384 M infrared camera having the following specific values:

Spectral range	3.5 - 5 μm
Detector	Cadmium mercury-tellurid detector (CMT)
Format	384 x 288 pixel
Cooling system	Stirling cooling
Pixel size	20 μm x 20 μm
Maximum sampling frequency	132 Hz
Dynamic range	14 bits
NETD at 20 °C	20 mK

A program allows registering the time sequences and computing amplitude and phase images. For lockin thermography, four halogen beamers with a power of 1000 W each

are used. The four spotlights allow a nearly homogeneous distribution of light on the component's surface. An Edevis company beamer dimmer (Varintens dimpac 6 x 2.5 kW or EDEVIS EDE CU3000) is used to dim the light. It is controlled by a signal generator which allows modulating and reducing the power of the lamps. In the tests, only 50 % of the lamps' power is used.

For optical lockin thermography, the non-steady regime (see Chap. 3.1.4) has to be eliminated in order to correctly compute the phase images. There are different methods of correcting the non-steady effect:

- Before beginning to modulate the lamps, the part is heated (e.g. switching the lamps on for a few seconds) until the mean temperature of the steady-state regime is reached.

- Waiting until the steady-state regime is reached.

- Correcting the sequence using a correction algorithm [Wu96] by subtracting the theoretical transient response (Chap. 3.1.4) to each pixel.

(a)   (b)
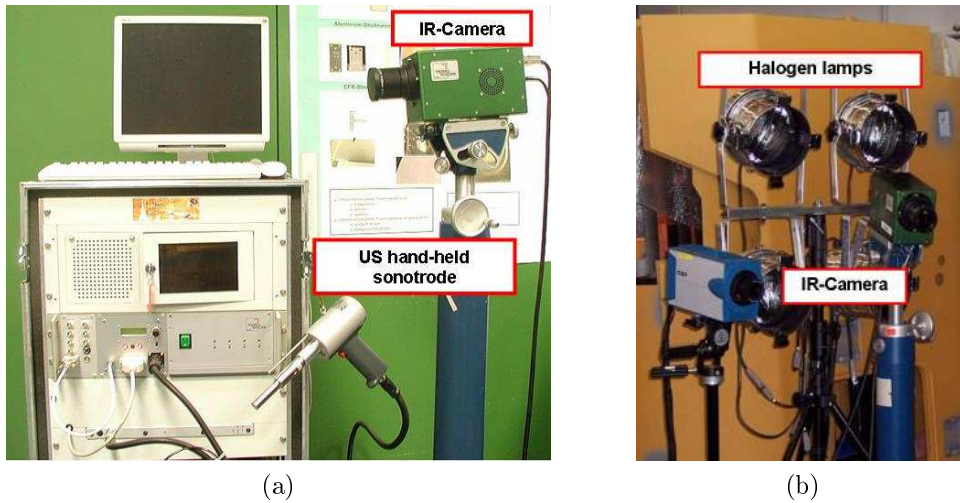
Figure 5.1: Thermography set-up of the Thermosensorik company (a) with the sonotrode gun and (b) with lamps for OLT.

Further, in order to avoid signal losses, the sampling frequency must correspond to at least twice the excitation frequency (Shannon sampling theorem). In the Thermosensorik system, the maximum sampling frequency is $f_s = 132$ Hz. It can be reduced by skipping frames and registering only each Nr_{sk} frame. The corresponding sampling frequency is

$$f_s = \frac{132}{(Nr_{sk} + 1)}, \tag{5.1}$$

where Nr_{sk} is the number of skipped frames. When working with a maximal excitation frequency of 1 Hz, the sampling frequency must be greater than 2 Hz. This condition is still respected when up to 66 frames are skipped.

Ultrasound waves are generated in the component by means of a sonotrode; here a Thermosensorik company hand-held gun Hg 20-1 shown in Fig. 5.1a. The time and power can

be varied. The ultrasound generator AGM-20-100P-230-B1 generates ultrasound waves with a frequency of 20 kHz and an adjustable power up to 1000 W. By pushing the start button, a pulse signal is triggered and the MPS software begins to register a time sequence.

The second device is provided by the Edevis company and is shown in Fig. 5.2. It is composed of the same beamer dimmer and of a camera, CEDIP JADE III MW. The characteristics of the camera are:

Spectral range	3.6 - 5.1 μm
Detector	Indium antimonide (InSb) detector
Format	320 x 240 pixel
Cooling system	Stirling cooling
Pixel size	25 μm x 20 μm
Maximum sampling frequency	120 Hz
Dynamic range	14 bits
NETD at 30 °C	25 mK

Figure 5.2: Thermography set-up of the Edevis company.

The measurements are performed either with the Thermosensorik company device or with the Edevis company device. The phase images are exported to the Matlab software in order to process the phasegrams.

5.2   Depth retrieval methods

This section shows how the phasegrams are processed to retrieve the depth of defects. Two different methods are used to evaluate the depths.

5.2.1 Histogram method

The first method that works on the global image uses phase information. The defect depth is retrieved through the relationship introduced in Eq. 2.9

$$d = C \cdot \mu = C \cdot \sqrt{\frac{\alpha_z}{\pi f_b}}, \quad C \approx 2. \tag{5.2}$$

By knowing the blind frequency f_b, the defect depth can be retrieved. The goal consists of retrieving the blind frequency of each defect automatically from a phasegram by using image processing algorithms. First, the parameter C is determined by using the theoretical phase-contrast point-spread function introduced in Chap. 3.

In Fig. 5.3a, the theoretical phase contrast function of a defect of diameter 20 mm is represented at different depths as a function of the modulation frequency. The theoretical curve is obtained by taking $\alpha =$[0.5 0.5 0.22] mm²s⁻¹. The blind frequency f_b is the frequency at which the function crosses the x-axis from positive to negative phase contrast for the first time with increasing frequency. It is determined automatically for several depths using the theoretical functions. Eq. 5.2 is fitted to the retrieved points to determine the parameter C. Fig. 5.3b shows the obtained points and the fitted curve of the defect depth vs. the blind frequency. A linear fit for computational performance can also be performed in the same way by taking d^2 to retrieve the proportional coefficient between the defect depth and the thermal penetration depth. Fig. 5.7a shows the result of the fit. In both cases, the factor C is found to be $C = 2.3$.
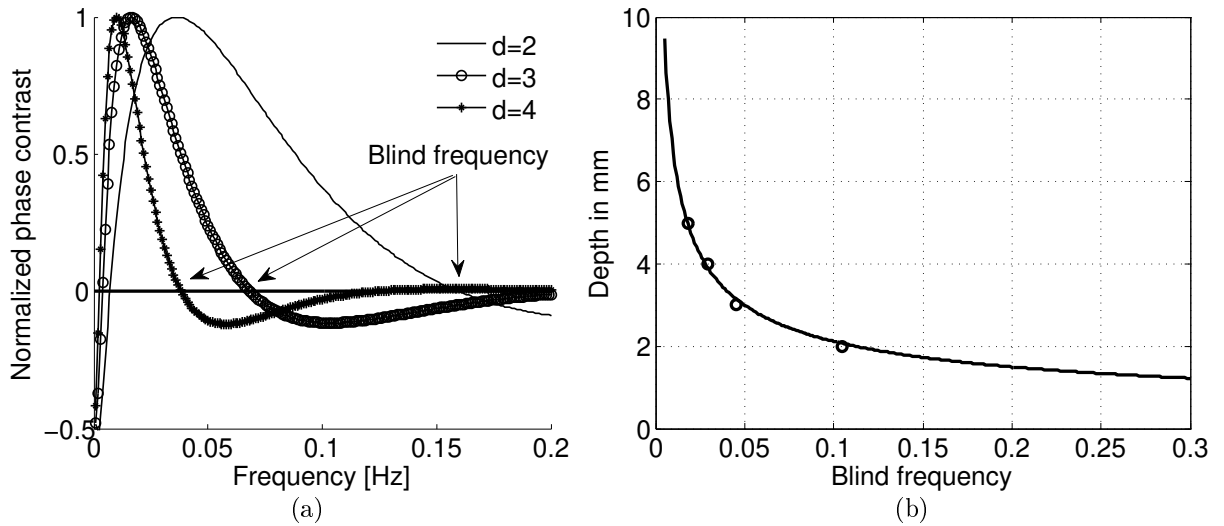
Figure 5.3: (a) Theoretical phase contrast function vs. frequency at different defect depths d, given here in mm; (b) Depth vs. the blind frequency (here $\alpha_z = 0.22 \cdot 10^{-6} m^2 \cdot s^{-1}$).

To evaluate the blind frequency, each phase image is segmented into defective and non-defective pixels by considering signal values with a SNR > 6 dB as defects (Chap. 4.2.3). The analysis of the histograms allows determining an upper limit; a threshold for each image for the detection of defects.

The blind frequency is determined in a discrete way. For each pixel, a detection vector d_i is built. When the pixel value in the $i - th$ phase image is above the corresponding
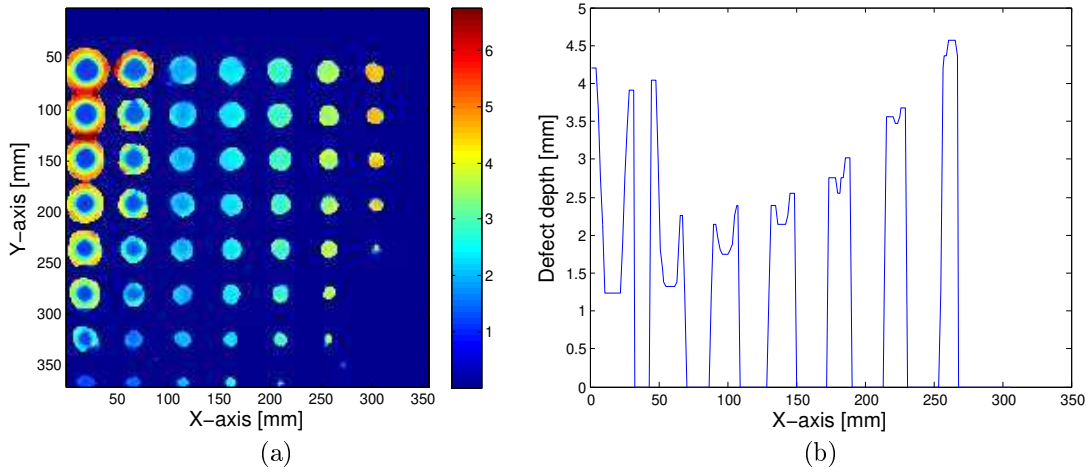
Figure 5.4: (a) Obtained depth-map with color coding. The color scale indicates the depth in mm; (b) Profiles of the defects of diameter 14 mm.

Table 5.1: Retrieved defect depths of different defects with the histogram method.

Given depth [mm]	1	1.5	2	2.5	3	4	5
Given diameter [mm]							
20	1.35	1.41	1.99	2.30	2.81	3.44	4.45
18	1.35	1.41	1.91	2.30	2.81	3.53	4.64
16	1.35	1.41	1.91	2.44	2.81	3.53	4.45
14	1.35	1.35	1.78	2.18	2.81	3.63	4.64
12	1.35	1.41	1.84	2.18	2.81	3.85	4.64
10	1.35	1.41	1.84	2.18	2.81	4.12	-
8	1.35	1.41	1.99	2.44	2.81	1.84	-
6	1.35	1.62	2.18	2.81	3.08	-	-

detection limit, the value of d_i is set to $d_i = 1$. Elsewhere, the value of d_i is set to $d_i = 0$. So, the detection vector is a series of '1'-elements, followed by a series of '0'-elements, which contains indirect information about the depth of the artificial defects. The index of the blind frequency corresponds to the last value '1' in the detection vector. A more precise value of the blind frequency can be obtained by performing a linear regression between the frequency corresponding to the last value 1 and the frequency corresponding to the index of the first value '0'.

The two-dimensional depth-map of plate I obtained from the phase images is shown in Fig. 5.4a. It must be noted that the lateral heat diffusion has not yet been taken into account so that the retrieved defect depth appears deeper at the borders than at the center (Fig. 5.4b). The retrieved defect depths are computed through the expression of Eq. 5.2 and are listed in Tab. 5.1. Satisfactory results are obtained except for the deep small defects which are not detected with this method.
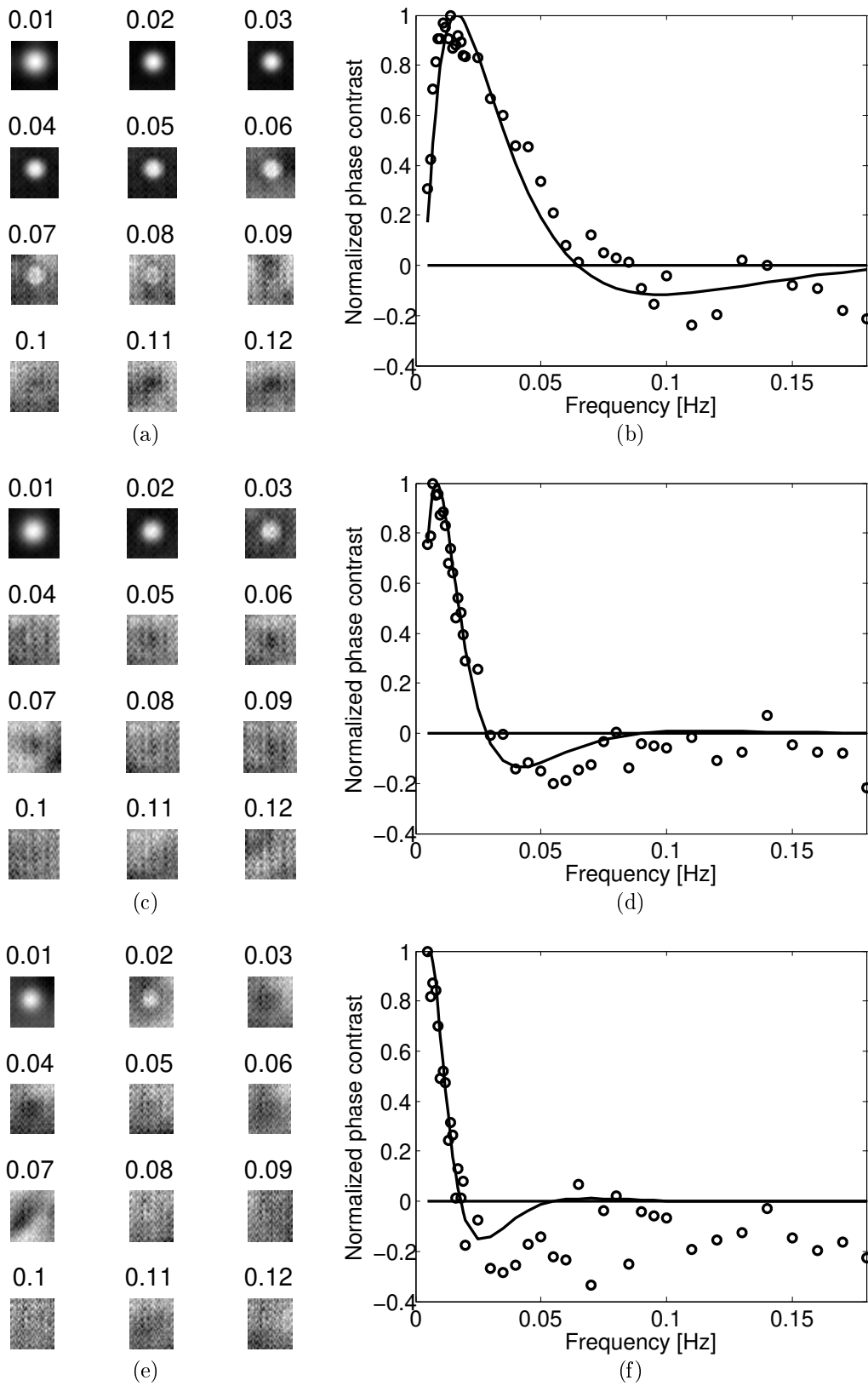
Figure 5.5: (a-c-e) Phase images of plate I at several frequencies given in Hz; (b-d-f) and phase contrast response as a function of frequency of plate I defects 20 mm in diameter situated at depths: (a-b) 2 mm, (c-d) 3 mm, and (e-f) 4 mm.

5.2.2 Fit of the theoretical PSF

The second method is based on a fit of the theoretical phase contrast function. It is therefore independent of the parameter C. The depth is determined by fitting the theoretical phase contrast to the measured phase contrast of each pixel through least square regression. Fig. 5.5 shows different phase images at several frequencies of defects situated at different depths, and the obtained fits to the phase contrasts. The fits are quite good at low frequencies whereas at higher frequencies, noise is more important. A depth-map is thereby obtained and is shown in Fig. 5.6.

From the results of the retrieved depths listed in Tab. 5.2, this method appears to be more accurate than the histogram method shown in Chap. 5.2.1. It gets rid of the parameter C of Eq. 5.2. However, the pixel-wise fit of the theoretical model for retrieving the depth takes very long. This fitting method is better suited for retrieving the depth of individual points, such as the center point of one defect (cluster).

Table 5.2: Retrieved defect depths by fitting the theoretical contrast function to data.

Depth [mm] Diameter [mm]	1	1.5	2	2.5	3	4	5
20	1.09	1.51	2.03	2.56	3.01	3.83	5.11
18	1.06	1.46	2	2.54	3.05	3.91	5.35
16	1.02	1.37	1.95	2.52	3.02	3.85	5.03
14	0.98	1.3	1.8	2.31	2.9	3.88	-
12	0.94	1.25	1.71	2.19	2.83	4.34	-
10	0.93	1.22	1.64	2.1	2.7	5.08	-
8	0.88	1.15	1.59	1.98	(4.69)	-	-
6	0.90	1.2	1.44	-	-	-	-

5.2.3 Effect of the defect size

Eq. 5.2 is only valid for extended defects. In Fig. 5.7b, the phase contrasts for different defect diameters are plotted. For a defect of diameter 1 mm, the phase contrast corresponds to that of a point-like defect. Yet for an increasing diameter, the phase contrast functions differ. Small defect indications disappear at higher frequencies. This can be explained by the fact that, by convolving the signal amplitude of a defect with the PSF, the value of a pixel is determined by the average values of the neighboring pixels. The neighboring pixels contribute to the image formation, whereas for a point-like defect, only the middle point plays a role. This contribution introduces a phase shift.

The same effect is observed in measurements. Smaller defect indications disappear at higher frequencies. From a given defect size (here from 15 mm diameter onwards), the phase contrast is constant.

In the experiments, the effect of the defect size is ignored for the determination of the depth. The phase contrast of an extended defect of diameter 20 mm is included in the
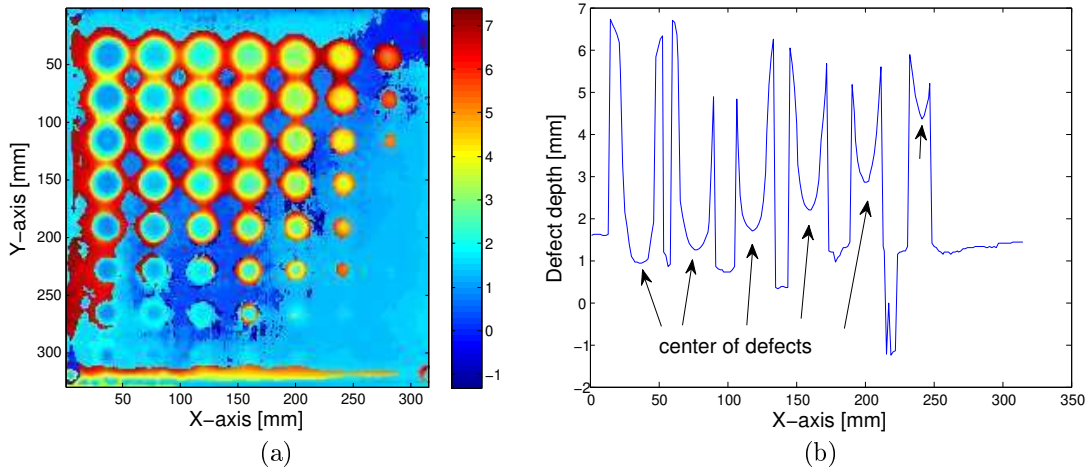
Figure 5.6: (a) Depth-map of plate I obtained with the fitting method. Each pixel is coded through a color indicating its depth. The color bar shows the relationship between color and pixels depth (in mm); (b) Line-scan of the depth-map for 2 mm depth.

calculations.
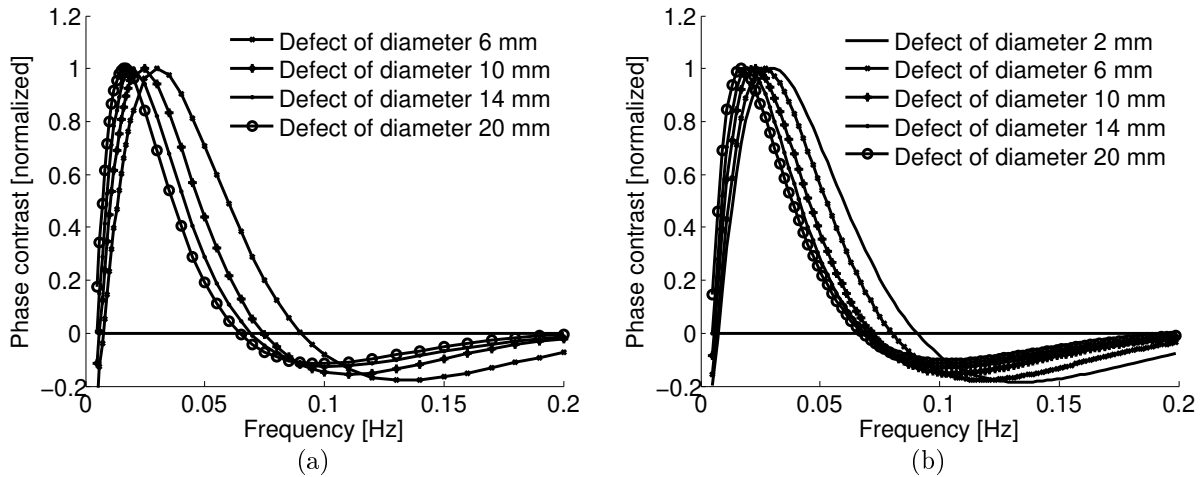
Figure 5.7: Comparison of the phase contrast with respect to the lockin frequency, according to different defect diameters. (a) Phase contrast fitted to measurements; (b) Theoretical phase contrast (here $d = 2$ mm, $\alpha = 0.5, 0.5, 0.2218$ mm$^2 \cdot s^{-1}$).

5.3 Size retrieval

As can be noticed from the lateral defect-profiles in Fig. 5.6b, there are remaining artifacts on the depth-map due to the lateral heat diffusion. Since the PSF depends on the defect depth, each planar defect has to be treated separately. So, a clustering step (see Chap. 4.3) allows the classification of defective pixels into groups. The depth at the center of the cluster is taken for deconvolution and as an input parameter for the theoretical PSF of Eq. 3.85. To retrieve the defect-shape, the extracted defects are deconvolved using a
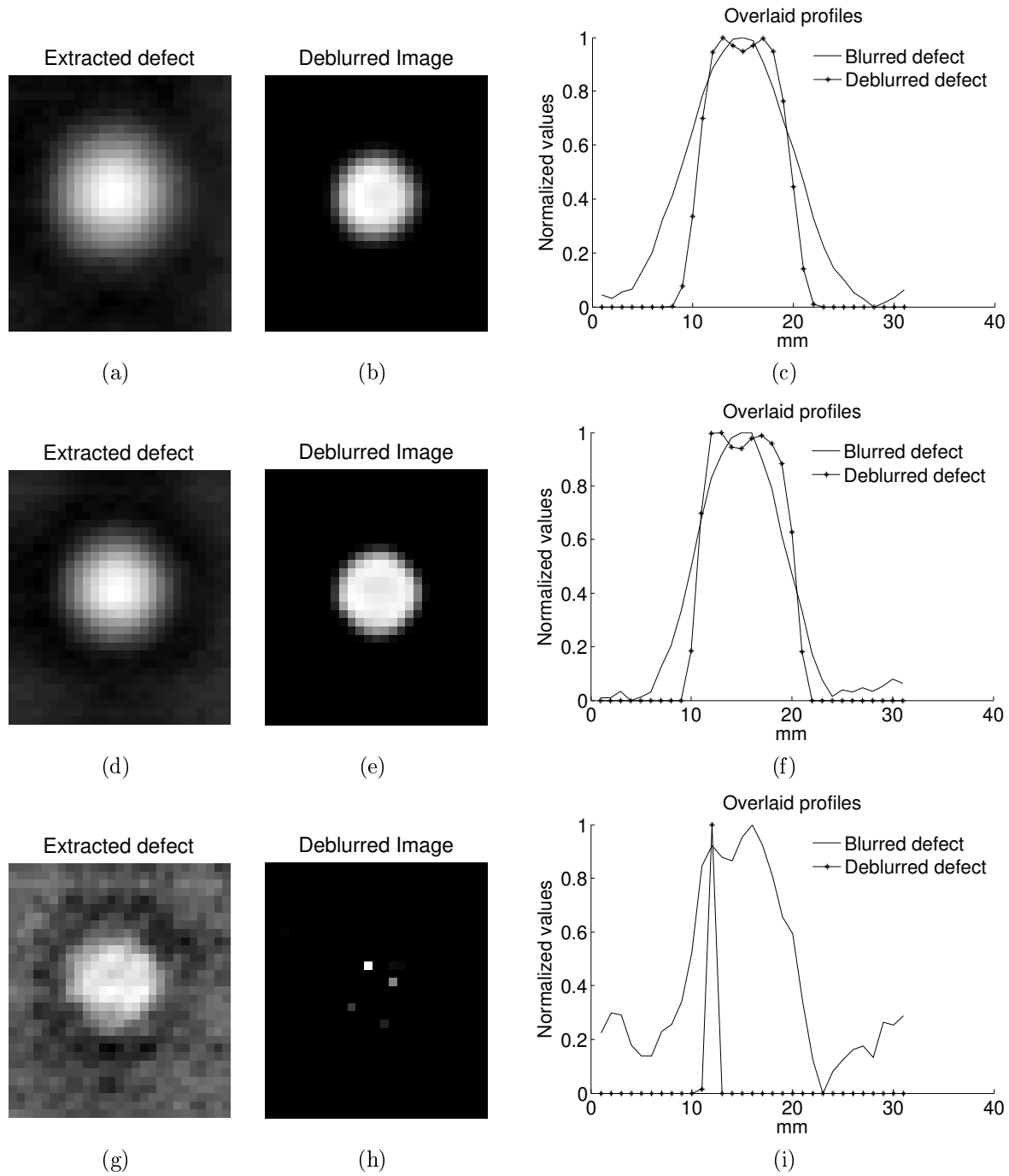
Figure 5.8: Deconvolved defects situated at 2 mm depth in phase images at frequencies (a-c) 0.01 Hz; (d-f) 0.02 Hz; (g-i) 0.06 Hz. The figures on the right show line-scans through the center of the defects.

Richardson-Lucy filter (see Chap. 4.4).

Fig. 5.8(a-c) shows a result of deconvolution. A value of $\alpha = [0.5; 0.5; 0.222]$ is taken as the anisotropic thermal conductivity. The defect is situated at a depth of 2 mm. The defect appears sharper.

An additional task is the determination of the optimal phase image that should be deconvolved in order to get a realistic map of the defect. It can be seen from Fig. 5.3a that the

Table 5.3: Typical frequencies for depths in various depths.

Defect depth [mm]	f_o [Hz]	f_b [Hz]	$f_o + \frac{f_b - f_o}{4}$ [Hz]
1	0.065	0.284	0.12
2	0.017	0.067	0.03
3	0.009	0.03	0.014
4	0.006	0.018	0.009
5	0.005	0.012	0.007

chosen frequency has to be smaller than the blind frequency. Fig. 5.8 shows the deconvolution of the phase image of the plate I defect situated at 2 mm depth and of diameter 20 mm for three different lockin frequencies, namely 0.01, 0.02, and 0.06 Hz. The latter one almost corresponds to the blind frequency and the SNR is very low. Consequently, the deconvolution of this image does not yield favorable results, whereas by taking the first two frequencies, the same deconvolution results are obtained. The best result should be achieved by choosing the frequency with the maximum SNR. From Fig. 5.3a, one can observe that there is a frequency called 'optimal frequency' [BW01], at which the phase contrast is at its maximum. However, at this frequency, a defect is more blurred and this blur is difficult to remove. Therefore, a frequency situated between the optimal f_o and the blind frequency f_b following

$$f_{deconv} = f_o + \frac{f_b - f_o}{4} \tag{5.3}$$

is chosen for the deconvolution of the defects.

Finally, to calculate the size of the defects, the full-width half-maximum (FWHM) criterion is used. The width of the defect signal at half of the maximum signal is taken as a measure. Some typical frequencies are represented in Tab. 5.3 for $\alpha_z = 0.22$ mm^2 s^{-1}.

5.4 Determination of material parameters

5.4.1 Retrieval of the thermal diffusivity in z direction

The thermal diffusivity in z-direction is determined in the same manner as for retrieving the depth. The retrieved parameters for different defect depths are listed in Tab. 5.4. The average value is $\alpha = 0.222 \pm 0.008$ mm^{2}s^{-1} ($\pm$ 4%) and is used for the next experiments.

Table 5.4: Retrieved coefficients with fit of the theoretical model. The mean value is $\alpha = 0.222 \pm 0.008$ mm^{2}s^{-1} ($\pm$ 4%).

Depth [mm]	1	1.5	2	2.5	3	4	5
α [mm^2·s^{-1}]	0.217	0.228	0.22	0.221	0.224	0.235	0.207

5.4.2 Retrieval of the thermal diffusivity in x and y direction

The next step consists of retrieving the coefficients of the heat diffusion in x- and y-directions. Therefore, the lateral blurring effect is studied. The idea is to compare the experimental PSF with its theoretical model and to derive α_x, α_y. The empirical PSF is determined by deconvolving a phase contrast image of a defect extracted from a measured phase image with its known shape function (see Chap. 4.4). The comparison between the retrieved PSF (empirical PSF) and the prediction of the theoretical phase contrast response (Eq. 3.96) is shown in Fig. 5.9. A defect depth of 1.5 mm and a defect diameter size of 20 mm are chosen as an example. The phase contrast image at a frequency 0.01 Hz, which corresponds to the optimal frequency for a depth of 1.5 mm, is used for the deconvolution. A value of $\alpha_x = \alpha_y = 0.5 \pm 0.1$ mm $^2 \cdot$s^{-1} is retrieved.
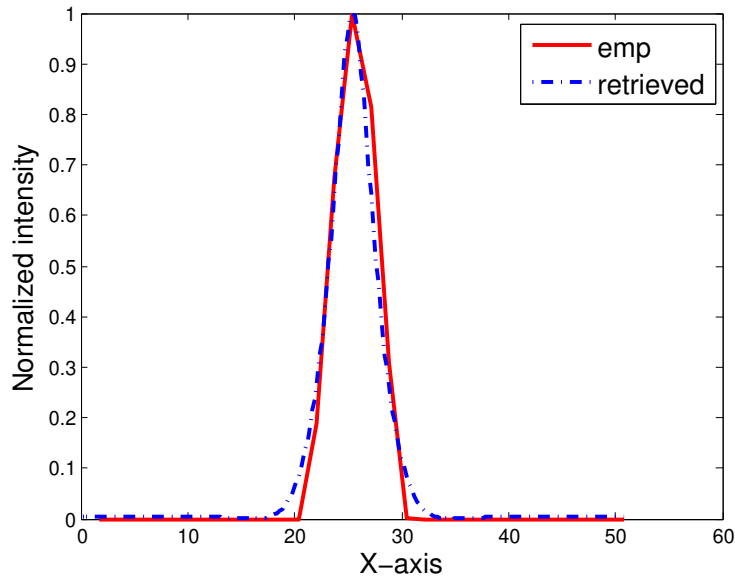
Figure 5.9: Overlay of profiles of the empirical and the theoretical PSF.

5.5 Analysis of planar defects

5.5.1 Final algorithm

In order to process thermal images, a set of methods are combined. The phase images are first scaled and deskewed to enable quantitative analysis. In a second step, the defect depth is determined. In a third step, the defects are clustered. Then, the images are deconvolved in order to eliminate the thermal blurring effect, which depends on the lockin frequency and on the defect depth. The algorithm can be summarized as follows:

1. Measurements of lockin phase images at several lockin frequencies

2. Computation of the phase contrast through a background subtraction algorithm

3. In each phase contrast image, segmentation of defects with the SNR method

4. Determination of the blind frequency f_b and of the depth through the relationship
   $$\text{depth}(i,j) = 2.3 \cdot \sqrt{\frac{\alpha}{\pi f_b(i,j)}}$$

5. Clustering of defects

6. Improvement of the depth estimation by fitting the phase contrast theoretical model to the phase contrast of the center of each defect

7. Deconvolution of each defect separately by taking the phase image at a frequency
   $f_{deconv} = f_o + \frac{f_b - f_o}{4}$

8. Obtaining a defect-map

5.5.2 Deconvolution of plate I

The two-dimensional map of the retrieved depths from phase images is shown in Fig. 5.10. The lateral effects of the blur still remain. One method of undoing lateral blurring is to take, for determining the corresponding PSF of a defect, either the depth at the center point or the mean depth of individual pixels. The depth of each cluster center (rather than the mean) is assigned to the defect.
Each defect is deconvolved using the corresponding PSF and the deconvolved defects are additionally classified following the FHWM criterion. The resulting depth-map is shown in Fig. 5.11. The retrieved depths with errors are shown in Fig. 5.12. The mean values of the retrieved depth are plotted with the error bars. The defects with a diameter larger than 10 mm are retrieved with an inaccuracy less than 20 %. The defects of 8 mm diameter have an inaccuracy between 13 to 36 %, the inaccuracy between 36 % is obtained for the defect at 4 mm depth. The depths of the defects of diameter 6 mm have 27 to 58 % inaccuracy. The maximum deviation occurs for small defects (4 mm deep, 8 mm wide).
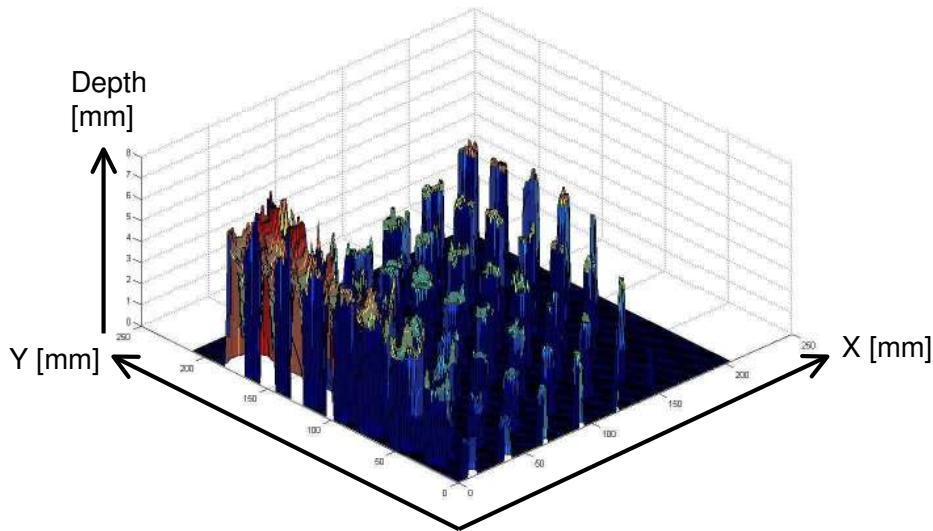
Figure 5.10: Depth-map of plate I with lateral thermal effects.
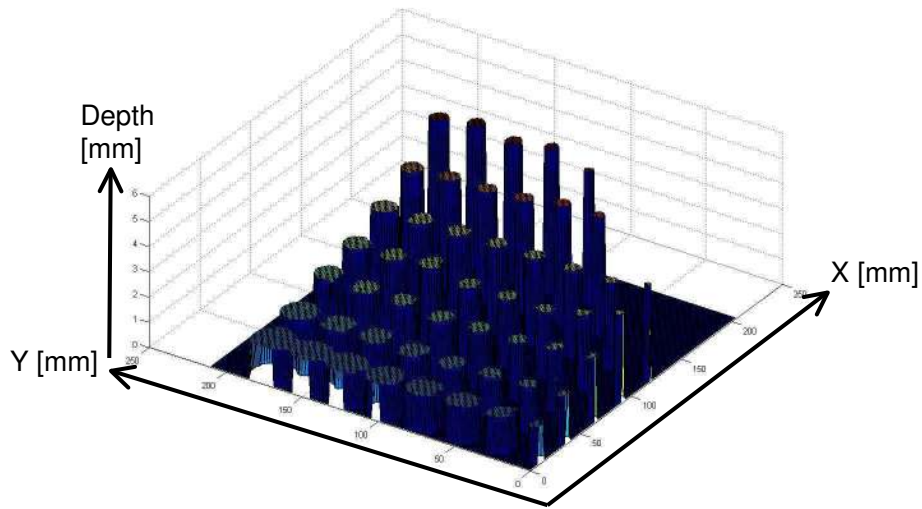
Figure 5.11: Obtained depth-map of plate I.

Fig. 5.13 shows the plot of the retrieved defect sizes as a function of their diameter. Size estimation has an error of around 2 mm in most cases. The defect size is well estimated for large defects. For defects of diameter between 12 mm and 20 mm, the inaccuracy is at most 20 %. For defects of a diameters between 6 and 10 mm, the inaccuracy is between 3.2 and 78 %. The defect diameters are better retrieved for defects at depths values between 1 and 2 mm depth. The innacuracy here is at most 6 %. For depths greater than 2 mm, there is an innacuracy between 13 to 78 % in the size estimation. Defects lying at 5 mm depth appear smaller than they are. Defect diameters smaller than 10 mm are not detected at this depth.
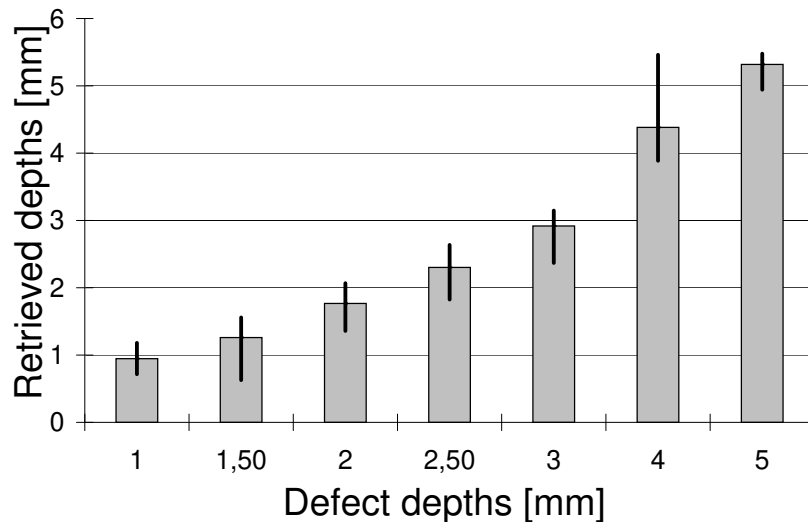
Figure 5.12: Schematic representation of retrieved depths on plate I. The sizes are given in mm.
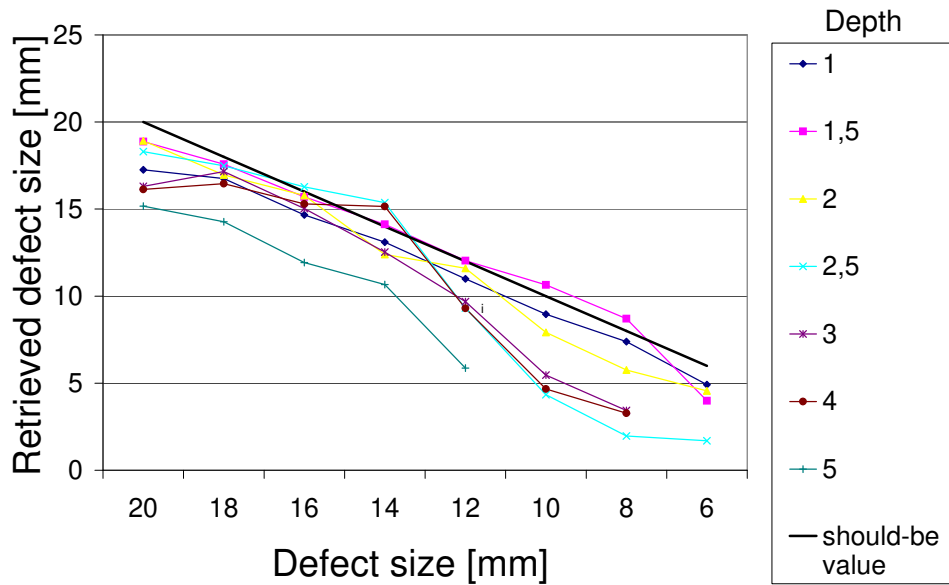
Figure 5.13: Retrieved defect diameters for different defect on plate I. The sizes are given in mm.

(a)   (b)   (c)   (d)
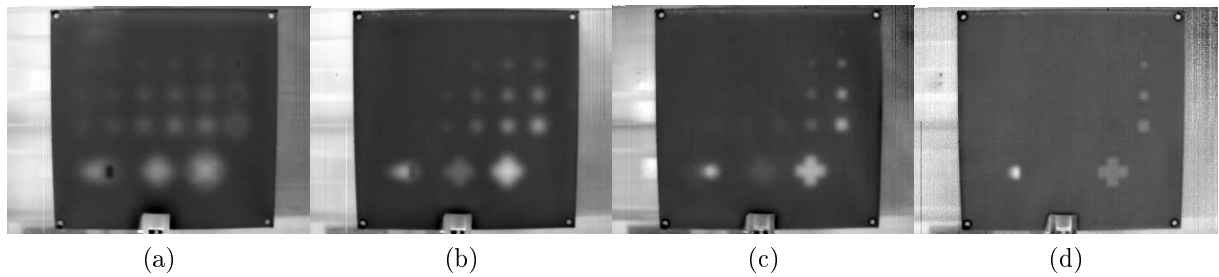
Figure 5.14: Example of lockin phase images obtained for different frequencies on plate II (a) 0.005 Hz, (b) 0.01 Hz, (c) 0.025 Hz, and (d) 0.05 Hz.

Extracted defect   Deblurred defect

(a)   (b)
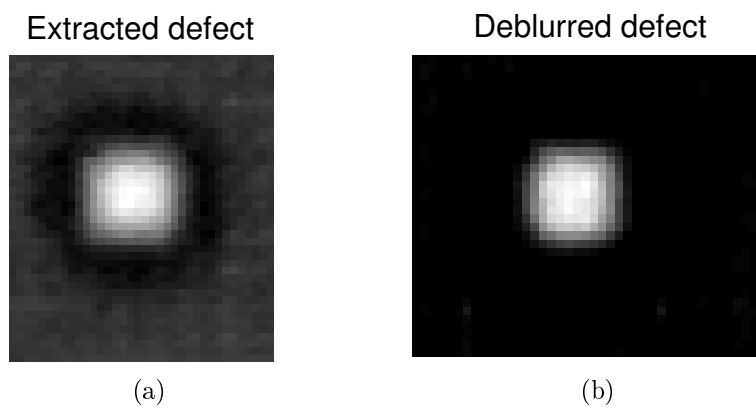
Figure 5.15: Deconvolved rectangular defect situated at 2 mm depth from the phase image at a frequency 0.03 Hz.

5.5.3 Deconvolution of plate II

The second part was manufactured with rectangular and cross-like defects. Fig. 5.14 shows phase images of plate II taken at different frequencies. The effect of the blind frequency and phase contrast reversal can be observed at 0.005 Hz for defects situated at 1 mm and 2 mm depth (wedge). In Fig. 5.15, a rectangular defect situated at 2 mm depths is deconvolved. The result of the deconvolution of both crosses situated at 2 mm and 4 mm depths are represented in Fig. 5.16. Frequencies of 0.03 Hz and 0.009 Hz, respectively, were taken for deconvolution using Eq. 5.3. The depth-map of the whole plate before deconvolution is shown in Fig. 5.17 and the final depth-map after deconvolution is shown in Fig. 5.18. The shape of the cross-like defects is well-retrieved.
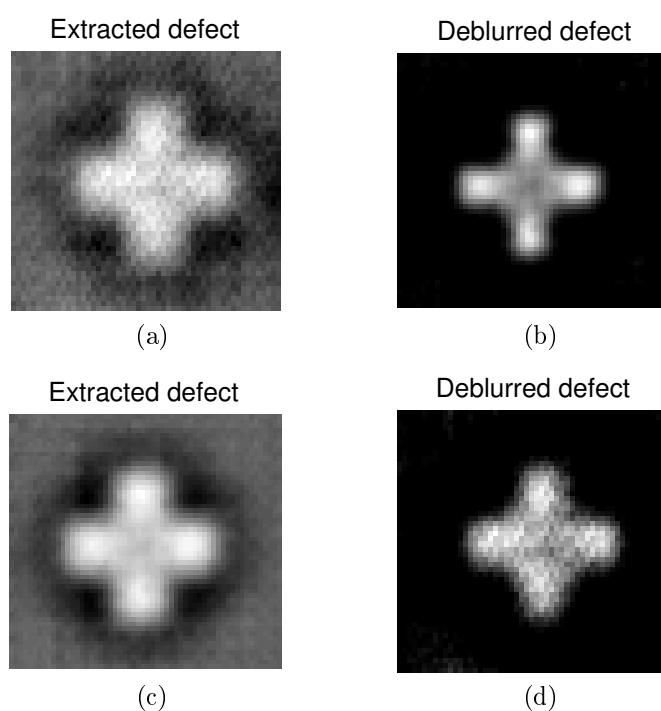
Figure 5.16: Deconvolved defects situated at depths of (a-b) 2 mm and frequency of 0.03 Hz; (c-d) 4 mm and frequency of 0.009 Hz.

5.6 Analysis of impact damages

Subsurface delaminations caused by an impact are investigated. Fig. 5.19a shows an image of a painted aircraft door composed of a honeycomb inner structure made of CFRP material. The test-piece was provided by EADS - MAS Manching. The part was damaged through controlled impacts of different energies between 2 and 12 Joules (see Fig. 5.19b). The resulting phase images obtained through lockin thermography are shown in Fig. 5.20. At a lockin frequency of 0.1 Hz, the thermal waves have penetrated to the honeycomb structure which becomes clearly visible.

Fig. 5.21 shows the obtained depth-map of the part. Here, no deconvolution algorithm is
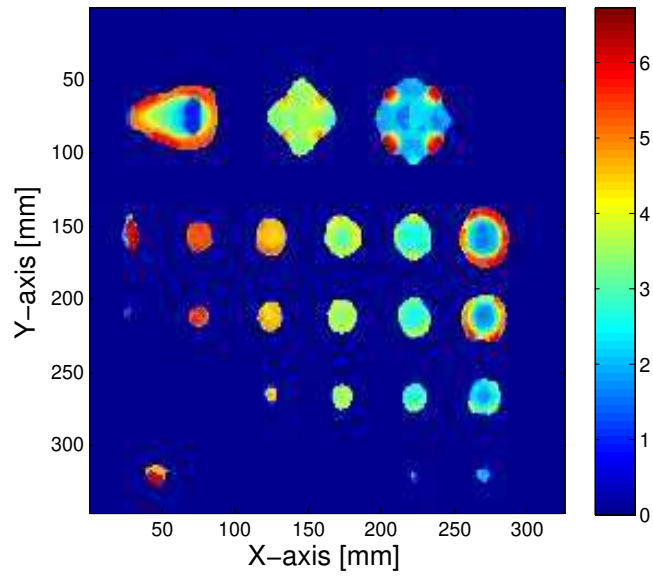
Figure 5.17: Obtained depth-map of plate II before the deconvolution algorithm is applied. The color scale indicates the depth in mm.
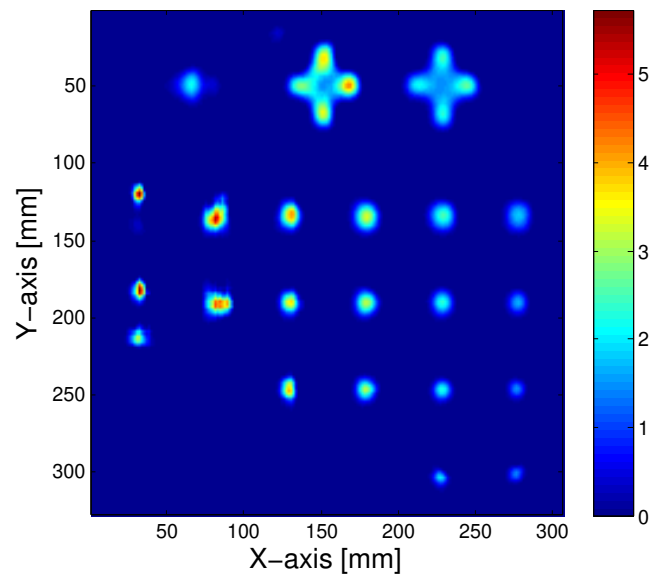
Figure 5.18: Reconstructed depth profiles of plate II with deconvolution. The color scale indicates the depth in mm.

applied since damages are situated at very low depths, so that the blurring effect can be ignored.

(a)   (b)
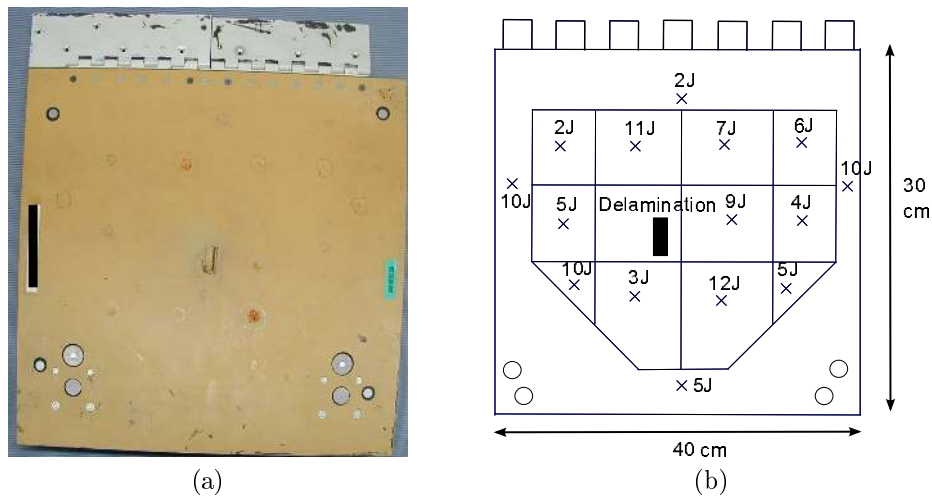
Figure 5.19: Photograph of an aircraft door with artificial impact damages (plate III).

(a)   (b)   (c)
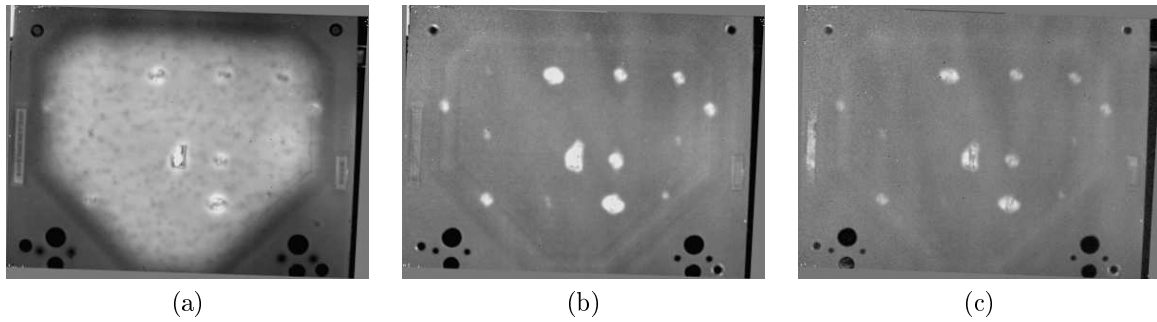
Figure 5.20: Phase images of plate III, an aircraft door, at frequencies (a) 0.1 Hz; (b) 0.4 Hz; (c) 0.6 Hz.

5.7   Limits of the algorithm

The described algorithm is only applicable to planar defects because their depth must be constant for the deconvolution. Consequently, the wedge of plate II could not be evaluated precisely. Future work should extend the algorithms to arbitrary geometries of defects and of components. The theoretical phase contrast could be used to simulate directly the thermal response of a defect and to compare it to the thermal measurements to optimize iteratively the shape function. The parameters could be initialized with the result of the presented algorithm of planar defect shape analysis. As an example, a simulation of the wedge has been performed. The wedge is represented in Fig. 5.22 and the simulations of the wedge in Fig. 5.23. Two frequencies of 0.005 and 0.05 Hz were taken as an example. The simulations concur well with the measurements.

83
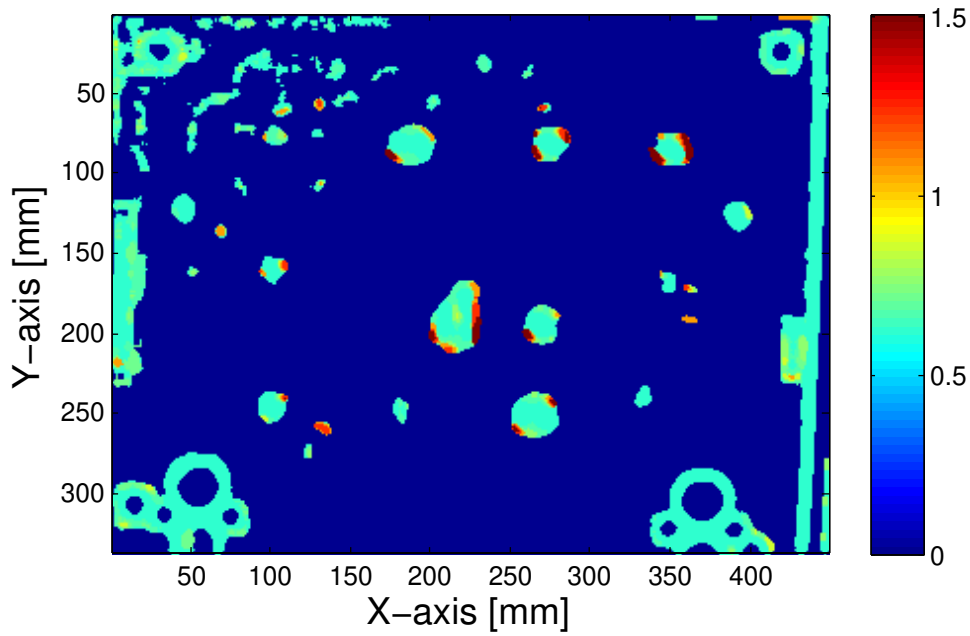
Figure 5.21: Depth-map obtained of the defects on an aircraft door. The color scale indicates the depth in mm.
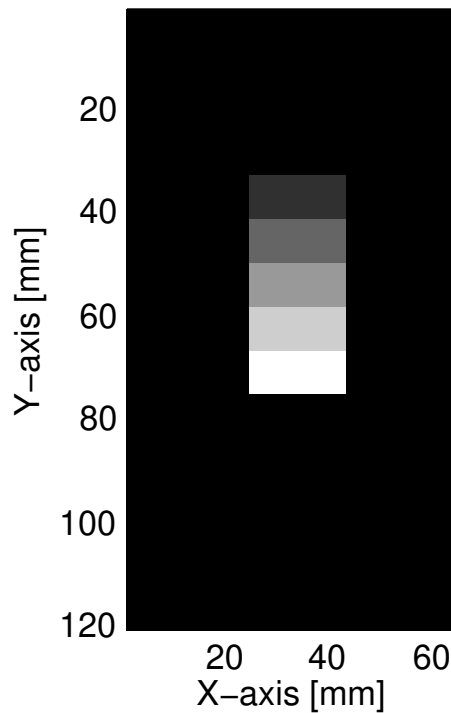
Figure 5.22: Model of the wedge.

5.8 Conclusion

An algorithm was presented, which consists of different image processing steps and allows the retrieval of the defect depth and shape in a semi-automated way. A theoretical model of the phase contrast leads to improvement in the estimation of the defect depths and allows the deblurring of defects.
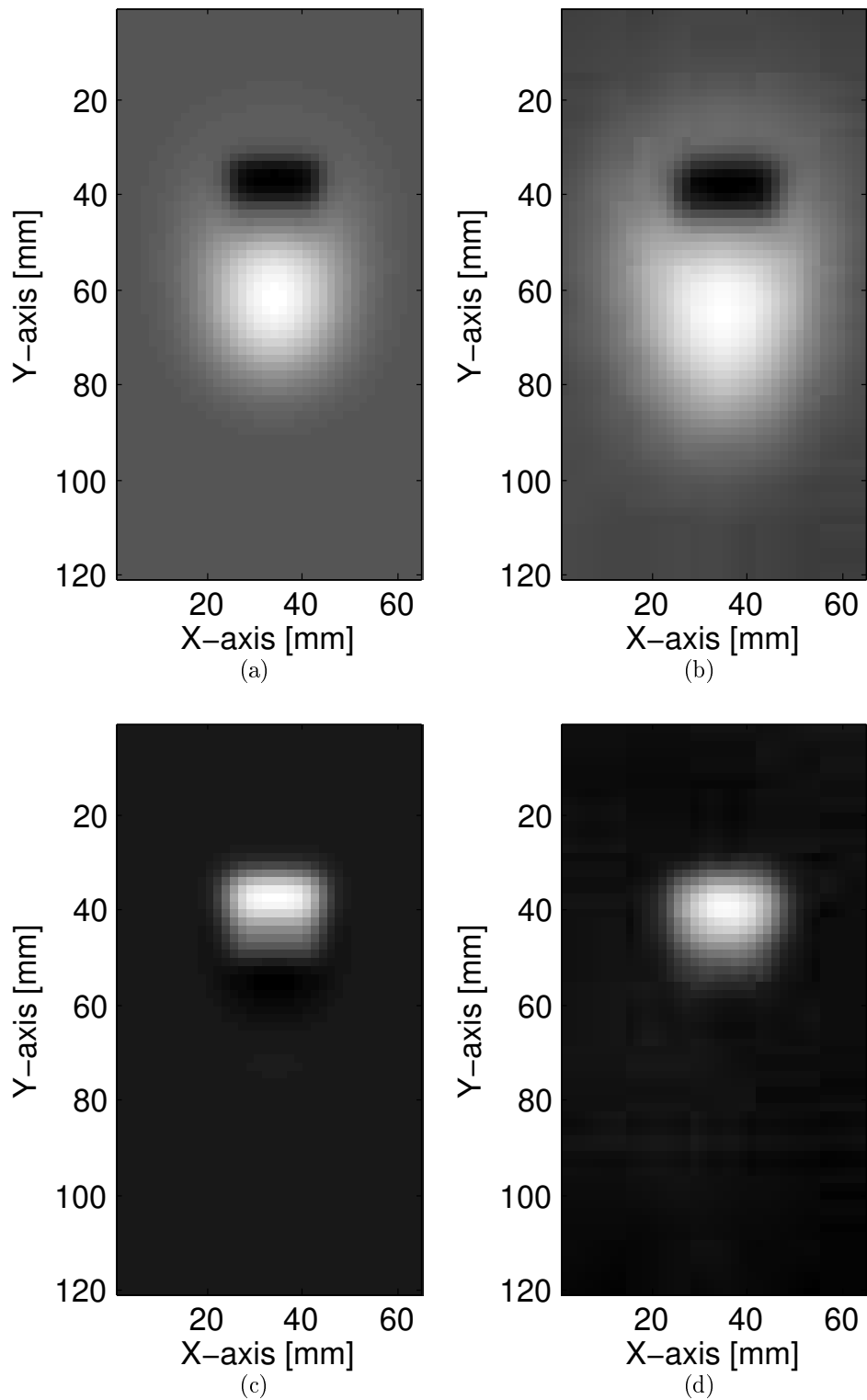
Figure 5.23: Simulations (left) and measurements (right) of the phase images of a wedge at frequencies (a-b) 0.005 Hz) and (c-d) 0.05 Hz.

The algorithm was applied to an anisotropic material. An anisotropic PSF had to be computed. The measurements and consecutive analysis of a plate of CFRP material with

blind holes showed satisfying results. The defect depth could be retrieved with an accuracy between 3 to 37 % for defects larger than 10 mm diameter and 27 to 58 % for smaller defect sizes. The largest deviation occurred for the smallest deep defects. The defect sizes were retrieved with an accuracy of 6 mm. The 6 mm large defects could not be detected for depths greater than 3 mm and the defects at 5 mm depth could be detected only for defects with diameters larger than 10 mm. The shape of both cross-like defects and rectangular defects are easily retrieved. The algorithm only works for planar defects.

Chapter 6

Panoramas for the measurement of defect growth in long complex shaped components

At Eurocopter, fatigue and stress tests are performed on new CFRP components for qualification purposes. NDT is used before and after the loadings in order to detect and characterize the apparition or growth of defects such as fractures or cracks. After a fatigue test, examiners want to find out if potential damages have changed and compare the defect sizes at two different times to determine the growth. Thermographic imaging of the same aircraft part is done from different perspectives and after long periods of time.

Panorama techniques can be used to match or overlay two images made from different positions and possibly at different times, but for curved shapes, other transformations have to be employed. Another task is to test long aircraft components. Several phase images have to be taken in order to get images with sufficient resolution. Image processing techniques are used to create panoramas. The two main tasks are:

- Superposition of two images in order to directly compare the growth of damages;

- Combination of neighboring images of complex shaped components to a panorama at different lockin frequencies.

Panorama programs as introduced in Chap. 4 for stitching images are readily available but have to be adapted since they focus on planar surfaces or landscapes that, at a large distance, behave as a planar surface. In this chapter, in order to compute the transformation between two images so that they can be matched, stitched or overlaid, features have to be selected in both images. The feature selection toolbox of the Matlab[1] program for manual selection of features is used and different automated feature detectors are tested. Affine and polynomial transformations to overlay images are also compared. It is shown at the example of a curved component that the manual selection of points works best, but amongst the automated feature detectors, the algorithm SIFT delivers good results as well.
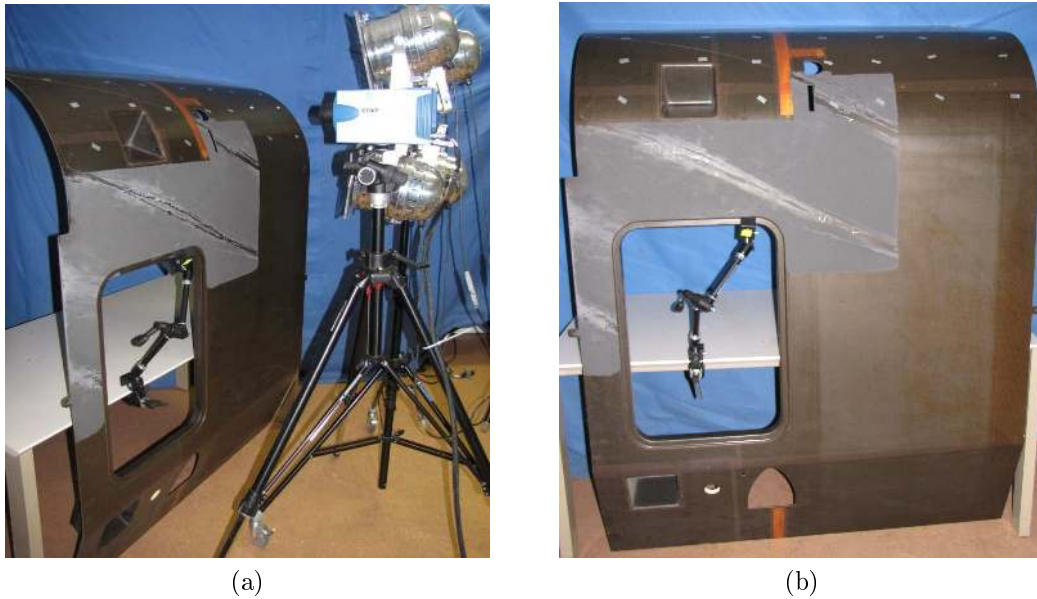
Figure 6.1: (a) Thermographic set-up and (b) investigated side panel (Component III). Only the upper part of the curved area is investigated.

6.1 Test of aricraft components

Measurements are conducted on a large, curved shaped aircraft component made of CFRP material (called Component III). It is a side panel of an helicopter and is provided by EADS-Eurocopter. Fig. 6.1 shows the set-up and the investigated component. Using the thermographic system of the Edevis company, five measurements are performed and the results are shown in Fig. 6.2.

Artificial markers of rectangular shape are used and glued onto the part in order to introduce artificial reference points. It should be noted that they may shadow potential damages. The phase images highlight the inner structure of the component and these characteristic features could also be used as markers. However, the thermal contrast is often too low to detect features automatically. The infrared live images taken before phase measurements are preferred to select features manually since the borders of the markers appear sharper.

The used markers are composed of aluminum that have a high reflectivity in infrared. They were cut to the desired shape from aluminum tabs. The rectangular shape was chosen so that feature detectors, like the Harris corner detector, allow one to detect corner features more easily.

The markers are fixed on the investigated components in such a manner that there are three arrays of three markers in each image, respectively. The overlap of two neighboring images should be around 60%, so that there are at least six markers in common.

---

[1]www.mathworks.com
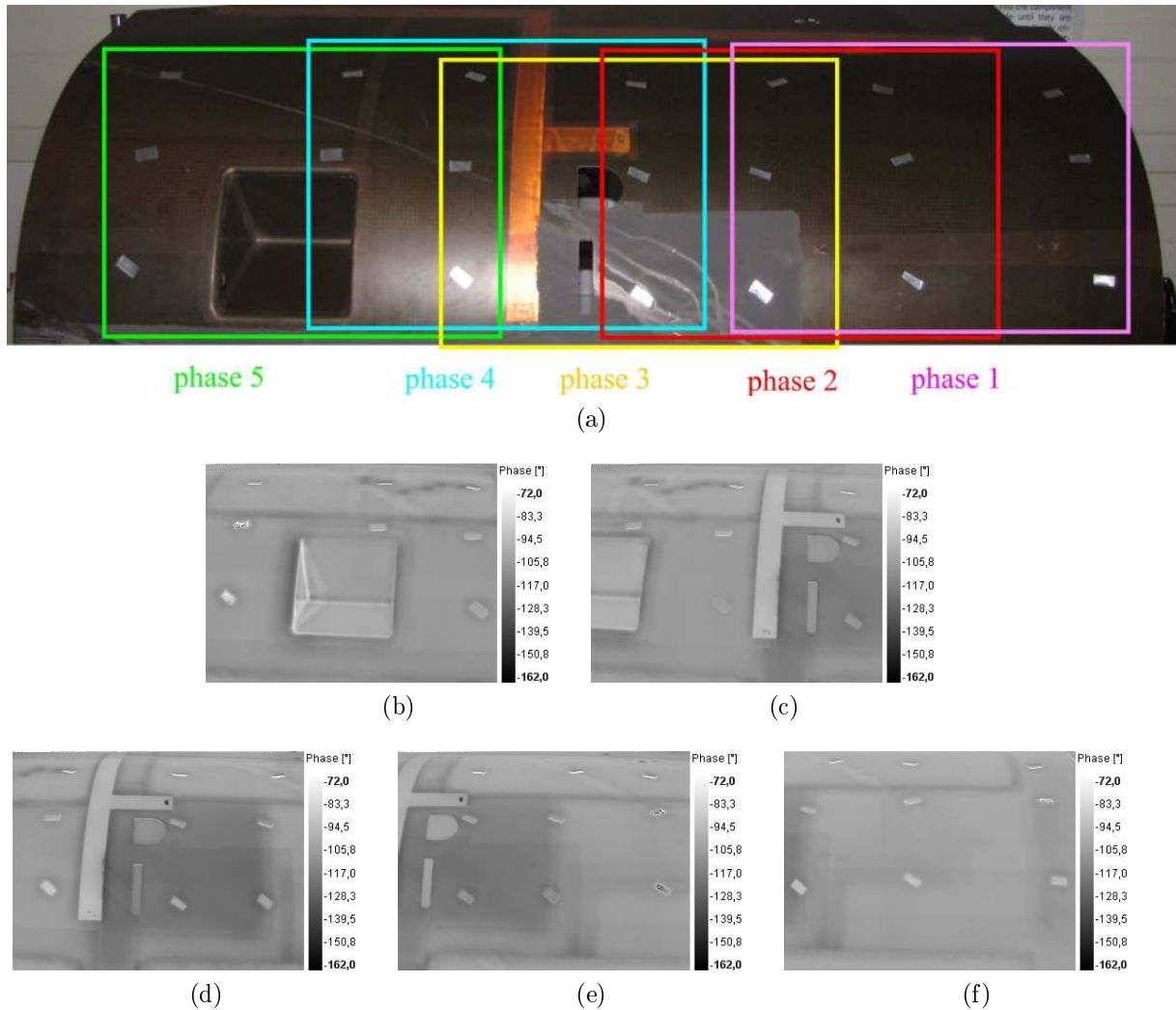
Figure 6.2: (a) The investigated area of the component shown in Fig. 6.1 is divided into five areas. The images (b-f) show the five phase images obtained with OLT at a frequency 0.01 Hz.

6.2 Feature selection

6.2.1 Manual feature selection

The idea first consists of selecting the corners of markers manually in both images to be stitched. For that purpose, Matlab owns a special tool called 'cpselecttool' that allows a user-friendly simultaneous, manual selection of corresponding features in two images (Fig. 6.3).

6.2.2 Automated feature selection

Different automated feature detectors were tested to stitch the phase images together. The polynomial transformation and the RANSAC algorithm (see Chap. 4.1.2) are used. The automated feature detectors Harris, SIFT, and SURF are tested.
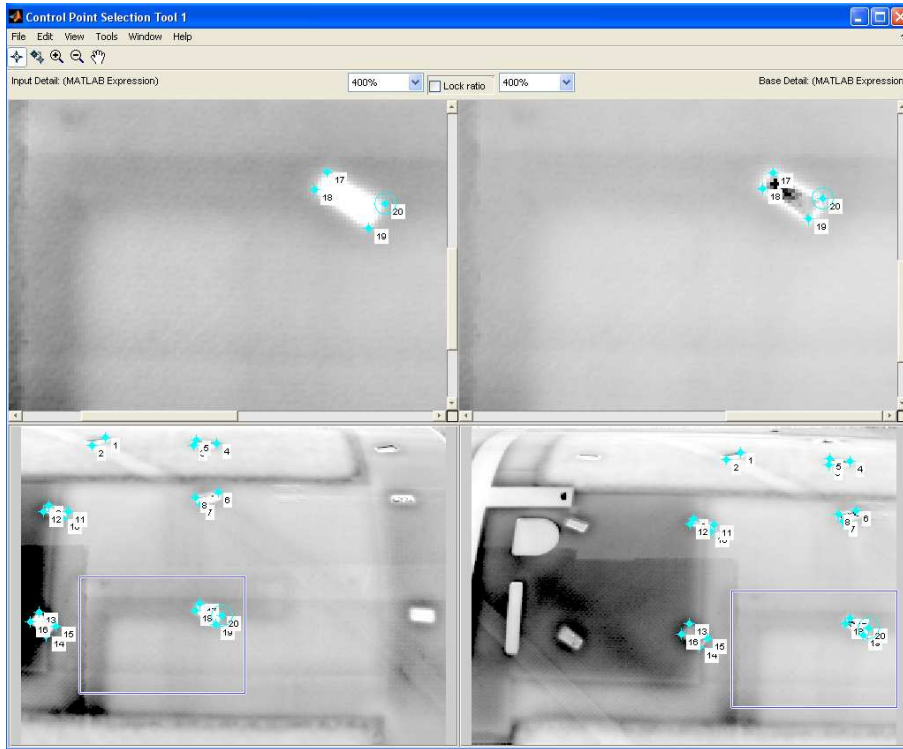
Figure 6.3: Features selected in overlapping images to be matched (phase 4 and 5 at 0.01 Hz).

6.3   Panorama reconstruction

The resulting panoramas for the three feature detectors of phase images 2 and 3 are shown in Fig. 6.4. Fig. 6.5 shows the result of the five matched regions of the large component computed with different feature detection methods. The resulting panoramic images are quite satisfactory, but the left image with the window is not stitched correctly in all cases.

6.4   Comparison of methods

6.4.1   Comparison between projective and polynomial transformations

A comparison between projective and polynomial transformations was performed. Fig. 6.6 shows the difference between both transformations. Fig. 6.6a and Fig. 6.6b show the panoramas obtained with the polynomial transformation whereas Fig. 6.6c and Fig. 6.6d show the result of the panoramas obtained with the projective transformation. For the projective transformation, one can observe that the overlay is quite good but in the lower part of Fig. 6.6c and in the curved region of Fig. 6.6d, the images do not match as good as with the polynomial transformation. Note that the phase images are stitched together without performing a grayscale intensity correction since the phase values are theoretically independent of the illumination parameters.

(a)   (b)

(c)   (d)
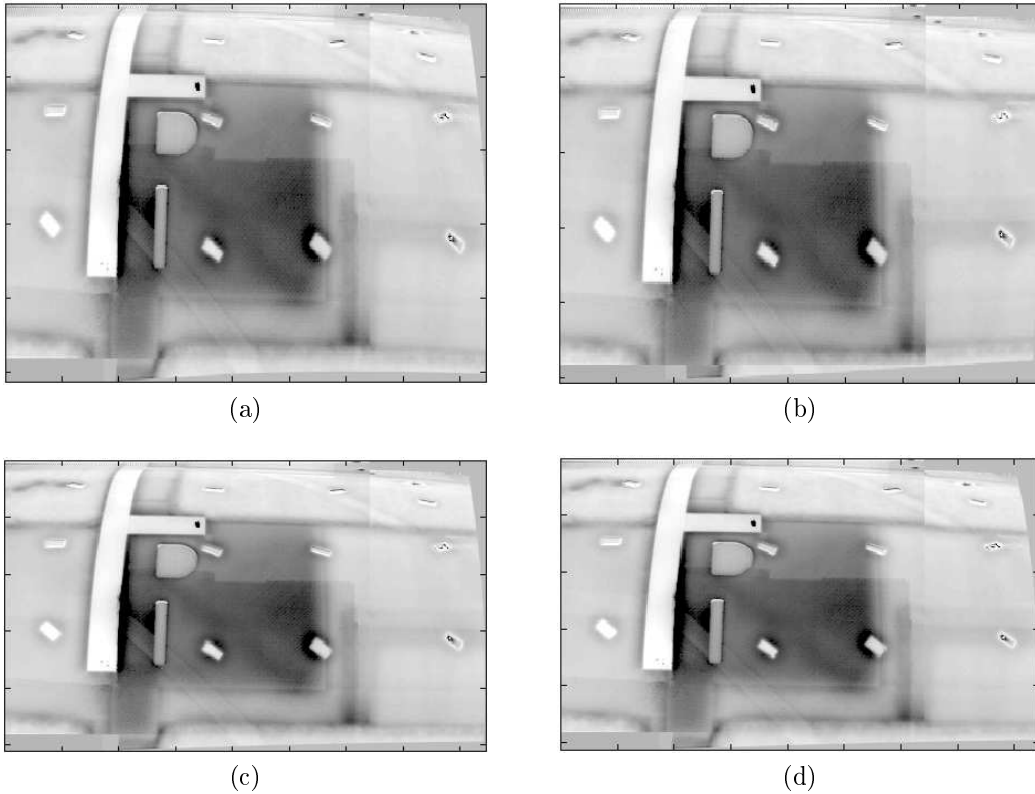
Figure 6.4: Panorama of two neighboring images (phase 2 and phase 3) obtained from (a) manual, (b) Harris, (c) SIFT, and (d) SURF features.

6.4.2   Comparison of feature detector methods

Fig. 6.7 shows the overlaid phase difference images of two measurements taken at two different times with different camera views. In order to compare the methods, the quality of the overlaid phase images (difference images) is compared using a numerical criterion. The difference of both phase images was taken and the mean computed through

$$\frac{\sqrt{\sum x_{ij}^2}}{n \times m}. \tag{6.1}$$

When the images are precisely overlaid, the value should be zero. The values of the four methods are listed in Tab. 6.1.

The manual method leads to the best results. The method SIFT yields the second best result and Harris the worst result. This can be explained by the lack of detected and matched features with this method. A better correlation method should be taken to improve the number of inliers for the computation of the transformation.

In order to evaluate the maximum displacement of the overlaid images, a pattern has been segmented and overlaid. The maximum deviation is found to be 1 pixel, except for the Harris method, where the maximum error is much higher.

Table 6.1: Mean values of the difference phase images.

Methods	Manual	Harris proj.	SIFT	SURF
Phase 1 (10^{-6} rad)	116	474	131	445
Phase 2 (10^{-6} rad)	164	601	256	178
Phase 3 (10^{-6} rad)	137	320	159	202
Phase 4 (10^{-6} rad)	198	557	214	228
Phase 5 (10^{-6} rad)	443	513	688	228

6.5 Conclusion

It can be shown that the stitching of panoramas and the overlay of images of curved surfaces are feasible and work best with polynomial transformation. For a precise overlay, interaction by the user is beneficial. The manual selection of features proved to work best. The algorithm SIFT is the second best working method whereas Harris does not work satisfactorily.

The developed methods allow one to create panoramic images and to overlay long complex shaped components taken from different camera views to perform a precise analysis of potential defect growth. The error is less than one pixel.
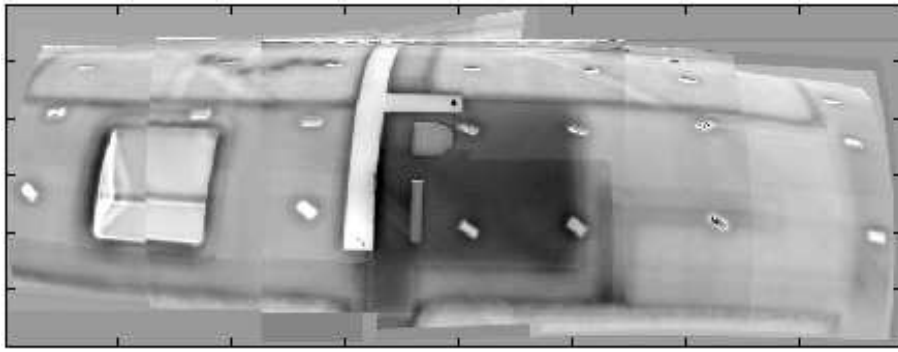
(a)
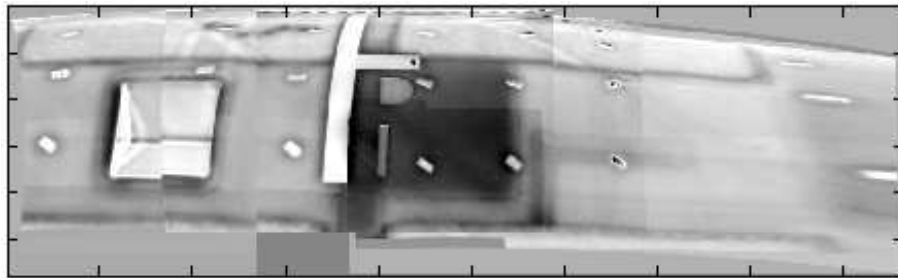
(b)
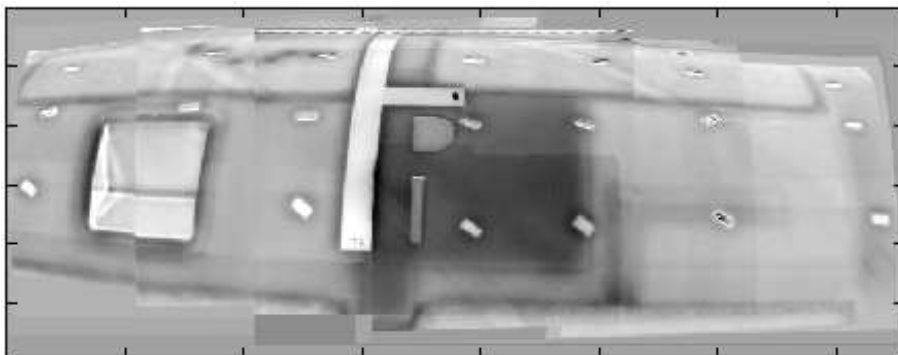
(c)
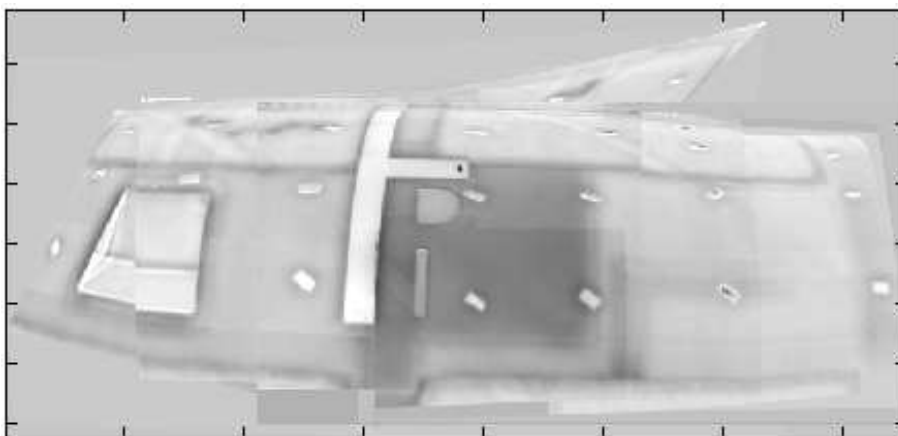
(d))

Figure 6.5: Panorama of five phase images obtained from (a) manual, (b) Harris, (c) SIFT, and (d) SURF features.
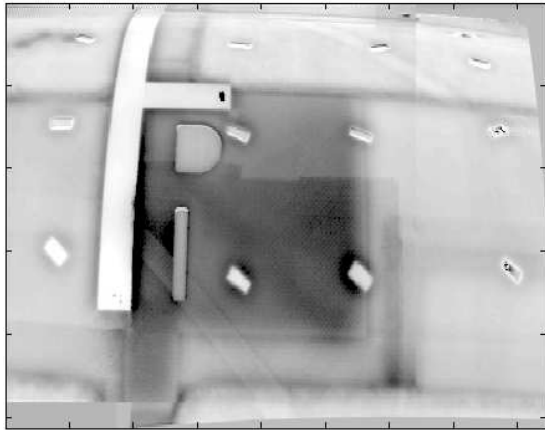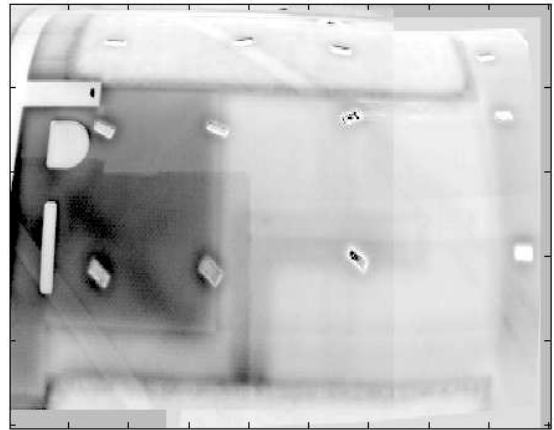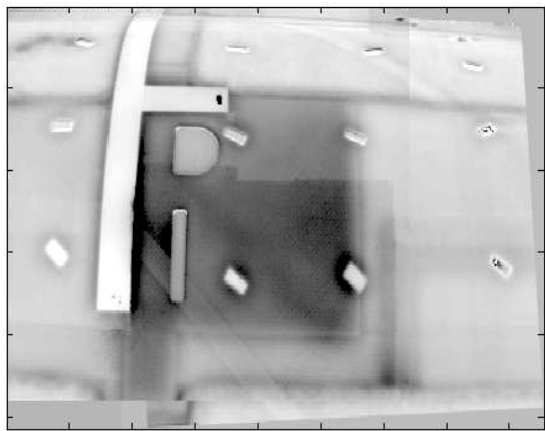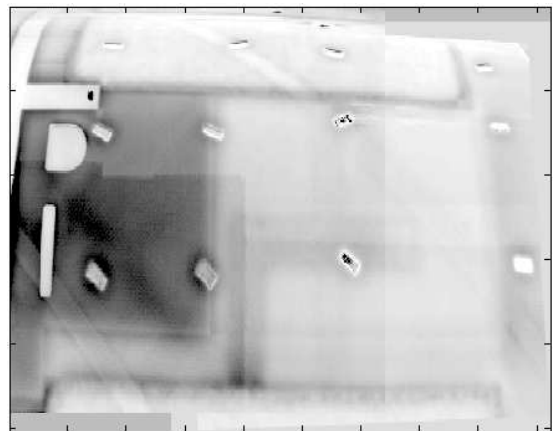
Figure 6.6: Panoramas obtained from (a) phase 2 and 3 with polynomial transformation; (b) phase 1 and 2 with polynomial transformation; (c) phase 2 and 3 with projective transformation and (d) phase 1 and 2 with projective transformation.
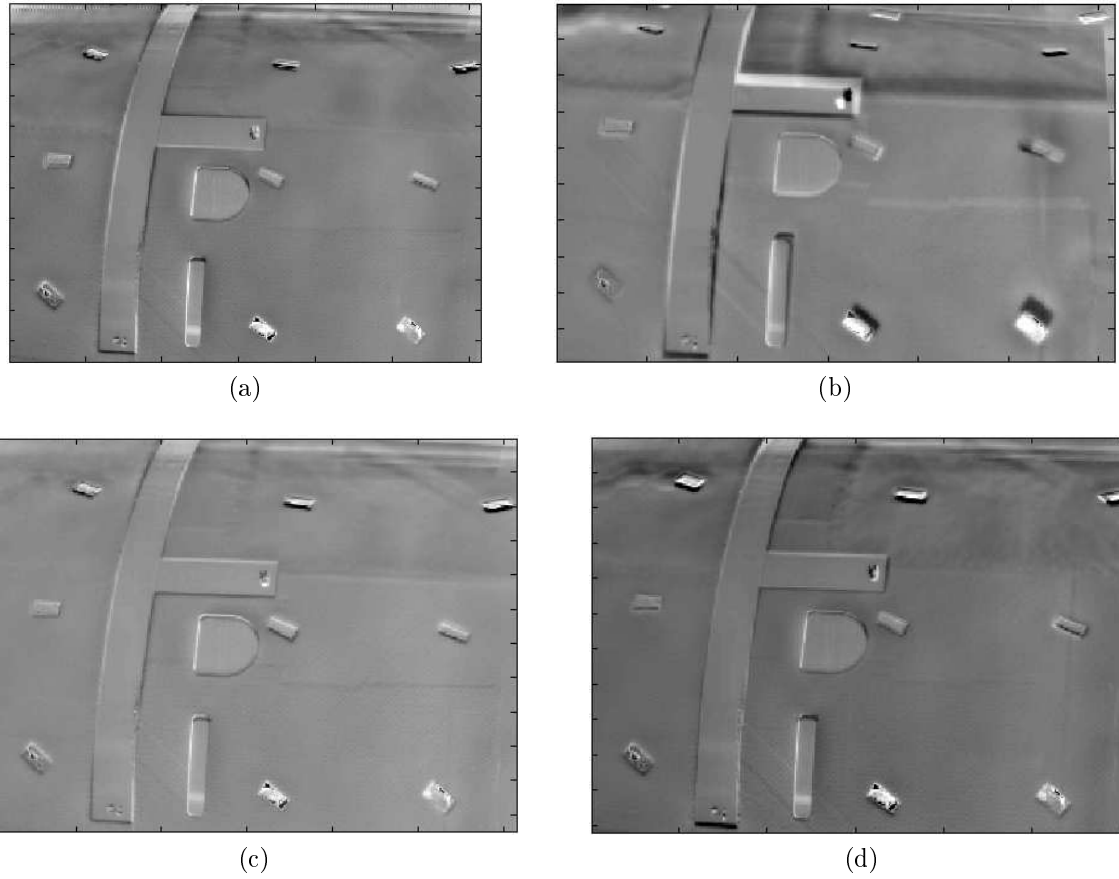
Figure 6.7: Difference of overlaid phase images (here phase 3) shown by using the (a) manual, (b) Harris, (c) SIFT, and (d) SURF feature selection methods.
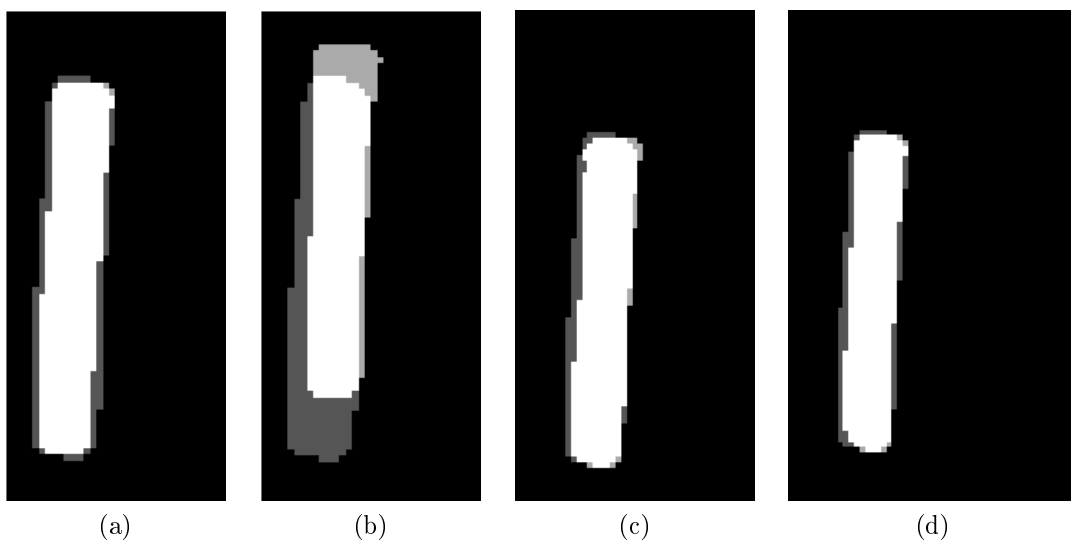
Figure 6.8: Overlay of segmented area by using the (a) manual, (b) Harris, (c) SIFT, and (d) SURF feature selection methods.

Chapter 7

Fusion of thermal images

With data fusion [GLTH00], the defect information of multiple non-destructive evaluation methods is combined so that a deeper insight of the defect area is achieved. Data fusion can be applied to all non-destructive testing (NDT) techniques. In order to exploit the complementary of both thermographic methods optical lockin thermography (OLT) and ultrasound induced thermography (UIT) for the detection of defects in CFRP material, an experiment is conducted to fuse both images. Measurements are simultaneously performed on a CFRP component with delaminations and image data fusion is performed. The thermal images are exported to the Matlab program and processed with the image processing algorithms described in Chap. 4. The images are fused. The defective pixels are segmented in both images and overlaid. It is shown that the common defective area is small. The fused measurements performed on a region of interest of a component are overlaid onto a photo of the whole component taken with a digital camera. This overlay is important to document a test.

7.1 Optical lockin thermography and ultrasound induced thermography: two complementary techniques

UIT and OLT both allow the successful detection of impact damages and in particular of delaminations. The information that is obtained from each method is different: With UIT, it is favorable to detect the borders of delaminations or closed cracks, while OLT allows the detection of the center of the delamination where the composite layers are well-disbonded. The difference is due to the different physical detection mechanism: UIT creates friction at closed cracks, meaning that the borders of a delamination are better highlighted. In OLT, the thermal wave is reflected at thermal boundaries. A high reflection coefficient is needed to detect the defect, meaning that an interface between two different mediums (for example, CFRP-air) is necessary but at the edges where the delamination is nearly closed, most of the wave is transmitted. This explains why the center of the delamination is well detected in OLT, while the border is not. Consequently, both thermographic methods are complementary.

Figure 7.1: Image of the CFRP stiffened panel (a) from the front side (b) from the rear side (Component IV).

7.2 Fusion of thermal images

A CFRP stiffened panel of approximately 1 m x 1.5 m with delaminations is used for the demonstration (Fig. 7.1). The test-piece is provided by Airbus. Damage can be clearly detected. Fig. 7.2 and 7.3 demonstrate the successful detection of delaminations with both techniques. In Fig. 7.3, different images of OLT with different lockin frequencies are shown. The indication of the delamination disappears at a frequency 0.03 Hz, which corresponds to a first-blind frequency, where a first-phase inversion occurs.

The images are segmented by considering regions with an SNR greater than 6 dB as defects (see Chap. 4.2.3). This criterion is applied to the OLT and UIT images obtained in Component IV.
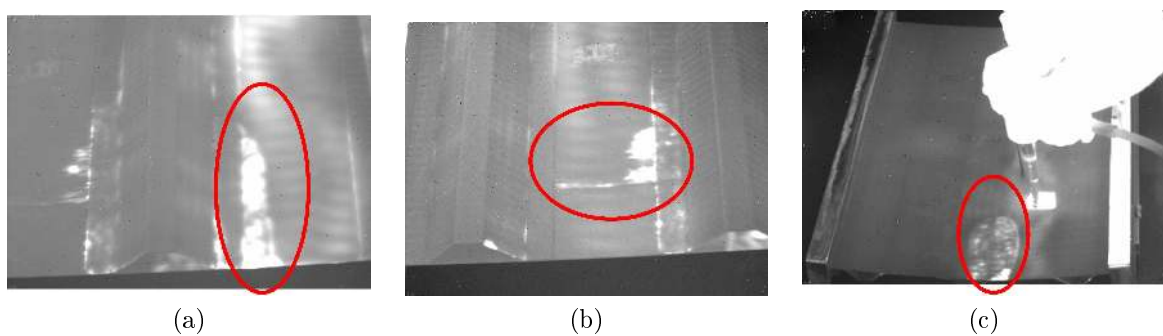
Figure 7.2: Different delaminations detection with UIT.

7.3 Results

In a first step, the images are rectified in order to be superimposed. The images were taken with different camera positions so that a superposition can only occur after this calibration step. The labels are detected using a semi-automated ellipse detection algorithm. The

(a)   (b)   (c)
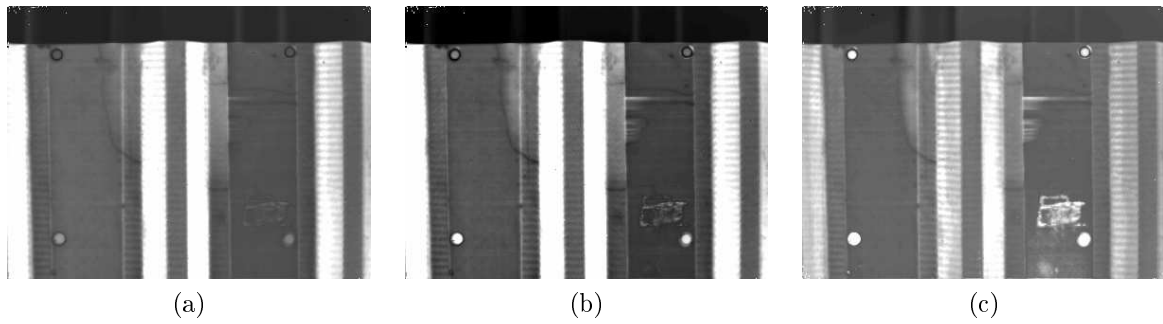
Figure 7.3: : Lockin thermography phase images with different excitation frequencies (a) 0.03 Hz (b) 0.06 Hz, and (c) 0.1 Hz.

(a)   (b)
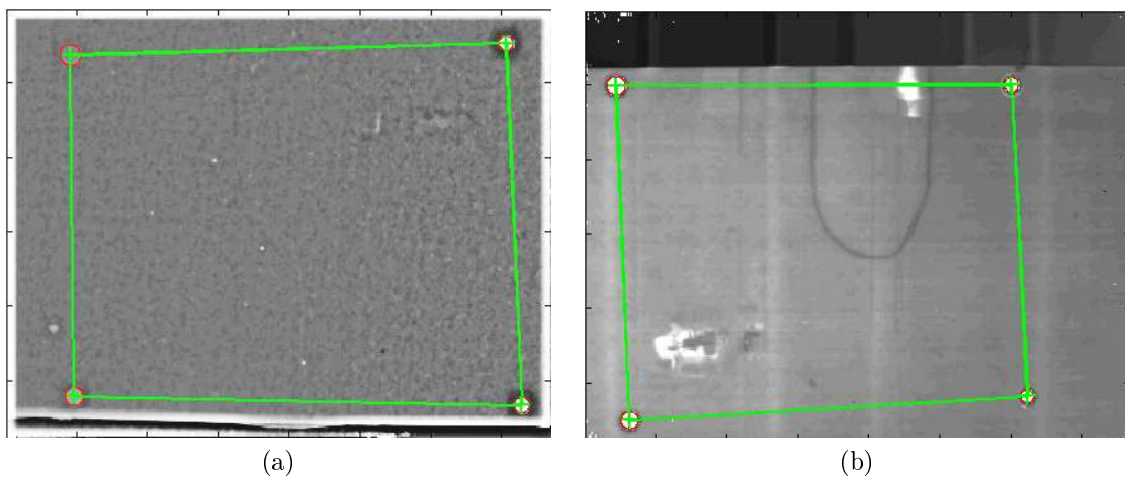
Figure 7.4: Detection of labels in the images using the ellipse detection algorithm (a) UIT (b) OLT.

user selects the raw positions of the labels and the algorithm computes precise sub-pixel positions of the labels. Fig. 7.4 shows the resulting correctly detected ellipses. A scale is introduced in the images of Fig. 7.5 after the distance between the labels is measured. This step allows quantitative analysis. Fig. 7.6 shows the superposition of both images. The visibility of the defect is improved.

For quantitative analysis of the defect area, the UIT and OLT images are segmented to extract only the defect area (Chap. 4.2.3). These areas are overlaid and compared (Fig. 7.7). For the segmentation, only the area of interest situated between the labels was analyzed. It should be noted that the defect area seen with UIT is larger than that with OLT. The red region in Fig. 7.8, which represents the common defect region, is quite small. This might be explained by the complementary defect information provided by the UIT and OLT techniques. Also, many noisy areas are detected in UIT images due to the appearance of steady wave patterns. For better visualization, the defect area can also be overlaid on a live image taken with a classic digital camera (Fig. 7.8).

In conclusion, it can be said that the combination of images of several NDT techniques through data fusion improves the detection of the defect areas. The characterization of the defect size becomes more reliable.

(a)   (b)
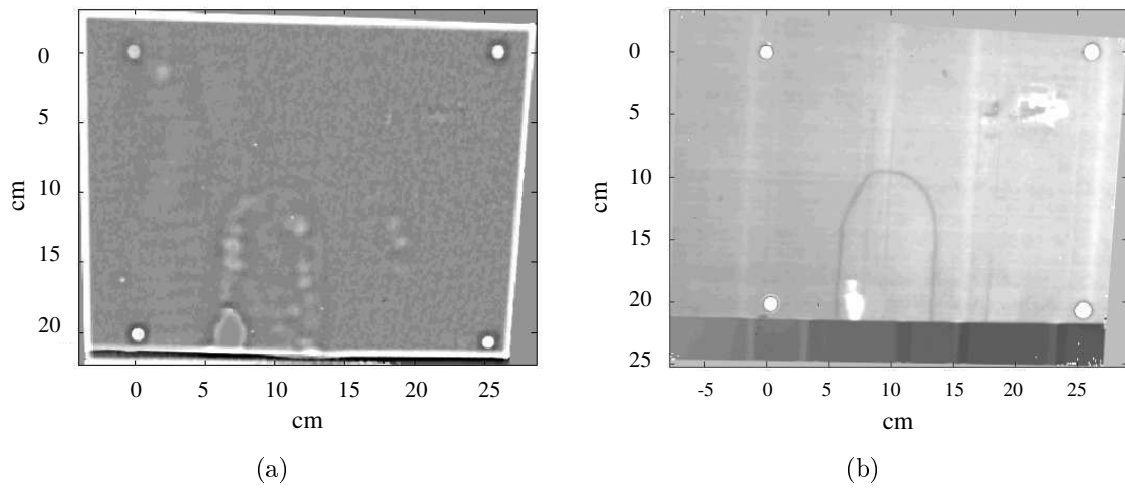
Figure 7.5: Rectified images with photogrammetry and introduction of scales in the images.
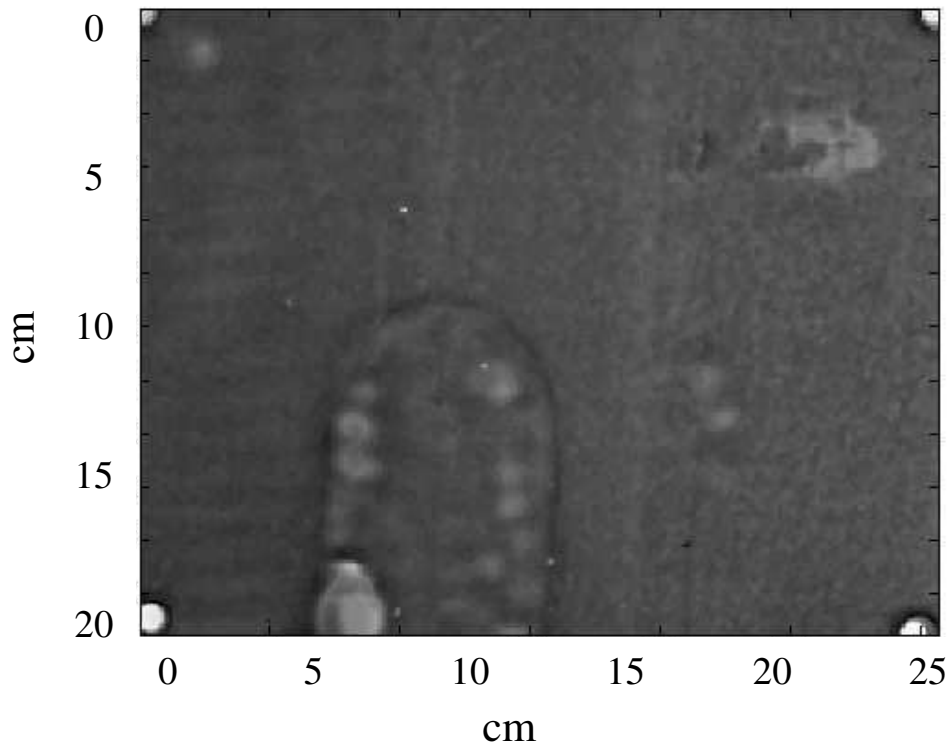

Figure 7.6: Fusion of images with OLT and IUT techniques.
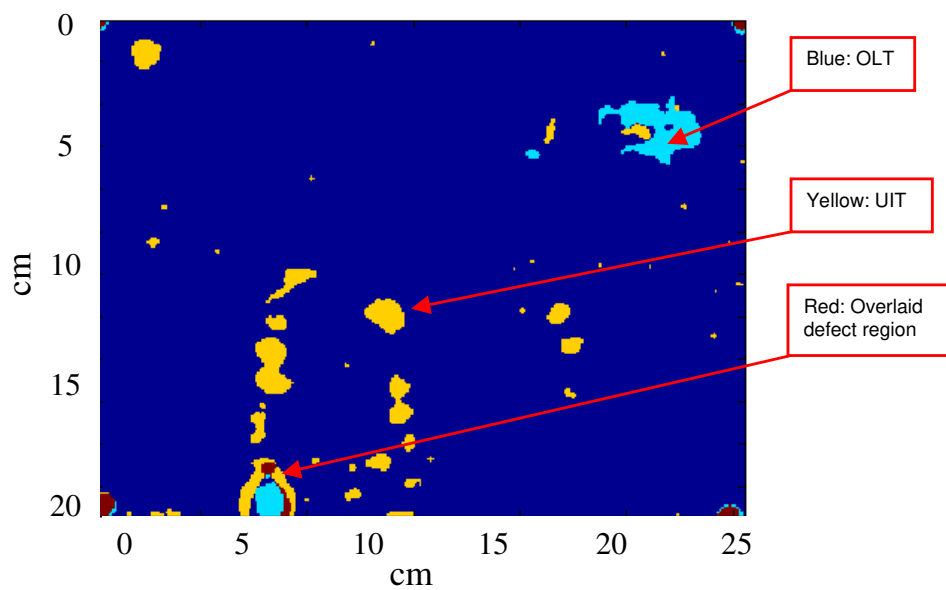
Figure 7.7: Overlay of segmented UIT and OLT images. The colored areas represent the defect region: blue being from the segmented OLT image, yellow being from the segmented UIT data, and red being the defect area detected in UIT and OLT.
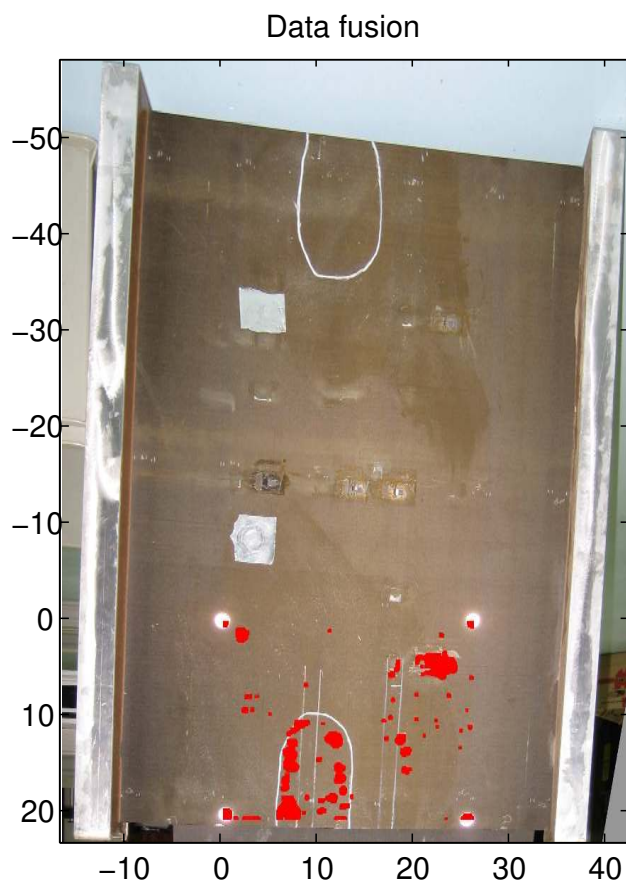

Figure 7.8: Representation of the defect area on a rectified live image taken with a digital camera.

Summary and outlook

This thesis helps to answers questions on the quantitative evaluation of defect parameters from thermal images to get information on defect sizes and depth automatically. It deals with the measurement and computational processing of thermal images obtained using optical lockin thermography (OLT). The thesis concentrates on non-destructive testing (NDT) of carbon-fiber reinforced plastics (CFRP) material with the OLT technique. It has been shown that the exact position of defects can be determined on flat or curved components through the developed overlaying techniques. Images of several imaging techniques can be overlaid. With OLT, it can be shown that the depth and size of defects can be determined precisely. These parameters need to be taken into account for simulations of fatigue and load tests in CFRP components for qualification purposes and for determining the investigation intervals of the components following the damage tolerance principle. Through this information, the simulations can be done with trustful defect models.

CFRP specimens with blind holes that simulate delamination defects were manufactured for the quantitative testing of measurement and analysis procedures. The goal of the thesis is the extension and the enhancement of quantitative thermography with image processing methods. Matlab was utilized as a computational environment. The developed algorithms are formulated as Matlab scripts. One major intention was the extraction of improved quantitative information; namely the size and the depth of potential defects. In the theoretical part of this thesis thermal diffusion is discussed based on the heat transfer equation. Penetration depth for thermal waves in CFPR material is derived. The reflection of thermal waves on defect borders is discussed. The phase and amplitude image formation, as shown in previous works, can be modeled through a convolution between a shape function and a complex point-spread function (PSF). The complex PSF for lockin thermographic images has been re-derived using Green's functions. The phase contrast represents the difference between a defective and a defect-free area. It is shown that the thermal phase contrast can be computed through the defect shape function and the imaginary part of the complex point-spread function.

Measurements of test specimens with lockin frequencies in the range of 0.005 to 0.3 Hz were performed. The comparison of measurements with the theoretical derived simulations are in good agreement. The phase contrast response has a typical form: a maximum is reached at a frequency f_0 called optimal frequency. At higher frequencies, the phase contrast assumes a zero value and a phase inversion occurs. The frequency f_b at which a defect indication disappears is called blind frequency. Another blind frequency is present at lower frequencies but up to 0.005 Hz it can only be observed for defects at a maximum depth of 1.5 mm in CFRP material. Additionally, the phase contrast response depends on the lockin frequency, the defect depth, and the defect size. It is clearly demonstrated that the theoretical phase contrast takes into account all these parameters. Here the effect of

the defect size was ignored for the retrieval of the defect depth, but the defect parameters can be retrieved with an accuracy of 3 to 58 % depending on the defect depth and size. A set of algorithms was combined for the quantitative extraction of size and depth of planar defects based on the measurement of phase contrast images. The algorithms were applied on test specimens and on an aircraft part. The algorithmic chain starts with the rectification of the images. After the estimation of the signal-to-noise ratio (SNR), boundary defective areas are recognized on pixel basis and clustered in each phase image. Defect depth information is retrieved with the estimation of the first blind frequency or alternatively with a fit of the theoretical phase contrast response to the measurements. Based on the depth information the theoretical PSF was calculated. It is shown, that phase images measured with an optimal lockin frequency of $f_o + \frac{f_b - f_o}{4}$ concur best with the defect shape after deconvolution. The defect sizes are evaluated with the full-width half-maximum (FHWM) criterion.
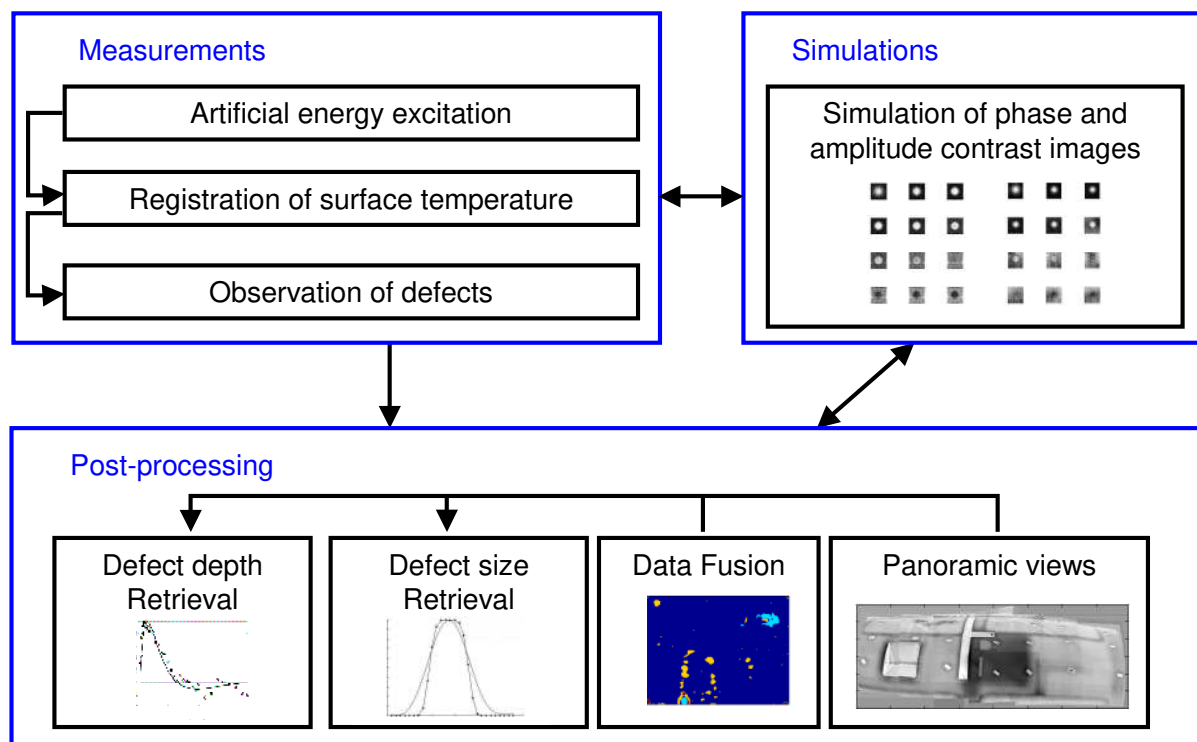
Figure 7.9: Overview of the developed post-processing methods and the realized simulations.

In order to quantitatively compare potential defect growth, for example before and after a fatigue test, methods are developed to overlay and match images of large and curved components since the measurements are taken under slightly different aspect angles. Therefore, aluminum markers are fixed on the components so that features can be selected manually or detected automatically in the images. Due to these features, a polynomial transformation between both images to be matched can be computed. For the automated reconstruction of panoramas, it has been shown that the features detection algorithm SIFT worked best.

Optical thermography is particularly adapted to detect the center of delaminations while the borders of delaminations are not detected with this technique. In contrast, ultrasound

induced thermography (UIT) detects cracks or borders of delaminations better. In order to use the complementary information of both techniques, the phase and thermal images are fused. By overlaying the segmented images, the common region appears, as expected, small. Fusion of NDT data improves the analysis of defects and the evaluation of the defect size.

It has been shown that the use of markers allows the introduction of scales to thermographic image data and in combination with newly developed deconvolution techniques a significantly improved estimation of defect sizes is realized. Furthermore it is demonstrated that the use of markers allows, despite the low-contrast nature of thermographic OLT images, the fabrication and generation of extended panoramas. The data fusion of images obtained with different thermographic methods, namely OLT and UIT, was also enabled by the use of markers.

The full exploitation of the information contained in the phase images measured with a set of excitation frequencies allows improved determination of defect depths. The summary of the contribution of this thesis in words of quantitative analysis of defects is schematized in Fig. 7.9.

Thermography is a method that is used mostly during research and development to qualify components. It is used during in-service inspections as a complementary method to analyse the extent of impact damage detected through visual inspection. The standard techniques during quality control are visual inspection, tap testing and ultrasound testing. However, thermography may be used in the near future specifically for investigating defects on critical component regions. On the helicopter structure, the defects are divided in several classes depending on the severity of the defect for the structure strength. At some locations, the presence of a defect is more critical for the system than on any other location.

In practice, with OLT, several lockin frequencies are used for performing tests on components to be sure to have one frequency different than the blind frequency to detect a defect. The automated determination of the defect depth is very useful in knowing the optimal frequency at which the defect size should be evaluated. On large helicopters especially, where many images of components have to be taken, this helps the inspector greatly to analyze huge quantities of data.

Finally, thermography allows seeing directly into a structure, a method which is not common in daily life. It is therefore not always easy for the user to understand what can be seen. In practice, the experience of a user is very important. Usually, defects are recognized by comparing the detected structures with known classes of defects from previous tests. With thermography, one can see more things than through visual inspection, but the most important thing always is to correctly classify these defects.

Through the developed overlaying techniques, it would be very interesting in future to use OLT during static or dynamic fatigue tests to observe the growth of cracks. Although OLT is not suitable for performing online measurements during a dynamic test due to the long registration times compared to load cycle time, it has great potential to be used for tests having break time between the loads or the static tests. OLT will certainly allow to improve the knowledge on the cause of the defects and their evolution.

Bibliography

[BA97] D.S.C. Biggs and M. Andrews. Acceleration of iterative image restoration algorithms. *Appl. Opt.*, 36:1766–1775, 1997.

[BA06] O. Breitenstein and F. Altmann. Inversion of microscopic lock-in thermograms in the presence of emissivity contrast. *NDT&E International*, 39:636–640, 2006.

[BCHSL92] J.V. Beck, K.D Cole, A. Haji-Sheikh, and B. Litkouhi. *Heat conduction using Green's functions*. Series in computational and physical processes in mechanics and thermal sciences, Hemisphere, London, UK, 1992.

[Ben75] J.-L. Bentley. Multidimensional binary search trees used for associative searching. *Comm. of the ACM, New York, USA*, 18:509 – 517, 1975.

[BGM$^+$07] A. Bub, S. Gondrom, M. Maisl, N. Uhlmann, and W. Arnold. Image blur in flat-panel detector due to compton scattering at its internal mountings. *Meas. Sci. Technol.*, 18:1270–1277, 2007.

[BL03a] O. Breitenstein and M. Langenkamp. *Lock-in thermography*. Springer Verlag Berlin Heidelberg, 2003.

[BL03b] O. Breitenstein and M. Langenkamp. *Lock-in thermography - basics and applications to functional diagnostics of electronic components*. Springer Verlag, Berlin, D, 2003.

[BL07] M. Brown and D. G. Lowe. Automatic panoramic image stitching using invariant features. *Int. J. of Computer Vision (Springer Ed.)*, 74:59–73, 2007.

[BLB$^+$08] D. Balageas, P. Levesque, P. Brunet, C. Cluzel, A. Déom, and L. Blanchard. Thermography as a routine diagnostic for mechanical testing of composites. *Quantitative Infrared Thermography*, 1:45–68, 2008.

[BP82] C. A. Jr. Bennett and R. R. Patty. Thermal wave interferometry: A potential application of the photoacoustic effect. *Appl. Opt.*, 21:49–54, 1982.

[BTVG06] H. Bay, T. Tuytelaars, and L. Van Gool. Surf: Speeded up robust features. *9th IEEE European Conference on Computer Vision, Graz , Austria, Leonardis, Bischof, Pinz, Springer Verlag, Berlin and New York*, 3954:404–417, 2006.

[Bus79] G. Busse. Optoacoustic phase angle measurement for probing a metal. *Appl. Phys. Lett.*, 35:759–760, 1979.

[Bus84] G. Busse. *Rasterbildverfahren mit optisch erzeugten Wärmewellen in der zer-störungsfreien Werkstoffprüfung.* Habilitationsschrift, Universität Stuttgart, 1984.

[BW01] W. Bai and B.S. Wong. Evaluation of defects in composite plates under convective environments using lock-in thermography. *Meas. Sci. Technol.*, 12:142–150, 2001.

[BWK92] G. Busse, D. Wu, and W. Karpen. Thermal wave imaging with phase sensitive modulated thermography. *J. Appl. Phys.*, 71:3962–3965, April 15 1992.

[Can86] J. Canny. A computational approach to edge detection. *IEEE Trans. Pattern Anal. Mach. Intell.*, 8:679–714, 1986.

[CFKT93] D.J. Crowther, L.D. Favro, P.K. Kuo, and R.L. Thomas. Inverse scattering algorithm applied to infrared thermal wave images. *J. Appl. Phys.*, 74:5828–5834, 1993.

[CJ46] H.S. Carlslaw and J.C. Jaeger. *Conduction of heat in solids.* Oxford Clarendon Press, UK, 1946.

[CKP⁺08] M. Choi, K. Kang, J. Park, W. Kim, and K. Kim. Quantitative determination of a subsurface defect of reference specimen by lock-in infrared thermography. *NDT&E international*, 41:119–124, 2008.

[CT65] J.W. Cooley and J.W. Tukey. An algorithm for the machine calculation of complex fourier series. *Math. Comp.*, 19:297–301, 1965.

[DZ08] A. Dillenz and G. Zenzinger. State of the art in thermal imaging. *International Symposium on NDT in Aerospace 2008, Fürth, Germany, DGZfP BB 114*, 2008.

[FB81] M. A. Fischler and R. C. Bolles. Random sample consensus: A paradigm for model fitting with applications to image analysis and automated cartography. *Comm. of the ACM, ACM (Ed.), New York, NY, USA*, 24:381–395, 1981.

[FHSW92] K. Friedrich, K. Haupt, U. Seidel, and H. G. Walther. Definition, resolution and contrast in photothermal imaging. *J. Appl. Phys.*, 72:3759–3764, 1992.

[FKvKJ06] O. Focke, M. Kalms, C. v. Kopylow, and W. Jueptner. Ndt of free formed cfrp composites with laser ultrasonic. In *12th A-PCNDT 2006, Auckland, New Zealand,*, 2006.

[FLSU01] J. Filsinger, T. Lorenz, F. Stadler, and S. Utecht. Method and device for producing fiber-reinforced components using an injection method. *European Patent EP1181149*, 2001.

[FPF99] A. Fitzgibbon, M. Pilu, and R. B. Fisher. Direct least square fitting of ellipses. *IEEE Trans. Pattern Anal. Mach. Intell.*, 5:476–480, 1999.

[GLTH00] X .E. Gros, Z. Liu, K. Tsukada, and K. Hanasaki. Experimenting with pixel level ndt data fusion techniques. *IEEE Trans. on Instr. and Meas.*, 49(5):1083–1090, 2000.

[Hex05] HexcelCorporation. *Hexcel Datasheet "Prepreg technology"*. No. FGU 017b, http://www.hexcel.com/, hexcel corporation edition, March 2005.

[Hom07] Christian Homma. *Untersuchungen zu Mechanismus und technischer Umsetzung der akustischen Thermographie*. PhD thesis, Saarbrücken, 2007.

[HS88] C. Harris and M. Stephens. A combined corner and edge detector. *Proc. of The 4th Alvey Vision Conference, M. M. Matthews, University of Manchester, UK*, pages 147–151, 1988.

[HW97] M. Hemmleb and A. Wiedemann. Digital rectification and generation of orthoimages in architectural photogrammetry. *International Archives of Photogrammetry and Remote Sensing*, 32:261–267, 1997.

[IC05] C. Ibarra-Castanedo. *Quantitative subsurface defect evaluation by pulsed phase thermography: Depth retrieval with the phase*. PhD thesis, Université Laval, Québec, 2005.

[ICGM04] C. Ibarra-Castanedo, D. González, and X. Maldague. Automatic algorithm for quantitative pulsed phase thermography calculations. In *CD of Proceedings 16th WCNDT - World Conference on Nondestructive Testing,*, 2004.

[ICM04] C. Ibarra-Castanedo and X. Maldague. Defect depth retrieval from pulsed phase thermographic data on plexiglas and aluminum samples. *Proc. SPIE - The International Society for Optical Engineering, Thermosense XXVI*, 5405:348–355, 2004.

[Lab] U.S. Air Force Research Laboratory. *Handbook of damage tolerant design*. Online Handbook.

[Lin98] T. Lindeberg. Detection with automatic scale selection. *Int. J. of Computer Vision (Springer Ed.)*, 30 (2):79–116, 1998.

[LJT+81] A. Lehto, J. Jaarinen, T. Tiusanen, M. Jokinen, and M. Luukkala. Amplitude and phase in thermal wave imaging. *Electr. Lett.*, 17:364–365, 1981.

[LKGH04] W. Li, J. Krehl, J.W. Gillespie, and D. Heider. Process and performance evaluation of the vacuum-assisted process. *J. Comp. Mat.*, 38 (20):1803–1814, 2004.

[LL67] L. Landau and E. Lifchitz. *Théorie de l'élasticité*. Ed. Mir, Moscou, 1967.

[LN07] S. Lugin and U. Netzelmann. A defect shape reconstruction algorithm for pulsed thermography. *NDT&E International*, 40:220–228, 2007.

[Low99] David G. Lowe. Object recognition from local scale-invariant features. *IEEE International Conference on Computer Vision, Corfu, Greece, September 1999*, pages 1150–1157, 1999.

[Luc74] L.B. Lucy. An iterative technique for the rectification of observed distributions. *Astron. J.*, 79:745–754, 1974.

[Luh03] T. Luhmann. *Nahbereichsphotogrammetrie: Grundlagen, Methoden und Anwendung*. Wichmann, 2003.

[LVV03] A. Likas, N. Vlassis, and J.J. Verbeek. The global k-means clustering algorithm. *Pattern Recognition*, 36:451–461, 2003.

[Mac67] J. B. MacQueen. Some methods for classification and analysis of multivariate observations. *Proc. of 5-th Berkeley Symposium on Mathematical Statistics and Probability, Berkeley, University of California Press,*, 1:281–297, 1967.

[Mal01] X. P.V. Maldague. *Theory and practice of infrared technology for nondestructive testing*. Wiley-Interscience, 2001.

[Man01] A. Mandelis. *Diffusion-wave fields-mathematical methods and Green functions*. 2001.

[Mau92] G.A. Maugin. *The thermomechanics of plasticity and fracture*. Cambridge University Press, USA, 1992.

[MKP90] X. Maldague, J-C. Krapez, and D. Poussart. Thermographic nondestructive evaluation (nde): An algorithm for automatic defect extraction in infrared images. *IEEE Trans. on Sys. Man and Cyb. SMC*, 20 No 3:722–725, 1990.

[MM96] X. Maldague and S. Marinetti. Pulse phase infrared thermography. *J. Appl. Phys.*, 79(5):2694–2698, 1996.

[MPT06] R. Mulaveesala, P. Pal, and S. Tuli. Interface study of bonded wafers by digitized linear frequency modulated thermal wave imaging. *Sensors and Actuators A: Physical*, 128:209–216, 2006.

[MR85] J.M. Milne and W.N. Reynolds. The non-destructive evaluation of composites and other materials by thermal pulse video thermography. *SPIE Proceedings, Andronicos G. Kantsios (Ed.). Bellingham Society for Photo-Optical Instrumentation Engineers*, 520:119–122, 1985.

[MS01] K. Mikolajczyk and C. Schmid. Indexing based on scale invariant interest points. *8th IEEE International Conference on Computer Vision (ICCV 2001), Vancouver, Canada*, 1:525–531, 2001.

[MT05] R. Mulaveesala and S. Tuli. Implementation of frequency modulated thermal wave imaging for non destructive sub-surface defect detection. *Insight-Non-destructive Testibg and Condition Monitoring*, 47:206–208, 2005.

[MWBR04] C. Maiershofer, H. Wiggenhauser, A. Brink, and M. Röllig. Quantitative numerical analysis of transient ir-experiments on buildings. *Infrared Physics & Technology*, 46:173–180, 2004.

[NK79] P. E. Nordal and S. O. Kanstad. Photothermal radiometry. *Phys. Scr.*, 20:659–662, 1979.

[NK80]   P. E. Nordal and S. O. Kanstad. Photothermal radiometry for spatial mapping of spectral and material properties. In E. A. ASH, editor, *Scanned image microscopy*, pages 331–339. London: academic Press, 1980.

[OHS05]   M. Omar, M. Hassan, and K. Saito. Optimizing thermography depth probing with dynamic thermal point spread function. *Infrared Physics & Technology*, 46:506–514, 2005.

[OHSA05] M. Omar, M.I. Hassan, K. Saito, and R. Alloo. Ir self-referencing thermography for detection. *Infrared Physics & Technology*, 46:283–289, 2005.

[PA08]   S. Pickering and D. Almond. Matched excitation energy comparison of the pulse and lock-in thermography nde techniques. *NDT&E International*, 41:501–509, 2008.

[Rei97]   M. Reigl. *Methoden zur Quantifizierung photothermischer Signale*. PhD thesis, University Ulm, 1997.

[Ric72]   W.H. Richardson. Bayesian-based iterative method of image restoration. *J.Opt. Soc. Am.*, 62(1):55, 1972.

[SH+95]   U. Seidel, K. Haupt, , H. G. Walther, J.A. Burt, and M. Munidasa. An attempt towards quantitative photothermal microscopy. *J. Appl. Phys.*, 78(3):2050–2056, 1995.

[SH06]   U. Schnars and R. Heinrich. Application of ndt methods on composite structures in aerospace industry. *Conference on damage in composite material 2006, NDT.net, R. Diederichs (Ed.)*, 12, 2006.

[She97]   S. M. Shepard. Introduction to active thermography for non-destructive evaluation. *Anti corrosion Methods and Materials*, 44:236–239, 1997.

[She01]   S. M. Shepard. Advances in pulsed thermography. *A.E. Rozlosnik, R.B. Dinwiddie ed.: Thermosense XXIII, Proc. SPIE (Society of Photo-Optical Instrumentation Engineers)*, 4360:511–515, 2001.

[SHZW06] O. Salvado, C. Hillenbrand, S. Zhang, and D.L. Wilson. Method to correct intensity inhomogeneity in mr images for atherosclerosis characterization. *IEEE Trans. on Med. Imag.*, 25:539–552, 2006.

[SLW+97] U. Seidel, T. T. N. Lan, H. G. Walther, B. Schmitz, J. Geerkens, and G. Goch. Quantitative characterization of material inhomogeneities by thermal waves. *Opt. Eng.*, 36 (2):376–390, 1997.

[SM00]   J. Shi and J. Malik. Normalized cuts and image segmentation. *IEEE Trans. Pattern Anal. Mach. Intell.*, 28(8):888–905, 2000.

[ST94]   J. Shi and C. Tomasi. Good features to track. *IEEE Conference on Computer Vision and Pattern Recognition CVPR94*, 1994.

[Sto04]   R. Stoessel. *Air-coupled ultrasound inspection as a new non-destructive testing tool for quality assurance*. PhD thesis, University Stuttgart, 2004.

[SWB94] U. Seidel, H. G. Walther, and J. A. Burt. A proposal for the reconstruction of buried defects from photothermal images. *Journal de Physique IV*, C7:C7–551–C7–554, 1994.

[Sze04] R. Szeliski. Image alignment and stitching: A tutorial. Technical report, Microsoft Research, 2004.

[TFCK92] R. L. Thomas, L. D. Favro, D. J. Crowther, and P. K. Kuo. Inversion of thermal wave infrared images. In *Proceedings of the Eurotherm Seminar n° 27, Quantitative infrared thermography QIRT 92, D. Balageas, G.Busse and G.M. Carlomagno (Ed.)*, 1992.

[TPW$^+$79] R. L. Thomas, J. J. Pouch, Y. H. Wong, L. D. Favro, Kuo P. K., and A. Rosencwaig. Subsurface flaw detection in metals by photoacoustic microscopy. *J. Appl. Phys.*, 51:1152–1156, 1979.

[Vav04] V. Vavilov. Evaluating the efficiency of data processing algorithms in transient thermal ndt. *Thermosense XXVI, Proceedings of SPIE*, 5405:336–347, 2004.

[VIN84] M. Vaez Iravani and M. Nikoonahad. Transform techniques for analysis of thermal wave propagation in anisotropic composite materials. *J. Nondestr. Ev.*, 4:3/4, 1984.

[WSRL07] J. Welter, S. Sathish, E. Ripberger, and E. Lindgren. Detection of localized heat damage in a polymer matrix composite by a thermoelastic technique. *Mat. Eval.*, 65(8):823–826, 2007.

[Wu96] D. Wu. *Lockin-Thermographie für die zerstörungsfreie Werkstoffprüfung und Werkstoffcharakterisierung.* PhD thesis, Fakultät Verfahrenstechnik der Universität Stuttgart, November 1996.

[WWJ07] C. Wallbrink, S.A. Wade, and R. Jones. The effect of size on the quantitative estimation of defect depth in steel structures using lock-in thermography. *J. Appl. Phys.*, 101:104907–104907–8, 2007.

[ZDRB03] T. Zweschper, A. Dillenz, Scherling D. Riegert, G., and G. Busse. Ultrasound excited thermography using frequency modulated elastic waves. *Insight*, 45(3):178–182, 2003.

[ZRDB03] T. Zweschper, G. Riegert, A. Dillenz, and G. Busse. Ultrasound burst phase thermography for applications in the automotive industry. *D.O. Thompson and D.E. Chimenti (Eds.): Review of Progress in Quantitative Nondestructive Evaluation*, 22:531–536, 2003.

Acknowledgments

I would like to particularly thank Prof. Arnold and Prof. Berveiller who allowed me to take part at the German-French graduate college on material science and to carry out my thesis in a bilingual context jointly between the Saarland University and the University Paul Verlaine Metz (cotutelle-de-thèse). Thanks to their commitment to and belief in French-German cooperation, I was able to participate at summer schools and undertake research stays at the French university. This allowed me to come into contact with two different university systems and to see the differences between German and French research. To be in contact with both cultures was particularly important for me since I grew up at the German-French border with exposure to both cultures.

The cooperation was made possible through the help and grant of the French-German university (université franco-allemande / deutsch-französische Hochschule). I am very grateful to the DFH-UFA[1] for their support of this thesis.

My thanks go to the referees Prof. Fournier and Prof. Walther for their fast and detailed reports.

Particular thanks go to Dr. Arning who accepted me into his department at EADS Innovation Works. I chose EADS for my interest in the aerospace industry and the fact that it is mainly a French and German company, similar my background. I thank Dr. Langmeier who supervised my PhD thesis. His advice and ideas helped me a lot towards completing my thesis. I also thank Dr. Stoessel who agreed to supervise my work on thermographic and non-destructive testing purposes. Thanks to him, I learnt a lot on thermography and carbon-fiber reinforced plastics material.

My thanks go to every one at EADS Innovation Works, Airbus, Eurocopter and MAS who provided the test components and contributed to the realization of the thesis. I thank Mr. Hauf and Mr. Oster for allowing me to use the equipment at Eurocopter for measurements during the thesis and for giving me the opportunity to continue my work on 'thermographic panoramas of large curved aircraft components' at Eurocopter.

Last but not least, my thanks go to my fiancé Daniel Maximilian Hoffmann for his advice, support and care during the period of my thesis. Thanks to my parents and my family for encouraging me all along my studies and supporting my travels between Munich, Saarbrücken and Metz and stays at Saarbrücken and Metz.

---

[1] www.dfh-ufa.org

Appendix A

From radiometry to lockin thermography

Harmonic thermal waves were utilized for the first time by Angström in order to determine the thermal diffusivity α of a material. The temperature was modulated with a frequency f at one end of a metallic bar and the phase difference ϕ of the propagating thermal wave was measured by two thermometers separated by a distance Δx. Fig. 7.10 illustrates the set-up of the experiment conducted by Angström. The phase shift is given by

$$\phi = \Delta x / \mu \tag{7.1}$$

and the thermal diffusivity can be calculated with

$$\mu = \sqrt{\frac{\alpha}{\pi f}}. \tag{7.2}$$
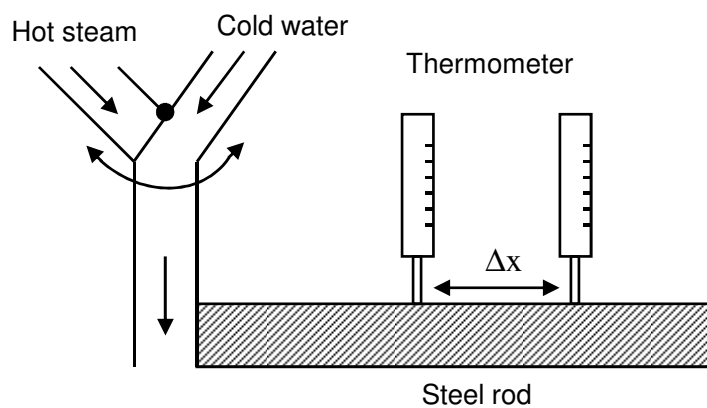
Figure 7.10: Experiment of Angström

In the 1960s and 1970s there were many experiments concerning the use of thermal waves (see for example [Bus84, Bus79]) and technology developments. One of them was described in the article of Nordal and Kanstad in 1978 [NK79, NK80]. They created a raster imaging system. This was the precursor to lockin thermography. Fig. 7.11a shows the principle of their set-up. A laser source, rather than halogen lamps, excited the part point-by-point. The light was modulated by the electric power supply. The temperature was measured by an infrared detector. In order to get the amplitude and phase images, a lock-in amplifier was used. This electronic device can extract a signal with a known carrier wave in a very noisy environment (up to SNR = -60 dB).
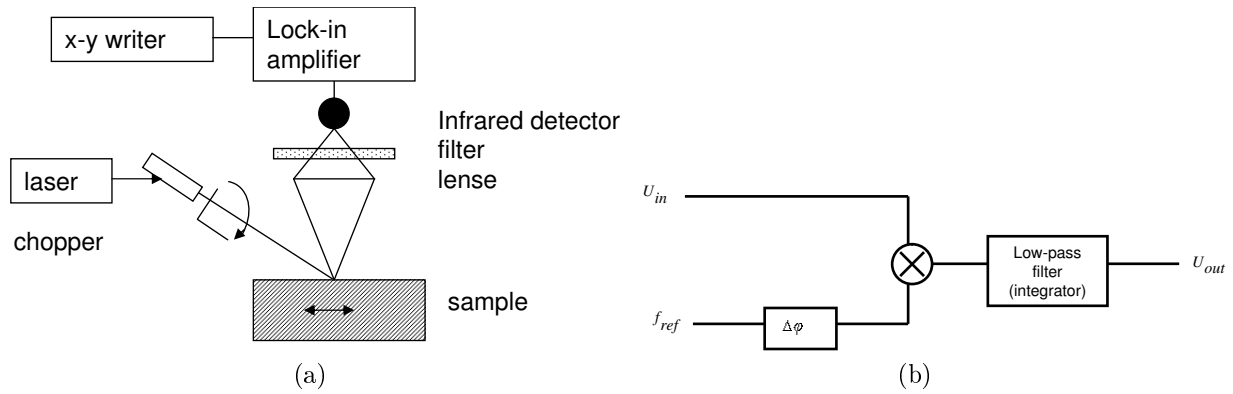
Figure 7.11: (a) Raster imaging system; (b) Principle of the lock-in amplifier.

The principle of a lock-in amplifier is the following: The input signal is integrated by the use of a low-pass filter. The role of the low-pass filter can be explained by a correlation where the measured signal is multiplied with a sinus function and integrated in the following way

$$U_{out} = \frac{1}{T} \int_{t-T}^{t} \sin \left[2\pi \cdot f_{ref} \cdot s + \Delta\varphi \right] U_{in}(s) ds. \tag{7.3}$$

The correlation of two signals (Eq. 7.3) that have different modulation frequencies equals zero, due to the fact that sinusoidal functions are orthogonal. This property is used to precisely measure the frequency of the input carrier function. When the frequency matches the input signal, the measurement is said to be "locked" to the reference signal. Then, the phase difference between reference and measurement is determined using a phase slider. The output signal of the correlation is proportional to the amplitude and to the cosine of the phase difference. It is at a maximum when the phase difference equals zero, showing that the correct phase shift between measurement and reference signal is obtained. With the amplifier, the phase and amplitude information is computed for one point. In order to obtain it for the whole surface, the part is scanned by either moving the laser source or the part.

The lock-in amplifier used in photothermal imaging to compute amplitude and phase images lends its name to the classic lockin thermography.

Appendix B

Pulse-phased thermography

In pulsed thermography (PT)[She01, MR85], a short heat pulse is generated in the material surface. The registration time is very short. The time sequence of each pixel is additionally Fourier transformed in pulse phased thermography (PPT), [MM96]. By performing the Fourier transform, a phasegram containing phase images at several frequencies is obtained.

The drawback of PT and PPT is that the energy of the signal is distributed amongst the frequencies and is low at high frequencies. The spectrum of the photothermal signal is represented in Fig. 7.13. The Fourier transform of a rectangular function $rect_a(t)$ is a sinus cardinal function $\frac{sin(\pi x)}{\pi x}$. The flash light should contain large amount of energy. The signal-to-noise ratio of phase images is high at low frequencies and no signal is presented at frequencies $f_i = n \cdot \pi$, where n is an integer. A good overview of the link between pulse-phase thermography and lockin thermography is given in [IC05].
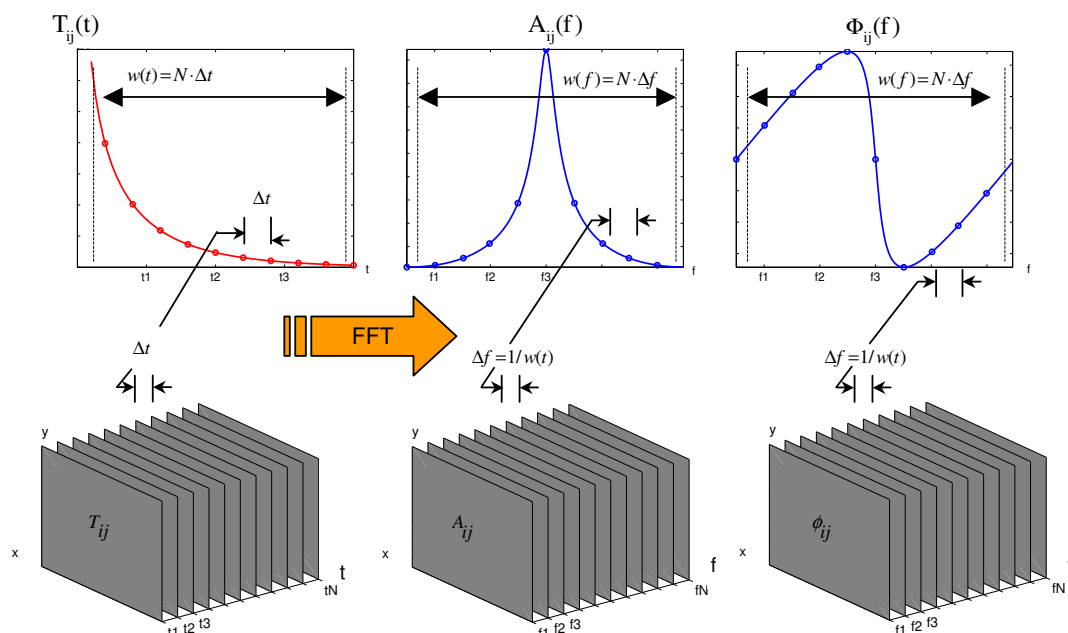
Figure 7.12: Computation of amplitude and phase images for PPT. (Left): Plot of the surface temperature against time (middle): Amplitude as a function of frequency (right): Phase function with respect to the frequency.

In the field of quantitative evaluation, previous work to detect defect depth was mostly
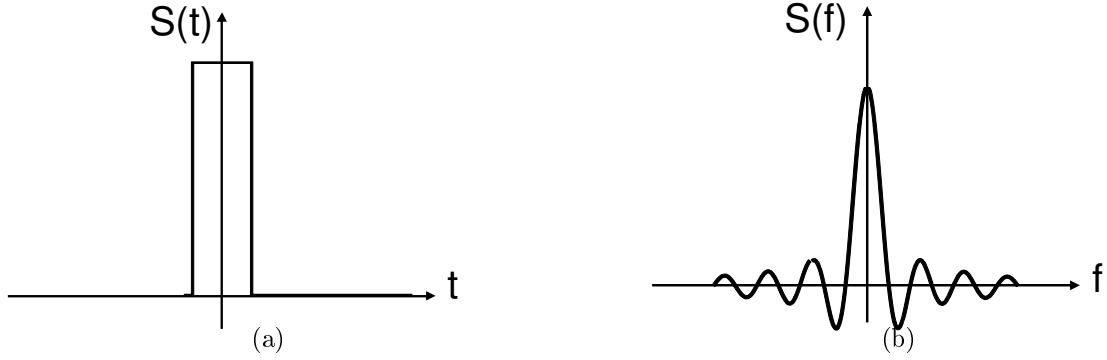
Figure 7.13: (a) Representation of a rectangle pulse excitation and (b) corresponding Fourier-transform.

performed with pulsed thermography on isotropic materials (for example, on steel or aluminum). The methods of quantitative evaluation with PT can be sorted into the methods that use the pulse series and that perform a transformation before getting quantitative parameters.

To improve correct defect detection with PT, different methods to compute thermal contrasts (i.e. the difference between a defective and non-defective area) were proposed [Mal01]. The thermal contrast C is defined by

$$C = I - I_{intact}, \tag{7.4}$$

where I is the thermal intensity of a point and I_{intact} is the thermal intensity of an intact defect-free area.

Problems include difficulty in finding an intact area and results that are affected by non-uniform heating. The differential absolute contrast (DAC),

$$C_{DAC}(i,j,t) = \Delta T(i,j,t) - \sqrt{\frac{t'}{t}} \Delta T(i,j,t'), \tag{7.5}$$

leads to an improved SNR and defect detection.

The defect depth is computed from the thermal sequence. In [MWBR04], the point of the maximal temperature contrast is taken as a criterion. A calibration curve, representing the time of maximal contrast with respect to the depth is obtained from simulations, allowing the correct depth and shape of defects to be found. Another method consists of taking the time point at which the defect becomes just visible (so-called early detection [Mal01]). The equation of heat diffusion allows the retrieval of the defect depth.

In [LN07], another method is reported where the defect is simulated and compared to the measurement. Following an iterative approach, the defect profile can, in this way, be retrieved. Approaches on the numeric simulation of the calibration of thermographic methods in isotropic materials were developed [LN07]. Finally, Shepard [She01] proposed a method, called thermographic signal reconstruction (TSR). It is a polynomial fit to each pixel with time. The temperature function with time on the surface of a component heated through a pulse is given by

$$\Delta T = \frac{Q}{e\sqrt{\pi t}}. \tag{7.6}$$

114

Taking the logarithm of Eq. 7.6, this leads to

$$\ln \Delta T = \ln \frac{Q}{e} - \frac{1}{2} \ln(\pi t). \tag{7.7}$$

Consequently, the logarithm of the temperature can be fitted by a function,

$$\ln[\Delta T(t)] = a_0 + a_1 \ln(t) + a_2 \ln^2(t) + ... + a_n \ln^n(t). \tag{7.8}$$

The time history of each pixel is replaced by a low order series using a least-square fit. The advantages are that TSR allows data and noise reduction for storing volumetric thermographic sequences. An overview of evaluating thermal sequences and especially the used image processing techniques is given in [Vav04]. Amongst others, neural networks, principal component analysis and the wavelet transform were tested in order to process the time sequences.

Many related works also exist in the field of pulsed-phased thermography. Similarly, the so-called blind frequency (i.e. the frequency at which the defect indication becomes visible, see Chap. 2.5.1) is determined. A correlation between the depth and the blind frequency enables the determination of the depth. The task lies in finding an accurate method to determine the blind frequency.

In [ICGM04], the blind frequency was determined by estimating the curve slope of the phase values that become a line in the higher frequency range. The high frequencies are taken for the estimation and the lowest frequency is decreased until the slope diverges from the non-defective slope. The lowest frequency corresponds to the blind frequency.

In [ICM04], the estimation of the blind frequency occurred when the thermal phase contrast (meaning the difference between the defective and non-defective area) became less than a given threshold, depending on the noise amplitude.

In [BLB+08] it is shown how quantitative thermography can be improved for defect evaluation during mechanical load testing on composite material. Active and passive thermography were used.

Frequency modulated lockin thermography

A good alternative to lockin thermography was presented in [MT05, MPT06]. Frequency modulated lockin thermography (FMLT) consists of frequency modulating the excitation signal and combining the advantage of lockin and pulsed thermography. The advantage of the FMLT registration technique is that the spectrum is a square, and thus, the energy is equally distributed in all excitation frequencies. Consequently, the amplitude and phase images should have a better quality than phase images obtained from PPT. Then, the registration time is faster than that of lockin thermography.

During the course of the thesis, FMLT measurements were carried out as well to compare the obtained images with OLT measurements. A frequency modulated signal can be represented by

$$x(t) = a(t)sin(\theta(t)), \qquad 0 \le t \le t_D \tag{7.9}$$

where $a(t)$ is the envelope of the modulated signal, which equals zeros outside the interval $[0, t_D]$ and $\Theta(t)$ is the phase of the modulated signal. The instantaneous frequency $f_m(t)$

is computed by way of

$$f_m(t) = \frac{1}{2\pi} \frac{d\theta}{dt}. \qquad (7.10)$$

With a linear modulation, $f_m(t)$ is a linear function of the time.

(a)   (b)
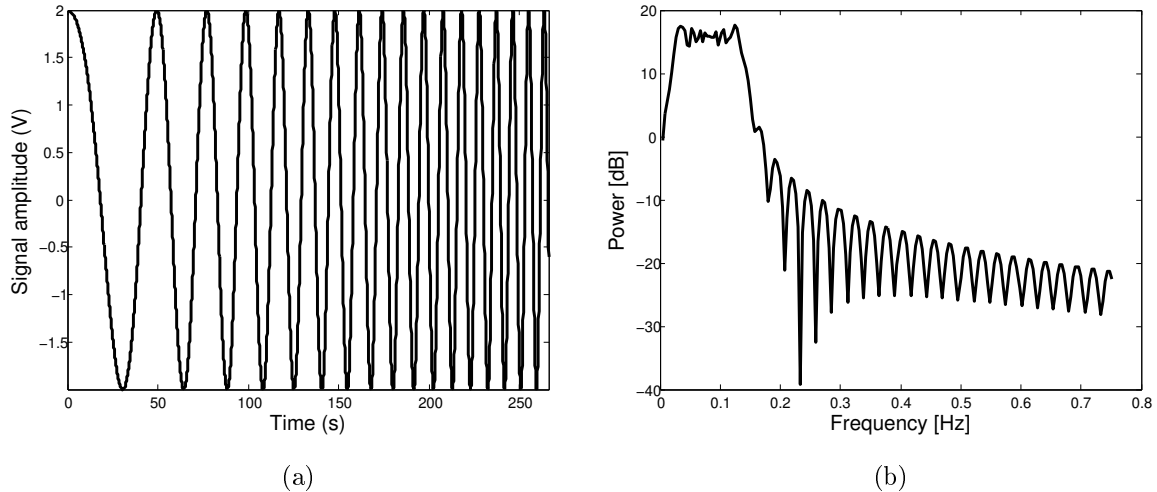
Figure 7.14: (a) Frequency modulated signal: frequencies vary between 0.01 and 0.12 Hz with a sampling frequency of 13.2 Hz and (b) its Fourier power spectrum.

The optimal sampling frequency and registration time were found via simulation. For evaluating frequencies between 0.01 and 0.12 Hz, the highest frequency of 0.12 Hz defines the minimum sampling frequency of 0.24 Hz. Simulations showed that a measuring period of at least 5 min is necessary.

In Fig. 7.14, the frequency modulated signal and its Fourier transform are plotted. The Fourier transform is not a perfect square since the observation is performed within a finite observation window. The perfect square is convoluted with a sinus cardinal function.

A test performed on a test-part of CFRP material is schematically represented in Fig. 7.15. The part contains several holes situated at different depths and of different diameters. For the measurements, a signal generator of the Agilent company is utilized. The lamps are modulated with a linear frequency sweep from 0.01 Hz to 0.12 Hz. A total of 3550 images with a sampling frequency of 13.2 Hz are recorded with the Thermosensorik set-up (see Chap. 5.1). The phase images are calculated with FFT and are shown in Fig. 7.16. As a comparison, the images obtained with optical lockin thermography at different frequencies are represented in Fig. 7.17. The defects detected with FMLT at 0.075 Hz and with OLT at 0.02 Hz are the same. The quality of images is lower with FMLT than with those of lockin thermography.

Ultrasound induced thermography

Ultrasound induced thermography is a method where ultrasound waves are injected into the material. Dissipative energy loss occurs inside the material in two ways ([LL67], [Mau92]):

- first, an intrinsic irreversible effect due inelastic ultrasonic absorption [Hom07].

116
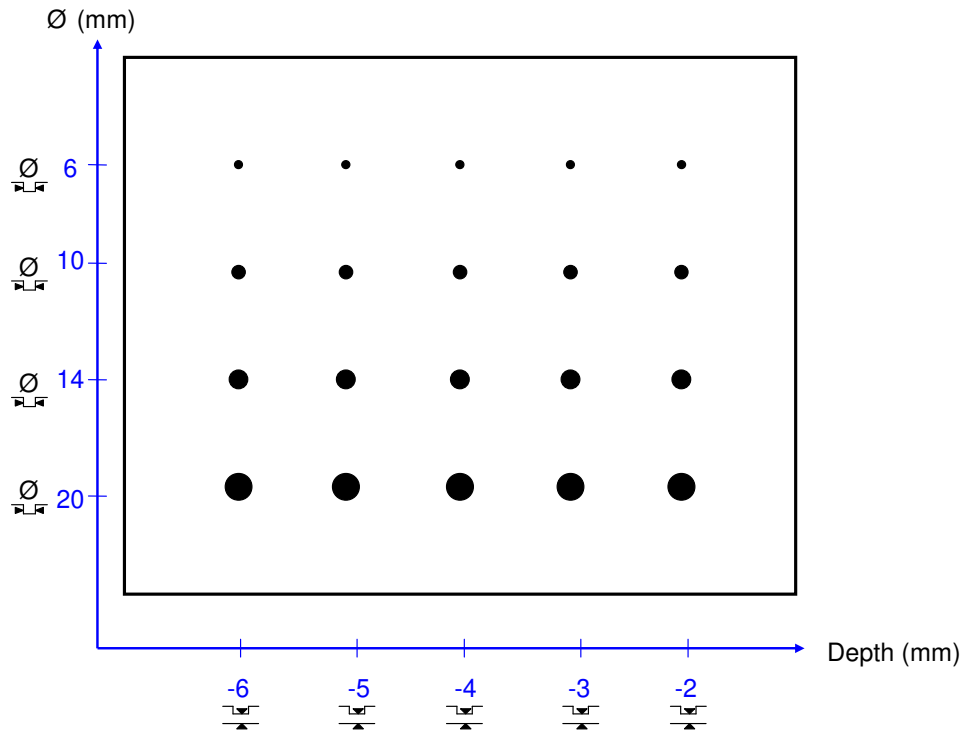
Figure 7.15: Scheme of the CFRP test-part with blind holes.

(a)   (b)   (c)
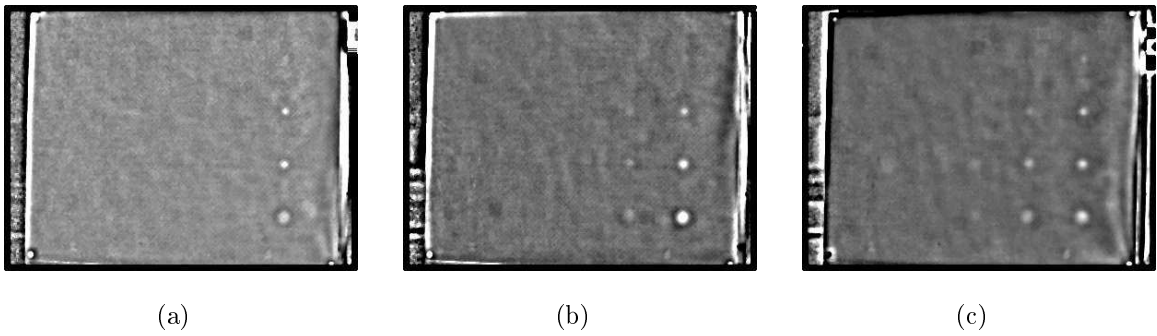
Figure 7.16: Phase images obtained of the test-part with FMLT at frequencies (a) 0.075 Hz (b) 0.041 Hz (c) 0.026 Hz.
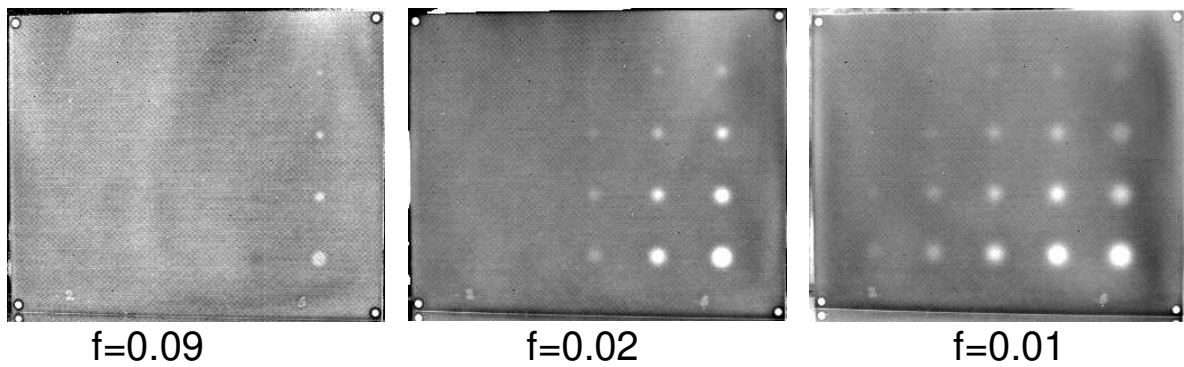
Figure 7.17: Obtained phase images with OLT.

- second, irreversible energy losses occur due to local friction at defects like closed cracks, dislocations, grain boundaries etc.

The principle of UIT is schematized in Fig. 7.18. After the elastic waves are injected, the generated heat propagates to the surface and an infrared camera is used to visualize the temperature distribution. The second type of energy losses is higher than the first one, causing the temperature at the component's surface to appear higher if defects are present within the thermal penetration length given by the ultrasonic frequency. In Fig. 7.19, an example of the detection of impact damage in composite component of honeycomb-carbon fibers is demonstrated.
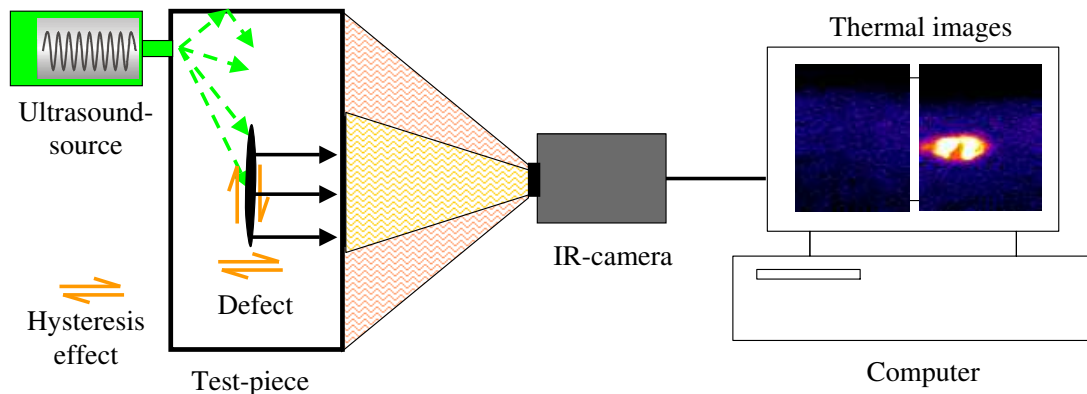
Figure 7.18: Principle of ultrasound induced thermography.

The use of UIT for the successful detection of damage in epoxy-carbon composite material has been demonstrated in many studies. For example, in [WSRL07], the heat-damage created through a quartz-lamp was successfully detected with UIT, which the authors called 'thermoelastic technique'.
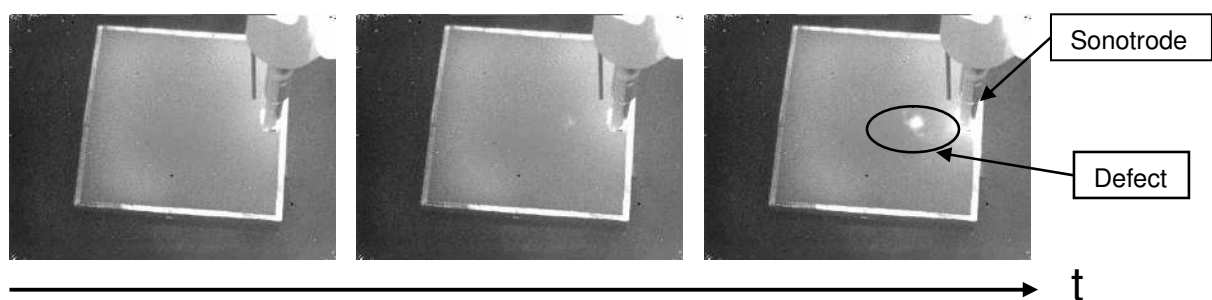
Figure 7.19: Detection of impact damage in a composite part with ultrasound induced pulsed thermography (UIT at times 0, 0.22 and 0.93 seconds after the start of ultrasound).

A limitation of the method is that, if using a single frequency, standing wave patterns may appear. Fig. 7.20 shows such a standing wave effect in UIT images of stiffened panels. The effect might also appear in small parts. The ultrasound waves are reflected between the two boundaries and standing waves are generated. By overlaying ultrasound frequencies or by using a frequency sweep [ZDRB03, ZRDB03], this phenomenon can be avoided.
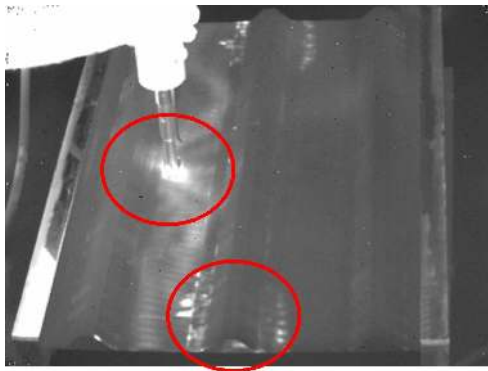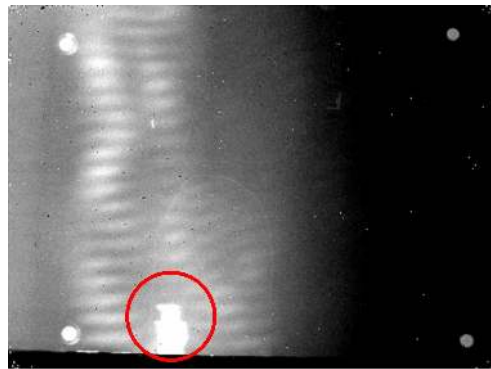
(a)   (b)

Figure 7.20: Detection of delaminations with UIT in a CFRP panel (a) on the rear side
and (b) on the front side with appearance of static waves patterns.

Appendix C: résumé en français

Analyse quantitative de défauts dans des pièces en matériau composite par la méthode de thermographie lockin

Plan

- Introduction
- Les matériaux composites renforcés en fibres de carbone
- Thermographie lockin
- Modèle théorique
- Résultats
- Comparaison des défauts
- Fusion de données
- Conclusion

Introduction

Dans le secteur de l'aéronautique, il est important de pouvoir détecter des défauts enfouis dans les structures et de les caractériser. Les méthodes classiques utilisées dans le domaine du contôle non-destructif sont les ultrasons et la tomographie aux rayons X assistée par ordinateurs. Cependant, la thermographie infrarouge connaît un intérêt grandissant pour les applications en aéronautique car elle permet de détecter des défauts sans contact et d'effectuer des mesures in-situ sur l'avion.

Jusqu'à présent, les méthodes thermographiques ne permettent qu'une détection et une analyse qualitative des défauts. Il est nécessaire de pouvoir caractériser quantitativement les défauts afin de retrouver leur taille et leur position.

Le but de ce travail de thèse est d'élaborer un procédé permettant de déterminer la taille des défauts (inclusions) dans des pièces en matériaux composites à base de fibres de carbone ainsi que de déterminer leur profondeur à partir de la thermographie lockin.
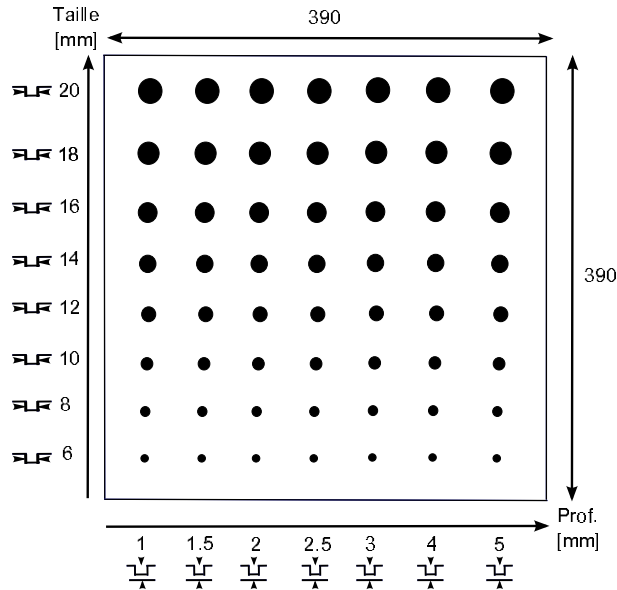
Figure 7.21: Schéma de la plaque I avec des défauts circulaires. Les dimensions sont données en mm.
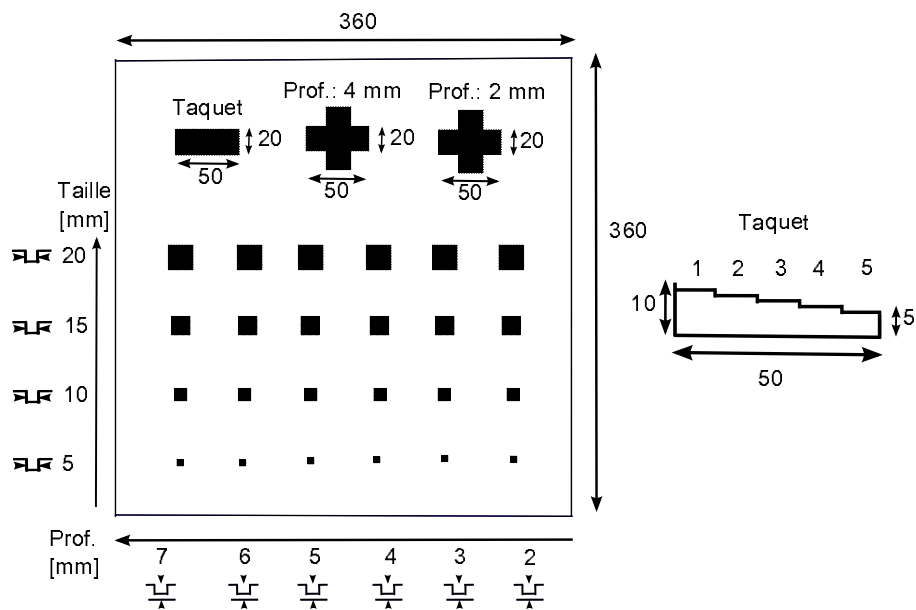
Figure 7.22: Schéma de la plaque II avec des défauts carrés et en forme de croix. Les dimensions sont données en mm.

Les matériaux composites renforcés en fibres de carbone

Les matériaux composites présentent un intérêt grandissant dans le domaine de l'aéronautique. Depuis les années 1975, le pourcentage des matériaux composites n'a fait que grandir dans les avions d'Airbus et les hélicoptères d'Eurocopter. Grâce à de bonnes propriétés mécaniques (résistance contre la fatigue et la corrosion) et à une masse volumique moins importante que celle des métaux, les constructeurs ont décidé d'introduire ce nouveau matériau dans les aéronefs. Parmi les matériaux composites, les matériaux composites renforcés en fibres de carbone sont les plus utilisés. Ils sont constitués de 60% de fibres et

40% de résine.

Deux plaques d'une épaisseur de 1 cm ont été produites pour la partie expérimentale en utilisant des fibres pré imprégnées dans la résine. Des trous de différentes tailles et profondeurs ont été percés à l'arrière des plaques pour simuler des défauts. La première plaque contient des trous de forme circulaire (Fig. 7.21) et la seconde des trous de forme carrée ainsi que des croix (Fig. 7.22).

Thermographie lockin

Avec la thermographie lockin, l'objet est illuminé avec une source lumineuse modulée de façon sinusoïdale. Les ondes thermiques se propagent dans le matériau et sont réfléchies aux frontières thermiques telles des inclusions ou cavités. Ces ondes réfléchies interfèrent à la surface du matériau avec les ondes incidentes et viennent créer un profil de température à la surface qui est enregistré par une caméra infrarouge (Fig. 7.23). Les images d'amplitude Am_n et de phase Φ_n sont calculées en utilisant la transformée de Fourier que l'on obtient par

$$F_n = \Delta t \sum_{k=0}^{N-1} T(k\Delta t)e^{-j2\pi nk/N} = \text{Re}_n + \text{Im}_n \tag{7.11}$$

où n représente le numéro des fréquences d'échantillonnage discrètes $n \in \{1,...,N\}$, Δt l'intervalle d'échantillonnage et Re_n et Im_n les parties réelles et imaginaires de la transformée de Fourier. Les images d'amplitude et de phase sont obtenues par les relations

$$Am_n = \sqrt{\text{Re}_n + \text{Im}_n}$$
$$\phi_n = \tan^{-1}\left(\frac{\text{Im}_n}{\text{Re}_n}\right). \tag{7.12}$$
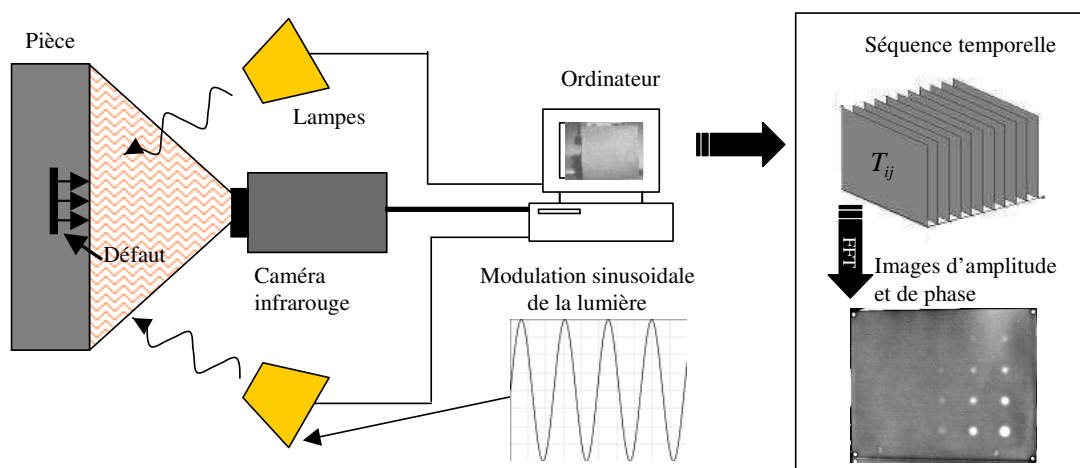
Figure 7.23: Principe de la thermographie optique lockin.

Avec la thermographie lockin, il existe une relation donnée par

$$d = C\mu \tag{7.13}$$

entre la profondeur d'un défaut d et la pénétration thermique μ qui est liée à la fréquence d'excitation f car $\mu = \sqrt{\frac{\alpha}{\pi f}}$. La constante C vaut environ 2 ($C \approx 2$) d'après [Bus79] et α représente le coefficient de diffusion thermique. Cette propriété est utilisée pour retrouver la profondeur des défauts. Ainsi, la fréquence d'excitation ou lockin doit être assez petite pour pouvoir observer des défauts profonds et doit correspondre à au moins une fois la pénétration thermique [She97]. Sur la Fig. 7.24, les images de phase de la plaque I sont représentées pour différentes fréquences d'excitation. Les défauts apparaissent plus clairs que le fond, disparaissent puis réapparaissent pour des fréquences plus basses en étant cette fois-ci plus foncés que l'arrière plan. Cette fréquence aveugle où les défaut disparaissent se nomme 'fréquence aveugle' et sera notée f_b ('blind frequency' en anglais). La profondeur du défaut est déterminée par

$$d = C\sqrt{\frac{\alpha}{\pi f_b}}. \tag{7.14}$$

Cependant, comme l'ont fait remarquer [She97], cette relation est valable que pour des défauts de grandes tailles, les défauts plus petits disparaissant déjà plus tôt. Il existe une loi empirique [She97] affirmant que la taille du défaut doit être au moins égale au double de sa profondeur pour pouvoir être détecté.

(a)   (b)   (c)   (d)
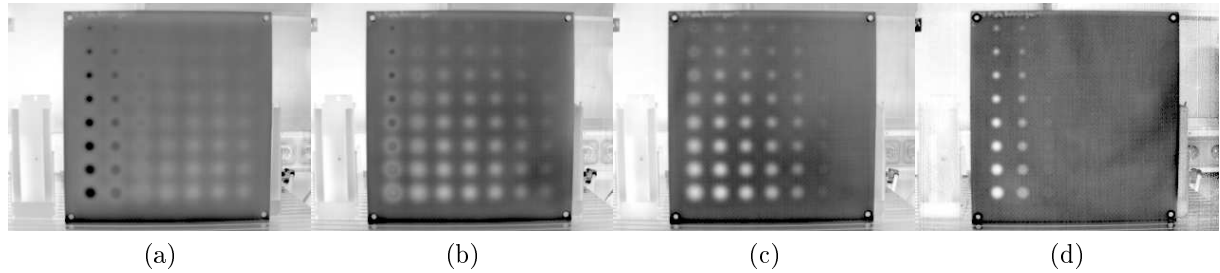
Figure 7.24: Exemple d'images de phase de la plaque I obtenues par thermographie lockin pour des fréquences d'excitation de (a) 0.05 Hz, (b) 0.01 Hz, (c) 0.02 Hz et (d) 0.08 Hz.

Modèle théorique

Les équations décrivant les phénomènes mis en jeux sont les équations de la conduction thermique. Le flux thermique selon la loi de Fourier est donné par

$$q = -\Lambda T_{,i} = -k_{ij}T_{,i}, \tag{7.15}$$

en utilisant la notation d'Einstein. Λ est le tenseur de conductivité thermique

$$\Lambda = \begin{bmatrix} k_{11} & k_{12} & k_{13} \\ k_{21} & k_{22} & k_{23} \\ k_{31} & k_{32} & k_{33} \end{bmatrix}. \tag{7.16}$$

On obtient l'équation de la chaleur dans un corps anisotrope

$$\rho C_P \dot{T} - (k_{ij}T_{,i})_{,j} = a \qquad (7.17)$$

où a est la quantité de chaleur des sources volumiques. Si le matériau est de plus homogène, on obtient

$$\rho C_P \dot{T} - k_{ij}T_{,ij} = a. \qquad (7.18)$$

Dans un corps isotropique et homogène, l'équation devient

$$\frac{1}{\alpha}\dot{T} - T_{,ii} = \frac{1}{k}a. \qquad (7.19)$$

Un changement de variable permet de passer du corps isotrope au corps anisotrope en effectuant l'opération

$$x_i \rightarrow x_i\sqrt{\frac{k_i}{k}}. \qquad (7.20)$$

Différents modèles à une dimension [BP82, BW01] ou tenant compte du flux thermique tridimensionnel [FHSW92, SH$^+$95, SLW$^+$97, PA08] ont été précédement développés. Pour le cas d'un matériau anisotrope, un modèle à une dimension a été développé pour un système à n couches [BW01]. [VIN84] a calculé une fonction anisotrope et présenté des simulations théoriques.
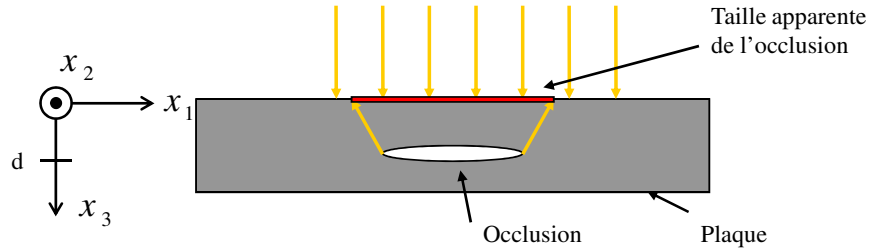
Figure 7.25: Schéma de la plaque supposée être suffisamment épaisse (modèle semi-infini) avec une occlusion plate située à une profondeur d. Dû à la diffusion thermique, un défaut apparaîtra plus grand et flou à la surface du matériau.

Dans ce travail, une fonction de point similaire à celle de [FHSW92] est déterminée en utilisant les fonctions de Green. L'image thermographique obtenue peut être modélisée par la convolution entre la fonction de point et la forme du défaut:

$$I = I_o \otimes h \qquad (7.21)$$

où I est l'image enregistrée floue, I_0 l'image nette et h la fonction de point ($\otimes$ désigne le produit de convolution). La formation d'images est modélisée dans un cas simple de matériau isotrope (Fig. 7.25) en utilisant les fonctions de Green et la théorie de Mandelis sur les champs harmoniques. La fonction de point (Eq. 7.23) détermine comment sera

représenté un point sur une image thermographique à une profondeur et fréquence lockin données. Pour un corps isotrope, on trouve pour le contraste de phase

$$h_{\Delta\Phi}(x_1, x_2; f_0, d) =$$
$$\mathrm{Im}\left[\frac{F_0}{4\pi k} \cdot R^2 \cdot \frac{\sigma^2 \cdot e^{-\sigma \cdot (r+d)}}{r} \left(\frac{d}{r}\left(1 + \frac{1}{\sigma r}\right) + 1\right)\right] \tag{7.22}$$

où $r = \sqrt{x_1^2 + x_2^2 + d^2}$, d est la profondeur du défaut, f est la fréquence d'excitation lockin, $\sigma = (1+i)\sqrt{\frac{\pi f}{\alpha}}$ et Im représente la partie imaginaire d'un nombre complexe. Un changement de variables permet de passer du cas isotrope au cas anisotrope [CJ46] et d'obtenir la fonction de point du contraste de phase pour un corps anisotrope

$$h_{\Delta\Phi a}(x_1, x_2; f_0, d) = \mathrm{Im}\left[\frac{F_o}{4\pi k} \cdot R^2 \cdot \frac{(1+i)^2}{\mu_1\mu_2\mu_3} \cdot \frac{e^{-(1+i)\left(r+\frac{d}{\mu_3}\right)}}{r} \cdot \right.$$
$$\left. \left(\frac{d}{\mu_3 \cdot r}\left(1 + \frac{1}{(1+i)r}\right) + 1\right)\right] \tag{7.23}$$

où $r = \sqrt{\frac{x_i^2}{\mu_i^2}}$ et $\mu_i = \sqrt{\frac{k_i}{\pi f_0 \rho C_P}} = \sqrt{\frac{\alpha_i}{\pi f_0}}$, $i \in \{1..3\}$ est la pénétration thermique.
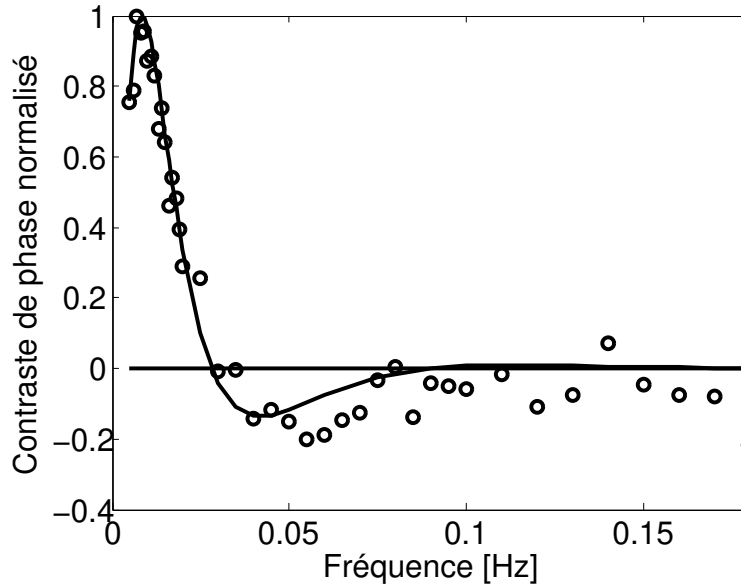
Figure 7.26: Correspondance entre modèle théorique et mesures de phase pour un défaut situé a une profondeur de 3 mm et de taille 20 mm.

Sur la Fig. 7.26, on voit que valeurs théoriques et mesures expérimentales correspondent de façon satisfaisante. Un défaut est mieux détecté si on choisit une fréquence d'excitation où le rapport signal bruit est maximum. Sur la Fig. 7.26, on constate qu'il y a une fréquence dite 'fréquence optimale' [BW01] pour laquelle le contraste de phase est maximum. Cependant, à cette fréquence, un défaut sera plus flou qu'à une fréquence plus élevée. C'est pourquoi une fréquence située entre les fréquences optimale f_o et aveugle f_b selon l'équation

$$f_{deconv} = f_o + \frac{f_b - f_o}{4} \tag{7.24}$$

est choisie pour déconvoluer un défaut. Les figures Fig. 7.28 et Fig. 7.27 montrent les mesures thermographiques de phase de différents défauts situés à plusieurs profondeurs et pour différentes fréquences lockin. Mesures et simulations correspondent bien.
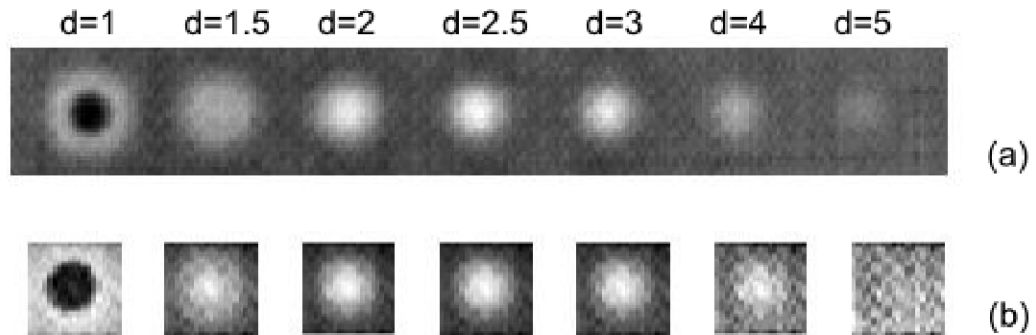
Figure 7.27: (a) Mesures thermographiques de phase d'un défaut à plusieurs profondeurs et (b) simulations correspondnates des défauts en prenant $\alpha = 0.28$ mm$^2 \cdot s^{-1}$ pour une fréquence lockin de 0.01 Hz.

Résultats

Ainsi, par un problème inverse (déconvolution), la taille du défaut peut être retrouvée. Un défaut extrait d'une image thermographique de phase à 0.02 Hz est illustré sur la Fig. 7.29. La forme du défaut est bien estimée en appliquant un algorithme de déconvolution. L'implémentation de l'algorithme de Richardson-Lucy [Luc74, Ric72] du programme informatique Matlab [2] est utilisé. Cependant, la profondeur du défaut doit être connue à priori.

Un algorithme informatique à été développé. Dans un premier temps, la profondeur du défaut est retrouvée en utilisant la fréquence aveugle (Eq. 7.13). Ensuite les défauts sont classifiés par régions puis déconvolués. Les étapes de l'algorithme sont les suivantes:

1. Mesures thermiques et obtention d'une séquence d'images de phase pour différentes fréquences d'excitation.

2. Calcul du contraste de phase pour chaque image de phase en utilisant un algorithme de soustraction de l'arrière plan.

3. Dans chaque image de contraste de phase, segmentation des défauts par la méthode du SNR.

4. Détermination de la fréquence aveugle f_b puis de la profondeur par la relation $d(i,j) = 2.3 \times \sqrt{\frac{\alpha}{\pi f_b(i,j)}}$.

5. Clustering des défauts.

---

[2]www.mathworks.com

(a) Image de phase 2 mm

(b) Simulation 2 mm

(c) Image de phase 3 mm

(d) Simulation 3 mm

(e) Image de phase 4 mm
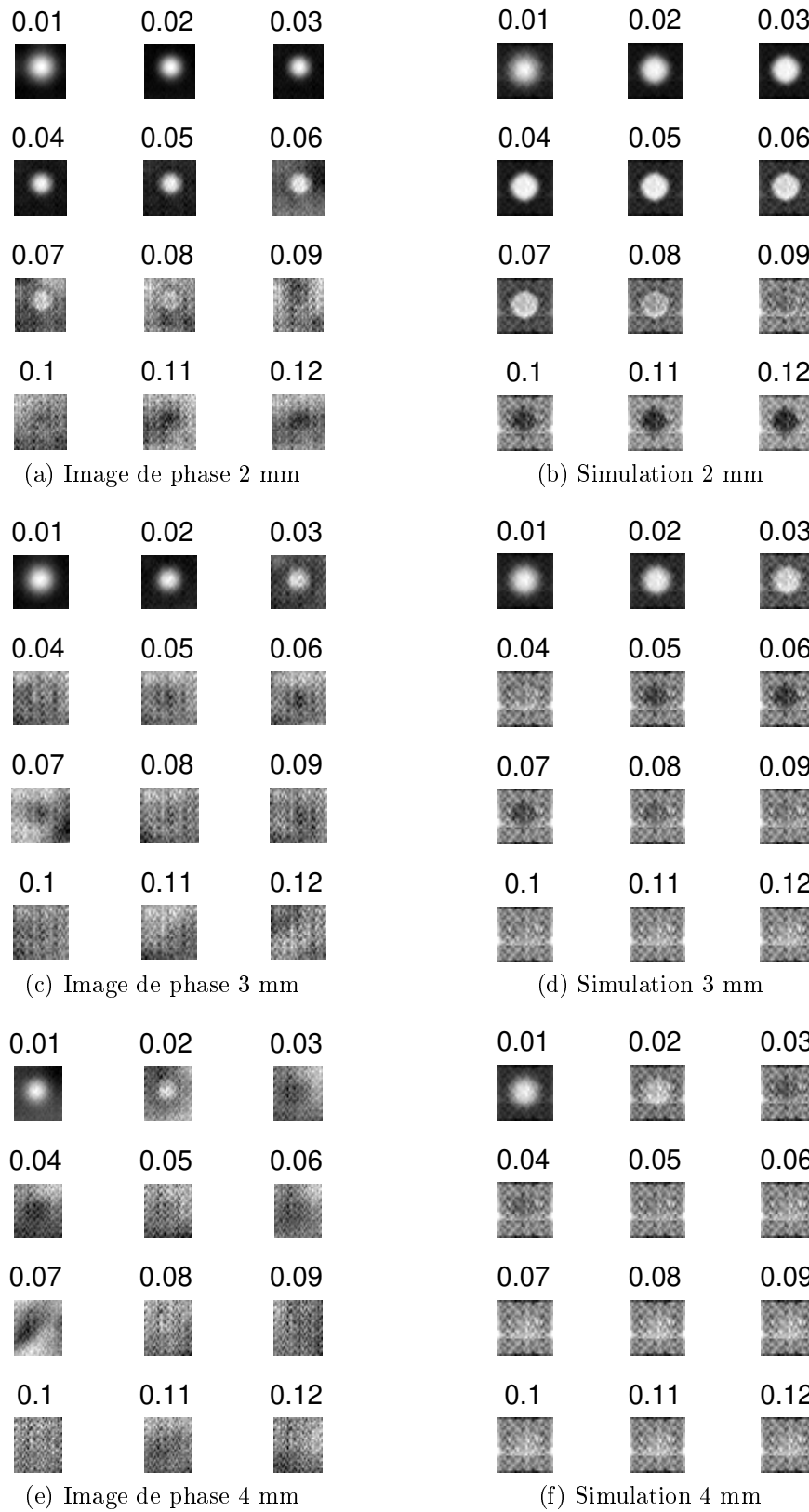
(f) Simulation 4 mm

Figure 7.28: (a-c-e) Mesures thermographiques de phase et (b-d-f) simulations d'un défaut à plusieurs profondeurs et à plusieurs fréquences lockin en prenant $\alpha = [0.5\ 0.5\ 0.27]$ mm$^2 \cdot s^{-1}$.

1. Amélioration de l'estimation de la profondeur par une régression entre la fonction du contraste de phase du modèle théorique et du centre du défaut.

2. Déconvolution de chaque défaut individuellement en prenant la fréquence $f_{deconv} = f_o + \frac{f_b - f_o}{4}$.

3. Obtention d'une carte des défauts indiquant leur profondeur.

L'algorithme a été appliqué sur une plaque I contenant des défauts de profondeurs et tailles différentes. Les positions et tailles des défauts sont bien estimées (Fig. 7.30). Les profondeurs retrouvées avec les domaines d'erreurs sont représentées sur la Fig. 7.31. La valeur moyenne des défauts estimée est représentée avec les domaines d'erreur maximum. Les défauts de diamètre supérieur à 10 mm sont estimés avec une marge d'erreur de 20 %. Les défauts de diamètre 8 mm ont une imprécision de 13 à 36 %, l'imprécision de 36 % étant atteinte pour le défaut profond à 4 mm. Les profondeurs des défauts de taille 6 mm ont une imprécision de 27 à 58 %. La déviation maximale est atteinte pour des défauts petits et profonds (4 mm de profondeur, 8 mm de diamètre).
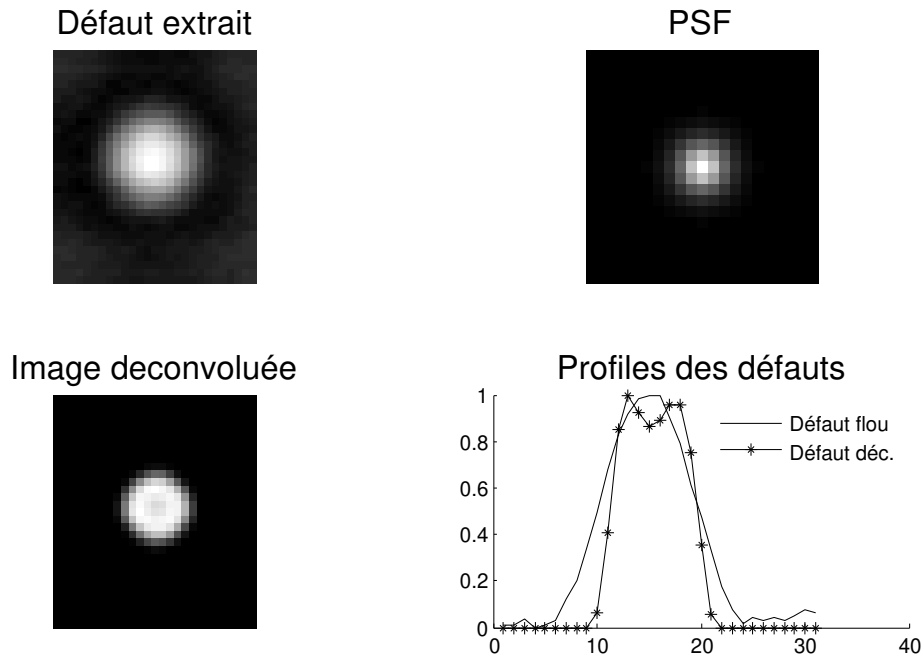
Figure 7.29: Image de phase (0.02 Hz) floue d'un défaut situé à 2 mm de profondeur et image du défaut déconvolué en utilisant la fonction de point (PSF). Les profils des défauts avant et après déconvolution sont superposés sur le diagramme du bas à droite.

La Fig. 7.32 montre les diamètres des défauts retrouvés. La taille est bien estimée pour des grands défauts. Pour les défauts de taille entre 12 et 20 mm, la précision maximale est de 20 %. Pour les défauts de diamètre entre 6 et 10 mm, la précision est entre 3.2 et 78 %. Les diamètres sont mieux retrouvés pour des défauts situés à une profondeur entre 1 et 2 mm: l'imprécision est dans ce cas de 6 %. A partir d'une profondeur de 2 mm, l'imprécision est entre 13 et 78 %. Les défauts situés à 5 mm de profondeur apparaissent plus petits et les défauts de taille inférieure à 10 mm ne sont pas détectés à cette profondeur.
Ensuite, l'algorithme est testé sur la plaque II contenant des défauts de forme carrée et en forme de croix. La Fig. 7.33 représente différentes images de phase obtenue pour différentes
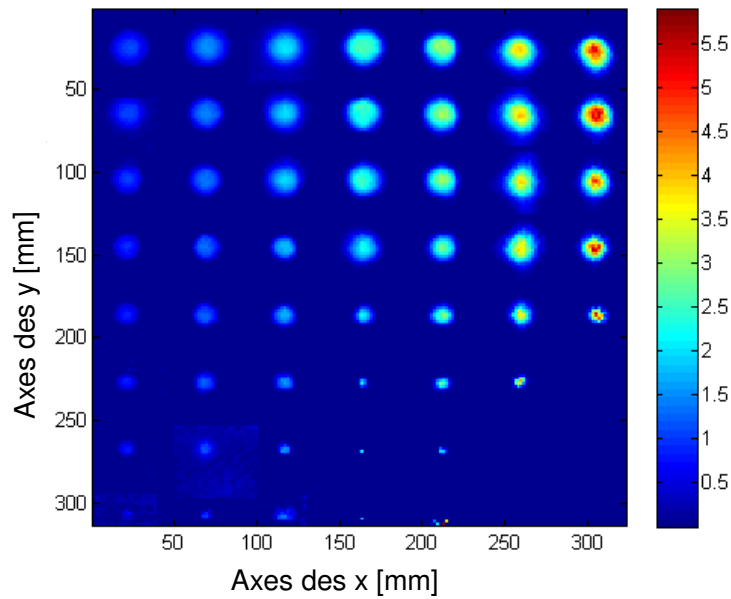
Figure 7.30: Reconstruction des profils des défauts par application de l'algorithme sur toute la plaque. La barre colorée sur la droite indique la profondeur des défauts en mm.
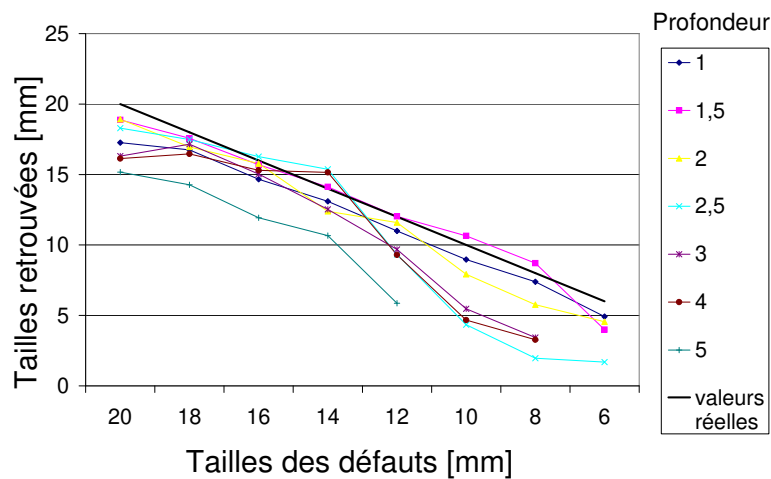
Figure 7.31: Représentation schématique des profondeurs estimées des défaut [mm].

fréquences d'excitation. L'effet de la fréquence aveugle peut à nouveau être observé à la fréquence d'excitation de 0.005 Hz pour un défaut situé à 1 mm de profondeur. La Fig. 7.34 montre la déconvolution d'un défaut carré situé a 2 mm de profondeur. Le résultat de la déconvolution des deux croix situées à 2 mm et 4 mm de profondeur est montré sur les Fig. 7.35 et Fig. 7.36, respectivement. Les défauts sont déconvolués à des fréquences de 0.03 et 0.009 Hz respectives. Elles correspondent aux fréquences de l'Eq. 7.24.

La carte des défauts de toute la plaque est montrée sur la Fig. 7.34 et la carte finale après application de la déconvolution est sur la Fig. 7.35. La forme de défauts en croix est bien retrouvée.
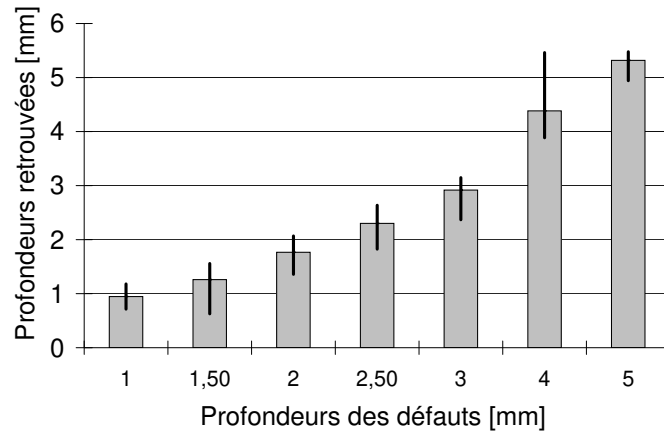
Figure 7.32: Taille des défauts (diamètres) estimée pour différentes profondeurs des défaut [mm].

(a)   (b)   (c)   (d)
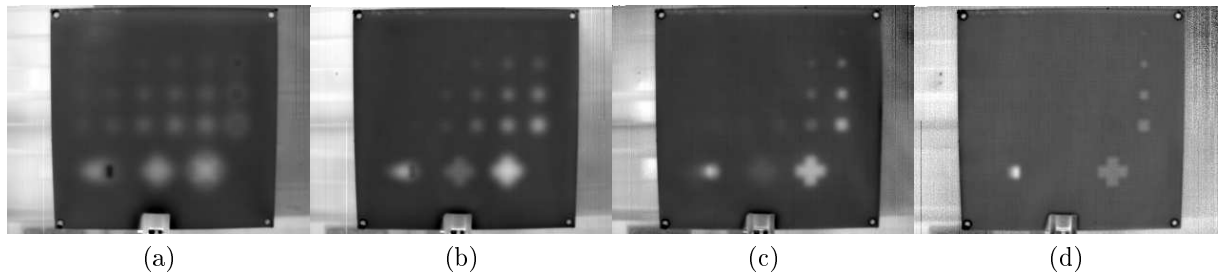
Figure 7.33: Exemple d'images de phase obtenues par thermographie lockin pour des fréquences d'excitation de (a) 0.005 Hz, (b) 0.01 Hz, (c) 0.025 Hz et (d) 0.05 Hz.
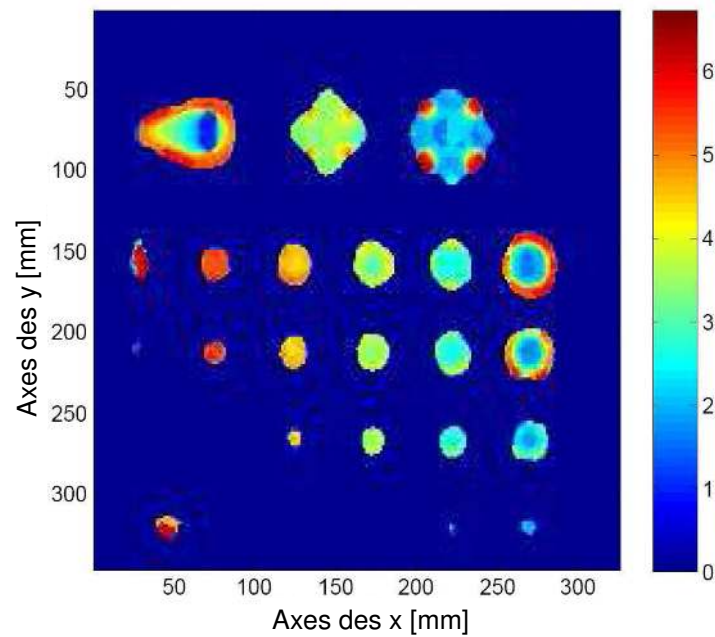
Figure 7.34: Carte des défauts de la plaque II obtenue avant déconvolution. La barre en couleur à droite de l'image code les profondeurs des défauts.
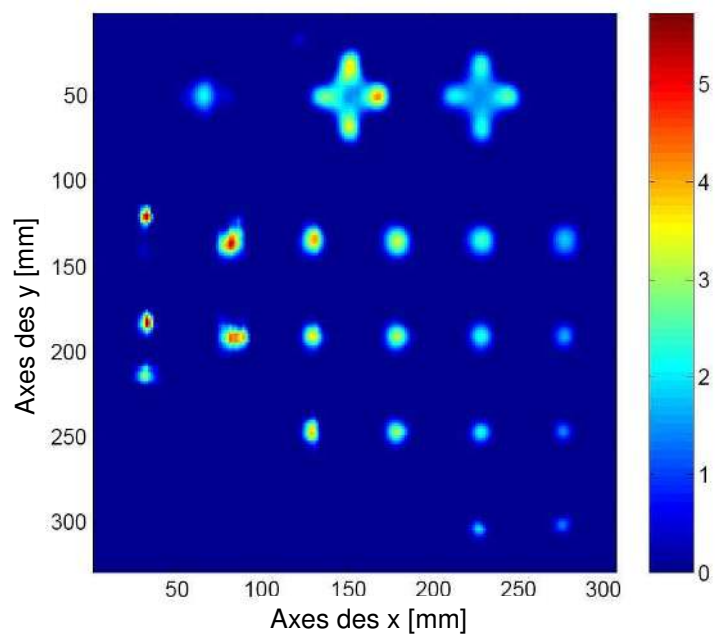
Figure 7.35: Carte de profondeur de la plaque II obtenue après déconvolution. La barre colorée sur la droite indique la profondeur des défauts en mm.
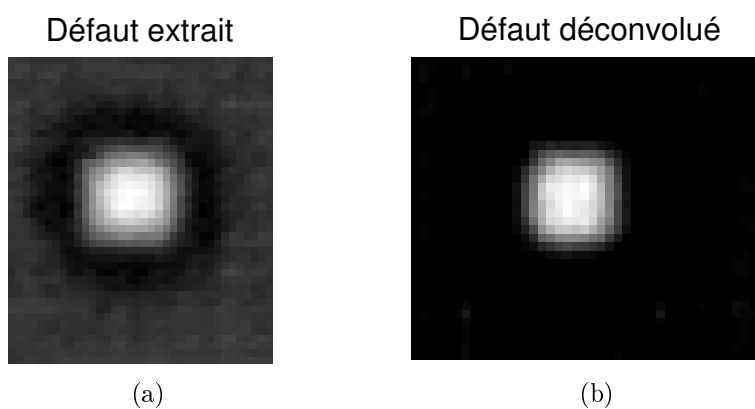
Figure 7.36: Défaut carré extrait et déconvolué de profondeur 2 mm à une fréquence de 0.03 Hz.

Défaut extrait

Défaut déconvolué

(a)

(b)

Défaut extrait

Défaut déconvolué

(c)

(d)
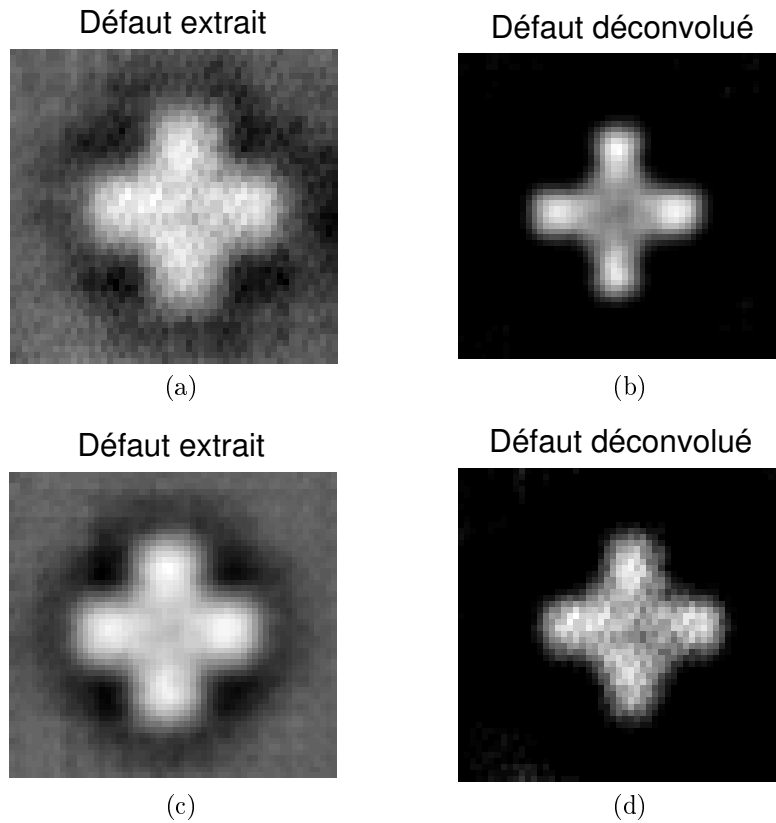
Figure 7.37: Défauts déconvolués situés à des profondeurs de (a-b) 2 mm à une fréquence de 0.03 Hz et de (c-d) 4 mm à une fréquence de 0.009 Hz.
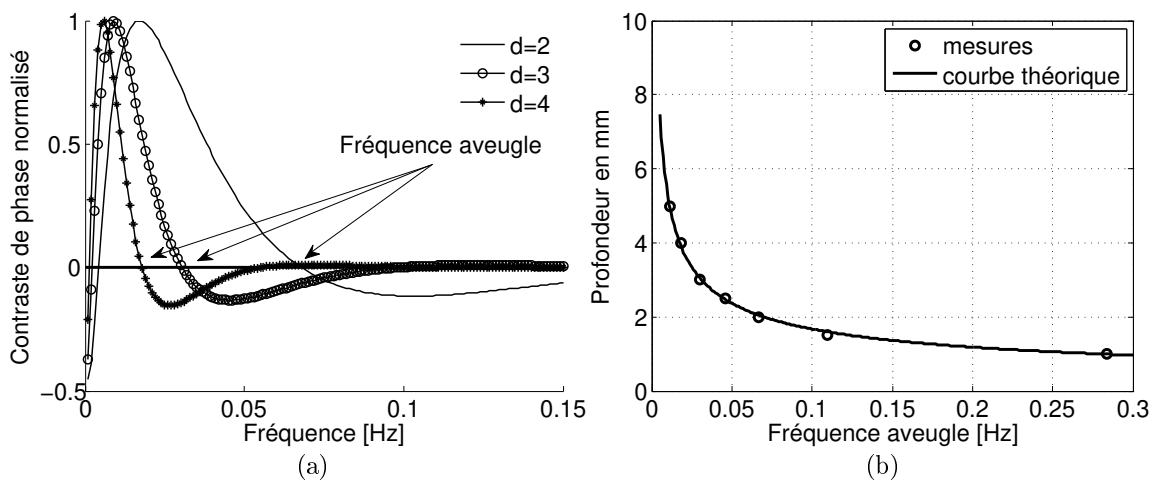
Figure 7.38: (a) Contraste de phase théorique en fonction de la fréquence pour différentes profondeurs de défauts (données en mm); (b) Profondeur en fonction de la fréquence aveugle ($\alpha_z = 0.22 \cdot 10^{-6} m^2 \cdot s^{-1}$)).

Comparaison des défauts

Dans le domaine du contrôle non-destructif, des mesures thermographiques sont effectuées sur des aéronefs puis répétées après un certain délai par exemple durant un contrôle ou après un test de fatigue. Les contrôleurs aimeraient pouvoir déterminer si des défauts ont évolués et pouvoir comparer la taille des défauts. Les systèmes thermographiques actuels ne permettent que d'effectuer les mesures thermographiques mais pas de comparer, superposer ou segmenter des mesures. C'est pour cela que des méthodes de traitement d'images sont développées ici afin de permettre une évaluation quantitative des défauts.

(a)   (b)
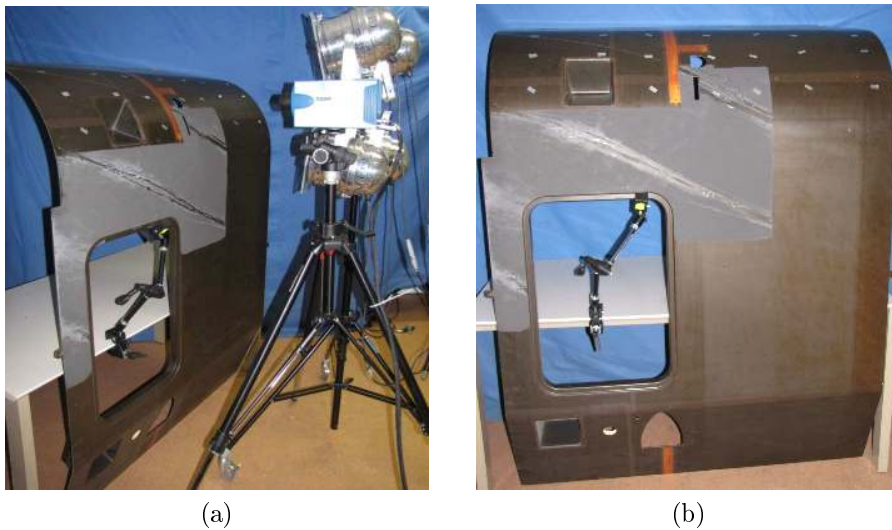
Figure 7.39: (a) Montage thermographique et (b) pièce étudiée. Seulement la partie supérieure courbe de la pièce est étudiée.

Des techniques panoramiques peuvent être utilisées pour superposer des images prises à des instants différents et avec des positions de la caméra différentes. Cependant, pour des surfaces courbes, d'autres techniques doivent être développées. De plus, plusieurs images thermographiques doivent être prises pour des grandes pièces afin d'obtenir une résolution suffisante. Les programmes de création de panoramas ne sont pas apropriés pour des surfaces courbes et doivent être adaptés à une prise de vue proche.

Un test a été effectué sur une pièce courbe mis à disposition par Eurocopter. La Fig. 7.39 montre le montage expérimental et la pièce étudiée. La partie courbe de la pièce (Fig. 7.40) est divisée en cinq parties et les mesures thermographiques sont effectuées avec le système thermographique de l'entreprise Edevis. Des marques artificielles de forme rectangulaire sont utilisées pour introduire des points de référence dans l'image. Les images thermiques prises avant excitation sont préférables aux images d'amplitude et de phase car le contraste des marques est plus important. Les marques sont en aluminium et peuvent être détectées dans des images thermiques car elles possèdent un haut coefficient de réflectivité. La forme rectangulaire est choisie afin de permettre à des détecteurs automatiques comme celui de Harris de détecter des coins. Les marques doivent être fixées sur la pièce. La partie commune de deux images voisines doit être de 60 % et posséder six marques communes. Les points de référence sont détectés soit de façon automatique avec les détecteurs de Harris [ST94], SIFT [Low99] et SURF [BTVG06], soit de façon manuelle grâce à l'interface
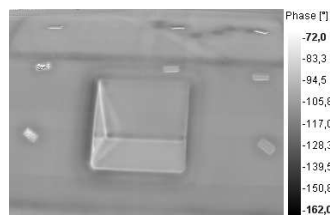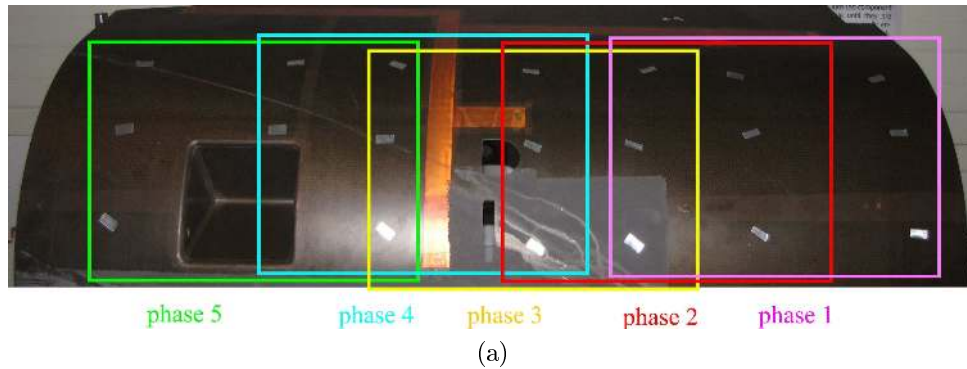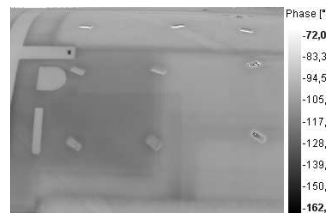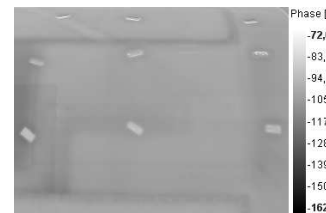
Figure 7.40: (a) La pièce étudiée de la Fig. 7.39 est divisée en cinq parties. Les images (b-f) montrent les cinq images de phase obtenues avec la thermographie lockin à une fréquence de 0.01 Hz.

graphique de Matlab (cpselect tool). La Fig. 7.41 montre les vues panoramiques obtenues à partir des cinq images de phase en utilisant les différents détecteurs de points de référence. Les résultats sont satisfaisants sauf pour l'image de gauche contenant une fenêtre: les images ne sont pas bien assemblées dans certains cas.

La méthode manuelle de sélection des points produit les meilleurs résultats. La méthode SIFT obtient la seconde place et la méthode de Harris fournit les plus mauvais résultats. Une meilleure méthode d'appariement devrait être développée pour ce détecteur de façon à améliorer le nombre de points appariés pour calculer la transformation entre les deux images.

De façon à déterminer le déplacement maximum entre deux images superposées, une structure est segmentée dans chaque image puis superposée (Fig. 7.42). La différence maximale entre deux images est un pixel sauf pour le cas du détecteur de Harris où elle est plus grande.
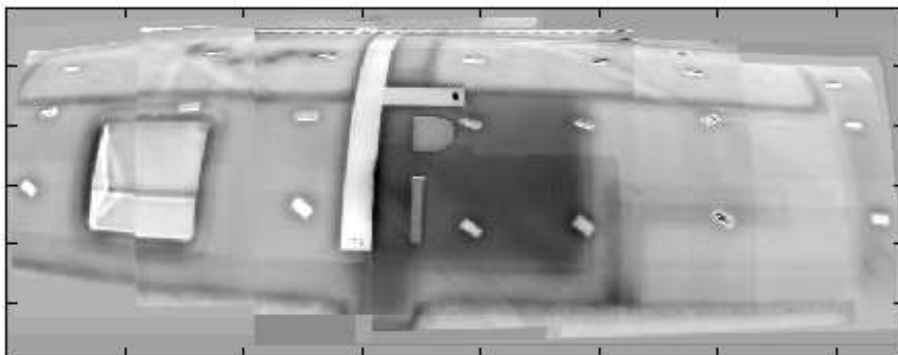
Dans des travaux futurs, la méthode SIFT est préférable pour une détection rapide et automatique de points de référence. La méthode manuelle est à utiliser si une grande précision est demandée et si le facteur temps ne joue pas de rôle.
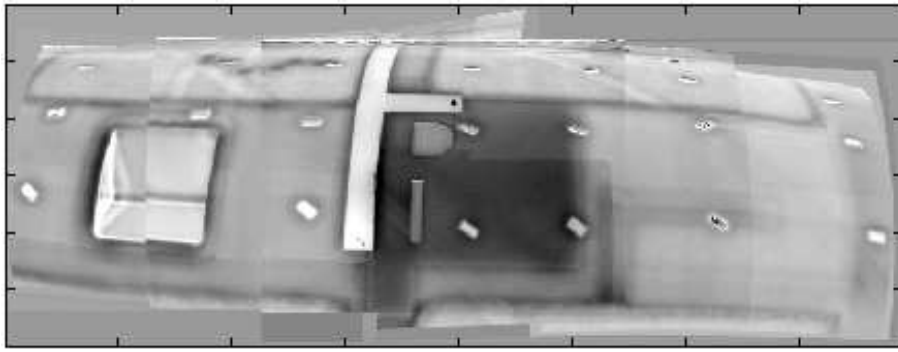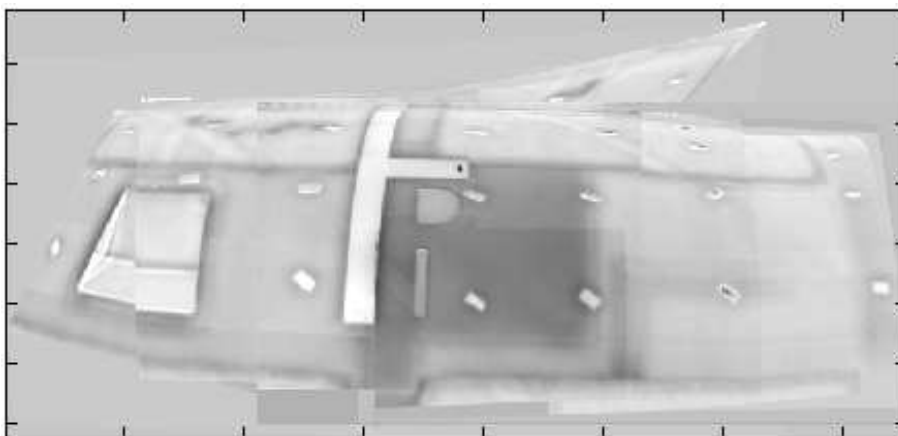
(a)
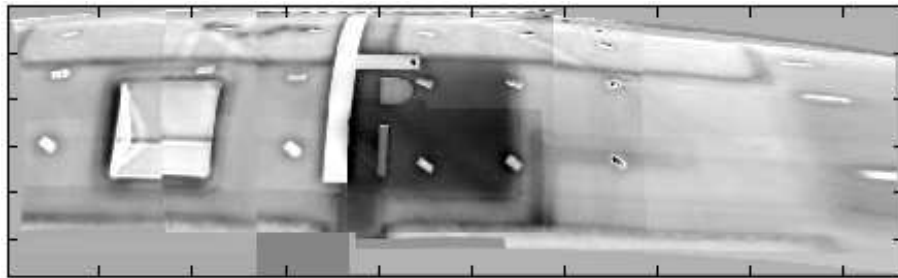
(b)

(c)

(d))

Figure 7.41: Panorama composé de cinq images de phase obtenu par détection (a) manuelle, (b) de Harris, (c) SIFT et (d) SURF de points caractéristiques.
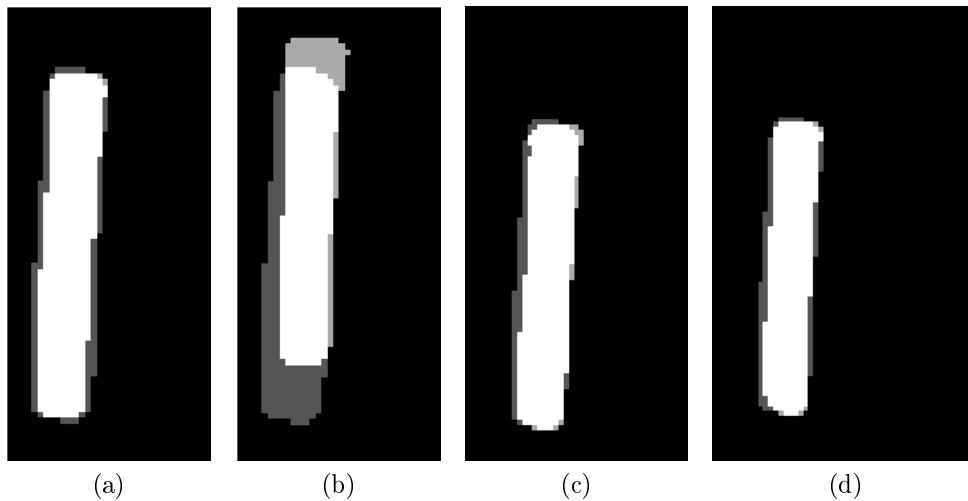
Figure 7.42: Superposition d'une structure segmentée en utilisant les méthodes de détection de points caractéristiques (a) manuelle, (b) de Harris, (c) SIFT et (d) SURF.

Fusion de données

La fusion de données [GLTH00] permet de combiner l'information contenue dans deux ou plusieurs images obtenues par des méthodes d'acquisition différentes. Elle peut être appliquée à n'importe quelle méthode de contrôle non-destructif. De façon à exploiter la complémentarité des méthodes de thermographie lockin et excitées par ultrasons, les images thermiques sont fusionnées.

Figure 7.43: Image de la pièce en matériau composite carbone-époxy (pièce III); (a) Devant de la pièce; (b) Arrière de la pièce.

Les méthodes de thermographie optique lockin et excitée par ultrasons permettent toutes les deux de détecter des impacts, mais l'information contenue dans les images est différente d'une méthode à l'autre: tandis que la thermographie optique lockin permet de détecter le
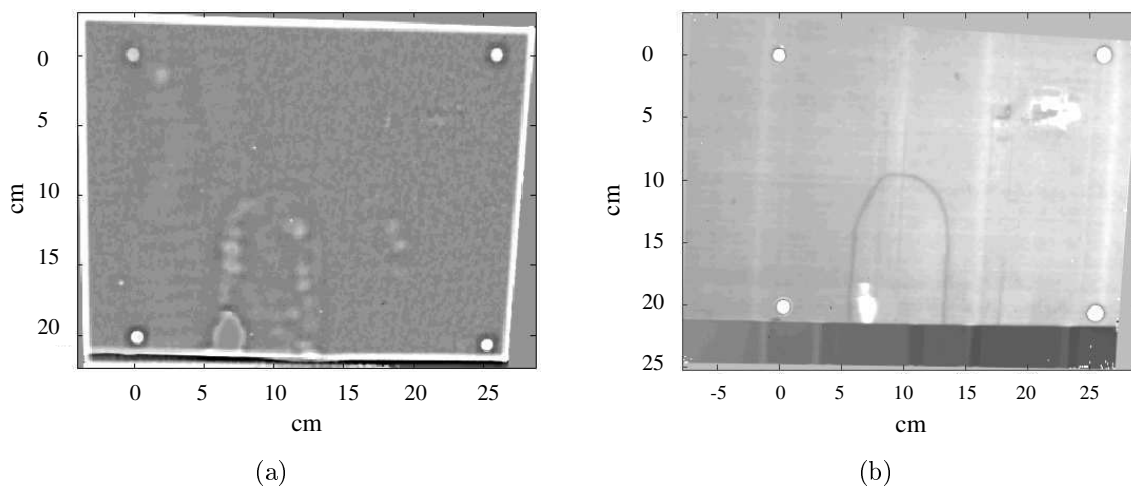
Figure 7.44: Images corrigées par photogrammétrie et introduction d'une échelle de mesure dans les images.
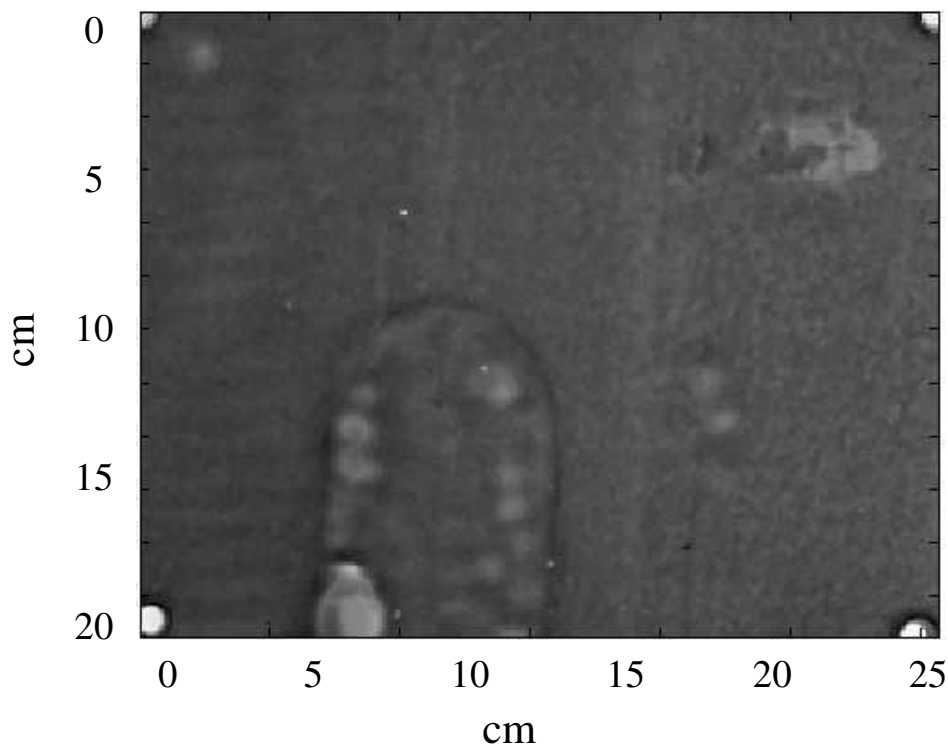

Figure 7.45: Fusion d'images obtenues par les méthodes de thermographie lockin (OLT) et de thermographie excitée par ultrasons (UIT).

centre d'un délaminage où les couches de fibres sont bien séparées, la méthode par excitation ultrasonore permet de détecter les bords des délaminages ou des fissures fermées. La différence est due aux différents mécanismes physiques de détection: avec la thermographie lockin, les ondes thermiques sont réfléchies au niveau des frontières thermiques. Un coefficient de réflexion élevé est nécessaire afin de détecter les ondes réfléchies. Aux bords des délaminages, les couches sont accolées et les ondes thermiques sont transmises. Les bords

ne sont pas détectés. Avec une excitation ultrasonore, des ondes mécaniques pénètrent le matériau. Elles provoquent une friction au niveau des défauts fermés où l'énergie mécanique est convertie en énergie thermique (dissipation) dans un cycle d'hystérésis. Les deux méthodes apparaissent être complémentaires.
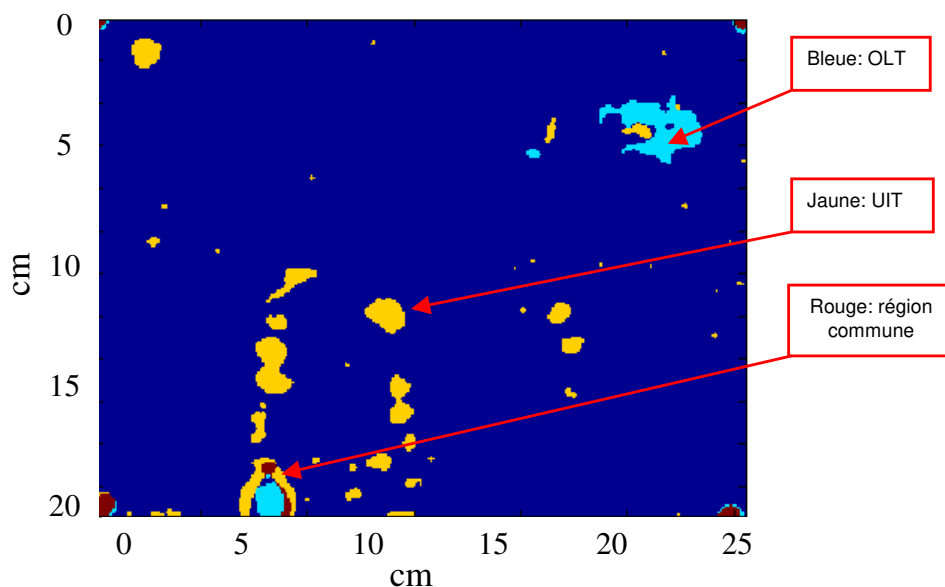

Figure 7.46: Superposition d'images segmentées obtenues par thermographie lockin et excitée par ultrasons. Les parties colorées représentent les défauts: la couleur bleue représente les défauts détectés par thermographie lockin, jaune par thermographie excitée par ultrasons et rouge la partie défectueuse commune aux deux méthodes.

Une expérience est menée sur une pièce de test avionique (pièce III) mise à disposition par Airbus. La pièce est faite en matériau composite renforcé en fibres de carbone et a une dimension d'environ 1 m sur 1.50 m (Fig. 7.43). La pièce possède des délaminages artificiels.

Les défauts sont bien détectés dans les deux images. La Fig. 7.44 montre à gauche l'image de phase obtenue par thermographie lockin et à droite l'image thermographique par excitation ultrasonore. Sur la Fig. 7.45 est représentée la fusion des deux images thermographiques.

Les images thermographiques sont ensuite segmentées afin de mieux visualiser la partie défectueuse. Pour cela, la valeur moyenne et la variance de la distribution gaussienne de l'histogramme sont estimées. Les valeurs des niveaux de gris ayant une valeur supérieure à $\mu+2\sigma$ sont considérées comme étant défectueuses. Les régions segmentées sont superposées et comparées (Fig. 7.46). Pour la segmentation, seule la partie située dans la zone d'intérêt entre les marques est analysée. On constate que la partie commune représentée en rouge est petite. Ceci confirme la complémentarité des deux méthodes. La partie défectueuse peut également être superposée à une image de la pièce entière prise par un appareil photo numérique (Fig. 7.47).

En conclusion, la fusion combine les atouts de plusieurs méthodes complémentaires telles la thermographie lockin et la thermographie excitée par ultrasons. Elle permet d'améliorer
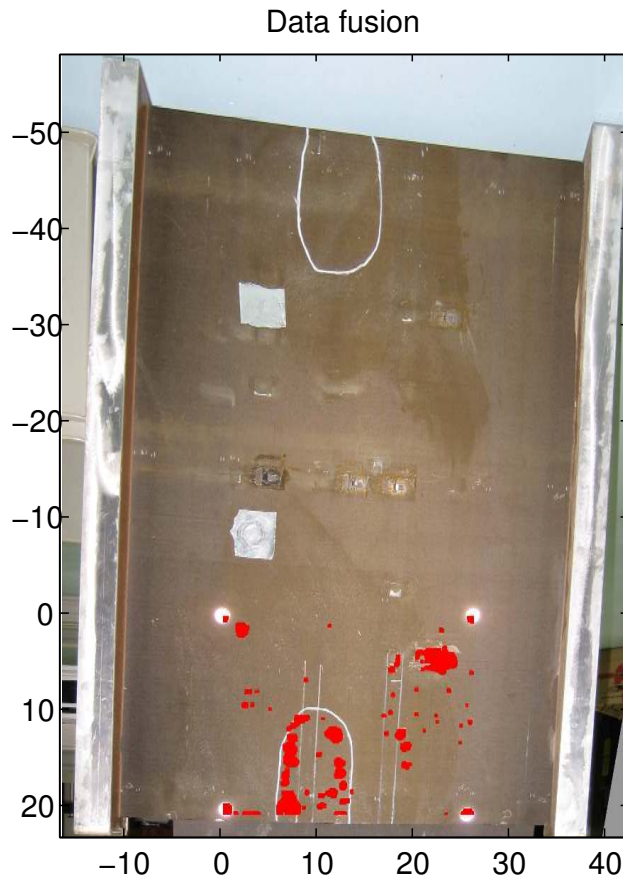
Figure 7.47: Représentation de la partie défectueuse totale sur une image prise par un appareil photo numérique.

la caractérisation quantitative des défauts.

Conclusion

L'analyse quantitative de défauts enfouis dans des matériaux composites destinés à l'aéronautique a été élargie. Ce travail ne s'attache qu'aux défauts planaires. Un mo- dèle théorique sur la formation d'image en thermographie infrarouge a été mis au point pour simuler les défauts détectés par thermographie lockin. Ce modèle permet de retrouver la profondeur et la taille de défauts enfouis, comme par exemple des cavités ou occlusions et de retrouver la forme du défaut par une déconvolution. Des simulations numériques ont été effectuées et comparées aux mesures et montrent bien la concordance des mesures avec le modèle thérorique.

Un algorithme a été mis au point pour retrouver taille et profondeur des défauts. Afin de combiner et superposées des images de méthodes thermographiques différentes, des méthodes de traitement d'images on été développées. Pour de surfaces courbes, une transformation d'ordre deux est prise et le détecteur SIFT s'avère être le meilleure après la sélection automatique de points de référence. Les méthodes de superposition sont appliquées pour fusionner des images de méthodes thermiques excitées par ultrasons et par méthode optique et une photographie de la pièce. La fusion permet de détecter l'ampleur du défaut.